Universiteit Gent
Faculteit Ingenieurswetenschappen en Architectuur
Vakgroep Informatietechnologie

Ontvangers gebaseerd op ringresonatoren in silicium voor optische interconnecties met meerdere golflengtes

Receivers Based on Silicon Ring Resonators for Multi-Wavelength Optical Interconnects

---

Peter De Heyn

Proefschrift tot het bekomen van de graad van
Doctor in de Ingenieurswetenschappen:
Fotonica
Academiejaar 2013-2014

Universiteit Gent
Faculteit Ingenieurswetenschappen en Architectuur
Vakgroep Informatietechnologie

Promotoren: Prof. dr. ir. Dries Van Thourhout
dr. ir. Joris Van Campenhout

Examencommissie:

Prof. dr. ir. Luc Taerwe (voorzitter)	Universiteit Gent, prodecaan
Prof. dr. ir. Dries Van Thourhout (promotor)	Universiteit Gent, INTEC
dr. ir. Joris Van Campenhout (promotor)	IMEC
Prof. dr. ir. Wim Bogaerts	Universiteit Gent, INTEC
Prof. Xin Yin	Universiteit Gent, INTEC
dr. Francesco Morichetti	Politecnico di Milano, DEIB
dr. Nicola Calabretta	TU Eindhoven, COBRA
dr. ir. Wouter Rogiest	Universiteit Gent, TELIN

Universiteit Gent
Faculteit Ingenieurswetenschappen en Architectuur

Vakgroep Informatietechnologie
Sint-Pietersnieuwstraat 41, B-9000 Gent, België

Tel.: +32-9-264.33.16
Fax.: +32-9-331.35.93

Dit werk kwam tot stand in het kader van het ERC-project ULPPIC en het EU project ICT-BOOM.

Proefschrift tot het behalen van de graad van
Doctor in de Ingenieurswetenschappen: Fotonica
Academiejaar 2013-2014

Dankwoord

Leuk, m’n boek is af en het bewijs heb je vast. Doctoreren: ✓.

Nice, maar ... wat is dat nu doctoreren? Het antwoord op die vraag wordt meestal beinvloed door perceptie. Voor sommigen ben je een gezellige flierefluiter die morgen bovendien kan uitslapen, voor een enkeling een ware held maar voor velen eerder een veredelde ambtenaar. Een dik boek schrijven met moeilijke woorden die niemand begrijpt en klaar is Kees. Natuurlijk hebben jullie allemaal een beetje gelijk. Zo gaat dat met percepties...

In mijn perceptie is succesvol doctoreren een makkie. Achteraf gezien toch. Het enige wat je nodig hebt is een grote dosis doorzettingsvermogen, een strakke gedrevenheid, toch wat inzicht in de zaak en een tikkeltje creativiteit. En als je al die eigenschappen niet allemaal hebt, ben je best maar sociaalvaardig genoeg om op zoek te gaan naar die mensen die er toch genoeg van hebben.

Het enige wat ik had toen ik aan mijn studies begon in 2004, was dat doorzettingsvermogen. Dat is iets dat ik met de paplepel en later met schouderklopjes van mijn ouders heb meegekregen. Steeds waren jullie daar om me met volle overtuiging in mezelf te laten geloven. Waar een wil is, is een weg. Dat is steeds jullie leuze geweest en nu ook de mijne. In mijn geval vaak met vallen en opstaan maar goed, zo gaat dat.

Al tijdens mijn eerste master jaar fotonica, wist ik dat ik wou doctoren. Ik denk dat het 1 van die simulatie practica was van professor Roel Baets waar we te maken kregen met een typisch probleem: de ringresonator, jaja die bestond toen al! En als ik me niet vergis was het het enthousiasme van assistent Tom Claes, nu collega en vriend en zelf grote fan van ringen, die mijn hartstocht heeft getriggerd. Zo zie je maar.

Toen ging het allemaal snel, het verhaal zou anders maar saai worden en voor ik het wist mocht ik in 2009 op gesprek komen bij Dries. Die voelt zich nog steeds ongemakkelijk als ik hem professor noem, dus ik zal het nu ook niet doen... Ik herinner me vooral dat je zei dat ik met mijn onderwerp wel eens werk zou kunnen vinden. Opgelet: in de fotonica, in Belgie, en dat buiten de academische wereld. Wow, van een visie gesproken Dries! Het was wel die visie die me over de streep heeft gehaald en voor de eerste gedrevenheid heeft gezorgd.

Alle begin is moeilijk en dat is ook zo bij een doctoraat. Bij mij liep het al mis na een half jaar wanneer ik te horen kreeg dat ik geen beurs kreeg. Het IWT geloofde er niet helemaal in. Achteraf gezien hadden ze ongelijk natuurlijk maar wel een serieuze deuk in mijn zelfvertrouwen. De wonderen zijn de fotonicawereld nog niet uit en voor ik het wist had Dries een beurs voor mij geregeld. Nogmaals bedankt voor het vertrouwen, Dries.

Elke beginnende doctoraatstudent heeft zijn zelfvertrouwen op een zeer laag pitje staan. Dat blijft meestal zo tot aan je eerste eigen succes, hoeveel je promotor ook in je gelooft. Het is dan ook van uiterst belang dat je dat succes zo snel mogelijk boekt. Mijn mentoren Diedrik en Bart, jullie hadden dat zelf al snel door en hebben me meteen op sleeptouw genomen. Dat betekende onderzoek gericht op inzicht, creativiteit, snelheid en durf. Wow, een manier van werken die ik nog steeds als leidraad gebruik. Weet je nog onze zotte L-golfgeleider, Bart? Dankzij jullie denkpatroon heb ik dan ook mijn eerste successen geboekt. Voor ik wist mocht ik naar Los Angeles om mijn ’TM’ idee te gaan verkondigen op de grootste conferentie in de fotonica. Met als kers op de taart een volledige afdaling in de Grand Canyon. Wat een ’awesome’ ervaring hé Thijs!

In mijn tweede jaar kreeg ik dan een nieuwe buur, den Thomas, die het liefst van al heel de dag zo veel mogelijk formules op 1 blad opschrijft. Leek me raar... Samenwerken met Thomas leek mij dan ook initieel niet zo nuttig. Maar wat bleek nu, Thomas kon net die dingen die ik niet kon. En al snel waren we een top team met als persoonlijk hoogtepunt het automatisch aansturen van de Agilent laser. Hierdoor konden onze componenten 100× sneller worden opgemeten. Ik weet nog goed hoe euforisch we waren die dag! Ook met Pauline, Martijn en Thijs kende we een enorm succes maar dan in de cleanroom. Met een eenvoudige stap konden we het rendement van een dagdagelijkske BCB bonding vertienvoudigen. Heerlijk zo van die bottom-up ontdekkingen. Achteraf bekeken zijn het net die kleine dingen die mij zo gedreven hielden.

Nadat ik helemaal op dreef was gekomen was het tijd voor verandering, ik wou, net als Bart en Diedrik, naar het buitenland, op avontuur! Eigengekozen bestemming: het Fraunhofer Institute HHI in Berlijn. Hier kon ik mij in de coolste stad van Europa bijscholen over detectoren en integratie. Wederom bedankt Dries, dat waren 6 fantastische maanden. Eenzaam was ik daar niet, elk weekend waren er vrienden op bezoek, alsook Dries zelf met zijn gezinnetje.

De trein van opportuniteiten stopte niet. Toen ik terugkwam uit Berlijn werd ik bijna letterlijk opgezogen door Joris uit imec. Wow, ik werd gevraagd door imec! Nu was het menens dacht ik. Ja Joris, daar ben je goed in, in mensen motiveren. Onze manier van werken klikte goed, al van dag 1. Resultaat gedreven ’work hard - play hard’. Ik ben blij dat ik uw team mocht vervoegen bij imec.

Verder wil ik nog een heleboel andere mensen bedanken. Professoren Gunther en Wim, jullie stonden letterlijk altijd voor mij paraat. Meetkamerspecialisten, Jeroen (imec) en Michael, zonder jullie hulp hadden mijn metingen nu nog niet afgeweest. Merci Steven voor al je hulp tijdens de fabricage van mijn detectoren, vooral toen ik in Berlijn zat en jij dus alles alleen hebt gedaan. Liesbeth, mijn favorietje aan de FIB, ik ga toch vooral onze gezellige kajaktocht onthouden! Jeroen en Andrea, voor de vele ontspannende surfsessies tijdens de werkuren (maar daarna rechtmatig ingehaald hoor, Roel). En dan heb je nog die meer dan 50 andere leeftijdsgenoten uit alle hoeken van de wereld, te veel om op te noemen. Please forgive me that I don’t mention your name. Eva, Thijs, Thomas, Diedrik, Bart, Yannick, Martijn, Raphael, Pieter en de zovele anderen, bedankt voor de zalige werksfeer.

Ook de vele vrienden toonden veel interesse in mijn werk, en steeds weer kreeg ik de kans om te zeggen waar ik mee bezig was. Vooreerst de Mengelemoezers: Peech, Pipes, Steven („Doet IBM dat al niet?”), Tim („Hoe zit het met die ringoscillators?”) en Willy. Willy heeft zich 4 jaar lang bezig gehouden met mensen te vertellen dat ik aan fotogenetica deed, bedankt. The girls: Hanne, Elise, Charlotte, Katja, Liesbeth, Lize, Sanne, Zjoske, Evake89, pendelvriendje Liesbeth.

En dan begon het schrijven, valt op zich goed mee eigenlijk. Zonder het schrijven zou een doctoraat nooit hetzelfde zijn. Een moment van zelfreflectie en concentratie. Een unieke periode in mijn leven. Merci Bart en Luc voor het nalezen. Bedankt promotoren en juryleden Dries, Joris, Wouter, Nicola, Francesco, Wim en Xin om kritisch door mijn boek te gaan. Jullie opmerkingen waren terecht!

Bedankt Kelly, Maarten en Liesbeth - jullie in het bijzonder zijn een grote mentale steun geweest tijdens het schrijven, misschien vooral in de vorm van de nodige en minder nodige afleidingen zoals dineetjes en late dansfeestjes - anyway het hielp! Ik weet trouwens zeker dat de nieuwe bewoner van de Peterkamer ook nen toffe pe gaat zijn. Dokter Fil, altijd paraat jij, dankzij jou kan ik toch nog mijn eigen dankwoord schrijven, bedankt voor de goede handzorgen!

Hanne, liefste Herpie, jij weet als geen ander hoeveel avonden en weekends er opgeofferd werden aan simulaties, design werk (met deadlines die elke week een week extra verlengd werden) en last-minute papers. Een sterke planner ben ik nooit geweest, daar kan jij dan een boek over schrijven, dat weet ik. Mijn excuses hiervoor. Ik weet wel dat jij 7 jaar mijn grootste fan bent geweest die mij bij elke keuze voor de 100% hebt gesteund, van Erasmus naar Kopenhagen tot samen verhuizen naar Berlijn. We hebben de wereld samen ontdekt hé. Ik ga altijd koesteren wat we hebben gehad en wat je me hebt geleerd van het (echtere) leven.

Elke en Luc, Cis en Sarah, tante Hilde, mams en paps, samen zijn we een top familie!

Antwerpen - Gent - Brussel - Leuven, April 2014
Peter De Heyn

Table of Contents

Nederlandstalige samenvatting

Silicium-fotonica

Optische verbindingen gemaakt in silicium worden beschouwd als een zeer waardig alternatief om grotere bandbreedtes in supercomputer en datacenter communicatie mogelijk te maken. Zeer compacte optische verbindingen kunnen de bandbreedte per oppervlakte vergroten ten opzichte van lange en tragere elektrische verbindingen. Zoals elk integratieplatform heeft ook Si fotonica de voorbije 10 jaar al een zeer brede waaier aan eenvoudige geïntegreerde fotonische circuits aangetoond. Zulke integratie kan zeer waarschijnlijk de eenheidskost verlagen en het fabricagerendement van toekomstige en meer grootschalige complexe circuits vergroten. Alle essentiële functies om een optische verbinding te realiseren zijn reeds gedemonstreerd en worden nu door allerhande instituten en onderzoekscentra verbeterd naar een hoger maturiteitsgehalte. De eerste commerciële producten gebaseerd op Si fotonische circuits worden nu reeds op de markt gebracht. Si gebaseerde fotonische componenten worden gemaakt door de meest geavanceerde CMOS fabricagetoestellen wat maakt dat men van dit platform de meest belovende resultaten mag verwachten. Si fotonica kan zo in het kielzog varen van de continue ontwikkeling in de zeer gevestigde en gestandaardiseerde CMOS elektronica industrie.

Licht kan geleid worden door golfgeleiders die bestaan uit twee transparante materialen met een verschillende materiaal index. Op het silicium-op-isolator (SOI) platform wordt licht geleid door het refractieve index verschil tussen silicium en siliciumdioxide (SiO_2). Het bereikte indexcontrast tussen de materialen Si en SiO_2 is een van de hoogst mogelijke. Deze eigenschap heeft twee belangrijke voordelen. Ten eerste kunnen golfgeleiders zeer compact worden gemaakt zodat het licht zeer nauw kan opgesloten worden: typisch Si golfgeleiders hebben een breedte van $450\,\mathrm{nm}$ en zijn $220\,\mathrm{nm}$ hoog. Hiermee wordt het mogelijk om twee golfgeleiders op minder dan $1.5\,\mu\mathrm{m}$ te plaatsen zonder enige koppeling. Ten tweede, licht kan geleid worden in zeer scherpe bochten (straal $< 3\,\mu\mathrm{m}$) zonder al te grote verliezen. Deze twee eigenschappen maken het mogelijk om minuscule fotonische circuits te maken met de hoogste functionele densiteit voor een zekere chipoppervlakte.

Deze eigenschappen samen met het hoge fabricagerendement zorgen ervoor dat Si fotonica beschouwd wordt als de meest belovende kandidaat voor toekomstige en zeer performante toepassingen in zowel lange- als korte-afstandscommunicatie.

De succesvolle integratie van fotonische componenten in Si zoals ontwikkeld in dit werk versnelt een verdere commercialisatie van kostenefficiënte en op grote schaal produceerbare optische verbindingen.

Ontvangers gebaseerd op ringresonatoren in silicium voor optische interconnecties met meerdere golflengtes

Deze studie behandelt de integratie van ontvangers gebaseerd op ringresonatoren in Si die met behulp van meerdere golflengtes de totale bandbreedte van een optische verbinding kunnen vergroten. Het gebruik van meerdere golflengtes op een enkele fysieke lijn wordt reeds meer dan twintig jaar gretig toegepast in lange afstand optische fibercommunicatie en wordt dan ook beschouwd als de meest effectieve manier om de bandbreedte te vergroten. Deze techniek noemen we golflengte divisie multiplexing of WDM. In dit werk hebben we twee toepassingsgebieden voor ogen waar we denken dat geïntegreerde fotonische circuits in Si een belangrijke rol kunnen spelen.

Toepassingen

In-band WDM label extractor De eerste toepassing in dit werk situeert zich in een zeer performante pakketschakelaar van een volledig optisch verbonden netwerk. De meest gangbare manier van pakketschakelen gebeurt echter door eerst de gehele optische datapakket naar het elektrisch domein te converteren. De pakketschakelaar beslist dan op basis van het adres naar welke uitgangspoort het datapakket moet gestuurd worden. De data zelf wordt achteraf terug naar het optische domein geconverteerd. Deze zeer snelle opto-elektronische conversies zijn echter energieverslindend en beperkt de schaalbaarheid van deze schakelaars. Het grootste deel van deze conversie kan echter vermeden door het inkomende datapakket in het optische domein te houden en enkel de informatie bestemd voor de schakelaar, te converteren naar het elektrisch domein. Deze techniek is een speciale variant van een volledig optische pakketschakelaar, aangezien het schakelen zelf nog elektrisch beslist wordt. Er bestaan ook zeer snelle en volledig optische adresherkenningsmethoden die deze beslissing optisch kunnen nemen maar deze zijn meestal zeer gesofisticeerd en moeilijk schaalbaar naar een groot aantal adressen. De routeringsinformatie wordt gecodeerd in het datapakket met behulp van een label. Dit label bestaat uit traag variërende signalen van meerdere golflengte (WDM) en wordt bovenop de eigenlijke data geplaatst. De golflengtes van het label passen in de spectrale band van het snel gemoduleerd datapakket zelf. We spreken van een in-band WDM label; dit is spectraal efficiënt. Door meerdere golflengtes te gebruiken kunnen we het aantal bereikbare adressen vergroten. Het label zelf is veel trager gemoduleerd dan het datapakket zelf. Om het trager variërende label te extraheren hebben we zeer smalbandige filters nodig op de golflengtes van het

WDM label. In dit werk ontwikkelen we een component die de in-band WDM signalen ontrafelt en extraheert van een snel gemoduleerd datapakket, en dit zonder het datapakket zelf te verstoren. Op deze manier kan het label asynchroon en parallel verwerkt worden. Het resultaat is een flexibele, vermogenefficiënte manier van adresherkenning met zeer korte vertragingstijden.

WDM data ontrafelaar De tweede toepassing in dit werk is een data ontvanger van een optische connectie dat elk WDM signaal ontrafelt. Deze optische connectie kan zeer kort zijn ($1\,\mathrm{cm}$ tot $10\,\mathrm{cm}$) bijvoorbeeld van chip naar chip en zou dan een belangrijke verbetering kunnen zijn voor een elektrische interconnectie. Ook interconnecties over langere afstanden zijn mogelijk, bijvoorbeeld van rek naar rek ($1\,\mathrm{m}$ tot $10\,\mathrm{m}$) of van server naar server ($10\,\mathrm{m}$ tot $1\,\mathrm{km}$). Dit zou dan een belangrijke verbetering kunnen zijn voor optische interconnecties met multimode fibers. Voor al deze opwaarderingen is het van vitaal belang dat een grote bandbreedte wordt bereikt en dit met een zeer laag vermogensverbruik.

Doel en uitdagingen

Veel interconnecties zijn bandbreedte gelimiteerd maar om bestaande interconnecties op te waarderen naar een volgende generatie is er een zeer kostenefficiënte en laagvermogen oplossing nodig. Het is op het eerste zicht een aantrekkelijk idee om een oplossing te bedenken dat gebruik maakt van een zeer compact fotonisch geïntegreerd component in Si. Maar veel uitdagingen maken deze WDM uitvoering in Si allesbehalve rechttoe rechtaan.

De ring resonator is de meest compacte golflengte-selectieve filter. Door deze component in serie te plaatsen op een gemeenschappelijke golfgeleider (de bus), kan men op een betrekkelijk eenvoudige manier een WDM ontrafelaar maken. In wat volgt specifiëren we de uitdagingen van deze WDM componenten gemaakt in Si. Later bespreken we per applicatie hoe we deze componenten geïmplementeerd hebben om de vele uitdagingen het hoofd te bieden. De bereikte resultaten zijn telkens kort beschreven.

Uitdaging 1 Een van de grootste uitdagingen om compacte WDM componenten te fabriceren in silicium is de grote gevoeligheid aan minuscule variaties in de dimensies van de gefabriceerde golfgeleiders. Door deze kleine fabricagevariaties, verandert de resonantie golflengte van een ringresonator ongewenst. Gebaseerd op een groot aantal metingen vonden we dat de resonantie golflengte tot wel $9\,\mathrm{nm}$ variëerde (3σ waarde) over de gehele wafer met een diameter van $200\,\mathrm{mm}$. Binnen een zelfde component ($\approx 1\,\mathrm{mm}$) kan de golflengte variëren tot $0.7\,\mathrm{nm}$ (3σ). Men kan een actief energieverslindend compensatieschema overwegen gebaseerd op de thermo-optische coëfficiënt van Si door het gebruik van kleine verwarmingselementen boven of naast de ring. Wat men ook kan doen is het ontwerp van deze component fabricagetolerant te maken. Om voor de variaties op waferschaal te compenseren zijn er nog steeds verwarmingselementen nodig. Omdat de ringresonatoren de compactste zijn ten opzicht van andere type filters, vereisen deze componenten het minste vermogen om afgesteld te worden.

Uitdaging 2 Een tweede uitdaging is de hoge thermo-optische coëfficiënt van Si. Deze maakt golflengte-selectieve filters in Si zeer gevoelig aan temperatuursveranderingen. Men kan een resonantieverschuiving verwachten van ongeveer $12\,\mathrm{GHz}$ (of $100\,\mathrm{pm}$ rond golflengte $1550\,\mathrm{nm}$) per Kelvin, onafhankelijk van het type filter. Deze dynamische temperatuursveranderingen kunnen daarom het ontvangende golflengte raster volledig verschuiven waardoor er geen communicatie meer mogelijk is. Actieve compensatie is mogelijk maar verbruikt ook veel energie. Daarom moet deze actieve compensatie zo efficiënt mogelijk gemaakt worden.

Uitdaging 3 Een derde uitdaging is de oppervlakteruwheid aan de zijkanten van een golfgeleider. Deze oppervlakteruwheid is gerelateerd aan de fabricagemethode en is moeilijk te vermijden. Dit zorgt er voor dat licht verstrooid wordt en dus een extra verlies introduceert. Een belangrijk deel van deze verstrooiing wordt echter terug opgevangen door de golfgeleider en propageert in de tegengestelde richting. Dit licht komt steeds weer dezelfde storingen tegen en wordt versterkt. Hoe langer het licht in de ring blijft hoe groter deze versterking. Het is dan ook voornamelijk in smalbandige ringresonatoren dat dit effect desastreus kan zijn voor de filter prestatie.

In-band WDM label extractor

Om het in-band WDM label zorgvuldig te extraheren van een snel gemoduleerd datapakket hebben we zeer smalbandige filters nodig. Om de kwaliteit van het datapakket niet te verstoren hebben deze filters een bandbreedte van $2.5\,\mathrm{GHz}$ of $20\,\mathrm{pm}$. Hierdoor kan de kanaalspatiëring van het label zeer dicht gemultiplexeerd worden met een spectrale afstand van $12.5\,\mathrm{GHz}$ of $0.1\,\mathrm{nm}$. Bovendien moeten deze filters een zeer laag insertie verlies vertonen om het vermogensbudget te minimaliseren. Een parallelle rij van zeer responsieve fotodiodes converteert het WDM label naar het elektrische domein.

Implementatie De hoge opsluitbaarheid van quasi-TE gepolariseerd licht in Si golfgeleiders laat ons toe om circuits te ontwerpen met zeer korte bochtstralen. We ontdekten echter dat het gebruik van deze polarisatie in Si golfgeleiders zeer nefast werkt in smalbandige ringresonatoren. Het teruggekoppelde licht zorgt er namelijk voor dat de bandbreedte van de resonantie gevoelig verbreedt wordt zodat de vereiste bandbreedte van $20\,\mathrm{pm}$ onmogelijk te behalen valt. We vonden ook dat de resonantie van de ringresonator voor bepaalde golflengtes in twee kleinere resonanties splitste, wat een direct gevolg van deze terugkoppeling is. Het gevolg is een onvoorspelbaar gedrag van een ringresonator met grote variaties op het insertieverlies en andere filterspecificaties. Bovendien stelde we vast dat deze

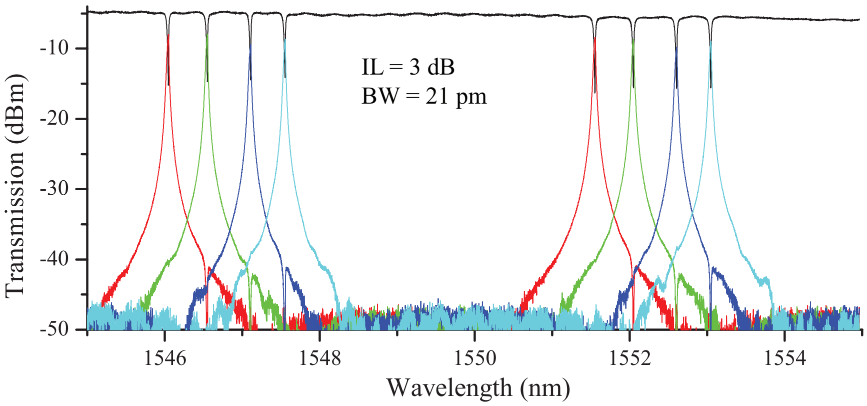

Figuur 1: De filterkarakteristiek van een vierkanaals in-band label demultiplexer gebaseerd op ringresonatoren met een zeer nauwe bandbreedte (quasi-TM mode).

verstrooiing tot zeer grote reflecties kon zorgen die opliepen tot $-10\,\mathrm{dB}$ van het originele ingangsvermogen. Dit kan tot negatieve gevolgen leiden zoals instabiliteit in de laser aan de verzenderkant.

Door golfgeleiders te gebruiken met een lagere opsluiting van het licht konden we wel de vereiste bandbreedte halen, zonder enige vorm van resonantiesplitsing. De gereflecteerde vermogensverhouding verlaagde met bijna $10\,\mathrm{dB}$. We valideerden deze oplossing met twee type golfgeleiders: een ondiep geëtste golfgeleider met een quasi-TE mode en een diep geëtste golfgeleider maar met een quasi-TM mode. Beide aanpakken verminderen de modebedekking met de verticale oppervlakteruwheid van de golfgeleider.

Resultaten Een vierkanaals ultra-dense WDM label demultiplexer is succesvol geëvalueerd om foutloos een label bestaande uit vier in-band signalen te extraheren van een $160\,\mathrm{Gb/s}$-gemoduleerd datapakket. Dit resultaat is tot stand gekomen door een nauwe samenwerking met de COBRA onderzoeksgroep van de TU Eindhoven. De filterkarakteristiek is getoond in Fig.1 en maakt gebruik van diepgeëtste golfgeleiders met een quasi-TM mode. De resonanties hebben een zeer superieure karakteristiek, met een bandbreedte (BW) van $21\,\mathrm{pm}$ en een insertieverlies (IL) van slechts $3\,\mathrm{dB}$.

Een heterogeen geïntegreerde InGaAs p-i-n fotodiode werd geoptimaliseerd om een zeer hoge responsiviteit ($> 1\,\mathrm{A/W}$) te verkrijgen voor zowel de TE als de TM gepolariseerde mode en wordt gebruikt om de optische WDM signalen om te zetten naar het elektrische domein met een snelheid van $> 10\,\mathrm{GHz}$. Elektrische verwarmingselementen worden gebruikt om voor kleine fabricagevariaties te compenseren. We hebben echter aangetoond dat door de nauwe spectrale bandbreedte van de filters het steeds mogelijk blijft een foutloze extractie te voltooien

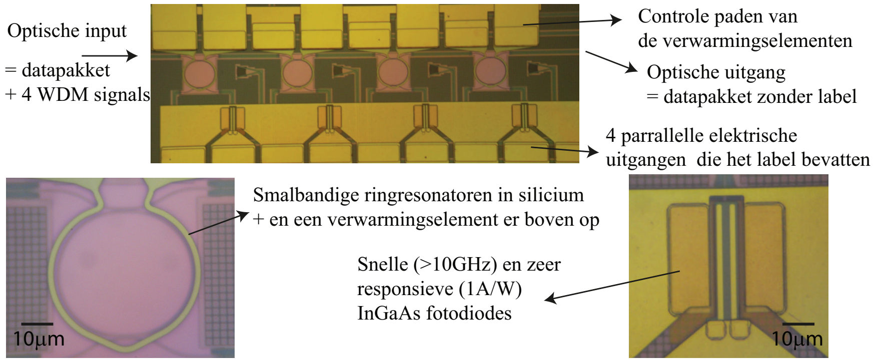

Figuur 2: Een microscoopfoto van een volledig geïntegreerde label extractor.

onafhankelijk van de exacte spectrale positie van de WDM signalen. Als de resonanties elkaar overlappen blijft actief afstemmen van de resonanties nodig. Een microscoop foto van de volledige geïntegreerde label extractor is getoond in Fig.2.

WDM data ontrafelaar

De eerst generatie van WDM optische interconnecties gebaseerd op het Ethernet protocol voor middelmatige afstand ($100\,\mathrm{m} - 2\,\mathrm{km}$) zullen waarschijnlijk gebruik maken van zeer breedbandige filters op een zeer wijd gespatieerd WDM raster, met kanaalspatieringen van $20\,\mathrm{nm}$ of $2500\,\mathrm{GHz}$ (CWDM). Dit werd overeengekomen in de $100\,\mathrm{Gb/s}$ *fiber optic task force* van de IEEE (IEEE P802.3bm - www.ieee802.org/3/). De keuze voor een CWDM grid komt omdat er geen vermogen over is om de externe lasers op een constante temperatuur te houden, wat er voor zorgt dat de golflengte sterk kan variëren ($\pm\,6.5\,\mathrm{nm}$). Een rechttoe rechtaan implementatie in Si is door die grote spectrale spanwijdte ($> 80\,\mathrm{nm}$) moeilijk. Dit komt omdat de roosterkoppelaars die verantwoordelijk zijn voor de in- en uitkoppeling naar de Si chip slechts een beperkte bandbreedte hebben ($\approx\ 30\,\mathrm{nm}$). Het gebruik van een horizontale koppeling biedt hier een oplossing voor maar maakt het veel moeilijker om de component te testen op grote schaal. Ons doel is daarom om een veel agressievere kanaal spatiëring van $300\,\mathrm{GHz}$ te gebruiken (DWDM), enkele malen smaller dan CWDM. Dit vergroot niet enkel de gezamenlijke bandbreedte maar ook het bandbreedteprobleem van de roosterkoppelaar. We zijn van mening dat deze aanpak zeer schaalbare WDM componenten zal opleveren die ook voor toekomstige generaties Ethernet-bandbreedte kunnen dienen ($400\,\mathrm{Gb/s}$ - $1.6\,\mathrm{Tb/s}$). Om deze smallere kanaalspatiëringen mogelijk te maken moeten de Si filters tolerant zijn voor dynamische temperatuursveranderingen maar ook voor golflengtevariaties van de externe lasers. Bovendien zijn er nog de fabricagevariaties die de centrale golflengte van een filter een ongewenste verschuiving kunnen geven. De filterrespons moet ook polarisatie onafhankelijk zijn zodat de optische interconnectie praktisch handelbaar is. In het algemeen is een polarisatie-onafhankelijk circuit niet voor de hand liggend omdat de golfgeleiders asymmetrisch zijn.

Implementatie Om de ongewenste verschuivingen van de centrale kanaalgolflengte te compenseren worden typisch individuele verwarmingselementen gebruikt, één voor elk kanaal. Dit zorgt er echter voor dat ook elk kanaal een eigen controle signaal nodig heeft zodat de optimalisatie van de gehele filterbank complex kan worden. Dit controlemechanisme vergroot niet enkel de oppervlakte van de chip maar ook het vermogensverbruik. We vergrootte daarom de bandbreedte van elk kanaal door het gebruik van een geoptimaliseerd ontwerp van een tweede-orde ringresonator. Deze resonator is dubbel zo groot als een eerste-orde ringresonator wat het vermogensverbruik voor het afstemmen van de resonanties verdubbelt. Op deze manier is de filter bank nu tolerant tegen golflengtevariaties op component niveau met een $3\,\sigma$-value van $0.7\,\mathrm{nm}$. Deze verbeterde contour van een tweede-orde ringresonator laat ons toe om slechts één collectief bestuurd verwarmingselement te gebruiken. Op deze manier kunnen we de absolute resonantiegolflengte van de filter veel eenvoudiger bijstellen zodat deze overlapt met het inkomende WDM raster. Om het vermogensverbruik tot een absoluut minimum te herleiden hebben we meerdere strategiën ontwikkeld. De belangrijkste is het verwijderen van de grootste warmtelekken, zoals het Si substraat onder de ring. Een polarisatie-onafhankelijk ontwerp is bereikt dankzij het gebruik van een tweedimensionale (2D) roosterkoppelaar.

Resultaat: een polarisatie-onafhankelijke $5{\times}20\,\mathrm{Gb/s}$ DWDM ontvanger We demonstreren een 5-kanaals DWDM data ontrafelaar met een kanaalspatiëring van $300\,\mathrm{GHz}$. Elk kanaal heeft een bandbreedte tot $20\,\mathrm{Gb/s}$. Eerst hebben we een volledig optische DWDM ontrafelaar gebruikt om op grote schaal te testen. Nadat de spectrale positie van de DWDM ontrafelaar geoptimaliseerd was vertoonde het slechtste kanaal een wafer-gemiddeld insertieverlies (IL) van $-1.39\,\mathrm{dB}$ en een overspraak tussen de kanalen (XT) van $-18.2\,\mathrm{dB}$. Daarna, integreerden we monolithisch gegroeide hogesnelheid germanium (Ge) detectoren om elk kanaal opto-elektronisch te termineren. Een schematische voorstelling van de gedemonstreerde polarisatie-onafhankelijke DWDM ontvanger is getoond in figuur 3. Een 2D roosterkoppelaar (GC) is gebruikt om het licht in zijn twee orthogonale componenten te verdelen over de twee ontkoppelde armen van de ontrafelaar. Het insertieverlies van deze roosterkoppelaar is $-6.5\,\mathrm{dB}$. De totale voetafdruk is $1.7\,\mathrm{mm} \times 0.28\,\mathrm{mm}$ en kan nog verder verkleind worden met het gebruik van kleinere elektrische paden. Indien we deze component zouden schalen naar 10 kanalen is deze ongeveer 40 keer compacter dan andere gerapporteerde DWDM ontvangers.

De polarisatie-onafhankelijke responsiviteit is zeer hoog ($0.1\,\mathrm{A/W}$) met de fiberuitgang als referentie. Bovendien is deze kanaalresponsiviteit uniform voor alle kanalen. De overspraak is beter dan $-15\,\mathrm{dB}$. Een opto-elektronische filterkarakteristiek van deze ontrafelaar is getoond in figuur 4. De bandbreedte van de fotodiodes is $20\,\mathrm{GHz}$ en vertoont uniforme s_{21} parameters. Deze s_{21} parame-

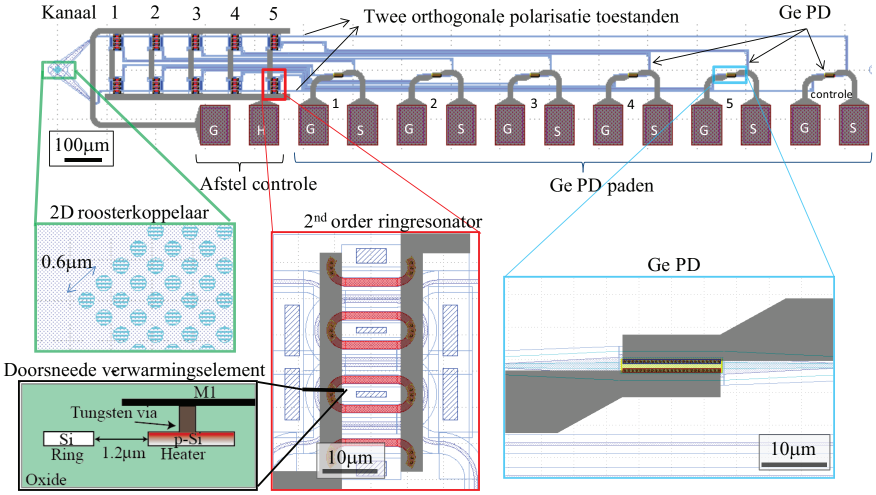

Figuur 3: Schema van de polarisatieonafhankelijke DWDM ontvanger dat gebruikt maakt van vijf tweede-orde ringresonatoren in Si, p++ gedopeerde Si verwarmingselementen met een collectieve besturing en hogesnelheid Ge fotodiodes.

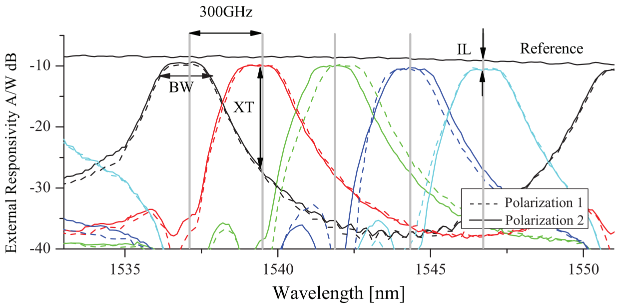

Responsiviteit	0.1 A/W
1dB BW	1.2 nm
Kanaal XT	< -15 dB
Kanaal IL	1.2 dB
PD responsiviteit	0.61 A/W
Donkerstroom	< 8 nA

Figuur 4: De opto-elektronische filterkarakteristiek van gefabriceerde vijfkanaals WDM Ge ontvanger voor beide polarisatie toestanden (volle en gestippelde lijnen).

ters samen met een open oogdiagram van een pseudo-random $20\,\mathrm{Gb/s}$ signaal is getoond in figuur 5. In een parallel onderzoek op hogesnelheids Ge detectoren toonden we aan dat snelheden van meer als $50\,\mathrm{GHz}$ haalbaar zijn. Met het gebruik van een meer geavanceerdere fabricagetechnologie op $300\,\mathrm{mm}$ wafers, toonden we ook aan dat we het aantal kanalen gemakkelijk konden uitbreiden naar 10. Dit zou resulteren in een $500\,\mathrm{Gb/s}$ ontvanger. De bovenvernoemde resultaten zijn tot stand gekomen door een nauwe samenwerking met het iSIPP team van imec.

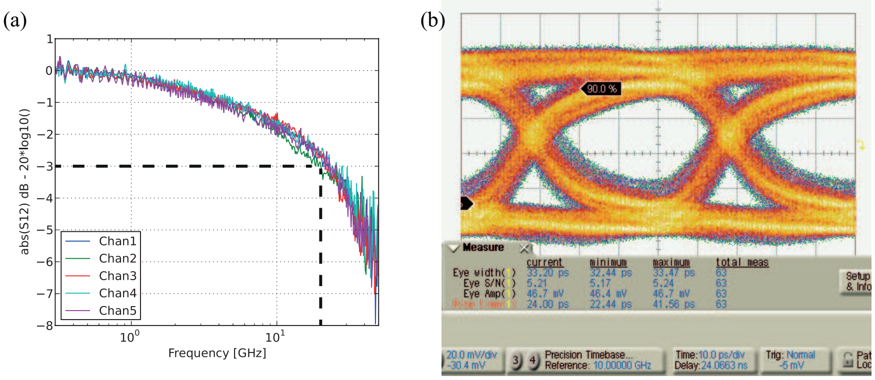

```
                current     minimum     maximum     total meas
  Eye width(1)  33.20 ps    32.44 ps    33.47 ps    63
    Eye S/N(1)  5.21        5.17        5.24        63
    Eye Amp(1)  46.7 mV     46.4 mV     46.7 mV     63
  Rise time(1)  24.00 ps    22.44 ps    41.56 ps    63
```

Figuur 5: (a) Uniforme S21 parameters die een opto-elektronische bandbreedte van $20\,\mathrm{GHz}$ *aantonen en (b) een open oogdiagram van een pseudo-random* $20\,\mathrm{Gb/s}$ *signaal.*

Conclusie

De succesvolle integratie van deze twee ontvangers gefabriceerd in Si demonstreert duidelijk de vele toepassingsmogelijkheden van dit Si platform voor een toekomstige kostefficiënte massaproductie. We denken dat we met deze twee demonstraties een significante bijdrage hebben geleverd aan de bestbekende en actuele staat van Si ringresonatoren. Twee klassen van ringresonatoren werden hiervoor gebruikt: een zeer golflengteselectieve ringresonator met een hele nauwe bandbreedte die tolerant is aan de oppervlakteruwheid van een golfgeleider en een breedbandige tweede-orde ringresonator die tolerant is tegen lokale fabricagevariaties.

English summary

Silicon photonics

Optical interconnects (OI) based on silicon (Si) photonics are considered as a viable alternative to copper electrical interconnects to enable further bandwidth scaling in supercomputer and datacenter communication. On the silicon photonics platform, a wide variety of photonic integrated circuits (PICs) have been demonstrated over the last decade. This integration can very likely lower the unit cost and increases the yield of future large scale and complex circuits, having a huge impact on the industry of next-generation OI. All essential functionalities to realize an OI have been demonstrated and are now being further enhanced to a greater maturity level. The first products are now being commercialized. The fact that Si photonic components are made by the most advanced CMOS fabrication tools makes it the most promising among other integration platforms since it can leverage on the continuous development of a well-established and standardized electronic industry.

Light can be guided in waveguides formed by two transparent materials with a different material index. In the silicon-on-insulator (SOI) platform the light is guided by the refractive index contrast between silicon and silicon dioxide. The high index contrast has two important advantages. First, one can make ultra-compact waveguides: typical Si waveguides have a width of $450\,\mathrm{nm}$ and a height of $220\,\mathrm{nm}$. Furthermore, the high confinement allows a very dense integration, e.g. two waveguides can be $1.5\,\mu\mathrm{m}$ apart without having any interference. Secondly, light can be guided without excessive losses in bends with a very short radius ($< 3\,\mu\mathrm{m}$). Those two properties enable ultra-compact PICs and hence the highest functional density per unit area.

Apart from the dense functionality, the high-yield fabrication technology of Si photonics makes it the most promising candidate for high-end applications in all kinds of interconnects ranging from long to intermediate range as well as for very short chip-level interconnects. The succesful integration of the Si photonic components developed in this work, facilitates the further commercialization of cost-effective and mass-manufacturable next-generation OI.

Receivers based on silicon ring resonators for multi-wavelength optical interconnects

Our study focuses on the integration of receivers based on Si ring resonators to increase the total bandwidth of an OI. The technique of using multiple wavelengths on a single physical line (also known as wavelength-division-multiplexing or WDM) has been used in long-haul fiber-optic communication for more than two decades. In this work we envision two application areas where we believe Si PICs can play an important role.

Applications

In-band WDM label extractor The first application is situated within a large-throughput switch of an all-optical interconnect network. The conventional way of routing is converting all the optical data to the electrical domain and decide based on the address to which output port the incoming data should be routed. Then the data packet is converted back to the optical domain. However, the large power consumption coming from the ultra-fast electro-optical conversions limits the scalability of such routers. An alternative approach that avoids these power-hungry conversions is keeping the majority of the data (the payload) in the optical domain and only convert the routing information (the header) to the electrical domain. This technique is typically referred to as all-optical packet switching, although the switching decision itself happens in this approach in the electrical domain. Ultra-fast all-optical header processing techniques, that can process the header information in the optical domain, are typically limited in the amount of addresses and is hence not suitable for large-port count switches. The routing information is encoded in the payload packet using a multi-wavelength (WDM) label that is superimposed within the spectral band of the highly-modulated payload. The in-band WDM label is therefore spectrally efficient and by increasing the amount of wavelengths one can scale the amount of addresses. The label is modulated at a much smaller rate than the payload. To extract the label one needs several narrowband filters at the wavelengths of the WDM label. In this work, we developed a WDM demultiplexer that extracts the WDM label from a highly-modulated payload without distorting the payload. Hence, the label can be processed asynchronously which enables a flexible, low-latency and power-efficient address recognition.

WDM data demultiplexer The second application is a WDM data demultiplexer that terminates an optical interconnect. This optical interconnect can be very short ($1\,\mathrm{cm} - 10\,\mathrm{cm}$) e.g. a chip-to-chip interconnect to upgrade the existing electrical interconnects. Longer ranges are also possible e.g. a rack-to-rack $1\,\mathrm{m} - 10\,\mathrm{m}$ or server-to-server interconnect ($10\,\mathrm{m} - 1\,\mathrm{km}$) to upgrade the existing (Ethernet) optical interconnects based on multimode fibers. A low power consumption and a high throughput are vital to upgrade existing interconnects.

Objectives and challenges

Many interconnects are limited in bandwidth, but in order to be upgraded to a next generation, a very cost-effective and low-power solution is needed. The idea of having a solution for these application based on a high-yield and low-cost Si photonic integrated WDM component, is very appealing. However several challenges impede a straight-forward implementation. In this work we use the ring resonator to build the WDM-enabled components. The ring resonator is the most compact wavelength-selective filter and by cascading them on a common bus waveguide, one can create a demultiplexer array. We specify first the challenges of these WDM components in Si and later we discuss their implementation for each application to cope with these challenges. We shortly describe the demonstrated results.

Challenge 1 One of the major challenges for realizing compact WDM optical devices in silicon is the high sensitivity to small variations in the dimensions of fabricated waveguides. Based on large wafer-scale measurements, the center wavelength of a ring resonator is found to vary up to $9\,\mathrm{nm}$ (3σ) across a typical wafer (diameter $200\,\mathrm{mm}$) and up to $0.7\,\mathrm{nm}$ (3σ) within a device ($\approx 1\,\mathrm{mm}$) due to fabrication variations. To compensate for these variations, either an active and often power-hungry compensation scheme should be considered relying on the thermo-optic coefficient of silicon (e.g. using top-heating elements) or the design should be made robust towards fabrication variations. Ring resonators requires the lowest power to be thermally tuned with respect to other filters (e.g. arrayed waveguide grating) due to their compactness.

Challenge 2 A second important challenge is the high thermo-optic coefficient of Si, which makes silicon wavelength-selective devices highly sensitive to temperature variations. One can expect a frequency shift of $12\,\mathrm{GHz}$ (or $100\,\mathrm{pm}$ at $1550\,\mathrm{nm}$) per Kelvin, independent of the kind of filter.

Challenge 3 A third challenge is the surface roughness at the sidewall of a waveguide. This surface roughness is fabrication related and is difficult to avoid. It causes the light to slightly couple counter-directionally. Especially in narrowband ring resonators, this effect drastically limits the filter performance.

In-band WDM label extractor

In order to extract the in-band WDM label from a highly-modulated payload, ultra-narrowband filters are needed. To not distort the quality of the payload, their bandwidth should be in the order of $2.5\,\mathrm{GHz}$ or $20\,\mathrm{pm}$. Therefore the WDM channel spacing can be ultra-dense, down to $12.5\,\mathrm{GHz}$ or $0.1\,\mathrm{nm}$. Additionally, these filters should exhibit a low insertion loss to optimize the power budget. An array of highly-responsive photodiodes converts the WDM label to the electrical domain.

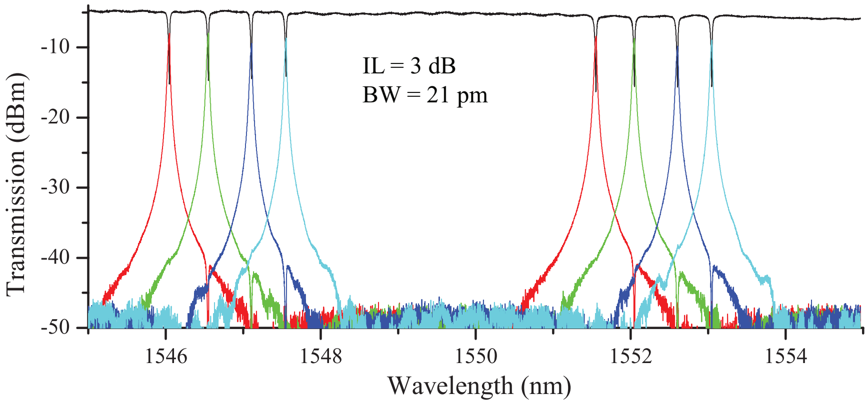

Figure 6: Filter characterization of the 4-channel label extractor based on narrow-bandwidth ring resonators using the quasi-TM mode.

Implementation The high confinement of Si waveguides enables very short bend radii. This results in very compact and dense structures. However, we found that standard strip waveguides using the quasi-TE polarization suffer from surface-roughness induced backscattering. In narrow-bandwidth ring resonators, the effect of counter-directional coupling is enhanced and the required bandwidth of $20\,\mathrm{pm}$ is not reached. Additionally, the resonance split in two components for certain wavelengths, which leads to large fluctuations in both insertion loss and extinction ratio. We also found that due to this backscattering, the reflected power ratio can reach up to $-10\,\mathrm{dB}$ which can possibly cause severe problems at the transmitting laser. Using less confined modes enabled us to design narrow-bandwidth ring resonators that are able to exhibit bandwidths $< 20\,\mathrm{pm}$ which are free from resonance splitting. The reflected power ratio decreased with almost $10\,\mathrm{dB}$. We validated this solution with two types of waveguides, a shallowly-etched waveguide using a quasi-TE mode and a strip waveguide using the quasi-TM mode. Both approaches are reducing the overlap with the vertical sidewalls, where the roughness is the most severe.

Results A four-channel ultra-dense WDM label extractor is evaluated to extract error-free an in-band label consisting out of four wavelengths from a highly modulated payload $160\,\mathrm{Gb/s}$ in collaboration with the COBRA group from TU/e. The transmission spectrum of this filter is shown in Fig.6. The resonances exhibit a superior characteristic with a bandwidth (BW) of only $21\,\mathrm{pm}$ and an insertion loss (IL) of $3\,\mathrm{dB}$.

A heterogeneously-integrated InGaAs p-i-n photodiode has been optimized to exhibit a high responsivity ($> 1\,\mathrm{A/W}$) for both the TE and TM mode corresponding to an internal efficiency of 85% and 95%. These photodiodes are used to

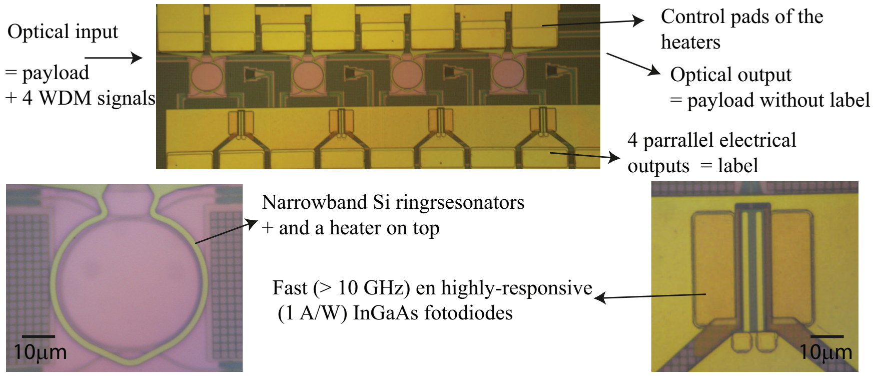

Figure 7: Microscope picture of the integrated label extractor.

convert the optical label to the electrical domain with a bandwidth of $> 10\,\mathrm{GHz}$. Electrical top-heating heaters are used to compensate for fabrication variations that detrimentally shift the resonances. However, we have shown that due to the narrowband spectral behaviour of filters, an error-free operation is always possible independent on the exact position of the resonances within the band. However, if resonances do overlap with each other, active tuning is required. A microscope picture of the fully integrated label extractor is shown in Fig.7.

WDM data demultiplexer

The coming generation of optical interconnects based on the Ethernet protocol will be most probably based on very broadband filters on a coarse WDM (CWDM) grid with a channel spacing of $20\,\mathrm{nm}$ ($2500\,\mathrm{GHz}$). This has been agreed in the IEEE P802.3bm $100\,\mathrm{Gb/s}$ fiber optic task force (www.ieee802.org/3/). That is because the wavelength accuracy of the WDM signals requires a temperature controller which substantially increases the total power consumption. However, a straight forward implementation of CWDM in Si is difficult due to the required wide spectral bandwidth ($> 80\,\mathrm{nm}$). The fiber grating couplers that are used to couple the light in and out of the Si chip only have a limited bandwidth ($\approx 30\,\mathrm{nm}$). The use of horizontal coupling can solve this bandwidth issue but makes it much more difficult to test the device on wafer scale. Our objective is to enable a much more aggressive channel spacing of $300\,\mathrm{GHz}$, several times denser than CWDM, which not only increases the aggregate bandwidth but also removes the bandwidth hurdle of the grating coupler. We believe that this will enable scalable WDM components for next-generation Ethernet-based OI aggregate bandwidths ($400\,\mathrm{Gb/s}$ - $1.6\,\mathrm{Tb/s}$). To enable this denser channel spacing, Si photonics WDM components must be robust towards ambient dynamic temperature variations, wavelength variations of the external laser array. Additionally the component should be tolerant against fabrication variations. A polarization-insensitive responsivity is required which enables a great flexibility in handling the OI. In general this is difficult to achieve due to the asymmetric waveguide dimension.

Implementation To compensate for the detrimental shifts in center wavelength of the channel, typically individual single-channel thermal heaters are used. However, for each channel an extra control signal is needed and the optimization of the whole filter bank can become quite complex. This control mechanism will not only increase the chip area but also the power consumption. Therefore, we improved the flat-top bandwidth of the filter response by using second-order ring resonators. This resonator is twice as large as a first-order ring resonator and hence the power consumption to tune the resonance is doubled. However, the filter array is now robust against device-scale wavelength variations with a $3\,\sigma$-value of $0.7\,\mathrm{nm}$. As a consequence, only one single heater is needed to collectively tune all channels for the larger wafer-scale channel wavelength variations. This implementation drastically simplifies the control algorithm and circuit. To optimize the power consumption of this heater, several strategies were developed. The most important one is the local removal of the Si substrate underneath the heated ring area, which removes the largest heat sink. A polarization insensitive design is achieved using a two-dimensional grating coupler.

Result: polarization-insensitive $5\times20\,\mathrm{Gb/s}$ DWDM receiver We demonstrate a 5-channel dense WDM data demultiplexer with a channel spacing of $300\,\mathrm{GHz}$. Each channel can handle data rates up to $20\,\mathrm{Gb/s}$. First, an optical-to-optical demultiplexer is used to verify the wafer-scale behavior. After collective tuning with integrated p-doped Si heaters, the second-order filter array exhibits a worst-channel insertion loss of $-1.4\,\mathrm{dB}$ and a crosstalk of $-18\,\mathrm{dB}$ (wafer-level average). Then, using monolithically-grown waveguide germanium photodiodes, an integrated high-speed opto-electronic conversion is terminating each channel. A schematic of the presented polarization-diversified DWDM Ge receiver design is shown in Fig.8. The 2D grating coupler is used to split the two orthogonal polarization states into two decoupled arms. The insertion loss (IL) of this grating is $-6.5\,\mathrm{dB}$. The total device footprint is $1.7\,\mathrm{mm} \times 0.28\,\mathrm{mm}$ and can further be decreased by using smaller electrical contacts. Scaling this component to 10 channels would result in a total component size ≈ 40 times smaller than reported for an arrayed waveguide grating based filter.

The polarization-insensitive fiber-referenced response is high ($0.1\,\mathrm{A/W}$) and moreover uniform over all channel responses. The channel crosstalk (XT) is for all channels better than $-15\,\mathrm{dB}$. The fiber-referenced responsivity spectrum of the as-fabricated WDM Ge receiver is shown for both polarization states in Fig.9. The bandwidth of the photodiodes is characterized to be $20\,\mathrm{GHz}$ with uniform s_{21} parameters and an open eye-diagram at $20\,\mathrm{Gb/s}$ shown in Fig.10.

Further research on Ge photodiodes have shown that the bandwidth can easily be scaled to $50\,\mathrm{Gb/s}$ and possibly faster. We also have shown that by using an advanced fabrication process on $300\,\mathrm{mm}$ wafers, the amount of channels can easily be increased to 10. This would enable ultra-compact WDM receivers up to

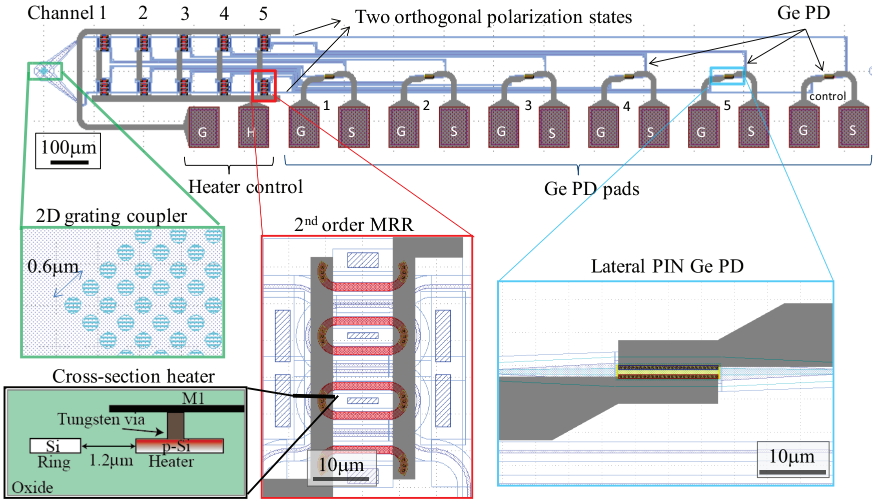

Figure 8: Schematic of a polarization-diversified DWDM receiver with five cascaded second order ring resonators, p++ doped Si heaters and Ge PDs.

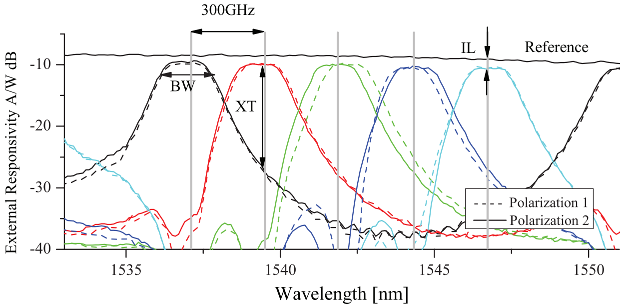

Responsivity	0.1 A/W
1dB BW	1.2 nm
Channel XT	< -15 dB
Channel IL	1.2 dB
PD responsivity	0.61 A/W
Dark current	< 8 nA

Figure 9: The fiber-referenced responsivity spectrum of the as-fabricated 5-channel WDM Ge receiver for both polarizations (solid/dashed lines).

$500\,\mathrm{Gb/s}$ in the very near future.

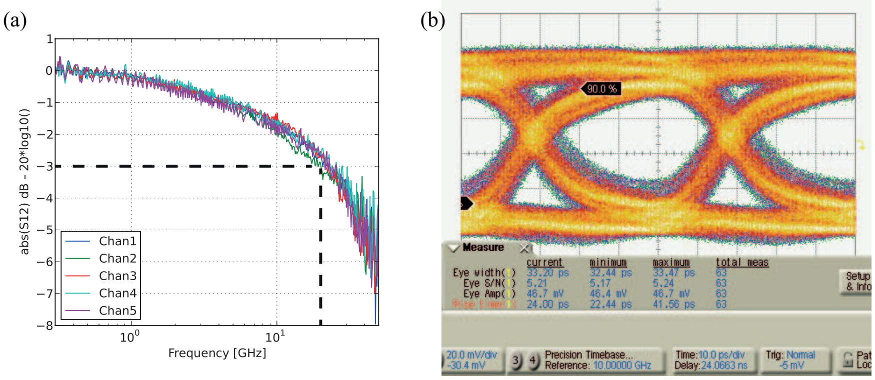

	current	minimum	maximum	total meas
Eye width(1)	33.20 ps	32.44 ps	33.47 ps	63
Eye S/N(1)	5.21	5.17	5.24	63
Eye Amp(1)	46.7 mV	46.4 mV	46.7 mV	63
Rise time(1)	24.00 ps	22.44 ps	41.56 ps	63

Figure 10: (a) Uniform s_{21} *parameters showing a opto-electronic* $20\,\mathrm{GHz}$ *bandwidth and (b) an open-eye diagram using a pseudo-random* $20\,\mathrm{Gb/s}$ *signal.*

Conclusion

The successful integration of these two receivers on a Si platform allows for very cost-effective and mass-manufacturable components. We believe that we have significantly enhanced the state-of-the-art performance of ring resonators. Two classes of ring resonators were used: a narrow-bandwidth first order ring resonator which is tolerant against sidewall roughness of a waveguide and a broad second-order ring resonator which is tolerant against local fabrication variations.

1

Introduction

1.1 Optical communication

Optical communication has been around for thousands years in the form of smoke signals or a flag semaphore. Optical communication as we know it today, as transferring information between a sender and receiver using modulated light, has been invented by Graham Bell already in 1880 with the creation of the photophone, only 4 years after his invention of the telephone. At the transmitter side (as shown in Fig.1.1(a)), he used the sun as a light source and converted the acoustic waves from his voice to modulate the light. This modulator was a simple flexible mirror, which transduced the acoustic waves (radio-frequency air-pressure waves) between a more convex or more concave state of the mirror. Hence the light was alternately scattered or condensed. By using a lens, this modulated light beam was focused to the receiver, in Bell's experiment, to his assistant 213 meters away. At the receiver side (as shown in Fig.1.1(b)), the modulated sun light was transduced back to an acoustic wave using a photo conductive cell at the focus point of a parabolic mirror. The electrical resistance of this cell is inversely proportional to the brightness of the light. The varying current was then transduced into acoustic waves using a normal earphone. Although Bell found the photophone his greatest invention, the photophone was never commercialized due to its dependency of the presence of clear sun light. The telephone, which could make use of conductive wires was far more reliable and dominated shortly after Bell's invention the world of communication.

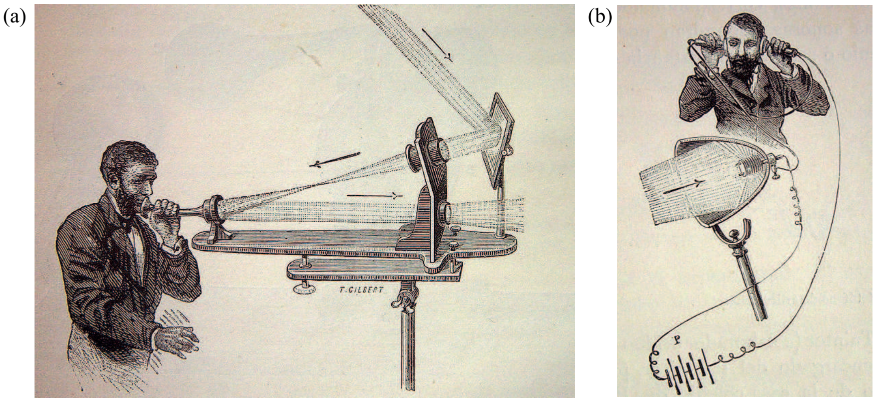

Figure 1.1: The photophone - an invention of Graham Bell in 1880 - as the first optical communication using the same principles as today's fiber-optic telecommunication, with (a) the transmitter and (b) the receiver side.

It took several decades with a number of technological advances before the first transatlantic telephone cable was laid in 1956 (TAT-1), carrying a total of 36 telephone lines. Before that, only telegraphic communication was possible with delay times up to several minutes. With the invention of the laser as a coherent light source, and the fiber-optic cable as a low loss transmission medium, optical communication became superior to electric communication for long-haul applications. The first fiber-optic transatlantic line was laid in 1988. In the meanwhile, the steady increase in demand for more bandwidth has been exponentially and doubles every 18 months [1], driving research in high performance fiber communication technologies. Especially techniques such as wavelength division multiplexing (WDM) and the realization of broad-band erbium doped fiber amplifiers (EDFA) increased the bandwidth of each fiber in a very cost-effective way. However, the need for more flexibility urged the need for a fast switching technique: all-optical packet switching.

1.2 All-optical packet switching

The original idea of all-optical networking has been around for more than 25 years in research communities and has been commercialized for long distance ($> 3000\,\mathrm{km}$) core networks in the late 1990s. The evolution, benefits, challenges and future vision of all-optical networking for core networks is well reviewed in [2]. The advantages of keeping all the data between sender and receiver in the optical domain are numerous since it allows arbitrary signal formats, bit rates and protocols to be transported and thus eliminating the opto-electronic bottleneck. Due to these unique properties, all-optical networks are usually referred to as trans-

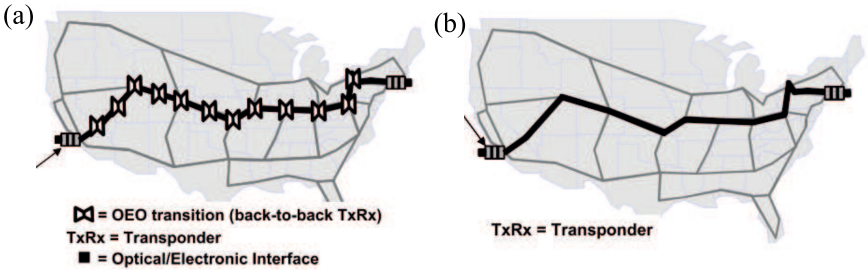

Figure 1.2: Illustration of a cross-country (USA) connection within the core or backbone with (a) tens of OEO conversions and (b) no OEO conversions. Figure taken from [2].

parent networks. Circuit connections at each node within the core network were considered to be quasi-static and could be fixed for several months. Therefore, switching by manually reconfiguring the circuit of the network was convenient enough.

However, the primary demand of networking companies shifted over the years from more transparency to reduced network costs and energy consumption. To fully deploy the network's resources and minimize the network costs, more flexibility in switching was needed. This need initiated the shift from static circuit switched networks to more dynamic packet switched networks [3]. Micro electro-mechanical system (MEMS) technology has been considered as an appropriate all-optical switching solution but can only perform slow millisecond switching [4]. Switching on the level of packets, typically requires ultra-fast signal processing to acquire the packet routing information and correctly set the switch output direction. The ease of scaling with respect to more WDM channels at stringent cost and power budget limitations [2], made electronic switching the technology of choice in large switching nodes in the core network. An example of such an electronic switch is the CRS-3 backbone router from Cisco, the world's fastest commercially available backbone router with a total aggregate bandwidth of $322\,\mathrm{Tb/s}$ (shown in Fig.1.3). Today's line rates are already at $40\,\mathrm{Gb/s}$, which is a necessary speed since the whole data packet needs to be read in order to control the output destination (IP level). At this high bandwidths the thermal dissipation of electronic circuits is very large and a technological breakthrough is needed to reduce this power consumption. In [5], it is calculated that the scalability of electronic packet switching is currently energy limited ($\approx 156\,\mathrm{Tb/s}$ per MW for the CRS-3 backbone router).

This energy limit means that the only way to increase the bandwidth is an improved power efficiency. One can do this by ultra-fast all-optical packet switching techniques but these techniques are typically limited in scalability. It has been proposed in [5], that one should find the best combination of electronics and photonics

Figure 1.3: The CRS-3, the world's fastest commercially available backbone router from Cisco with $322\,\mathrm{Tb/s}$ *total throughput.*

while keeping the data plane in the core of the network all-optical. For example, use electronic switch control and electronic edge routers while keeping the data all-optical for the core routers. Several implementations of optical packet switching architectures combine all-optical forwarding of the packet payload information together with an electronic processing of the packet header information.

1.3 Switching in data center networks

In large data centers and supercomputers networks, with a much smaller reach ($10\,\mathrm{m} - 1\,\mathrm{km}$) than long-haul core networks, the need for fast packet switching as a way to cope with the larger need for flexibility might be even larger. In addition, these systems are typically closed entities and therefore the bit rates and signal formats are more likely to be fixed following e.g. Ethernet, Infiniband or Fiber Channel standards. The need for higher performances drives the expansion of data centers or supercomputers, with more computing clusters that need to communicate with each other. At this moment, a fat tree topology is used to interconnect each cluster, as shown in Fig.1.4(a). However, this is not scalable in amount of interconnected clusters. The higher the tree, the more a packet needs to be switched and thus one can expect an increased amount of latency. This is typically described as the port-count dependent latency. The ever increasing demand on these systems, computing at tens of petaflops per second, is creating a real communication bottle neck among the thousands of nodes within these systems [6]. This has motivated research on low latency and large port-count optical packet switches [7]. In Fig.1.4(b), a possible alternative as proposed by the COBRA group of the Tech-

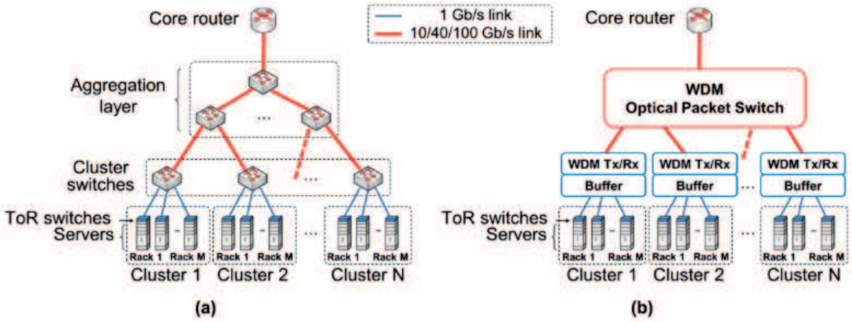

Figure 1.4: Typical data center network topology (a) and a possible data center topology employing a large port-count optical packet switch at cluster level (b). Figure taken from [9].

nical University of Eindhoven is shown [8, 9], where the optical packet switching occurs at cluster level with a centralized optical packet switch. Due to this highly distributed control, this approach is scalable without an increase in latency. A key building block in this architecture is an optical wavelength-and-space switching module (OWSSM). First demonstrations using discrete components are promising [8] but there is still lack of a low-cost and low-power solution.

1.4 Intra-data center optical interconnects

Today's intra-data center OIs, providing e.g. the connection between clusters and the switch, are typically using the lowest-cost solution based on multi-mode fiber, with simple but cheap transceivers. The most widely employed IEEE 802.3 Ethernet standard for this short range ($< 500\,\mathrm{m}$) is the 100GBASE-SR10 standard. This $100\,\mathrm{Gb/s}$ standard makes use of 10 separate multi-mode fibers with each a $10\,\mathrm{Gb/s}$ line rate (operating at wavelength $850\,\mathrm{nm}$). Increasing the bandwidth using this standard (e.g. by using more transceivers in a certain rack) is limited by the available front panel area. Enough front panel area should be open for cooling fans. The increase in line rate from $10\,\mathrm{Gb/s}$ to $25\,\mathrm{Gb/s}$ could solve this front area limitation by using only 4 multi-mode fibers instead of 10 (IEEE standard 100GBASE-SR4). However, at the same time also the required range of the OI increased due to the growing distance within a data center. Therefore, the newest data centers are likely upgrading their fiber network to more expensive transceivers but using lower-cost single-mode fiber. A single-mode fiber has a lower dispersion and can easily reach $10 - 40\,\mathrm{km}$. This upgrade also implies the shift to longer wavelengths $1310\,\mathrm{nm}$ (o-band) or $1550\,\mathrm{nm}$ (c-band) and the use of more expensive DFB lasers, typically used for long-range communication. Additionally, power consumption is one of the major operating expenses of today's data center, and upgrading to long-range equipment will only increase this power consumption (e.g. the use of a temperature controller or forward-error correction). Hence, the present need for a bandwidth-scalable approach with low power consumption for the next and future generation optical interconnect is very high.

The bandwidth scalability (to $400\,\mathrm{Gb/s}$ and later $1.6\,\mathrm{Tb/s}$ Ethernet data rates) and the stringent power budget are the most important criteria to choose between different approaches for tomorrow's implementation of a $100\,\mathrm{Gb/s}$ intermediate range solution. An implementation using a low-cost high-yield photonic integrated circuit (PIC) is almost unavoidable. With respect to non-integrated alternatives, a PIC does not only decrease component and assembly costs but also promises lower power consumption. Several approaches to fulfill these requirements have been demonstrated in a PIC implementation ranging from a simple 4-lane parallel single mode (PSM4) [10] fiber implementation to more dense 1-lane solutions such as space-division multiplexing (SDM) [11], pulse-amplitude modulation (PAM), or wavelength-division multiplexing (WDM) [12, 13]. Each approach has its own advantages regarding specific system requirements such as power consumption and future reach and bandwidth scalability.

1.5 Chip-level optical interconnect

Optical interconnects are also increasingly considered as an unavoidable technology shift to solve the chip-level bandwidth problem electrical interconnects are facing. The only solution at hand to scale the bandwidth of electrical interconnects is to increase the clock speed or to reduce the range. Increasing the clock speed is limited by the corresponding heat consumption per unit area. Despite the ever-decreasing size of a transistor by improving the fabrication technology, total chip area tends to increase and hence reducing the interconnect range seems not possible either. This is partly due to an increased complexity of the circuit but also due to a scaling problem of electrical interconnects itself. It turns out that one cannot simply downscale copper circuits without increasing the interference between different paths and increasing group delay (increased capacitance and resistance). Therefore, high-performance CPUs have been made parallel using multicores working at lower clock speed some years ago. This temporarily solved the power budget problem and could enhance the computing power drastically. However, the computing gain one can reach by solving a problem using parallel cores is still limited by the I/O bandwidth between the CPU and a shared memory.

An optical interconnect offers several advantages with respect to copper high-speed electrical interconnects (e.g. the PCI express bus). The most important is the area consumption, one can scale the dimensions of an optical waveguide without increasing the group delay. In addition, optical interconnects can handle multiple data streams on a single physical waveguide using WDM techniques and are hereby superior to electrical interconnects regarding bandwidth for a certain amount of chip area.

To be able to compete with electronic interconnects, chip-level and chip-to-chip optical interconnects need to meet stringent targets for the power efficiency ($\approx 1\,\mathrm{pJ/bit}$ [14]) and should be able to work over large temperature variations.

1.6 Silicon photonics optical interconnects

Optical interconnects (OI) based on silicon (Si) photonics are considered as a viable alternative to electrical interconnects to enable further bandwidth scaling in supercomputer and data center communication, but also in chip-level interconnects. On the silicon photonics platform, a wide variety of photonic integrated circuits (PICs) has been demonstrated over the last decade. This integration can very likely lower the unit cost and increases the yield of future large scale and complex circuits, having a huge impact on the industry of next-generation OI. All essential functionalities to realize an OI have been demonstrated and are now being further enhanced to a greater maturity level. First products are now commercialized (e.g. a $4 \times 28\,\mathrm{Gb/s}$ PSM4 transceiver from Luxtera). The fact that Si photonic components are made with the most advanced CMOS fabrication tools, makes it in our opinion the most promising among other integration platforms since it can leverage on the continuous development of a well-established and standardized electronic industry. Only recently, a first monolithically integrated silicon nanophotonics receiver in a $90\,\mathrm{nm}$ CMOS technology node has been demonstrated by IBM [15].

Light can be guided in waveguides formed by two transparent materials with a different refractive index. In the silicon-on-insulator (SOI) platform the light is guided by the refractive index contrast between silicon and silicon dioxide. The high index contrast has two important advantages. First, one can make ultra-compact waveguides: typical Si waveguides have a width of $450\,\mathrm{nm}$ and a height of $220\,\mathrm{nm}$. Furthermore, the high confinement allows a very dense integration, e.g. two waveguides can be $1.5\,\mu\mathrm{m}$ apart without having any crosstalk between them. Secondly, light can be guided without excessive losses in bends with a very short radius ($< 3\,\mu\mathrm{m}$). Those two properties enable ultra-compact PICs and hence a very high density per unit area.

In Fig.1.5(a), a SEM picture of a cross section of a photonic wire implemented in a SOI platform used in this work is shown. The buried oxide layer underneath the Si device layer is thicker ($2\,\mu\mathrm{m}$) than typical SOI wafers used for CMOS to avoid leakage of the optical power to the Si substrate.

Apart from the dense functionality, the high-yield fabrication technology of Si photonics makes it the most promising candidate for high-end applications in all

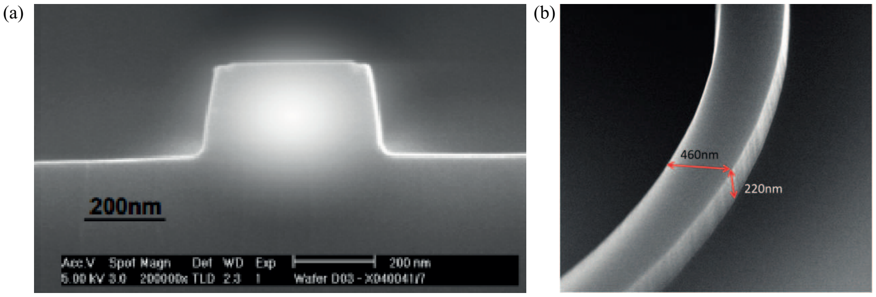

Figure 1.5: (a) A SEM picture of a cross section of photonic wire ($450 \times 220\,\mathrm{nm}^2$) *in silicon. Picture from [16]. (b) the birds-view perspective of a bend photonic wire.*

kinds of interconnects ranging from long to intermediate range as for very short chip-level interconnects. The successful integration of the Si photonic components developed in this work will facilitate the further commercialization of cost-effective and mass-manufacturable next-generation OI.

1.7 Envisioned applications of this work

In this work we investigate the adoption of the multi-wavelength (WDM) technique to enhance the performance of an optical interconnect. Two WDM-enabled receivers on Si photonics are envisioned. The first receiver is used to extract the address encoded with a WDM signal within an all-optical packet switch. The second receiver demultiplexes the data signals and terminates an optical interconnect.

1.7.1 Application 1 - in-band WDM label extractor

In this variation of all-optical packet switching, the data stays in the optical domain and both the header processing and switching are performed electronically (see also Fig.1.4). As proposed in [5], this configuration seems very promising regarding the reduction in power consumption and improved scalability while keeping the latency low. An important step is to extract the address or forwarding routing information from the ultra high-speed optical packets or payload ($40 - 160\,\mathrm{Gb/s}$). To encode the forwarding routing information in the payload, a low-speed ($1 - 2\,\mathrm{Gb/s}$) multi-wavelength label is used. The label is superimposed within the same spectral band of the payload with the same length as the packet duration. Using narrowband filters one can extract this in-band WDM label without distorting the packet. Each WDM signal of the label is sent on a different wavelength and the can be positioned very close to each other due to their narrow bandwidth. This label can be processed asynchronously and in parallel (each wavelength at the same time) and controls the output configuration of the switch. An illustration

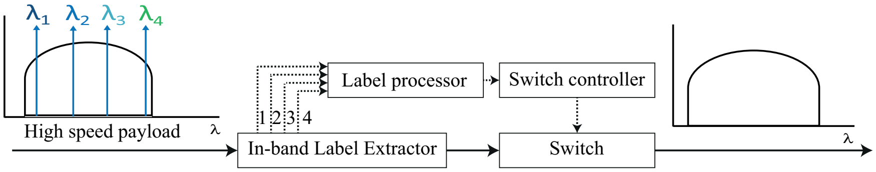

Figure 1.6: In-band label technique using 4 parallel coded multiple in-band wavelengths.

of this component is shown in Fig.1.6, where 4 parallel in-band wavelengths are used as the optical label. In order to extract the in-band WDM label from the payload, ultra-narrowband filters with a bandwidth of $2.5\,\mathrm{GHz}$ or $20\,\mathrm{pm}$ are needed to not distort the payload. With this bandwidth the WDM channel spacing can be ultra dense, down to $12.5\,\mathrm{GHz}$ or $0.1\,\mathrm{nm}$. Each WDM signal is then converted to the electrical domain by a fast photodiode (bandwidth $1 - 10\,\mathrm{GHz}$). Additionally, the power budget needs to be as low as possible which is translated on component level into optical filters with a small insertion loss and photodiodes with a high responsivity.

1.7.2 Application 2 - WDM data demultiplexer

The coming generation of optical interconnects based on the Ethernet protocol will be most probably based on very broadband filters on a coarse WDM (CWDM) grid with a channel spacing of $20\,\mathrm{nm}$ ($2500\,\mathrm{GHz}$). This has been agreed in the IEEE P802.3bm $100\,\mathrm{Gb/s}$ fiber optic task force (www.ieee802.org/3/). That is because the wavelength accuracy of the WDM signals requires a temperature controller which increases substantially the total power consumption. However, a straight forward implementation of CWDM in Si is difficult due to the wide spectral bandwidth ($> 80\,\mathrm{nm}$). That is because the fiber grating couplers that are used to couple the light in and out of the Si chip have only a limited bandwidth ($\approx\ 30\,\mathrm{nm}$). The use of horizontal coupling can solve this bandwidth issue but it makes it much more difficult to test the device on wafer scale. Our goal is to enable a much more aggressive channel spacing of $300\,\mathrm{GHz}$, several times denser than CWDM, which both increases the aggregate bandwidth and removes the bandwidth hurdle of the grating coupler. We believe that this will enable scalable WDM components for next-generation Ethernet-based OI aggregate bandwidths ($400\,\mathrm{Gb/s}$ - $1.6\,\mathrm{Tb/s}$). To enable this denser channel spacing, Si photonics WDM components must be tolerant towards ambient dynamic temperature variations, wavelength variations of the external laser array and be fabrication tolerant. Also a polarization-insensitive responsivity is required which enables a great flexibility in handling the OI. In general this is difficult to achieve due to the asymmetric waveguide dimension. The high-speed signals ($20 - 40\,\mathrm{Gb/s}$) are converted using highly-responsive high-bandwidth photodiodes. This WDM receiver can be used in an intra-data center optical interconnect for future Ethernet, Infiniband and Fiber Channel data rates (all evolving to $> 1\,\mathrm{Tb/s}$) but also increase the chip-to-chip (PCIe) or on-chip bandwidth.

1.8 Silicon photonics integrated circuits

1.8.1 WDM filters

Filters realized with ring resonators using a high-index contrast platform such as SOI can be made very compact, and can be designed with large free-spectral ranges. A microscope picture of a first-order ring resonator is shown in Fig.1.7(d). Ring-based WDM components have been demonstrated with a considerably smaller footprint [17] compared to other filter implementations. By cascading several ring resonators, one can create a very scalable and compact demultiplexer as shown in Fig.1.7(e). Other types of WDM filter are an arrayed waveguide grating (AWG) (Fig.1.7(a)), a Mach-Zehnder interferometer (Fig.1.7(b)) and an Echelle grating (Fig.1.7(c)). These filter types are based on feed-forward self interference, in contrast to the feed-backward filter principle of a ring resonator based filter. Using a feed-forward filter, one does not have the ability to tune each channel separately by e.g. a top-integrated heating element. Feed-forward filters are in general considerably larger than a ring resonator. Besides enabling high integration density, the compactness of ring-based filters enables low-power thermal tuning. Higher-order, multi-ring filters enable a higher design freedom compared to first-order single-ring designs, allowing filters to be designed with wider channel bandwidths and steeper channel roll off characteristics [18]. The resulting flat-top channel response can be exploited to improve the crosstalk and insertion loss of the WDM filter.

1.8.2 Challenges for WDM filters on SOI

One of the major challenges for realizing compact WDM filters (but also in general for any optical device) on SOI is the sensitivity of these components to variations in waveguide dimensions. These include linewidth variations during the lithographic pattern definition as well as thickness variations of the top silicon layer of the SOI stack [22]. Linewidth variations can be present both at the device scale ($1-100\,\mu\mathrm{m}$), chip scale ($1-20\,\mathrm{mm}$) or wafer scale (up to $200\,\mathrm{mm}$). Variations at the local device scale are typically much smaller ($\approx 1\,\mathrm{nm}$) than the global variations found across a full wafer ($\approx 10\,\mathrm{nm}$ and higher). Silicon thickness variations typically occur at the wafer scale, with variations of $10\,\mathrm{nm}$ and more across a full wafer [22].

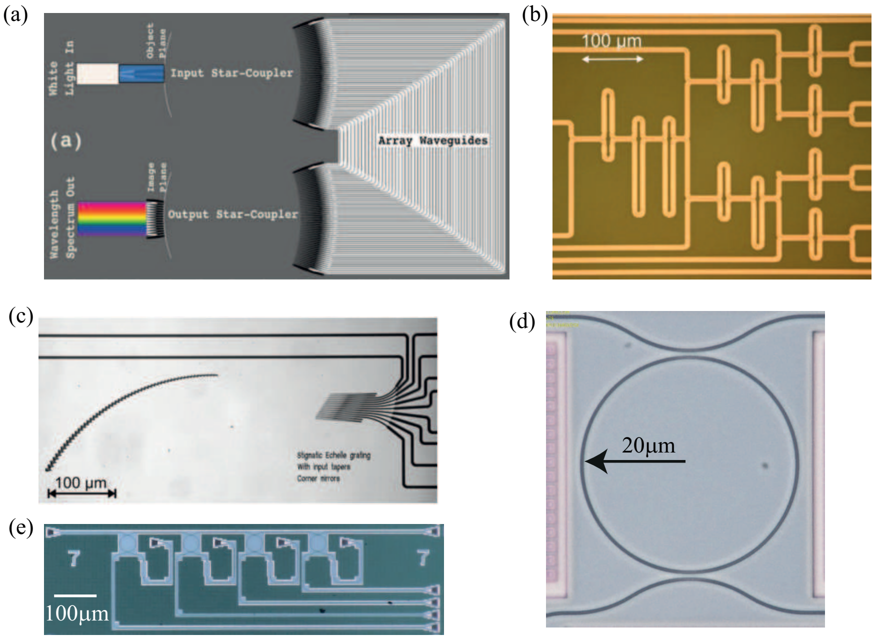

Figure 1.7: (a) Arrayed waveguide grating (taken from [19]), (b) Mach-Zehnder interferometer (taken from [20]), (c) Echelle grating (taken from [21]), (d) a first-order ring resonator and (e) a cascaded ring-based WDM filter.

In addition, silicon wavelength-selective devices are known to be highly sensitive to temperature variations. These perturbations directly influence the effective refractive index and give rise to a detrimental shift of the resonance wavelength of WDM filters such as ring resonator based filters [23], either on device, chip or wafer scale [22]. To compensate for the detrimental shifts in center wavelength of the channel, typically individual single-channel thermal heaters are used. However, for each channel an extra control signal is needed and the optimization of the whole filter bank can become quite complex.

A third challenge is the surface roughness at the sidewall of a waveguide. This surface roughness is fabrication related and is difficult to avoid. It causes the light to slightly couple counter-directionally. Especially in narrowband ring resonators, this effect drastically limits the filter performance [24].

1.8.3 Photodiodes

A photodiode converts photons into electrons and is commonly used to terminate an optical link as a receiver. This so-called opto-electronic conversion is possible due to the band gap formation in semiconductors, where the energy of a photon can excite an electron to the conduction band. Their more recent integration on a Si platform allows for a very efficient detection of the on-chip propagating light.

In this work, the goal is to fabricate a photodiode that can be integrated on a Si platform and detects high-speed signals around $1550\,\mathrm{nm}$. Two attractive materials that can be integrated on silicon are III-V compound semiconductors such as indium gallium arsenide (InGaAs) and germanium (Ge). InGaAs photodiodes are very well developed since 1979 [25] and are now considered to exhibit the highest performance amongst high-speed photodiodes. Their miniaturization on a monolithically-integrated platform have demonstrated photodiodes with a record bandwidth up to $120\,\mathrm{GHz}$ and a $0.5\,\mathrm{A/W}$ responsivity [26]. However, InGaAs related materials are expensive which limits their usability to small-footprint but very high-performance products, packaged to perform a single functionality. A cost-effective solution is found in using heterogeneously integrated III-V material on silicon, as demonstrated in [27, 28]. By means of a heterogeneous die-to-die or die-to-wafer bonding technique, small areas of III-V material are integrated on top of a Si waveguide platform. The Si chip is used for various passive optical functionality such as filtering and acts as a carrier for small III-V dies that can provide active functionality. On the other hand, Ge can be directly integrated on Si by epitaxial growth and is in addition CMOS compatible. The rapidly growing interest in Ge-on-Si devices has improved the photodiode performance tremendously over the last years. Various demonstrations of ultra-fast Ge photodiodes [29, 30] are starting to show similar performances compared to InGaAs photodiodes [31] with bandwidths exceeding $40\,\mathrm{GHz}$ at high responsivities ($> 0.7\,\mathrm{A/W}$). However, only limited demonstrations of integration with complex filters are present.

1.9 The objective of this work and outline

The objective of this work is to demonstrate WDM-enabled photonic integrated receivers with these functionalities:

1. An in-band label extractor to enable the all-optical packet switching of very high-speed optical data packets using ultra narrowband Si ring resonators. A label consists of multiple WDM signals which all have a bandwidth of $1-10\,\mathrm{GHz}$. After being extracted by an ultra-dense WDM demultiplexer they are converted to the electrical domain using InGaAs photodiodes.
2. A dense WDM data demultiplexer which is tolerant against fabrication variations and can cope with temperature and laser wavelength variations. Input signals can have a bandwidth up to $20-40\,\mathrm{Gb/s}$ and are converted to the electrical domain using Ge photodiodes.

The ring resonator and photodiode are the two main building blocks for the demonstrators and will be discussed first, respectively in chapter 2 and 3. The focus is set on bringing the reader the necessary understanding on how these components were optimized in this work. However, these chapters will give extra insight in the typical design trade-offs. In chapter 2, two types of ring resonators are optimized: narrow and broadband ring resonator filters. In chapter 3, two types of high-performance photodiodes integrated on silicon are discussed. The first type is a III-V InGaAs photodiode heterogeneously integrated on Si. The second type of photodiode is a CMOS-compatible germanium photodiode, monolithically grown on Si.

The rest of the book is devoted to discussing the demonstrated photonic integrated receivers. In chapter 4, four narrowband ring resonators are cascaded to form a 4-channel in-band label extractor. The fabrication of the ring resonators and InGaAs photodiodes is discussed as well as two system tests.

In chapter 5, second-order ring resonators are cascaded to form a dense WDM demultiplexer with Ge photodiodes. In a first stage we focus on a 5-channel $300\,\mathrm{GHz}$ demultiplexer which is extensively investigated with the objective of improving its robustness against local and wafer-level fabrication variations. In chapter 6, the performance of this component is further enhanced by increasing the total aggregate bandwidth and decreasing the power consumption.

1.10 Publications

1.10.1 International Journals

1. **P. De Heyn**, J. Luo, S. Di Lucente, N. Calabretta, H.J.S Dorren, D. Van Thourhout, ”In-Band Label Extractor Based on Cascaded Si Ring Resonators Enabling 160Gb/s Optical Packet Switching Modules”, Submitted to Journal of Lightwave Technology, (2014).

2. **P. De Heyn**, J. De Coster, P. Verheyen, G. Lepage, M. Pantouvaki, P. Absil, W. Bogaerts, J. Van Campenhout, D. Van Thourhout, ”Fabrication-Tolerant Four-Channel Wavelength-Division-Multiplexing Filter based on Collectively Tuned Si Microrings”, Journal of Lightwave Technology, 31(16), pp. 2785-2792 (2013).

3. **P. De Heyn**, D. Vermeulen, D. Van Thourhout, G. Roelkens, ”Silicon-on-Insulator All-Pass Microring Resonator Using a Polarization Rotating Coupling Section”, IEEE Photonics Technology Letters, 24(14), pp.1176-1178 (2012).

4. W. Bogaerts, P. De Heyn, T. Van Vaerenbergh, K. De Vos, S. Selvaraja, T. Claes, P. Dumon, P. Bienstman, D. Van Thourhout, R. Baets, ”Silicon microring resonators”, Lasers & Photonics Reviews, 6(1), pp. 47-73 (2012).

5. C. Stamatiadis, F. Gomez-Agis, L. Stampoulidis, K. Vyrsokinos, I. Lazarou, H.J.S. Dorren, L. Zimmermann, K. Voigt, D. Van Thourhout, P. De Heyn, H. Avramopoulos, ”The BOOM project: towards 160 Gb/s packet switching using SOI photonic integrated circuits and hybrid integrated optical flip-flops”, Journal of Lightwave Technology, 30(1), pp. 22-30 (2012).

6. C. Stamatiadis, K. Vyrsokinos, L. Stampoulidis, I. Lazarou, A. Maziotis, J. Bolten, M. Karl, T. Wahlbrink, P. De Heyn, Z. Sheng, D. Van Thourhout, H. Avramopoulos, ”Silicon-on-Insulator Nanowire Resonators for Compact and Ultra-high speed All-optical Wavelength Converters”, Journal of Lightwave Technology, (2011).

1.10.2 International & national conferences

1. **P. De Heyn**, J. De Coster, P. Verheyen, G. Lepage, M. Pantouvaki, P. Absil, W. Bogaerts, D. Van Thourhout, J. Van Campenhout, ”Polarization-Insensitive 5x20Gb/s WDM Ge Receiver using Compact Si Ring Filters with Collective Thermal Tuning”, The Optical Fiber Communication Conference and Exposition (OFC) and The National Fiber Optic Engineers Conference (NFOEC) 2014, United States, (2014).

2. M. Pantouvaki, P. Verheyen, G. Lepage, J. De Coster, H. Yu, P. De Heyn, A. Masood, W. Bogaerts, P. Absil, J. Van Campenhout, ”8x14Gb/s Si Ring WDM Modulator Array with Integrated Tungsten Heaters and Ge Monitor Photodetectors”, The Optical Fiber Communication Conference and Exposition (OFC) and The National Fiber Optic Engineers Conference (NFOEC) 2014, United States, (2014).
3. S. Selvaraja, P. De Heyn, G. Winroth, P. Ong, G. Lepage, C. Cailler, A. Rigny, K. Bourdelle, W. Bogaerts, D. Van Thourhout, J. Van Campenhout, P. Absil, ”Highly uniform and low-loss passive silicon photonics devices using a 300mm CMOS platform”, The Optical Fiber Communication Conference and Exposition (OFC) and The National Fiber Optic Engineers Conference (NFOEC) 2014, United States, (2014).
4. J. Van Campenhout, P. Verheyen, M. Pantouvaki, P. De Heyn, S. Selvaraja, G. Lepage, J. De Coster, M. Rakowski, J. Ryckaert, A. Masood, S. Pathak, W. Bogaerts, P. Dumon, D. Van Thourhout, R. Baets, P. Absil, ”25Gb/s Silicon-Photonics WDM Platform for Low-Power Optical I/O”, The 3rd International Symposium on Photonics and Electronics Convergence -Advanced Nanophotonics and Silicon Device Systems- (ISPEC2013), Japan, (2013).
5. M. Pantouvaki, P. Verheyen, G. Lepage, J. De Coster, H. Yu, P. De Heyn, P. Absil, J. Van Campenhout, ”20Gb/s Silicon Ring Modulator Co-Integrated with a Ge Monitor Photodetector”, 39th European Conference and Exhibition on Optical Communication, United Kingdom, (2013).
6. **P. De Heyn**, J. Luo, A. Trita, S. Pathak, S. Di Lucente, H. Dorren, N. Calabretta, D. Van Thourhout, ”A Compact Integrated 40Gb/s Packet Demultiplexer and Label Extractor on Silicon-on-Insulator for an Optical Packet Switch”, 39th European Conference and Exhibition on Optical Communication (ECOC) , United Kingdom, pp. paper Th.2.A.5 (2013).
7. S. Di Lucente, P. De Heyn, J. Luo, D. Van Thourhout, H.J.S. Dorren, N. Calabretta, ”160 Gb/s Optical Packet Switch Module Employing SOI Integrated Label Extractor”, 18th OptoElectronics and Communications Conference held jointly with 2013 International Conference on Photonics in Switching (OECC/PS), Japan, pp. paper TuT3-1 (2013).
8. **P. De Heyn**, S. Verstuyft, S. Keyvaninia, A. Trita, D. Van Thourhout, ”Tunable 4-Channel Ultra-Dense WDM Demultiplexer with III-V Photodiodes Integrated on Silicon-on-Insulator”, Asia Communications and Photonics Conference (ACP) , China, pp. 1-3 (2012).
9. **P. De Heyn**, D. Vermeulen, T. Van Vaerenbergh, B. Kuyken, D. Van Thourhout, ”Ultra-high Q and finesse all-pass microring resonators on Silicon-on-Insulator

using rib waveguides”, 16th European Conference on Integrated Optics and technical exhibition, Spain, pp. paper 195 (2012).

10. P. Verheyen, G. Lepage, J. Van Campenhout, M. Pantouvaki, P. Absil, P. De Heyn, W. Bogaerts, P. Dumon, S. Selvaraja, ”Co-integration of Ge detectors and Si modulators in an advanced Si photonics platform”, SPIE Photonics Europe 2012, 8431, Belgium, pp. paper 39 (2012).

11. J. Van Campenhout, M. Pantouvaki, P. Verheyen, H. Yu, P. De Heyn, G. Lepage, W. Bogaerts, P. Absil, ”Silicon-Photonics Devices for Low-Power, High-Bandwidth Optical I/O”, Integrated Photonics Research, Silicon And Nano Photonics , United States, pp. paper ITu2B.1 (2012).

12. T. Claes, D. Vermeulen, P. De Heyn, K. De Vos, G. Roelkens, D. Van Thourhout, P. Bienstman, ”Towards a silicon dual polarization ring resonator sensor for multiplexed and label-free structural analysis of molecular interactions”, XI Conference on Optical Chemical Sensors and biosensors (EUROPTRODE XI), Spain, pp. 159 (2012).

13. G. Roelkens, S. Keyvaninia, S. Stankovic, M. Tassaert, N. Hattasan, A. Gassenq, P. De Heyn, Y. De Koninck, P. Mechet, R. Kumar, M. Muneeb, D. Vermeulen, G. Morthier, R. Baets, D. Van Thourhout, ”III-V-on-silicon membrane photonics for near-infrared and mid-infrared applications”, 16th European Conference on Integrated Optics (ECIO 2012), Spain, (2012).

14. D. Vermeulen, P. De Heyn, T. Van Vaerenbergh, W. Bogaerts, G. Roelkens, ”Silicon-on-Insulator polarization rotating micro-ring resonator”, IEEE Photonics Conference (IPC), United States, pp. 875-876 (2011).

15. C. Stamatiadis, L. Stampoulidis, K. Vyrsokinos, I. Lazarou, L.Zimmermann, K.Voigt, L. Moerl, J. Kreissl, B. Sedighi, Z. Sheng, P. De Heyn, D. Van Thourhout, M. Karl, T. Wahlbrink, J. Bolten, A. Leinse, R, Heidemann, F. Gomez-Agis, H.J.S Dorren, A. Pagano, E. Riccardi, H. Avramopoulos, ”The ICT-BOOM project: Photonic Routing on a Silicon-On-Insulator Hybrid Platform”, 15th Conference on Optical Network Design and Modeling (ONDM), Italy, (2011).

16. **P. De Heyn**, B. Kuyken, D. Vermeulen, W. Bogaerts, D. Van Thourhout, ”High-performance low-loss siliconon- insulator microring resonators using TM-polarized light”, The Optical Fiber Communication Conference and Exposition (OFC) and The National Fiber Optic Engineers Conference (NFOEC) 2011, , United States, pp. paper OThV2 (3 pages) (2011).

17. L. Moerl, P. De Heyn, D. Van Thourhout, ”Optical coupling of SOI waveguides and III-V photodetectors”, French Symposium on Emerging Technologies for Micro-nanofabrication, France, (2010).
18. **P. De Heyn**, B. Kuyken, D. Vermeulen, W. Bogaerts, D. Van Thourhout, ”Improved intrinsic Q of Siliconon- Insulator microring resonators using TM-polarized light”, Proceedings of the 2010 Annual Symposium of the IEEE Photonics Benelux Chapter, Netherlands, pp. 197-200 (2010).
19. G. Roelkens, D. Vermeulen, L. Liu, T. Spuesens, R. Kumar, P. Mechet, K. Huybrechts, S. Keyvaninia, S. Stankovic, M. Tassaert, P. De Heyn, K. Komorowska, S. Selvaraja, D. Van Thourhout, G. Morthier, R. Baets, R. Halir, ”III-V/silicon photonic integrated circuits for FTTH and optical interconnect”, IB2COM, Spain, (2010).
20. D. Vermeulen, T. Spuesens, P. De Heyn, P. Mechet, R. Notzel, S. Verstuyft, D. Van Thourhout, G. Roelkens, ”III-V/SOI photonic integrated circuit for FTTH central office transceivers in a PTP network configuration”, ECOC, Italy, pp. Tu.5.C.2 (2010).

References

[1] A Stavdas, C T Politi, T Orphanoudakis, and A Drakos. *Optical packet routers : how they can efficiently and cost-effectively scale to petabits per second*. Journal of Optical Networking, 7(10):876–894, 2008.

[2] Adel a. M. Saleh and Jane M. Simmons. *All-Optical Networking: Evolution, Benefits, Challenges, and Future Vision*. Proceedings of the IEEE, 100(5):1105–1117, May 2012.

[3] A M J Koonen, Ni Yan, J J Vegas Olmos, Idelfonso Tafur Monroy, Christophe Peucheret, Erik Van Breusegem, and Evi Zouganeli. *Label-Controlled Optical Packet Routing Technologies and Applications*. IEEE Journal of Selected Topics in Quantum Electronics, 13(5):1540–1550, 2007.

[4] Shun Yao, S J Ben Yoo, and Biswanath Mukherjee. *All-Optical Packet Switching for Metropolitan Area Networks : Opportunities and Challenges*. IEEE Communications Magazine, (March):142–148, 2001.

[5] S. J. Ben Yoo. *Energy Efficiency in the Future Internet: The Role of Optical Packet Switching and Optical-Label Switching*. IEEE Journal of Selected Topics in Quantum Electronics, 17(2):406–418, March 2011.

[6] Christoforos Kachris and Ioannis Tomkos. *A Survey on Optical Interconnects for Data Centers*. IEEE Communications Surveys & Tutorials, 14(4):1021–1036, 2012.

[7] European Union’s 7th Framework Programme. *LIGHTNESS: Low latency and high throughput dynamic network infrastructures for high performance datacentre interconnects*. 2012.

[8] Jun Luo, Stefano Di Lucente, Abhinav Rohit, Shihuan Zou, Kevin A Williams, Harm J S Dorren, and Nicola Calabretta. *Optical Packet Switch With Distributed Control Based on InP Wavelength-Space Switch Modules*. IEEE Photonics Technology Letters, 24(23):2151–2154, 2012.

[9] S Di Lucente, J Luo, R Pueyo Centelles, A Rohit, S Zou, K a Williams, H J S Dorren, and N Calabretta. *Numerical and experimental study of a high*

port-density WDM optical packet switch architecture for data centers. Optics express, 21(1):263–9, January 2013.

[10] *Luxtera's 4x28Gbs transceiver using PSM4.*, 2013.

[11] A M J Koonen, Haoshuo Chen, Henrie P A Van Den Boom, and Oded Raz. *Silicon Photonic Integrated Mode Multiplexer and Demultiplexer*. IEEE Photonics Technology Letters, 24(21):1961–1964, 2012.

[12] C R Doerr, L Chen, L L Buhl, and Y Chen. *Eight-Channel SiO / Si N / Si / Ge CWDM Receiver*. IEEE Photonics Technology Letters, 23(17):1201–1203, 2011.

[13] Long Chen, Christopher R. Doerr, Larry Buhl, Yves Baeyens, and Ricardo a. Aroca. *Monolithically Integrated 40-Wavelength Demultiplexer and Photodetector Array on Silicon*. IEEE Photonics Technology Letters, 23(13):869–871, July 2011.

[14] David A. B. Miller and By David A B Miller. *Device Requirements for Optical Interconnects to Silicon Chips*. Proceedings of the IEEE, 97(7):1166 – 1185, July 2009.

[15] Solomon Assefa, Huapu Pan, Steven Shank, William M J Green, Alexander Rylyakov, Clint Schow, Marwan Khater, Swetha Kamlapurkar, Edward Kiewra, Carol Reinholm, Teya Topuria, Philip Rice, Christian Baks, and Yurii Vlasov. *Monolithically Integrated Silicon Nanophotonics Receiver in 90nm CMOS Technology Node*. In OFC/NFOEC 2013 - 2013 Conference on Optical Fiber Communication and the National Fiber Optic Engineers Conference, page OM2H.4, 2013.

[16] Pieter Dumon. *Ultra-Compact Integrated Optical Filters in Silicon-on-insulator by Means of Wafer-Scale Technology*. PhD thesis, Ghent University, 2007.

[17] Wim Bogaerts, Shankar Kumar Selvaraja, Pieter Dumon, Joost Brouckaert, Katrien De Vos, Dries Van Thourhout, and Roel Baets. *Silicon-on-Insulator Spectral Filters Fabricated With CMOS Technology*. IEEE Journal of Selected Topics in Quantum Electronics, 16(1):33–44, 2010.

[18] B.E. Little, S.T. Chu, P.P. Absil, J.V. Hryniewicz, F.G. Johnson, F. Seiferth, D. Gill, V. Van, O. King, and M. Trakalo. *Very High-Order Microring Resonator Filters for WDM Applications*. IEEE Photonics Technology Letters, 16(10):2263–2265, October 2004.

[19] Shibnath Pathak, Michael Vanslembrouck, Pieter Dumon, Dries Van Thourhout, and W. Bogaerts. *Optimized Silicon AWG With Flattened Spectral Response Using an MMI Aperture*. Journal of Lightwave Technology, 31(1):87–93, 2013.

[20] Folkert Horst, William M J Green, Solomon Assefa, Steven M Shank, Yurii A Vlasov, and Bert Jan Offrein. *Cascaded Mach-Zehnder wavelength filters in silicon photonics for low loss and flat pass-band WDM (de-) multiplexing*. Optics express, 21(10):11652–11658, 2013.

[21] F. Horst, W.M.J. Green, B.J. Offrein, and Y.a. Vlasov. *Silicon-on-Insulator Echelle Grating WDM Demultiplexers With Two Stigmatic Points*. IEEE Photonics Technology Letters, 21(23):1743–1745, December 2009.

[22] Shankar Kumar Selvaraja, Patrick Jaenen, Wim Bogaerts, Dries Van Thourhout, Pieter Dumon, and Roel Baets. *Fabrication of Photonic Wire and Crystal Circuits in Silicon-on-Insulator Using 193nm Optical Lithography*. Journal of Lightwave Technology, 27(18):4076–4083, 2009.

[23] Sahnggi Park, Kap-Joong Kim, In-gyoo Kim, and Gyungock Kim. *Si microring MUX / DeMUX WDM filters*. Optics Express, 19(14):14627–14633, July 2011.

[24] Zhen Sheng, Liu Liu, Sailing He, Dries Van Thourhout, and Roel Baets. *Silicon-on-insulator microring resonator for ultra dense WDM applications*. 2009 6th IEEE International Conference on Group IV Photonics, pages 122–124, September 2009.

[25] John E Bowers and Charles A Burrus. *Ultrawide-band long-wavelength p-i-n photodetectors*. Journal of Lightwave Technology, 5(10):1339–1350, 1987.

[26] Andreas Beling, Heinz-gunter Bach, Gebre Giorgis Mekonnen, Reinhard Kunkel, Detlef Schmidt, and A Abstract. *Miniaturized Waveguide-Integrated p-i-n Photodetector With 120-GHz Bandwidth and High Responsivity*. IEEE Photonics Technology Letters, 17(10):2152–2154, 2005.

[27] G. Roelkens, J. Brouckaert, D. Van Thourhout, R. Baets, R. Notzel, and M. Smit. *Adhesive Bonding of InPInGaAsP Dies to Processed Silicon-On-Insulator Wafers using DVS-bis-Benzocyclobutene*. Journal of The Electrochemical Society, 153(12):G1015, 2006.

[28] Joost Brouckaert, Gunther Roelkens, Dries Van Thourhout, and Roel Baets. *Thin-Film IIIV Photodetectors Integrated on Silicon-on-Insulator Photonic ICs*. Journal of Lightwave Technology, 25(4):1053–1060, April 2007.

[29] Solomon Assefa, Fengnian Xia, and Yurii a Vlasov. *Reinventing germanium avalanche photodetector for nanophotonic on-chip optical interconnects*. Nature, 464(7285):80–4, March 2010.

[30] Laurent Vivien, Andreas Polzer, Delphine Marris-morini, Johann Osmond, Jean Michel Hartmann, Paul Crozat, Eric Cassan, Christophe Kopp, Horst Zimmermann, and Jean Marc Fédéli. *Zero-bias 40Gbit/s germanium waveguide photodetector on silicon*. Optics Express, 20(2):5905–5907, 2012.

[31] Jifeng Liu, Rodolfo Camacho-Aguilera, Jonathan T. Bessette, Xiaochen Sun, Xiaoxin Wang, Yan Cai, Lionel C. Kimerling, and Jurgen Michel. *Ge-on-Si optoelectronics*. Thin Solid Films, 520(8):3354–3360, February 2012.

2

Ring resonator design and simulation

The aim of this chapter is to design two classes of filters based on ring resonators, fabricated in the high-index contrast silicon-on-insulator platform. The first filter class that we discuss is the narrowband ring resonator. We demonstrate that the strong waveguide confinement has an important drawback that limits the photonic circuit designer to build narrowband filters: sidewall roughness induced backscattering. An important part of this chapter is devoted to solve this issue by optimizing ring resonators using less-confined optical modes. These ring resonators can be used for e.g. an ultra-dense WDM label extractor as discussed in chapter 4. The second filter class is the higher-order ring resonator which have the unique ability to broaden the bandwidth of the resonance without increasing the crosstalk. This property enables fabrication-tolerant dense WDM receivers as discussed in chapter 5 and 6.

2.1 Introduction

A ring resonator is probably the most popular optical component developed in integrated platforms in research due to its unmatched compactness and wide deployability. Applications vary from narrow and wide-band filters [1–3], high-speed low-power modulators [4], compact all-optical switches [5], long delay lines [6, 7], highly sensitive biosensors [8, 9], efficient lasers [10–12] and thermal bi-stability enabled reservoir computing [13] among others. Ring resonators are extensively described in literature [14–16]. In what follows, we will briefly summarize all

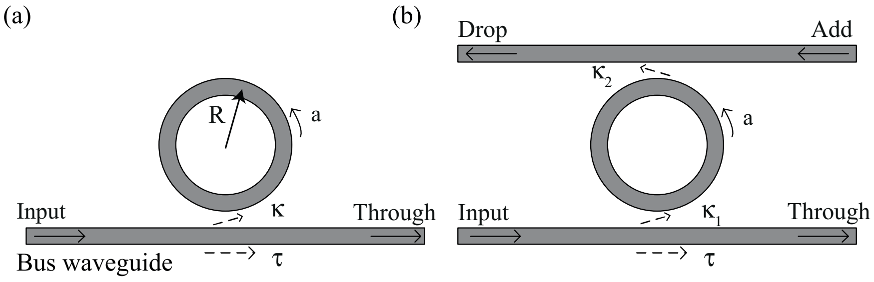

Figure 2.1: General schematic view of (a) an all-pass ring resonator (b) add-drop ring resonator. Picture adapted from [16].

concepts and formulas that are needed to describe the functional behaviour of ring resonators. In section 2.1.1 and 2.1.2, we start by presenting the analytical formulas for an all-pass and add-drop ring resonator structure respectively. In section 2.1.3, we will discuss several performance metrics that are used in this work to describe the behavior of a ring resonator.

2.1.1 All-pass ring resonators

In its simplest form a ring resonator can be configured as a so-called all-pass (AP) filter as shown in Fig.2.1(a). The term *ring resonator* is typically used to indicate any looped resonator, but stricto senso it is a circular ring with radius R. When the shape is elongated with a straight section along one direction (typically along the coupling section) the term *racetrack resonator* is also used. Both filter shapes are used throughout this work, where the extra straight section along the coupling section (denoted as L_c) is used to increase the coupling between bus and ring waveguide. However, we will use the name ring resonator for both types since all equations apply to both shapes. The basic spectral properties of an AP ring resonator can easily be derived by assuming continuous wave operation. Under the assumption that reflections back into the bus waveguide are negligible (which is not necessarily the case, see section 2.1.4), we can write the ratio of the transmitted (through) and incident (input) electric field in the bus waveguide as [14, 16]:

$$\frac{E_{\text{through}}}{E_{\text{input}}} = e^{i(\pi+\phi)} \frac{a - \tau e^{-i\phi}}{1 - \tau a e^{i\phi}}. \tag{2.1}$$

$\phi = \beta L$ is the single-pass phase shift, with L the round trip length and β the propagation constant of the circulating mode. a is the single-pass amplitude transmission, including both propagation loss (i.e. scattering and bend loss) in the ring and additional loss in the couplers. By squaring equation 2.1, we obtain the intensity transmission T.

$$T = \frac{I_{\text{through}}}{I_{\text{input}}} = \frac{a^2 - 2\tau a \cos\phi + \tau^2}{1 - 2a\tau \cos\phi + (\tau a)^2} \tag{2.2}$$

with τ the self-coupling coefficient. Similarly, we can define κ as the cross-coupling coefficients, and so τ^2 and κ^2 are the power splitting ratios of the coupler, and they are assumed to satisfy $\tau^2 + \kappa^2 = 1$, which means there are no losses in the coupling section. This assumption can introduce a small error on the transmission power levels. The width of the resonance remains correct, as long as the losses that are introduced by the couplers are included in the resonator round trip loss coefficient a.

We find the ring to be on resonance when the phase ϕ is a multiple of 2π, or when the wavelength of the light fits a whole number of times (m) inside the optical length of the ring:

$$\lambda_{\text{res}} = \frac{n_{\text{eff}} L}{m}, m = 1,2,3..., \tag{2.3}$$

At this wavelength, the input of the ring (bus to ring) interferes constructively with the fields traveling inside the ring, and the output of the ring (ring to bus) interferes destructively with the fields traveling in the bus. Thus the power is build up inside the ring. A typical ring radius is between 5 and $20\,\mu\text{m}$, which corresponds with a number for m from 50 to 200 using standard Si waveguides ($450 \times 220\,\text{nm}^2$ and using the quasi-TE mode). For ideal cavities with zero attenuation, $a \approx 1$, the transmission is unity for all values of detuning ϕ. For non-ideal cavities and under critical coupling the transmission at resonance drops to zero. The coupled power is then equal to the power loss in the ring $1 - a^2 = \kappa^2$ or $\tau = a$. In this situation the fraction (κ^2) of the build-up power traveling in the ring that couples from the ring back to the bus, is equal to the self coupling τ^2 and interferes destructively. We say that the ring is critically coupled and light at the resonance wavelength cannot escape the ring. From the input side there is no light that can pass the ring. The light stays in the rings until it is absorbed or scattered away. The smaller the losses inside the ring, the lower the required coupling that is needed to fulfill the critical coupling condition. But also, the lower the coupling, the longer it takes to build up the power to a steady state value. Together, due to a low loss and low coupling, the light will travel longer before it is lost. Hence, it will pass the directional coupler more times and will do more round trips than when the coupling or the ring losses are larger. As a consequence, the resonance wavelength condition (λ_{res}) becomes more strict and the resonances become sharper, exactly the same as for any other resonance structure e.g. a Fabry-Perot cavity. If the coupling is larger than the losses inside the cavity, the ring is over-coupled. In the case where the coupling is smaller than the losses, the ring is under-coupled.

2.1.2 Add-drop ring resonators

When the ring resonator is coupled to two waveguides, the incident field is partly transmitted to the drop port (see Fig. 2.1(b)). The transmission of the add-drop (AD) ring to the through and the drop port is then derived as follows:

$$T_{\mathrm{through}} = \frac{I_{\mathrm{through}}}{I_{\mathrm{input}}} = \frac{\tau_2^2 a^2 - 2\tau_1\tau_2 a\cos\phi + \tau_1^2}{1 - 2\tau_1\tau_2 a\cos\phi + (r_1\tau_2 a)^2} \tag{2.4}$$

$$T_{\mathrm{drop}} = \frac{I_{\mathrm{drop}}}{I_{\mathrm{input}}} = \frac{(1-\tau_1^2)(1-\tau_2^2)a}{1 - 2\tau_1\tau_2 a\cos\phi + (\tau_1\tau_2 a)^2} \tag{2.5}$$

If the attenuation is negligible ($a \approx 1$), critical coupling occurs at symmetric power coupling (κ_1=κ_2 or $\tau_1 = \tau_2$). In the realistic case of a lossy resonator, critical coupling occurs when the losses match the self-coupling as $\tau_2 a = \tau_1$ and hence asymmetric power coupling is needed. In this work only symmetric power coupling is used. One can follow the same reasoning as in the case of an AP ring: the smaller the losses inside the ring and the lower the coupling to and out of the ring, the longer the light stays in the ring. As a consequence the wavelength resonance condition becomes more strict and hence the resonance sharper.

2.1.3 Spectral characteristics

The characteristic spectra and parameters of both an all-pass and add-drop ring configuration are indicated in Fig.2.2. The full-width-half-maximum (FWHM) is usually denoted as 3-dB bandwidth (abbreviated as BW or BW$_3$). The insertion loss (IL) of the drop response is defined as the ratio of the maximum level at the drop port (T$_{\mathrm{drop}}$) to the maximum level of the through port (T$_{\mathrm{through}}$). The extinction ratio (ER) of the through response is defined as the ratio between the minimum of the through port (T$_{\mathrm{through}}$) with respect to the maximum of the through port.

Within a first order approximation of the dispersion, the wavelength range between two resonances or free spectral range (FSR) in function of wavelength equals:

$$\mathrm{FSR} = \frac{\lambda^2}{n_g L} \tag{2.6}$$

with L the round trip length. The group index (n_g) takes into account the dispersion of the waveguide and is defined by

$$n_g = n_{eff} - \lambda_0 \frac{dn_{eff}}{d\lambda}. \tag{2.7}$$

The group index, and the corresponding group velocity $v_g = \frac{c}{n_g}$, describes the velocity at which the envelope of a propagating pulse travels and is a characteristic of a dispersive medium (or waveguide).

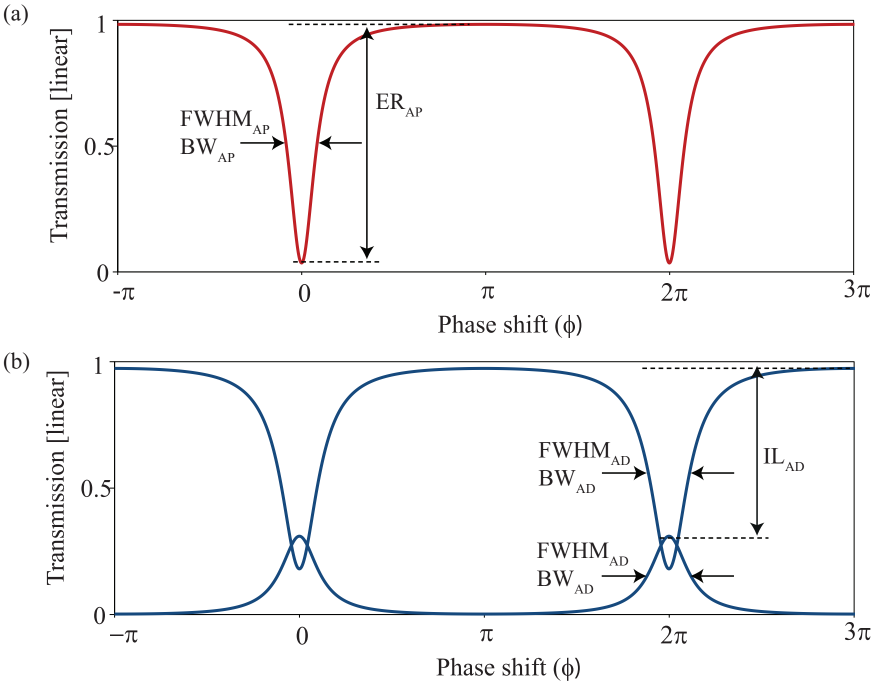

Figure 2.2: Transmission spectrum of (a) an all-pass ring and (b) the two outputs of add-drop ring with the important spectral features indicated. Figure adapted from [16].

The shape of the transmission curves approximates a Lorentzian curve in the vicinity of the resonance. We will use this property to fit the measured transmission spectra with $\Delta\lambda$ the FWHM or BW. Note that this equation can be used for both a through and drop response.

$$y(\lambda) = \text{baseline} + \frac{\text{A}(\Delta\lambda/2)^2}{(\lambda - \lambda_{\text{res}})^2 + (\Delta\lambda/2)^2} \tag{2.8}$$

The finesse of a resonance is defined as the ratio of FSR and resonance width,

$$\text{Finesse} = \frac{\text{FSR}}{\text{BW}} \tag{2.9}$$

It is thus a measure for the sharpness of resonances relative to their spacing. The quality factor (Q-factor) is a measure for the sharpness of the resonance relative to its central frequency,

$$\text{Q-factor} = \frac{\lambda_{res}}{\text{BW}} \tag{2.10}$$

The mathematics behind the finesse and Q-factor are described in numerous text books and publications [14, 17, 18]. The finesse is found to represent within a factor of 2π the number of round-trips made by light in the ring before its intensity is reduced to $1/e$ of its initial value. The power build up in the resonator can be calculated as the $\frac{\text{finesse}}{\pi}P_{input}$ with P$_{input}$ as the input power. The Q-factor represents the number of oscillations of the field before the circulating energy is depleted to $1/e$ of the initial energy. To determine the Q-factor, the ring resonator is excited to a certain level and the rate of power decay is measured. However, a more straight-forward way is the use of Eq.(2.10) by measuring the BW of the resonance.

A distinction is made between *loaded* Q and *intrinsic* Q. The intrinsic (or unloaded) Q of a resonator is the Q-factor when the resonator would not be coupled to waveguides. When coupling to a waveguide, additional losses are introduced to the cavity, namely the coupling to the bus waveguide. Hence, the loaded Q is always smaller than the intrinsic Q. We always mean *loaded* Q when referring to Q-factor, unless it is specifically mentioned otherwise. If an all-pass ring filter is critically coupled, the losses in the cavity are equal to the coupling from the bus to the ring. In other words, the intrinsic Q is the double of the loaded Q at critical coupling. In this way, one can easily estimate the cavity losses and thus also the intrinsic Q as follows [17, 19, 20]:

$$Q_{\text{loaded}} = \frac{Q_i}{2} = \frac{\pi n_g}{\lambda_0 \alpha} \tag{2.11}$$

with α the total propagation loss per unit length and n$_g$ the group index. Note that this assumes that the coupling section is lossless (i.e. $\kappa^2 + \tau^2 = 1$) which is not necessarily the case. One approach of estimating the propagation loss is lowering the coupling between the bus and the AP ring resonator. This way, the cavity losses are dominated by the cavity losses and $\mathrm{Q}_{\mathrm{loaded}}$ approaches Q_i. The effective propagation loss A can then be estimated using following formula:

$$A[\mathrm{dB/cm}] = 4.3\frac{2\pi n_g}{\lambda_{0[\mathrm{cm}]}Q_{\mathrm{loaded}}} \tag{2.12}$$

where the factor 4.3 comes from $10\log_{10}\exp(1)$.

In [21], an useful formula for add-drop ring resonators is deduced that gives a closed-form expression for the round trip amplitude loss coefficient a (as used in Eq.(2.5) on page 2-4) and is shown in Eq.(2.13). The extinction ratio (ER), FSR and 3dB bandwidth ($\Delta\lambda$) are the only parameters that are to be determined. Note that ER should be expressed on a linear scale and not in decibel.

$$1 - a^2 = \frac{2\pi\Delta\lambda\sqrt{\mathrm{ER}})}{\mathrm{FSR}} \tag{2.13}$$

From a^2, one can calculate the round trip loss [dB] as $-10\log 10(a^2)$. A similar formula is found to determine the cross-coupling factor between the bus and ring (κ^2).

$$\kappa^2 = \frac{\pi\Delta\lambda(1 - \sqrt{\mathrm{ER}})}{\mathrm{FSR}} \tag{2.14}$$

2.1.4 Counter-directional coupling

Counter-directional coupling is the mutual coupling between the clockwise and counterclockwise propagating mode. When there is coupling, this will result in a net power transfer from the intentionally excited forward mode to the backward propagating mode, and this coupling also causes distortion of the ideal Lorentzian-shaped spectrum by resonance splitting. To understand resonance splitting due to counter-directional coupling, one can describe this system in temporal coupled-mode theory (TCMT) [18, 22, 23].

In an ideal resonator (e.g. circular symmetric, with perfect sidewall smoothness and without a coupling section), the forward and backward traveling-wave modes are uncoupled, frequency-degenerate eigenmodes of the system. However, in practice, due to small perturbations the two traveling-wave modes can couple. The traveling waves are then no longer uncoupled. Therefore, a new base of two uncoupled modes, which are the eigenmodes of the system, is chosen, e.g. two orthogonal standing waves (symmetric and antisymmetric with respect to a reference plane perpendicular to the bus waveguides as in [18]). Two different superpositions of the forward and backward traveling-wave mode can be used for this purpose. Forward propagating light in the waveguide will then excite the symmetric and antisymmetric mode 90° out of phase. Due to symmetry breaking, these uncoupled eigenmodes are no longer degenerate, resulting in a resonance frequency shift and thus the spectrum will show resonance splitting.

In principle, this perturbation could be induced by the presence of a bus waveguide [22], since the two standing waves will feel a slightly different environment (effective refractive index) causing the supermodes to resonate on a slightly different frequency. From the traveling-wave viewpoint, the directional coupler is then a periodically phase-matched scatterer into the backward propagation direction, thus building up the power in the counter-propagating mode and splitting the supermodes. A good introduction about the modeling of the back-reflection caused by the coupling section can be found in [24]. Also sidewall-roughness-induced backscattering has been predicted [25] and demonstrated [23, 26] to lead to deleterious resonance splitting. In higher-order filters, with several coupling sections, it might limit designers to obtain a good extinction ratio. A solution is been proposed in [22] by choosing for a longer and weaker directional coupler that covers several propagation wavelengths of the ring mode, thus reducing the difference in environment between the modes.

Little et al. show in [25] that if the time to deplete the ring due to counter-directional coupling becomes smaller than the time to charge up the ring to its steady-state value, resonance splitting becomes visible in the spectrum of the resonator. This behavior is usually translated into $R > \kappa$ with R the mutual field coupling between the forward and backward propagating mode and κ^2 the external power coupling. Because it is often desirable to keep κ low to achieve a narrow bandwidth, even minor reflections will cause problems in high-Q devices.

This effect is demonstrated in Fig.2.3, where the simulated transmission spectra are shown of an add-drop ring resonator with radius $5\,\mu\mathrm{m}$ and mutual coupling between the forward and backward propagating mode $R = 0.0053$. In Fig.2.3(a), the power coupling κ^2 is 0.0169. Because $\kappa^2 > R$, no resonance splitting is detected. From the moment the coupling is reduced, resonance splitting can become visible. This is shown in Fig.2.3(b), where $\kappa^2 = 0.0036$ which is smaller than R and hence resonance splitting becomes visible.

To clearly visualize the effect of counter-directional coupling, the transmission spectra of the same ring configurations is simulated with $R = 0$, as shown in Fig.2.3(c) and (d). In the case of $\kappa^2 > R$, the effect of counter-directional coupling is visible in the increased IL ($-1.2\,\mathrm{dB}$ with respect to $-0.5\,\mathrm{dB}$), decreased ER ($-17\,\mathrm{dB}$ with respect to $-24\,\mathrm{dB}$) and increased 3dB BW ($120\,\mathrm{pm}$ with respect to $100\,\mathrm{pm}$). In the case of $\kappa^2 < R$, the effect of counter-directional coupling on the filter performance becomes much more drastic. The IL (as the maximum of one of the split resonances) is now $-6.5\,\mathrm{dB}$, which is $-4.3\,\mathrm{dB}$ larger with respect to the case where $R = 0$. Also for the ER, the performance is degraded from $-12\,\mathrm{dB}$ to $-5\,\mathrm{dB}$. The definition of the 3dB BW becomes inadequate. Note that the larger the mutual coupling, the larger the resonance splitting becomes.

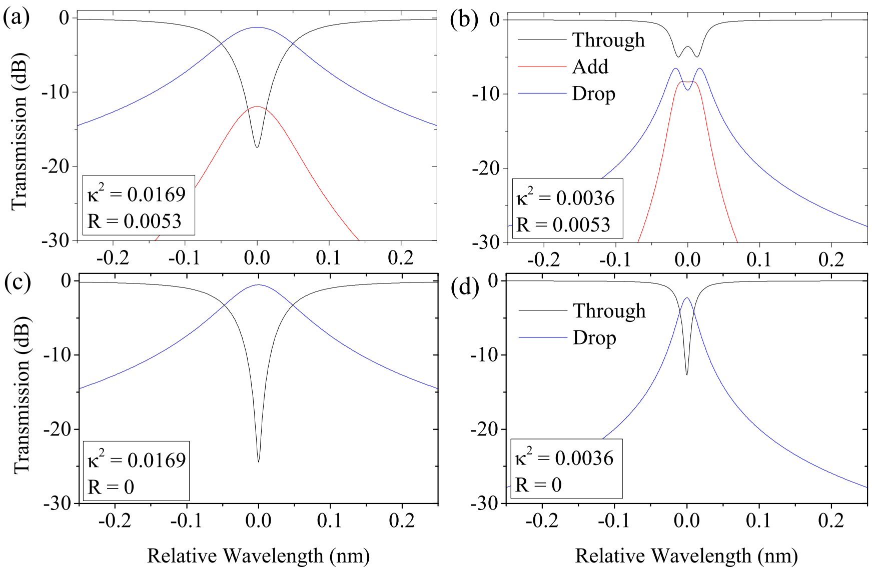

Figure 2.3: The effect of counter-directional coupling on the spectral behaviour of an add-drop ring resonator (radius $5\,\mu\mathrm{m}$*) when (a)* $\kappa^2 > R$ *and (b)* $\kappa^2 < R$*. In (c) and (d), the transmission spectra are shown for the same ring configuration but when no counter-directional coupling is present (R=0). A propagation loss of* $3\,\mathrm{dB/cm}$ *is assumed.*

Next to resonance splitting, counter-directional coupling also causes power reflecting back into the input waveguide and/or the add-port. This reflected power is also shown in Fig.2.3(a) and (b). This backreflection is strongly enhanced by the resonance effect of the ring [27]. The longer the light inside the ring, the stronger the enhancement. In Fig.2.3(a), this reflected power has a ratio of $-12\,\mathrm{dB}$ with respect to the input power. These high reflection can cause instability in the transmitting laser. In Fig.2.3(b), the ratio is even larger ($-8.2\,\mathrm{dB}$).

In silicon waveguides, sidewall corrugation is typically considered to have the largest impact on the counter-directional coupling and hence resonance splitting. In a straight waveguide this counter-directional coupling is known as surface-roughness induced backreflection. These reflections can be accurately quantified by inverse Fourier transforming the reflection spectrum as demonstrated in [27–29].

Following the arguments in [17, 25, 30], the depth of the sidewall corrugation is mostly considered as a stochastic variable, corresponding with a Gaussian correlation function with a fixed variance and correlation length. Both the variance and correlation length are determined by the fabrication process. It is experimentally demonstrated that backscattering is indeed a wavelength dependent random process whose statistics is independent of the shape, size, refractive index contrast, and technology of the waveguide [31].

To simulate the transmission spectrum of an add-drop resonator with the presence of counter-directional coupling R, one can use the following formulas (derived based on [16, 25]). The field transmission of the drop, add and through port are listed in equations (2.15),(2.16) and (2.17).

$$t_{\text{drop}} = \frac{-\sqrt{a}\kappa^2 \exp(-j\phi/2)A}{1-\tau^2 a \exp(-j\phi)A} \tag{2.15}$$

$$t_{\text{add}} = \frac{-\sqrt{a}\tau^2\kappa_2 B \exp(-j\phi/2)}{1-\tau^2 a \exp(-j\phi)A} \tag{2.16}$$

$$t_{\text{through}} = \frac{\tau - a\tau\kappa^2 \exp(-j\phi)A}{1-\tau^2 a \exp(-j\phi)A} \tag{2.17}$$

Factor A and B are defined as follows

$$A = \frac{\tau_R - a\tau^2 \exp(-j\phi)}{1-\tau_R a\tau^2 \exp(-j\phi)} \tag{2.18}$$

$$B = \frac{jR}{1-\tau_R a\tau^2 \exp(-j\phi)} \tag{2.19}$$

with $\tau_R = \sqrt{1-R^2}$.

2.2 Losses in a silicon ring resonators

In this section an overview is given of several loss mechanisms in ring resonators. The loss in a ring resonator limits in general its performance.

To comply with a single-mode condition (for one polarization, at $1550\,\text{nm}$ wavelength) the cross section dimensions should be submicrometer in size or $\approx \lambda/n$, with typically increasing widths for decreasing thicknesses. The most commonly used dimensions are between $400\,\text{nm}$ and $500\,\text{nm}$ in width, and between $200\,\text{nm}$ and $250\,\text{nm}$ in height [32–35]. In this work we typically use $450\,\text{nm} \times 220\,\text{nm}$ waveguides with $n_{\text{eff}} = 2.45$ and $n_g = 4.3$ for the quasi-TE mode. We will refer to this waveguide type as the Si *strip* waveguide.

Propagation losses in silicon waveguides originate from multiple sources, and recent advances in process technology have brought the losses of Si strip waveguide down to $2-3\,\text{dB/cm}$ [32, 36] for waveguides with an air cladding and less than $2\,\text{dB/cm}$ with an oxide cladding [37]. On an advanced 300mm CMOS platform, Selvaraja et.al. have shown recently ultra-low propagation losses of $0.45 \pm 0.12\,\text{dB/cm}$ [38]. In the following we discuss two typical loss mechanisms in a ring resonator using silicon strip waveguides: surface-roughness scattering and excess bend losses (i.e. the extra loss induced in a bent waveguide). Using

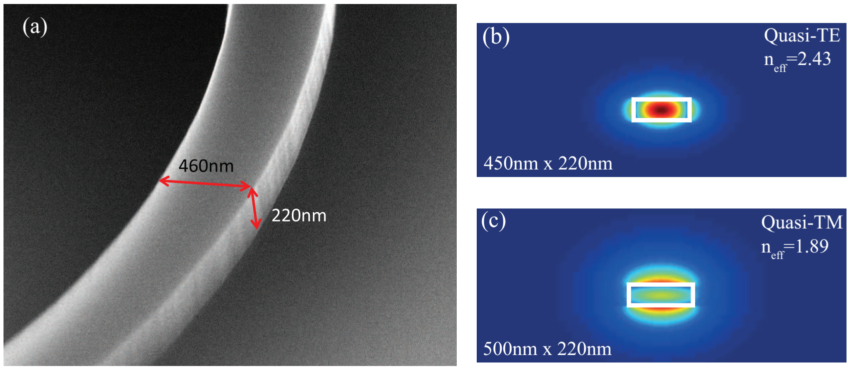

Figure 2.4: (a) Bird's eye SEM view of a photonic wire waveguides fabricated with the process from [36]. The sidewall roughness is clearly visible. (b) and (c): the intensity profiles of the fundamental quasi-TE and quasi-TM mode in a silicon strip (oxide cladding).

high optical powers, additional loss mechanisms occur from two-photon absorption and free carrier absorption [26] but are not relevant in this work. Also, light can be coupled to radiative modes in the substrate. However, this substrate leakage decreases exponentially with bottom cladding thickness [39]. For a bottom oxide of $2\,\mu\mathrm{m}$, these losses are negligible for the TE ground mode and in the order of $0.001\,\mathrm{dB/cm}$ for the TM ground mode [40].

2.2.1 Surface-roughness scattering

Light scattering at sidewall roughness is considered to be the most important effect [40, 41] which explains the loss reduction using an improved lithography process. Due to the nature of the lithography fabrication process, roughness on the vertical sidewalls of the waveguide is unavoidable. This is visible on Fig.2.4(a). A lot of effort is put into the optimization of fabrication processes to minimize the surface-roughness. The losses are correlated with the periodicity of the roughness as well as its dimensions, and scale dramatically with the index contrast, polarization and waveguide dimensions [42]. Scattering at top surface roughness is small ($\approx\ 0.1\,\mathrm{nm}$) [40, 41]. The sidewalls are expected to exhibit a larger roughness as the typical fabrication process involves a dry etch process.

To understand the strong interaction between the sidewall and the propagating light, we plot the intensity mode profiles of strip waveguide in Fig.2.4(b) and (c) for respectively a quasi-TE and quasi-TM mode. At the core/cladding interface, the normal component of displacement $D = \epsilon E$ must be continuous. Therefore the field amplitude at the cladding side of the interface will be stronger for a mode with the dominant E-field polarized normal to the interface. If the waveguide

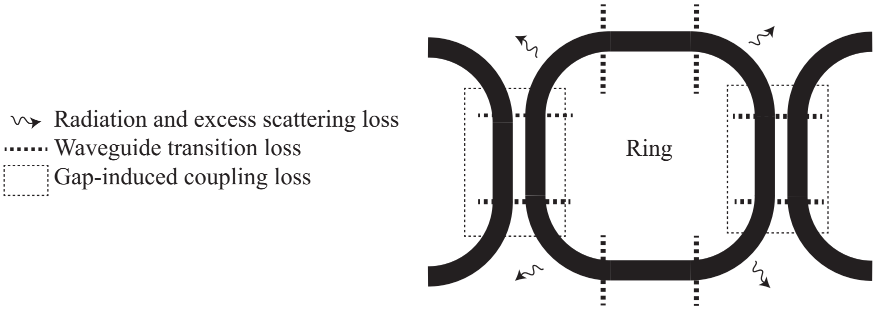

Figure 2.5: An illustration of the different bend loss mechanisms in a ring resonator.

width is larger than its height (the most commonly used geometry), the ground mode will be quasi-TE polarized. This mode will have a strong discontinuity on the sidewall surface. Likewise, the quasi-TM mode will have a discontinuity on the top and bottom surface.

2.2.2 Bend losses

The strong modal confinement (for TE-polarization) in SOI wires allows for very sharp bends with radius down to $1 - 3\,\mu\mathrm{m}$ and this with low leakage power. However, several relatively small loss mechanisms are present at various positions in the ring. Analyzing the loss in bent waveguides is rather complex since it consist of many different sources, which are typically very small. As bends are an essential component of a ring resonator, the excess bend loss should be kept under control. This can be accomplished by tuning the waveguide cross section [43, 44] or by engineering the bend shape [37]. An overview of the losses is given in the following list, with an illustration shown in Fig.2.5.

- **Radiation loss**: stricto senso, radiation loss is the extra leakage power due to a bend. However, the scattering loss might be influenced by waveguide bending, as the mode is pushed outwards. This excess scattering loss is considered separately.

- **Excess scattering loss**: the increase field strength at the surface roughness could cause increase amount of scattering (and backscattering).

- **Waveguide transition loss**: at the transition between a bend and a straight waveguide, mode mismatch can occur. Hence, this loss is expected to be larger for a sharper bend radius.

- **Gap-induced coupling loss**: a directional coupler with a small gap can cause a non-adiabatic transition of the propagation light. This loss does not appear in a simple bend. However since the adiabaticity is inverse proportional to the bend radius, we do consider the gap-induced coupling loss as part of the bend loss.

- **Loss due to coupling to other modes:** especially for wider waveguides or for non-vertical sidewalls coupling between TE and TM modes or to higher order modes can be expected as well [45] but is not considered in this work.

A complete study that aims to disentangle the different loss mechanisms is not yet demonstrated. For every waveguide dimension, radius and cladding, another loss mechanism is dominant which makes a clear conclusion very difficult. However, in this section we try to give an overview of reported values on bend losses, explain the different mechanism responsible for these losses and link different research results to each other.

Note that typical ring losses are extremely small, in the order of $0.04\,\mathrm{dB}$ for a ring resonator with radius $4.5\,\mu\mathrm{m}$, which seems at first sight negligible. This round trip loss corresponds with an effective propagation loss of $12.4\,\mathrm{dB/cm}$. This is much larger than the typical propagation loss in straight strip waveguides which is in the order of $2\,\mathrm{dB/cm}$.

We start our review on how to simulate bend loss. Later, we give an overview of reported bend loss values measured using spirals (cut-back technique) and explain how this measurement can be performed more accurately using ring resonators. This section ends with a discussion on reported values of waveguide transition loss and gap-induced coupling loss.

Simulating bend loss One can simulate bend loss using 2D modal analysis methods, e.g. finite difference method (FDM) or finite element method (FEM) or use the more accurate 3D finite-difference time-domain (FDTD) method. Using a 2D method, only radiation loss is considered whereas the 3D method also includes the waveguide transition loss and coupling to other modes. A comparative study of simulation methods for losses in ultra-sharp bends is provided in [44], claiming that modal analysis methods are overestimating the radiation losses.

Using modal analysis methods, the pure bend loss can be determined from the imaginary part of the propagation constant. Let $\vec{E}(x,y)$ be the electric field along the cross-section of a waveguide. Then the light travels along the z-axis as follows:

$$\vec{E}(x,y) = \vec{E_0}(x,y)\exp(-j\beta z) \tag{2.20}$$

with β the propagation constant. The real part (β_R) represents the phase propagation and the imaginary part β_I the attenuation. β_I can be calculated based the imaginary part of the effective refractive index ($\Im(n_{eff})$).

$$\alpha = \frac{2\pi}{\lambda_0}\Im(n_{eff}) \tag{2.21}$$

To calculate the intensity loss of the light (A) after 1 unit length (e.g. 1 meter), the ratio of the electric fields is squared resulting in the following equation.

$$A\left[\frac{1}{\mathrm{m}}\right] = \frac{I(1)}{I(0)} = \left(\frac{E(1)}{E(0)}\right)^2 \tag{2.22}$$

$$= \exp\left(\frac{2\pi}{\lambda_0}\Im(n_{eff})2\right) \tag{2.23}$$

This can be converted into a more commonly used unit A[dB/cm] by calculating the $10\log_{10}$ of eq.2.23, where the factor 100 comes from the conversion from m into cm.

$$A\left[\frac{\mathrm{dB}}{\mathrm{cm}}\right] = 10\log_{10}(\exp\left(\frac{2\pi}{\lambda_0}\Im(n_{eff})\frac{2}{100}\right)) \tag{2.24}$$

$$= 10\log_{10}(\exp(1))\frac{2\pi}{\lambda_0}\Im(n_{eff})\frac{2}{100} \tag{2.25}$$

$$= 4.343\frac{2\pi}{\lambda_0}\Im(n_{eff})\frac{2}{100} \tag{2.26}$$

$$= \frac{0.545}{\lambda_0[m^{-1}]}\Im(n_{eff}) \tag{2.27}$$

For a typical strip waveguide with an oxide cladding and waveguide dimensions $450 \times 220\,\mathrm{nm}$, the $90°$ radiation loss of a $2\,\mu$m-bend is simulated to be $0.001\,\mathrm{dB}$. Increasing the waveguide width to $500\,\mathrm{nm}$, decreases the radiation loss with a factor 5 down to $0.0002\,\mathrm{dB}$. One can understand this by the fact that the confinement for wider waveguides is larger. However, using a 2D calculation, we are unable to calculate coupling to other modes. The possible coupling to other modes (higher order or different polarization) can safely be neglected when indeed a waveguide is perfectly rectangular, at least when the bend radius is not to sharp and a symmetric cladding is used [44]. In reality, the waveguide edges are tilted with an estimated angle of $82°$ [36]. Note that this angle is likely to be improved using better technology. In [44], a 3D-FDTD method is used to estimate the bend losses. Note that this 3D method also takes into account the transition loss at the start and the end of the bend. Using the same waveguide dimension and wavelength, a much larger value is found. This indicates that the transition loss in a bend is much larger than the radiation loss, or that the modal analysis is underestimating the radiation losses. Note that the latter would be in contrast with reference [44] that states that the modal analysis is over-estimating the bend losses. In Tab.2.2, an overview of the simulated losses are given.

To estimate the excess scattering loss, one could use a 2D mode solver to investigate the increased field strength at the sidewall of a waveguide in function of radius. In the following we give an overview of reported values on (total) bend losses, which will be several times larger than what we have simulated.

type	R (μm)	W (nm)	90° loss (dB)	method
radiation	2	450	0.001	2D modal
radiation	2	500	0.0002	2D modal
radiation	1	450	0.09	2D modal
total	1	450	0.35	3D-FDTD [44]
total	2	450	0.07	3D-FDTD [44]

Table 2.2: Simulated radiation losses using a 2D modal analysis and simulated bend losses 3D-FDTD [44]. Waveguides have an oxide top cladding and a height of 220nm. Wavelength is 1550nm.

Reported bend loss measurements Around $1550\,\mathrm{nm}$ excess 90° bend losses of a $500\,\mathrm{nm}$ wide SOI waveguide amount to $0.009\,\mathrm{dB/turn}$ for a $5\,\mu\mathrm{m}$ bend radius, to $0.071\,\mathrm{dB/turn}$ for a $1\,\mu\mathrm{m}$ radius bend [36]. Very similar values were found for a $450\,\mathrm{nm}$ wide waveguide. Other reported loss values [32] for a 90° bend using $445\,\mathrm{nm}$ wide SOI waveguides are $0.086\,\mathrm{dB/turn}$ for a $1\,\mu\mathrm{m}$ radius bend and $0.013\,\mathrm{dB}/90^\circ$ for a $2\,\mu\mathrm{m}$ bend radius bend.

Note that these reported values are using a cut-back method, which is based on long spirals where they measure the difference in total transmission loss for a varying number of bends in the spiral. The number of bends reaches typically up to several dozens, especially for low bend losses. In [32], a spiral with 20 bends did not have enough bends to measure the loss of a $5\,\mu\mathrm{m}$ bend. And also in [36], where hundreds of bends are used, still a large uncertainty is reached (large error bar).

The cut-back method gives a good indication of a 90° bend loss, however loss includes (twice) a straight to bend waveguide transition. To estimate the bend loss of a circular ring resonator, the cut-back method will hence over-estimate the bend loss. The sum of the loss coming from four 90° bends and the excess loss from the directional coupler is called the cavity loss.

As introduced earlier in Eq.(2.13) on page 2-7, one can use a ring resonator to measure the cavity losses (explained in [21]). Assuming that the bend losses are the dominant factor (larger than the straight waveguide loss), a ring resonator can be used to measure the bend losses instead of long spirals [46]. Using an air-clad strip waveguide of $450 \times 250\,\mathrm{nm}$ in a circular ring resonator (R = $5\,\mu\mathrm{m}$), the cavity loss is calculated to be $0.028\,\mathrm{dB}$ [46]. This corresponds to $0.007\,\mathrm{dB}$ for a 90° bend at wavelength $1550\,\mathrm{nm}$. The width of the bus is slightly larger than the ring ($500\,\mathrm{nm}$). By increasing the width of the ring waveguide to $600\,\mathrm{nm}$, the cavity losses is drastically decreased to $0.011\,\mathrm{dB}$ or $0.0027\,\mathrm{dB}$ for a 90° bend. Note that in this ring there is no straight-to-bend waveguide transition. However, there might be an extra loss coming from the coupling section. For both rings, a rather large gap of $300\,\mathrm{nm}$ is used. Also in [46], they found that the bend losses are increasing for longer wavelengths. This is also predicted by 3D-FDTD simulation [44]. A

Ref.	λ (nm)	R (μm)	W (nm)	H (nm)	90° loss (dB)	method
[36]	1550	5	450/500	220	0.009	cut-back
[36]	1550	3	450/500	220	0.02	cut-back
[36]	1550	1	450/500	220	0.071	cut-back
[32]	1550	1	445	220	0.086	cut-back
[32]	1550	2	445	220	0.013	cut-back
[46]	1550	5	450	250	0.007	ring
[46]	1550	5	600	250	0.0027	ring

Table 2.3: An overview of some reported values on excess bend losses. R, W and H stands respectively for radius, width and height of the waveguide. All values are measured at $1550\,\mathrm{nm}$. *Both in [36] and [32], waveguides have an air cladding. In [46], the top cladding is air and side cladding is oxide.*

mode at longer wavelengths is indeed less confined. In other words, the effective width of the waveguide is decreased. An overview of the reported bend losses is given in Tab.2.3.

Comparing these results to the simulation results shown in Tab.2.2, one can conclude that

1. Simulated radiation loss using a 2D modal analysis is either under-estimated or negligible with respect to waveguide transition loss and/or excess scattering loss.

2. Simulated bend loss using 3D-FDTD analysis is over-estimating the bend loss (or is not performed properly in [44]).

3. Using wider waveguides or shorter wavelengths results in smaller bend loss. This results from both from ring resonator measurements as from simulation.

4. Using the transmission spectrum of circular ring resonator as a method to estimate the 90° bend loss gives comparable results to the more commonly used cut-back method. This indicates that the waveguide transition loss is comparable with gap-induced coupling loss.

In the following two paragraphs, this waveguide transition loss and gap-induced coupling loss is further discussed.

Waveguide transition loss The simplest way to eliminate mode mismatch between straight and bend waveguides is using perfectly circular rings. One would expect that the losses in such a ring resonator are smaller than the reported values described above. In the next sections we will investigate the losses in circular ring resonators. A possible drawback of using circular ring resonators is that it can become more difficult to couple enough light from the bus waveguide to the ring. This typically leads to narrow gap configurations which can introduce extra coupling losses as well.

In [21], a way to differentiate between the pure 90° bend loss and transition loss is demonstrated. This is performed by comparing the cavity loss of a ring resonator with four separate straight sections with a ring resonator with only two straight sections (at the directional coupling). In that experiment (partly) air-clad strip waveguides with dimensions $500 \times 250\,\mathrm{nm}^2$ are used. They found that the straight-to-bend waveguide transition loss is $0.025\,\mathrm{dB}$ for each transition using a $4.5\,\mu\mathrm{m}$ bend. This is found after an easy calculation using their reported values. Consequently, the pure 90° bend loss (thus the bend loss explicitly without transition loss but including the normal propagation loss) is found to be $0.01\,\mathrm{dB}$ per 90° turn. Note that the reported bend values in [32, 36] are excluding straight propagation loss but including transition loss. Although slightly different waveguides are used, we find that the transition loss alone ($0.025\,\mathrm{dB}$ as obtained in [21]) is already larger than the total bend loss (i.e. scattering, radiation and transition loss together) of $0.013\,\mathrm{dB}$ per 90° turn. This difference could partly be explained by the different waveguide cladding used in the two experiments. By using an oxide cladding, the mode is less confined and hence the waveguide transition loss is expected to be larger than by using an air cladding. One can conclude that it remains difficult to link different reported loss values with each other.

Gap-induced coupling loss It is reported in [47] that a directional coupler with smaller gap introduces larger gap-induced losses. Then, the sum of the squared cross- and self-coupling coefficients is smaller than 1, i.e. $(\kappa^2 + \tau^2) < 1$. In [47], the author combines two ring resonator structures, to disentangle the gap-induced loss from the ring-cavity loss (i.e. any loss expect the gap-induced loss). For very narrow gaps ($< 117\,\mathrm{nm}$) and bend radius of $6.5\,\mu\mathrm{m}$, they concluded that this gap-induced coupling loss is larger ($0.06\,\mathrm{dB}$) than the cavity losses ($0.04\,\mathrm{dB}$) (using air-clad strip waveguides). However, their technique is prone to large errors since two ring resonator configurations are needed to characterize the loss. Recently in [48], yet another method is used to assess the gap-induced coupling loss and compare this with simulated values (quasi 3D-FDTD). Using a strip oxide-clad waveguide ($500 \times 250\,\mathrm{nm}$) forming a circular ring resonator with a short bend radius $2.75\,\mu\mathrm{m}$, they demonstrate a gap-induced coupling loss of $0.02\,\mathrm{dB}$. So far, only little research has been published on this topic and many questions remain open. E.g. it is not yet investigated what the influence is of the waveguide dimension and directional coupler configuration (straight or curved bus) on these extra losses. Also it is not clear from the empirical investigation reported in [47, 48], whether the gap-induced coupling loss comes from a smaller waveguide gap as a fabrication challenge or from a higher coupling strength. Following the first idea, waveguide dimensions that enhance the confinement of the mode in the Si core, e.g. a wider strip waveguide, will also decrease the coupling strength. Hence, smaller gaps will be needed to foresee enough coupling. This could lead to extremely narrow gaps that are below the fabrication resolution. Gaps smaller than this limit, e.g. $< 100\,\mathrm{nm}$, could not be fully etched. Hence, extra losses could arise from an uncompleted gap definition. This could lead to mode conversion and thus extra losses. Following the second idea, narrowing the gap also leads to stronger cross-coupling strengths (κ per unit length). Hence, the directional coupling section becomes less adiabatic with potentially more mode conversion and thus more loss. Using less-confined modes will enhance significantly the coupling strength and larger gaps can be used to foresee the same coupling in a certain directional coupler configuration.

2.2.3 Conclusion

In this section we have reported on three different losses in ring resonators, specifically for strip silicon waveguides. We have given the state of the art by summarizing the few reported experimentally assessed values for bend losses. We can conclude that bend losses are much larger than the pure scattering loss dominating the loss of straight waveguides. Bend losses do include radiation losses, excess scattering loss, waveguide transition loss and a gap-induced coupling loss. Depending on the configuration and the required coupling and radius, each of these loss mechanisms may dominate. To our knowledge, no comprehensive study has been published to distinguish between the different cavity losses in ring resonators and their gap or ring radius dependence. In the following section, we will compare different methods to assess the cavity loss in high-quality ring resonators.

2.3 Spectral response of a ring resonator

An overview of some typical obtained spectra of ring resonators using Si strip waveguides is given and several shortcomings are described. These shortcomings are a direct consequence of the high-confinement property of Si waveguides and can be explained by a phenomenon that is called counterdirectional coupling, as discussed in section 2.1.4. This phenomenon, where the propagating light is scattered backwards is induced by the surface roughness at vertical edges of a waveguide and degrades the performance of narrowband filters.

2.3.1 Measurements

In Fig.2.6, the spectra of two circular ring resonators with a different cross coupling κ are shown, both with radius of $5\,\mu\mathrm{m}$. A tunable laser is used to characterize

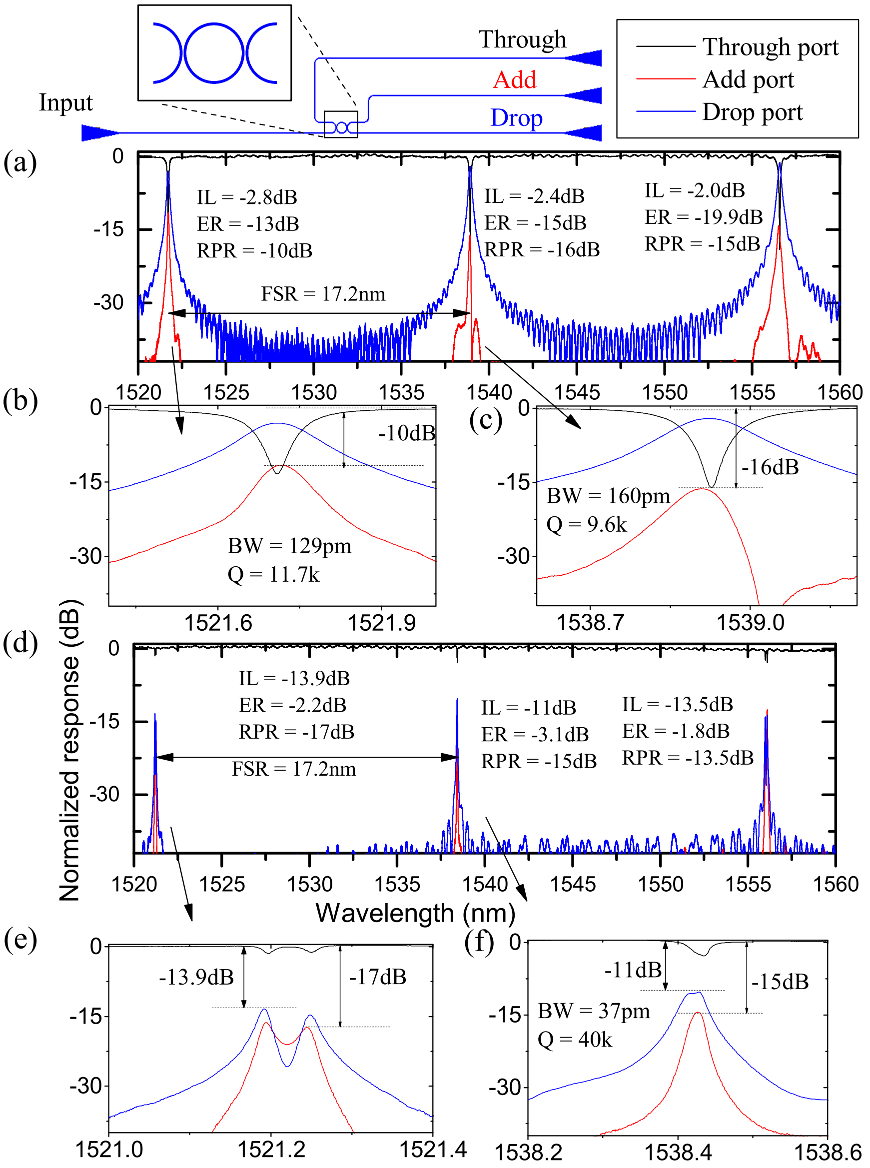

Figure 2.6: Two typical spectra of an AD ring resonator with R=5 μm and (a) gap 200 nm and (b) gap 400 nm are shown. The FSR is 17.2 nm. For each spectrum, a more detailed plot of two resonances (c)-(d) are given on top of (a) and (e)-(f) below (b). The reflected power (RF) ratio is reaching levels up to -10dB in (c). Mask picsoi33.

the components with a resolution of $1\,\mathrm{pm}$. Grating couplers are used for coupling quasi-TE polarized light in and out the chip. Both bus and ring waveguide have a dimension of $450 \times 220\,\mathrm{nm}^2$. The waveguides have an oxide top-cladding and both rings have a free-spectral-range (FSR) of $17.2\,\mathrm{nm}$ which corresponds to a group index of 4.38 using Eq.2.6. In the following we discuss each ring resonator separately. The first ring has a larger cross coupling than the second ring (gap of $200\,\mathrm{nm}$ versus gap of $400\,\mathrm{nm}$).

Ring A: gap 200nm In Fig.2.6(a) the spectrum of a ring resonator with gap of $200\,\mathrm{nm}$ is shown. A symmetric coupling section is used, with a curved bus waveguide (same radius as the ring), as shown at the top of Fig.2.6. Using this directional coupler configuration, the power coupling κ^2 is simulated to be 1.6% using a 3D-FDTD simulation (see section 2.5 on page 2-42 for more information). With a propagation loss of $2\,\mathrm{dB/cm}$, this would correspond with a BW of $137\,\mathrm{pm}$ or a Q-factor of 11000 at $1550\,\mathrm{nm}$. In Fig.2.6(a), we show the insertion loss (IL), extinction ratio (ER) and reflected power ratio (RPR) of the three measured resonances. The RPR is defined as the maximum power detected at the *add* port with respect to the maximum power at the *through* port. This power originates from backscattering at the sidewall surface roughness, which is enhanced by the resonance of the ring resonator, as discussed in 2.1.4. The same power can be expected back into the input port. The RPR is wavelength dependent and ranges from $-10\,\mathrm{dB}$ for the left resonance (enlarged in Fig.2.6(b)) to $-15\,\mathrm{dB}$ for the middle resonance (enlarged in Fig.2.6(c)). Both ER and IL are fluctuating largely, which is partly due to the wavelength dependency of the cross coupling and partly due to the wavelength dependent backscattering. The longer the wavelength, the larger the coupling and thus the smaller the IL and the larger the ER. The bandwidth (BW) is measured to be $129\,\mathrm{pm}$ and $160\,\mathrm{pm}$ for respectively the left and the middle resonance resulting in Q-factor of 11700 and 9600. With a FSR of $17.2\,\mathrm{nm}$, a finesse of 133 is reached.

Ring B: gap 400nm Next, the gap is enlarged from $200\,\mathrm{nm}$ to $400\,\mathrm{nm}$ and the power coupling κ^2 between bus and ring is drastically lowered. The resulting spectrum is shown in Fig.2.6(d). Due to the lowered coupling, the BW of the resonances is expect to be much smaller. In the enlarged Fig.2.6(e), the resonance shape measured around $1521.2\,\mathrm{nm}$ at three output ports is split into two sharp resonances with a wavelength separation of $57\,\mathrm{pm}$. This phenomenon is called resonance splitting and originates from the coupling between the forward and backward propagating mode (as discussed in section 2.1.4). At this point it is important to see that the middle resonance (enlarged in Fig.2.6(f) and measured around $1538.4\,\mathrm{nm}$) is not showing resonance splitting, resulting in a high Q-factor of 40k and a BW of $37\,\mathrm{pm}$. With a FSR of $17.2\,\mathrm{nm}$, this results in a high finesse of 452. However the IL and ER is rather poor and measured to be respectively $-11\,\mathrm{dB}$ and $-3.1\,\mathrm{dB}$. The right resonance (measured at $1556\,\mathrm{nm}$) is showing resonance splitting as well with an even larger resonance splitting of $107\,\mathrm{pm}$ (not shown in Fig.2.6) and hence we can say that this resonance splitting is highly wavelength dependent. However, in both cases the RPR is very close to the power at the drop port.

Discussion Note that the spectra shown in Fig.2.6 are *typical* in the meaning of ‘not specifically classified as best or worst’. They were by purpose designed to exhibit a narrow bandwidth or high Q-factor and hence a small bus-to-ring power coupling was required. Both examples reveal two major problems using Si ring resonators for high-Q filters. The first problem is the high reflected power ratio (RPR) at the resonance wavelength that can cause problems at preceding circuit components, e.g. backreflections can cause laser instability. The second problem is the detected resonance splitting, which broadens the resonance significantly and can induce large IL fluctuations. The last two problems are caused by resonance-enhanced backscattering. Apart from backscattering, surface roughness enhances as well the scattering in bends of light in strongly confined waveguides which potentially explains the huge propagation losses in $5\,\mu\mathrm{m}$ bends. This severely limits the realization of narrowband ring resonators with an intrinsic Q ranging between 60000 and 90000.

2.3.2 Cavity loss analysis

In this section we will apply two quick methods to experimentally assess the cavity loss of a ring resonator based on the measured spectra in last section. A first method is using the bandwidth of the one of the split resonances of a weakly coupled ring resonator (ring B) and can hence not be applied on the spectra of ring A. The second method is using the analytical equations without the presence of counter-directional coupling to disentangle the internal loss and external coupling as derived in [21]. The equations are also listed in Eq.(2.13) and (2.14). In this method, the BW, ER and FSR is used. As seen in Fig.2.3, the effect of counter-directional coupling has an important influence on both BW and ER if the internal loss and external coupling is kept constant. The larger the external coupling, the smaller this deviation. Both BW and ER are drastically influenced in ring B due to resonance splitting in such a way that we can only apply this method for ring A.

Method 1 - intrinsic Q: As demonstrated in [20] for all-pass ring resonators, the coupling strength between the forward and backward propagation mode is visible in the amount of resonance splitting. If the external coupling and internal loss is small enough with respect to the mutual coupling in such a way that the resonance is clearly split, the intrinsic Q (Q_i) can the be derived based on the BW of one of the two split resonances. Assuming the bus-to-ring coupling (κ^2) to be much smaller than the internal loss (a^2) we could apply Eq.2.12 and calculate the propagation loss. For the resonance around $1521\,\mathrm{nm}$ we found a BW of $17 \pm 0.5\,\mathrm{pm}$ or a Q-factor of $90k \pm 2k$. Using formula Eq.2.12 this corresponds with a propagation loss of $8.3\,\mathrm{dB/cm}$. The difference with the resonance around $1556\,\mathrm{nm}$ is remarkable. This resonance has a much broader BW of $26.2\,\mathrm{pm}$ or a Q-factor of 60k. This corresponds with a much larger propagation loss of $12.4\,\mathrm{dB/cm}$. Both propagation losses are much larger than what is reported for straight waveguides, typically in the order of $3\,\mathrm{dB/cm}$ (see section 2.2). However, even with these high extracted values for the propagation loss ($8.3 - 12.4\,\mathrm{dB/cm}$), the effective round trip loss calculated based on Q_i is still relatively low and ranges between $0.026 - 0.039\,\mathrm{dB}$ for respectively the left and the middle resonance. Without the normal propagation loss of $3\,\mathrm{dB/cm}$, this corresponds with an excess roundtrip loss of $0.0166 - 0.03\,\mathrm{dB}$ or with a $90°$ excess loss of $0.0041 - 0.0075\,\mathrm{dB}$. This value is slightly smaller than extracted $90°$ excess loss by using a long spiral as reported in [37] (i.e. $0.009\,\mathrm{dB}$) but is very similar. The difference between the two values could come from the difference between waveguide transition and gap-induced coupling loss as discussed in section 2.2.2. Please note that the waveguides used in this circular $5\,\mu\mathrm{m}$-radius ring has an oxide cladding whereas the waveguide in [37] has an air cladding and a radius of $4.5\,\mu\mathrm{m}$.

Method 2 - analytical: By applying Eq.(2.13) on the middle resonance of ring A shown in Fig.2.6, a total round trip loss of $0.045\,\mathrm{dB}$ is found. Subtracting the assumed $3\,\mathrm{dB/cm}$ scattering loss present in a straight waveguide, this corresponds with a $11.4\,\mathrm{dB/cm}$ extra propagation loss or an excess cavity loss of $0.036\,\mathrm{dB}$. With the internal loss Note that Eq.(2.13) starts from a formulation without counter-directional coupling and a deviation could be expected. However, the extracted value corresponds very well with the extracted values found in the previous paragraph using the split resonance of ring B (gap $400\,\mathrm{nm}$).

Discussion Both methods are corresponding very well with the reported value of excess bend loss using a long spiral. In [37], no wavelength dependency of the bend loss is presented. However based on our (limited) extracted values (using method 1 and 2), it seems that the propagation loss is lower for shorter wavelengths. In [46], this tendency is confirmed and explained by the fact that at shorter wavelengths the optical mode is better confined and thus exhibits a lower bend loss. Using a little ticker Si waveguides of $250\,\mathrm{nm}$ (instead of $220\,\mathrm{nm}$), the effective propagation loss in a ring resonator with radius $5\,\mu\mathrm{m}$ is ranging between $7\,\mathrm{dB/cm}$ at $1535\,\mathrm{nm}$, $9.5\,\mathrm{dB/cm}$ for $1555\,\mathrm{nm}$ to $12\,\mathrm{dB/cm}$ for $1570\,\mathrm{nm}$. These reported values are very well in line with our values, given the difference in waveguide thickness and technology.

By comparing the results extracted from circular ring resonators (including normal and excess scattering, radiation and gap-induced coupling loss) and spirals (including normal and excess scattering, radiation and waveguide transition loss), one could conclude that either (cfr. Fig.2.5)

- the gap-induced coupling loss is small compared to the pure bend loss (radiation and excess scattering)

- the gap-induced coupling loss is similar to waveguide transition loss.

All types of losses are expected to increase for longer wavelengths or smaller waveguides. Also, we expect that the bend loss (including excess scattering, radiation, waveguide transition and gap-induced coupling loss) is decreased for larger radii. However, by repeating this analysis on similar circular ring resonators (gap 200 and $400\,\mathrm{nm}$) but with larger radii (i.e. 10 and $20\,\mu\mathrm{m}$), one would expect to see a difference cavity loss. The bend loss should drop as it evolves slowly in a straight waveguide. However, using the larger radii, the bus-to-ring power coupling does increase drastically in such a way that the bandwidth of the split resonance is broadened by the external coupling (cfr. method 1). The ring resonators with a $400\,\mathrm{nm}$ gap and a radius of 10 and $20\,\mu\mathrm{m}$ are having both a bandwidth around $16\,\mathrm{pm}$ which corresponds with a propagation loss of $8\,\mathrm{dB/cm}$. However, this includes the cross coupling to the bus waveguides and is not representing the cavity loss alone. By applying Eq.(2.13) (cfr. method 2) on the resonators with larger radii but with a smaller gap of $200\,\mathrm{nm}$, we found that the round trip losses are even increased instead of decreased. The ring resonator with a radius of $10\,\mu\mathrm{m}$ has a round trip loss of $0.14\,\mathrm{dB}$. Subtracted by the straight propagation loss ($3\,\mathrm{dB/cm}$), an excess round trip loss of $0.12\,\mathrm{dB}$ is found. For a ring resonator with radius of $20\,\mu\mathrm{m}$, the total and excess round trip loss is respectively $0.22\,\mathrm{dB}$ and $0.18\,\mathrm{dB}$. In other words, the gap-induced coupling loss seems to increase for larger radii which looks counter-intuitive since the coupling section is then more adiabatic. The most acceptable explanation is that Eq.(2.13) does not apply to resonators with to larger coupling to backward propagating modes. Further investigation is needed, which might imply more complex fitting functions that include the coupling to backward propagating modes [49]. However, using a ring radius of $5\,\mu\mathrm{m}$, a good agreement was found between the different extraction methods.

2.3.3 Conclusion

We have researched AD ring resonators using silicon strip waveguides with low bus-to-ring power coupling ($\leq\ 1.6\%$). High finesse values with a maximum of 425 were found which is due to the large FSR and the relatively low cavity losses.

However, we also found that counter-directional coupling to backward propagating modes can split the resonances and causes an increased wavelength dependent behavior of the IL and ER. Also a high reflected power ratio reaching a level of $-10\,\mathrm{dB}$ was found that could cause instability of the input laser. Two approaches were used to estimate the cavity losses. For ring resonators with a radius of $5\,\mu\mathrm{m}$, the cavity losses of $\approx 0.036\,\mathrm{dB}$ corresponds well with the bend losses extracted from a cut-back method using spirals [37]. Using larger radii, results become vague due to the lack of proper equations for ring resonators with strong backscattering and further investigation is needed. In the following section, focus is put on how to decrease this backscattering allowing to minimize the bandwidth without resonance splitting.

2.4 Narrowband Si ring resonators

In this section we look into the ability of Si ring resonators to have narrowband resonances. In order to increase the Q-factor and thus the BW, it is crucial to reduce the losses in the cavity. One way is to increase the circumference to reduce the bend losses of the ring. There are also second-order effects playing, e.g. increasing the bend radius could enhance the adiabaticity of the directional coupler. Increasing the bend radius also allows the designer to use wider gaps for a given coupling due to the enlarged coupling from the bend section. Both effects could have an influence on losses (and backscattering) originating in the coupling section as explained in section 2.1.4. Even very small scatter points are important since they are enhanced by the resonating effect. Many of these effects are strongly depending on the exact waveguide dimension and coupler configuration. In this section, it is of particular interest to design narrowband filters with a FSR that is still large $\approx 5\,\mathrm{nm}$. In addition we want to have a low insertion loss $< 3\,\mathrm{dB}$.

2.4.1 Strategies to lower the impact of sidewall roughness

Besides minimizing the surface-roughness by fabrication optimization, theoretical approaches based on three-dimensional analysis have been developed to adjust the cross section for a certain polarization to minimize the scattering and backscattering efficiency [42, 50]. However, one has to take into account other effects such as polarization rotation and coupling to higher order modes, both resulting in an increased bend loss. Mode conversion can happen especially in waveguides where the sidewall is not exactly vertical [51, 52] and proper 3D-FDTD simulations should be considered.

In general one can say that for a certain polarization, lowering the confinement of the optical mode will automatically lower the electric field strength at the overlap with the sidewall surface roughness. This can be done by using e.g.

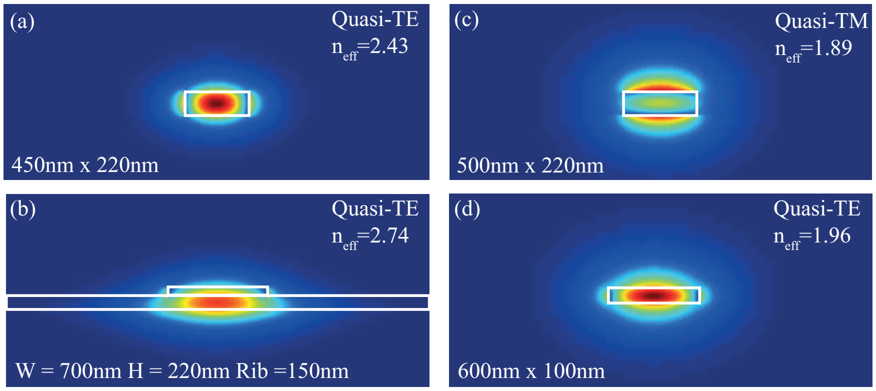

Figure 2.7: Waveguide cross-sections and mode of (a) TE-strip (b) TE-rib (c) TM-strip (d) TE-shallow strip at $1550\,\mathrm{nm}$.

broader waveguides or decreasing the index contrast of the cladding. Hence, lowering the confinement will always increase the radiation loss. In Fig.2.7(d), a surface-roughness optimized waveguide cross-section for TE-polarized light presented in [53] is shown. This shallow-strip has been used with $7\times$ less scattering loss than a standard design (Fig.2.7(a)). With a shallow height of only $100\,\mathrm{nm}$ and a width of $600\,\mathrm{nm}$, this cross-section is single mode. Although this approach is promising, the actual fabrication is not available at imec and hence this waveguide type has not been used in this work. However, the same authors demonstrated a higher-order ring resonator using this type of waveguide [54]. In [46], slightly multi-moded waveguides are used to increase effectively the Q-factor of a ring resonator. This effect has been characterized carefully in [29] where indeed $7-8\,\mathrm{dB}$ less backscattering has been measured using a $600\,\mathrm{nm}$ width instead of single-moded $450\,\mathrm{nm}$ width. However, this type of waveguide is not characterized in this work.

Within some restrictions in etch depths we present two novel approaches which minimizes backscattering on a $220\,\mathrm{nm}$ Si device layer platform: the rib waveguide using the quasi-TE mode and a strip waveguide using the quasi-TM mode.

First, a rib waveguide defined by a partial etch, is used to guide quasi-TE light. This partial etch is $70\,\mathrm{nm}$ deep, which is the same etch depth that is used to define fiber grating couplers and leaves a Si rib of $150\,\mathrm{nm}$. In Fig.2.7(b), a waveguide cross-section with its associated (TE) mode profile is shown. The rib width is designed to be $700\,\mathrm{nm}$. Making the width wider makes the waveguide multi mode. If one compares this mode profile with a standard strip waveguide shown in Fig.2.7(a), a much smaller overlap with the vertical sidewalls can be seen. Due to the lower horizontal confinement, this optical mode will need a larger bend radius to limit the bend loss which reduces the FSR. The rib waveguide structure has been proven to lower the scattering losses in straight waveguides considerably down to $0.272\,\mathrm{dB/cm}$ [37]. In section 2.4.2 (‘TE-rib waveguide’), we will employ this rib waveguide in several ring resonator configurations, both AP and AD. In [55], rib waveguides with a height of $380\,\mathrm{nm}$, a partial etch of $120\,\mathrm{nm}$ and a $700\,\mathrm{nm}$ width are employed to lower the propagation loss and achieve a critically-coupled AP ring resonator with a Q factor of 35000. A rather large radius of $50\,\mu\mathrm{m}$ is used, which was an improvement with respect to earlier demonstrations of rib waveguides with typical ring radius up to $150\,\mu\mathrm{m}$ and larger [56]. In this work, we try to decrease the radius even more and show a critically-coupled AP ring resonator with record-high Q-factors of 400000 with a radius of $25\,\mu\mathrm{m}$. Part of this work was published in [57]. These results are a two-fold improvement with respect to similar work presented in [7] using the same radius.

Our second approach is using the quasi-TM mode in strip waveguides. While in general TE-light is the preferred polarization, as TE is the ground mode of the waveguide, there are advantages in using the TM mode. Because of its lower overlap with the vertical sidewalls, it will experience less scattering and hence less backscattering. Fig.2.7(c) a strip waveguide is shown but with the mode profile of the fundamental quasi-TM mode superimposed. Using TM-polarized light in a waveguide cross section of $500\,\mathrm{nm} \times 220\,\mathrm{nm}$, more than an order of magnitude less scattering loss is expected, based on [42]. This is a result of two effects: first, the electrical field of the TM mode is oriented mainly in the vertical direction, so no discontinuity is created on the vertical sidewalls. Secondly, the TM mode is less confined in the vertical direction ($\mathrm{n_{eff}} = 1.89$), which results in a smaller modal overlap with the vertical sidewalls. Theoretical predictions by [42] have been verified by backscattering measurements of straight waveguides in [29]. In section 2.4.3 (‘TM-strip waveguide’), this waveguide approach employed to design narrowband filters is extensively investigated. In [19], a quasi-TM mode has been used in Si strip waveguides with a higher Si thickness of $450\,\mathrm{nm}$ and a width of $500\,\mathrm{nm}$ to demonstrate a critical Q-factor of 139000 using AP ring resonator with a radius of $20\,\mathrm{nm}$. In this work we demonstrate very similar results but using $220\,\mathrm{nm}$ high waveguides. Preliminary results of this work were published in [58].

2.4.2 TE-rib waveguides

As discusses earlier, we limit the investigation on the rib waveguides by fixing the etch depth to $70\,\mathrm{nm}$, i.e. the same etch depth that is used to define the trenches of a fiber grating coupler. We start with 2D FEM simulation of the bend loss of a 90° turn in function of rib width and waveguide radius. Next, we look into the spectral behavior of AD ring resonators using TE-rib waveguides. Later, these low-loss TE-rib waveguides are employed in an all-pass (AP) ring resonator configuration.

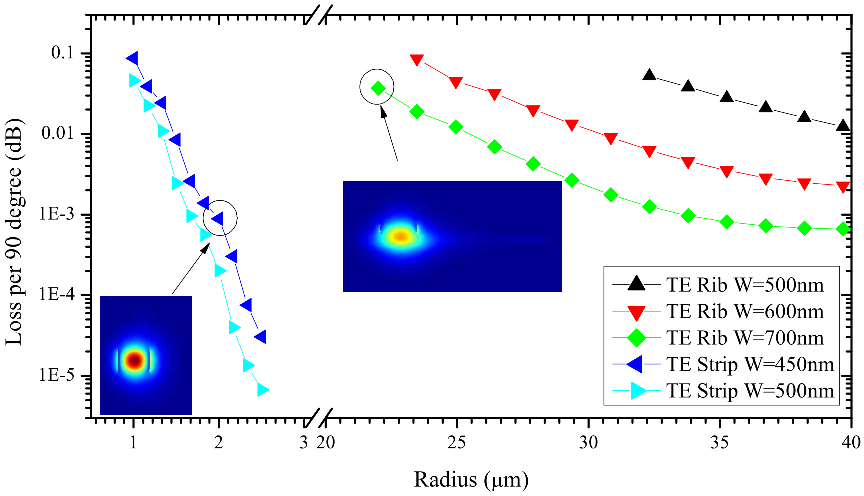

Figure 2.8: Simulated radiation losses based on the 2D-FEM calculated imaginary refractive index. Both Si strip and rib waveguides are considered and the resulting loss is expressed in 90° bend loss for varying width and radius. For a wider waveguide width, the losses drastically decrease. However, coupling to other modes is not considered and could possibly introduce losses for wider waveguide widths.

Radiation losses in TE-rib waveguides In Fig.2.8, the simulated 90° bend losses of typical oxide-clad strip and rib waveguide in function of radius are shown. A 2D modal analysis is used. Note that these losses are an estimation of the radiation losses only and exclude coupling to other modes. Also in this figure, one can see an intensity profile of the ground mode of the bend and notice the mode is pushed towards the right. From this figure one clearly deduces that the bend losses decrease drastically for a larger width and this for both strip and rib waveguides.

AD ring resonators Four typical AD ring resonator spectra using strip waveguides with waveguide width $700\,\mathrm{nm}$ and radius $25\,\mu\mathrm{m}$ are shown in Fig.2.9. The rings are characterized at all three output ports (i.e. through-, drop- and add-port) using a tunable laser with a resolution of $1\,\mathrm{pm}$ and low input power ($< -30\,\mathrm{dBm}$) to avoid thermal transient effects. From Fig.2.9(a) to (d), the gap is increased from $0.3\,\mu\mathrm{m}$ to $0.6\,\mu\mathrm{m}$ with steps of $100\,\mathrm{nm}$. According to Fig.2.8, the 90° bend loss for this waveguide type is estimated to be $0.01\,\mathrm{dB}$ or $0.04\,\mathrm{dB}$ per round trip. In other terms, there is an estimated $2.55\,\mathrm{dB/cm}$ extra propagation loss due to radiation loss. The FSR range of all four rings is $4\,\mathrm{nm}$ which corresponds with a group index of 3.77. Increasing the gap, lowers the bus-to-ring coupling and the bandwidth becomes more narrow. The 3dB BW of the drop response (denoted as BW_3) starts at $85\,\mathrm{pm}$ as shown in Fig.2.9(a) and goes down to $15.2\,\mathrm{pm}$ as shown

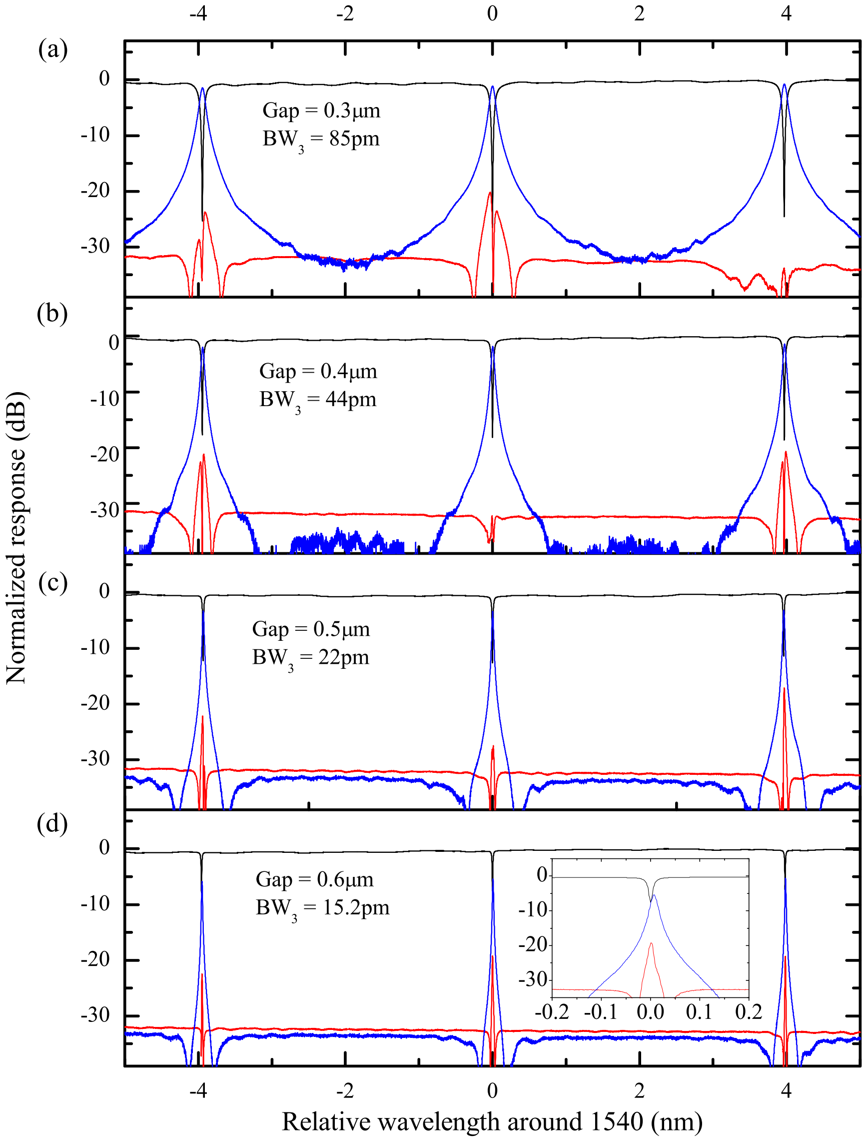

Figure 2.9: Add-drop ring spectra using TE-strip waveguides with width 700 nm *and radius* 25 μm, *characterized around* 1540 nm.

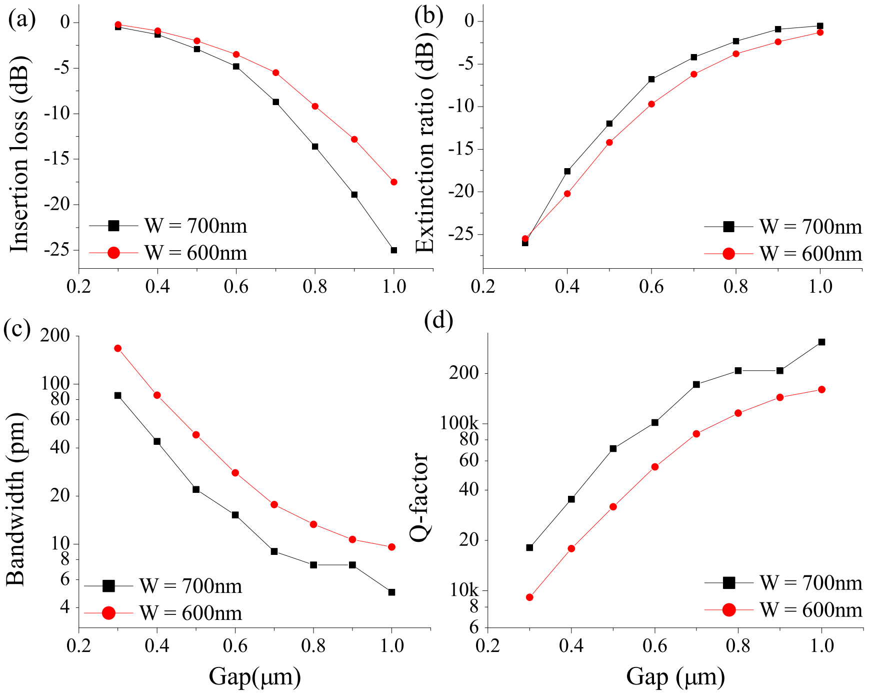

Figure 2.10: Add-drop ring properties of the oxide-clad TE-rib waveguide with rib width (W) 600 and $700\,\mathrm{nm}$*, radius* $25\,\mu\mathrm{m}$*. A single resonance around* $1550\,\mathrm{nm}$ *has been used to determine the spectral properties for each ring. The mask set of these rings is sipp06.*

in Fig.2.9(d). This results in a Q-factor and finesse that range respectively from 18000 up to 100000 and from 47 up to 263. Note that this finesse is still smaller than the one achieved using strip waveguides due to the smaller FSR (see Eq.(2.9)). However, no resonance splitting is present, which results in a relatively low IL of $5\,\mathrm{dB}$ as visible in the inset of Fig.2.9(d). Also the reflected power ratio (RPR) stays for all gap configurations below $-20\,\mathrm{dB}$. These two findings indicate indeed an important drop in backscattering resulting in superior ring resonator characteristics.

In Fig.2.10, the spectral properties of a broader range of AD ring resonators is shown. The gap is varied between 0.3 and $1.0\,\mu\mathrm{m}$ both for a waveguide width of 0.6 and $0.7\,\mu\mathrm{m}$. From (a) to (d), we plot respectively the IL, the ER, the 3dB BW and the Q-factor. From this Fig.2.10, one can follow the effect on the spectral properties for increasing gap and hence a decreasing bus-to-ring cross coupling. Using a slightly smaller rib width of the waveguide increases the coupling strength and hence a larger cross coupling is expected. Indeed one can find a smaller IL and a broader BW for a constant gap if the rib width is decreased to $0.6\,\mu\mathrm{m}$. For

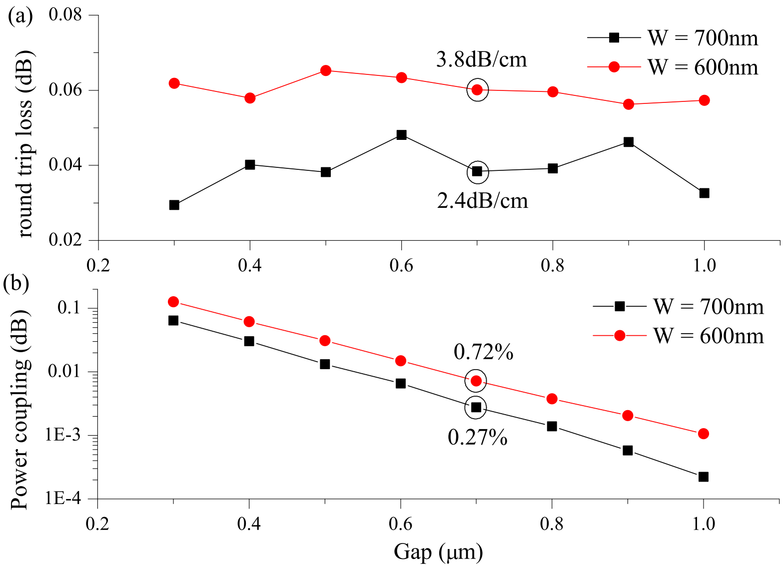

Figure 2.11: The cavity loss and cross coupling extracted from the spectral characteristics plot in Fig.2.10 using Eq.(2.13) *and* (2.14)*.*

a certain IL, say $-5\,\mathrm{dB}$, the BW of the resonance using a 0.6 and $0.7\,\mu\mathrm{m}$ wide waveguide is respectively $18\,\mathrm{nm}$ and $15.2\,\mathrm{nm}$ which indicates indeed a slightly larger propagation loss using the smaller waveguide. Using the wider rib waveguide one can achieve a BW of around $5\,\mathrm{pm}$ which corresponds to a very high Q of around 300000. Note that this BW is very close to the measurement limit of our setup and ideally the wavelength resolution should be improved.

Using Eq.(2.13) and (2.14) one can calculate respectively the corresponding cavity losses and the effective cross coupling. The extracted cavity losses in function of gap are shown in Fig.2.11(a). Indeed, the round trip loss is smaller than using the wider rib width and is around $0.04\,\mathrm{dB}$ and $0.06\,\mathrm{dB}$ for respectively a rib width of 0.7 and $0.6\,\mu\mathrm{m}$. This corresponds to an effective propagation loss of respectively $2.4\,\mathrm{dB/cm}$ and $3.8\,\mathrm{dB/cm}$. For a rib width of $0.7\,\mu\mathrm{m}$, this corresponds very well with the simulated cavity losses shown in Fig.2.8, indicating that the cavity losses are mainly determined by radiation losses and not by scattering.

In Fig.2.11(b), the extracted cross coupling between bus and ring waveguide is shown in function of gap. Indeed, as discussed before, the coupling is smaller using a wider rib width. For a gap of $0.7\,\mu\mathrm{m}$, the cross coupling is 0.27% and 0.72% respectively for a rib width of 0.7 and $0.6\,\mu\mathrm{m}$.

AP ring resonators In the following we characterize a similar set of ring resonators but in an AP configuration. In Fig.2.12(a), the Q-factor is plot in function

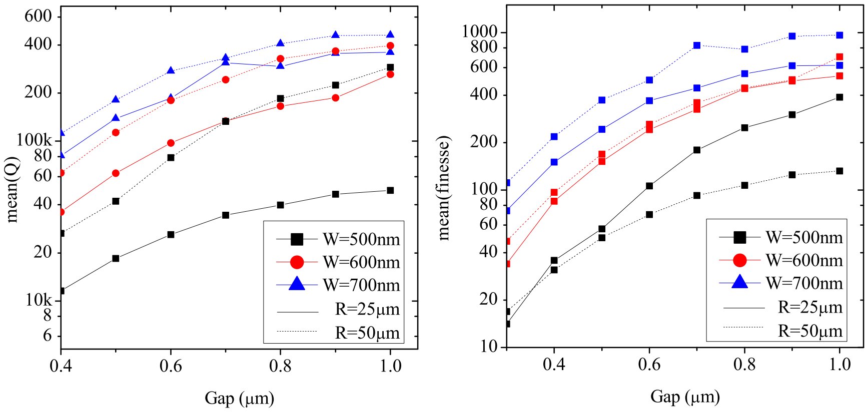

Figure 2.12: The mean (a) Q_l and (b) finesse over all resonances per ring between $1520\,\mathrm{nm}$ *and* $1560\,\mathrm{nm}$ *as a function of gap for varying waveguide width (W) and radius (R).*

of gap, and this for waveguides with rib widths of 0.5, 0.6 and $0.7\,\mu\mathrm{m}$ and also for a radius of 25 and $50\,\mu\mathrm{m}$. The extracted Q is gathered by fitting a Lorentzian function (as in Eq.(2.8)) to all the resonances between 1520 and $1560\,\mathrm{nm}$. The mean value is plot for each ring configuration. As expected, due to a lower cross coupling, the loaded Q will evolve into the intrinsic Q for increasing bus-to-ring waveguide gap. In what follows we focus on these close to intrinsic Q-factors. By studying the effect of the ring radius on the Q-factor and finesse, we can learn about the bend losses in a qualitative way.

For a waveguide rib width of $0.5\,\mu\mathrm{m}$, Fig.2.12(a) shows that using a larger radius, the Q-factor increases drastically due to the decreasing bend loss. For waveguide with a rib width $0.6\,\mu\mathrm{m}$ the Q-factor is nearly double for a ring resonator with radius $50\,\mu\mathrm{m}$ in comparison with one with radius $25\,\mu\mathrm{m}$. For a rib width $0.7\,\mu\mathrm{m}$ this difference vanishes indicating a significantly reduced bend loss.

In Fig.2.12(b), the same data set is plot but now represented using the finesse. For a ring resonator with waveguide rib width $0.7\,\mu\mathrm{m}$, the finesse using a radius of $50\,\mu\mathrm{m}$ is indeed half of the finesse of a $25\,\mu\mathrm{m}$ radius. This indicates that the propagation loss is equal for both bend radii. Consequently the bend loss is negligible. Using a narrower waveguide rib width of $0.6\,\mu\mathrm{m}$, the finesse of the $50\,\mu\mathrm{m}$ bend radius becomes equal to the one of the $25\,\mu\mathrm{m}$ radius indicating again an increasing bend loss for decreasing waveguide width. When the coupling becomes large, such as in the case with waveguide width $0.5\,\mu\mathrm{m}$ and small gaps ($< 0.5\,\mu\mathrm{m}$) any effect of the intrinsic Q is hidden.

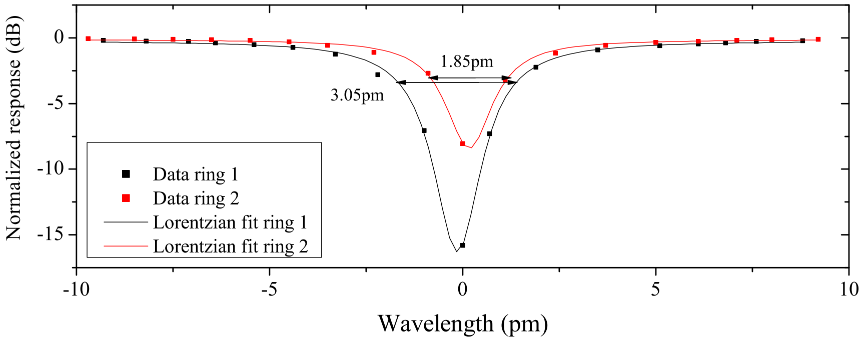

Figure 2.13: Two record-high-quality resonances of AP ring resonators using TE-rib waveguides with rib width $0.7\,\mu\mathrm{m}$.

Record AP ring resonators In Fig.2.13, two record-high-quality resonances coming from two different AP ring resonators are shown. Their waveguide rib width is $0.7\,\mu\mathrm{m}$ and the gap of the coupling section is also $0.7\,\mu\mathrm{m}$. Ring 1 with radius of $25\,\mu\mathrm{m}$ is critically coupled with an ER of $-16\,\mathrm{dB}$ and has a BW of $3.05\,\mathrm{pm}$. This narrow BW corresponds with a Q-factor of 508000 and a finesse of 1300 around wavelength $1550\,\mathrm{nm}$. Ring 2 with a radius of $50\,\mu\mathrm{m}$, exhibits an even smaller BW of $1.85\,\mathrm{pm}$ which corresponds with a Q-factor of 820000 and a finesse of 790. Ring 2 is slightly under coupled. Note that a wavelength resolution of $1\,\mathrm{pm}$ used in this experiment is fairly low for these ultra-narrow resonances and caution is needed using these data as a reference. However, we could use them as an upper limit of our experiment. We can calculate the propagation losses that correspond with these extracted Q-factors. Ring 1 in Fig.2.13, is critically coupled such that the intrinsic Q-factor (Q_i) is double this value (Eq.(2.11)). This would corresponds to an intrinsic Q-factor of roughly 1 million or to a propagation loss of $0.17\,\mathrm{dB/cm}$ using Eq.(2.12).

2.4.3 TM-strip waveguides

The second approach to lower the overlap with the vertical sidewall roughness is using the quasi-TM mode which is much less confined than the quasi-TE mode. In Fig.2.7, a cross-section is given of such a TM-mode in a strip waveguide, with n_{eff} of 1.89. Similar to the TE-rib approach, we expect a higher bend loss and/or substrate loss due to the lower confinement. In contrast with the TE-rib approach, the TM-strip has an optical mode that is much more out of the Si device layer and is therefore much more sensitive to its surrounding. For sensing applications this is a huge advantage but for further CMOS integration or integration with electrical contacts, the quasi-TM mode could suffer from extra absorption from e.g. overlap with top metal layers. In this section we give an overview of the spectral behavior of AD ring resonators using TM-strip waveguides for varying bend radii and discuss the extracted round trip losses.

In Fig.2.14 the transmission spectra (through, drop and add) of four AD ring resonators with radius of $20\,\mu\mathrm{m}$ is shown around a wavelength of $1540\,\mathrm{nm}$. The waveguide has an oxide cladding and a width of $0.5\,\mu\mathrm{m}$. In Fig.2.14, the gap is increased from $0.4\,\mu\mathrm{m}$ to $1.0\,\mu\mathrm{m}$ with steps of $0.2\,\mu\mathrm{m}$. Note that the coupling strength is much larger for the quasi-TM mode than for the quasi-TE mode using the same waveguide due to the lower confinement of the TM mode. From Fig.2.14, it is clear that the reflected power ratio (RPR) is again much lower than using a TE-strip waveguide. For the larger gaps, the RPR stays well below $-20\,\mathrm{dB}$. For the largest gap, shown in Fig.2.14(d), the RPR reaches levels of $-15\,\mathrm{dB}$ (left and right resonance). Also, no resonance splitting is found, which results in stable resonances with a high performance. Other filter characteristics such as insertion loss (IL), extinction ratio (ER), 3dB bandwidth (BW) and Q-factor are plotted in Fig.2.15(a)-(d) for the middle resonances of Fig.2.14. The FSR of this design is measured to be $6\,\mathrm{nm}$, which corresponds to a group index of 3.15. Note that this group index is rather small with respect to the simulated value of 3.4. This would correspond to an effective waveguide height of just below $200\,\mathrm{nm}$ (instead of $220\,\mathrm{nm}$) and/or a smaller width. Both waveguide effects would lead to an even smaller confinement and hence a higher bend and substrate loss as a consequence.

Also AD ring resonators with a smaller and larger radius (R) of respectively $15\,\mu\mathrm{m}$ and $30\,\mu\mathrm{m}$ were characterized and their spectral characteristics are also shown in Fig.2.15. One can see that the performance of ring resonators with radius 20 and $30\,\mu\mathrm{m}$ is very similar with a Q-factor that reaches almost 100000 using a gap of $1.0\,\mu\mathrm{m}$ and an IL that is around $-5\,\mathrm{dB}$. For the ring resonator with radius $20\,\mu\mathrm{m}$ this corresponds to a finesse of 352.

We could then apply again Eq.(2.13) and (2.14) to extract the round trip loss and the power coupling. These results are shown in Fig.2.16. From Fig.2.16(a), one can notice that the round trip losses tend to increase for smaller gaps indicating some gap-induced coupling loss. This is especially clear for radius 20 and $30\,\mu\mathrm{m}$. The round trip loss for radius $15\,\mu\mathrm{m}$ is rather constant around $0.08\,\mathrm{dB}$ which corresponds to an effective propagation loss of $8 - 8.8\,\mathrm{dB/cm}$. This constant loss could be explained by a larger gap-independent radiation loss that dominates the round trip loss. The extracted effective propagation loss using radius 20 and $30\,\mu\mathrm{m}$ and a large gap $(1.0\,\mu\mathrm{m})$ is respectively 3 and $2.6\,\mathrm{dB/cm}$. This small difference indicates that the bend loss is small and the propagation loss is dominated by e.g. scattering or substrate leakage. In Fig.2.16(b), the power coupling in function of gap is shown. One would expect that using the smallest ring radius of $15\,\mu\mathrm{m}$, the smallest coupling is achieved. Instead we find that the coupling is larger than using a radius of $20\,\mu\mathrm{m}$. This could be explained by the fact that the mode is very loosely confined in the $15\,\mu\mathrm{m}$ radius bends. This effect causes a larger bend loss

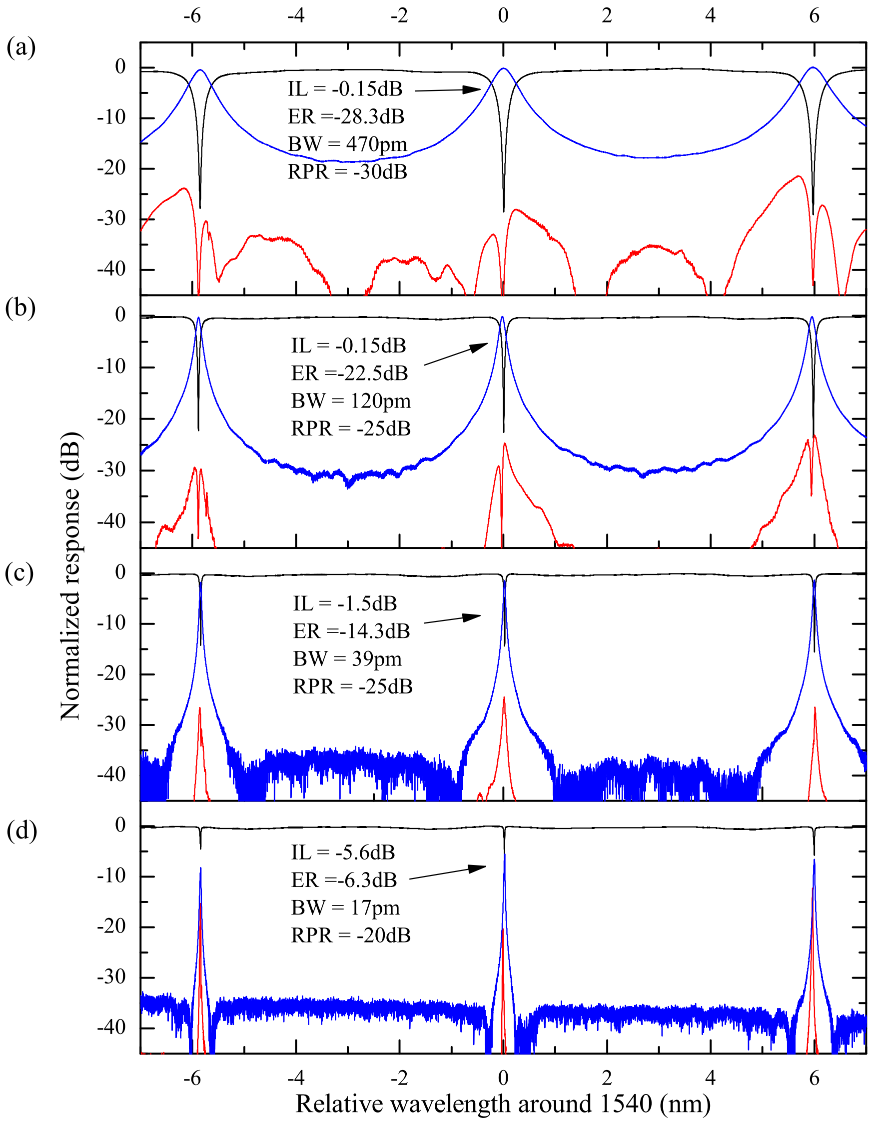

Figure 2.14: Overview of four AD ring resonators using oxide-clad TM-strip waveguides with a waveguide width of $0.5\,\mu\text{m}$ *and a ring radius of* $20\,\mu\text{m}$*. The gap is varied between (a)* $0.4\,\mu\text{m}$*, (b)* $0.6\,\mu\text{m}$*, (c)* $0.8\,\mu\text{m}$ *and (d)* $1.0\,\mu\text{m}$*. Mask set picsoi31.*

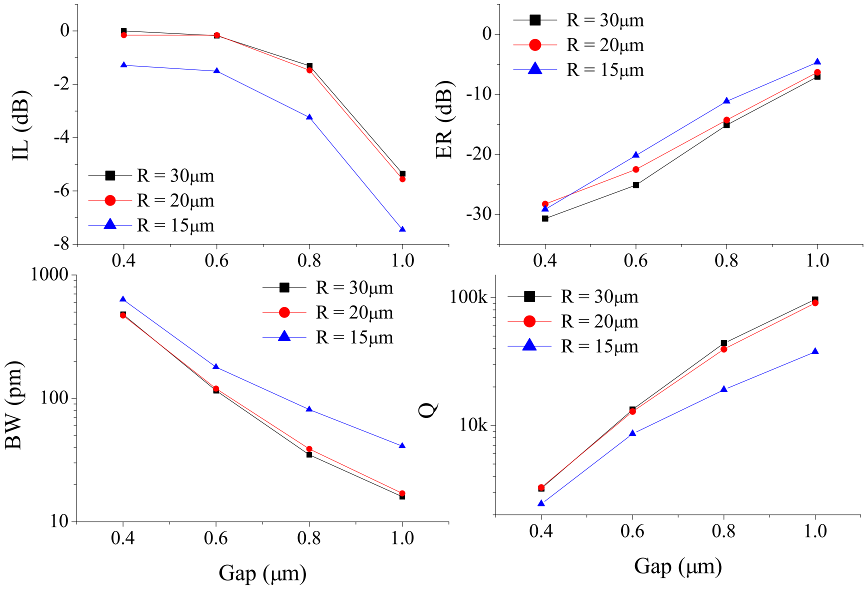

Figure 2.15: Spectral filter characteristics of AD ring resonators using oxide-clad waveguides close to $1540\,\mathrm{nm}$ *in function of gap and this for three different ring radii (*30, 20 *and* $15\,\mu\mathrm{m}$*).*

but also a larger coupling strength.

In the following experiment, we investigate the influence of a straight part in the coupling section which makes the circular ring resonator a so called racetrack ring resonator. The advantage of using a racetrack is that larger gaps can be used. The potential disadvantage is that this racetrack could introduce extra round trip losses and hence degrade the performance of the filter. Based on this experiment, the narrowband label extractors used in chapter 4 were optimized. As explained later, the FSR requirement for these narrowband filters was $5\,\mathrm{nm}$ and the BW must be around $20\,\mathrm{pm}$ with a maximum IL of $5-6\,\mathrm{dB}$. Three different ring resonator configurations were designed, one perfectly circular with a ring radius of $23\,\mu\mathrm{m}$ and two racetrack ring resonators with respectively a coupling length of 4 and $8\,\mu\mathrm{m}$. To maintain the FSR of $5\,\mathrm{nm}$ the radius had to be decreased to respectively 22 and $21\,\mu\mathrm{m}$. The gap variation for those three ring configurations is chosen in such a way that the cross coupling variation is the same. The gap of the circular rings starts at $0.65\,\mu\mathrm{m}$ and is increased to $1.1\,\mu\mathrm{m}$ in steps of $50\,\mathrm{nm}$ (10 rings in total). To maintain the same cross coupling, this gap variation is increased with respectively 100 and $200\,\mathrm{nm}$ for the racetrack configuration with coupling length (L_c) 4 and $8\,\mu\mathrm{m}$. All ring resonators were characterized around $1550\,\mathrm{nm}$ with the highest resolution of $1\,\mathrm{pm}$. The filter characteristics are plot in Fig.2.17 in function

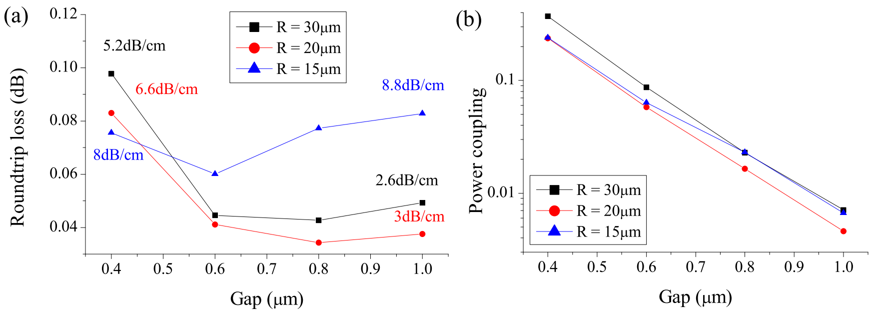

Figure 2.16: The extracted (a) round trip loss and (b) bus-to-ring power coupling for several AD ring resonators using oxide-clad strip waveguides (width = $0.5\,\mu$m) in function of bus-to-ring gap and this for varying ring radius (R).

L_c	1	2	3	4	5	6	7	8	9	10
0	0.65	0.7	0.75	0.8	0.85	0.9	0.95	1.0	1.05	1.1
4	0.75	0.8	0.85	0.9	0.95	1.0	1.05	1.1	1.15	1.2
8	0.85	0.9	0.95	1.0	1.05	1.1	1.15	1.2	1.25	1.3

Table 2.4: Gap variation in function of ring number for each ring resonator configuration. All values are expressed in μm.

of ring number. Based on this number one can then deduce the gap from Tab.2.4.

In Fig.2.17(a), the IL in function of ring number is plot showing a very similar result for the three ring resonators configurations. In Fig.2.17(b), the ER in function of ring number is showing a better result for the circular ring resonator configuration. This improved performance is even better visible in Fig.2.17(c), where the BW of the circular ring resonator is the smallest for all the gaps with respect to the other configurations, and this for a similar IL. This effect is also visible in the maximum Q-factor that is reached. This is Q-factor is 185k and is achieved by the circular ring resonator (i.e. for the largest gap of $1.1\,\mu$m), shown in Fig.2.17(d).

We verify our findings with Eq.(2.13) and (2.14) to extract the round trip losses and power coupling. These numbers in function of ring number are shown in Fig.2.18. From Fig.2.18(a), it is clear that indeed the circular ring resonator configuration has the smallest round trip losses, which explains the superior spectral characteristics shown in Fig.2.17. The reason for this improved performance is not unambiguously and uniquely determined. First, using a racetrack resonator instead of a circular ring resonator, an extra loss mechanism is introduced: waveguide transition loss. This extra loss originates from the bend-to-straight transition (as discussed in section 2.2.2). Since this mode is only loosely confined, we expect that this transition loss would be relatively larger than for highly confined

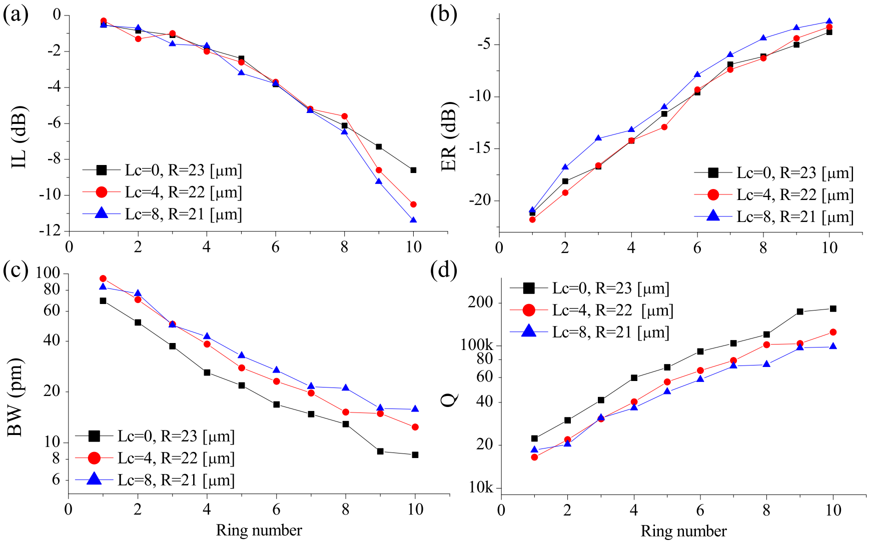

Figure 2.17: The spectral characteristics of the three different ring configurations with constant FSR = 5 nm *using oxide-clad TM-strip waveguides. Mask set sipp06.*

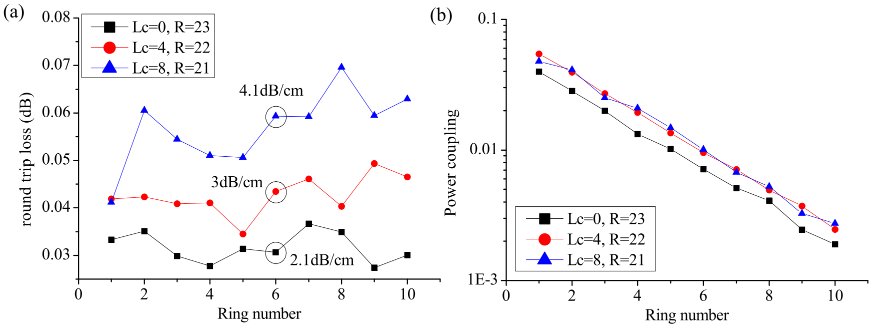

Figure 2.18: Extracted round trip losses and power coupling based on data shown in Fig.2.17.

modes (for the same radius). On the other hand, since in this experiment a constant FSR was required, also the bend radius is decreased when the extra racetrack is used. Hence, not only the transition loss is increased but also the bend loss is (typically exponentially as shown in Fig.2.8) increased. A similar experiment with constant radius could differentiate between these losses. A very similar behavior was found for the TE-rib approach. In Fig.2.18(b), the extracted power coupling in function of ring number is shown, indicating a very similar coupling for each ring number. From Fig.2.18(a), it is clear that indeed the circular ring resonator configuration has the smallest round trip losses, which explains the superior spectral characteristics shown in Fig.2.17. The reason for this improved performance is not unambiguously and uniquely determined. First, using a racetrack resonator instead of a circular ring resonator, an extra loss mechanism is introduced: waveguide transition loss. This extra loss originates from the bend-to-straight transition (as discussed in section 2.2.2). Since this mode is only loosely confined, we expect that this transition loss would be relatively larger than for highly confined modes (for the same radius). On the other hand, since in this experiment a constant FSR was required, also the bend radius is decreased when the extra racetrack is used. Hence, not only the transition loss is increased but also the bend loss is (typically exponentially as shown in Fig.2.8) increased. A similar experiment with constant radius could differentiate between these losses. A very similar behavior was found for the TE-rib approach. In Fig.2.18(b), the extracted power coupling in function of ring number is shown, indicating a very similar coupling for each ring number.

2.4.4 Performance comparison

So far, both the TE-rib and the TM-strip approach have demonstrated narrowband filters with high performance. Using the lower-confined waveguide modes, resonance splitting is eliminated and RPR is significantly reduced. However, specifically for the TE-rib waveguide approach, we expect a worse fabrication tolerance since this waveguide is created using a partial etch. This partial etch can vary both in depth and in width. Further investigation is needed to confirm that this leads to larger wafer non-uniformity with respect to the TE-strip waveguides. Using the TM-strip approach, one would expect a smaller fabrication tolerance since this mode is less dependent on the exact waveguide width. However, this mode is highly dependent on the exact waveguide thickness. This thickness dependency of the TM-approach is much larger in comparison with the width dependency of the TE-strip approach due to the asymmetric waveguide dimensions. On the other hand, wafer-scale thickness variations are expected to be in the order of $10\,\mathrm{nm}$ [41].

What we believe is the main difference between TE-rib and the TM-strip approach is the wavelength dependency of their spectral characteristics. In the fol-

name	Radius [μm]	width [μm]	gap [μm]	FSR [nm]	BW [pm]
TE-strip	20 (n_g = 4.35)	0.45	0.2	4.34	119
TE-rib	25 (n_g = 3.76)	0.7	0.5	4.02	31.3
TM-strip	30 (n_g = 3.15)	0.5	0.8	4	30.8

Table 2.5: Overview design parameters of the compared three AD ring resonators. The radius is chosen to match a FSR of $4\,\mathrm{nm}$ *and the gap is chosen such that the IL is around the same levels.*

lowing investigation, three AD ring resonators which have a similar IL and the same FSR of $4\,\mathrm{nm}$ are compared. All three rings have an oxide cladding. The first ring employs the conventional TE-strip waveguide with a width of $450\,\mathrm{nm}$. Using this waveguide approach, the group index is 4.35. A ring resonator with radius of $20\,\mu\mathrm{m}$ corresponds then to a FRS of $4.34\,\mathrm{nm}$. Using a gap of $200\,\mathrm{nm}$, the resulting BW is $119\,\mathrm{pm}$. This ring will be further referred to as the *TE-strip* ring. The second ring employs the waveguides that were fabricated using a partial etch, the so-called TE-rib approach with waveguide width $700\,\mathrm{nm}$. The group index of this waveguide type is 3.76 and by using a ring radius of $25\,\mu\mathrm{m}$, the FSR is $4.02\,\mathrm{nm}$. The gap is chosen to be $0.5\,\mu\mathrm{m}$, with a resulting BW of $31.3\,\mathrm{pm}$. The last ring resonator is using the TM-strip approach with waveguide width $500\,\mathrm{nm}$. With a group index of 3.15, the FSR is $4\,\mathrm{nm}$ when the radius is set to $30\,\mu\mathrm{m}$. With a gap of $0.8\,\mu\mathrm{m}$ the resulting BW is $30.8\,\mathrm{pm}$. In Tab.2.5, the design parameters are listed as well as the extracted FSR and BW (characterized around the wavelength of $1540\,\mathrm{nm}$).

In Fig.2.19, the spectra of these three ring resonators are characterized at their through, drop and add port for a broad wavelength range ($1518 - 1560\,\mathrm{nm}$). This way, we can characterize the wavelength dependency of the filter specifications (IL, ER and RPR). A wavelength resolution of $1\,\mathrm{pm}$ is used. In Fig.2.19(a), the transmission spectra using a TE-strip ring approach are shown. The cross coupling is large enough to avoid resonance splitting but the RPR (defined as the normalized power at the add port) is reaching high values ($> -10\,\mathrm{dB}$) at shorter wavelengths. In Fig.2.19(b) and (c), the resulting spectra using respectively the TE-rib and the TM-strip approach is shown. A drastically improved BW is immediately noticed indicating an improved propagation loss as discussed before. RPR levels are also significantly lower.

In the following we will discuss the wavelength dependency of the typical filter specifications such as IL, ER and RPR. Each resonance shown in Fig.2.19 is analyzed and each acquired specification is plot in Fig.2.20 in function of the resonance number (from short to long wavelength). In Fig.2.20(a), the wavelength dependency of the IL is shown for the three waveguide approaches. One can notice that the IL using the TE-strip approach fluctuates the most with a value ranging

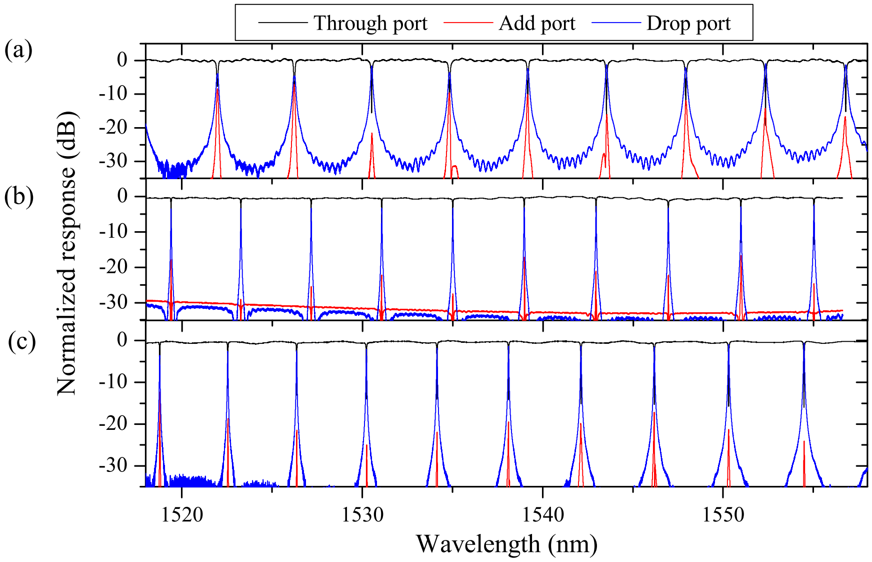

Figure 2.19: Three ring resonator spectra using respectively (a) TE-strip, (b) TE-rib and (c) TM-strip waveguide approach. The details of the devices are listed in Tab.2.5.

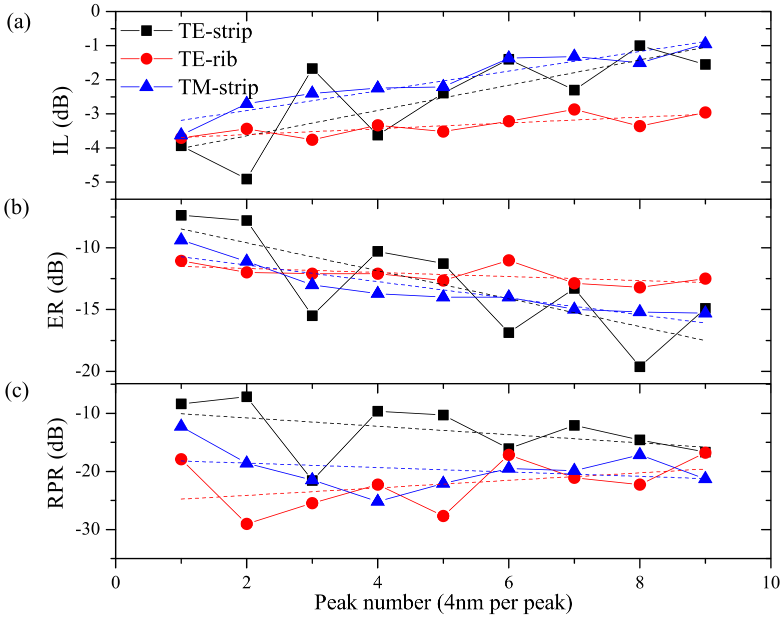

Figure 2.20: The wavelength dependency of the (a) IL (b) ER and (c) RPR in function of resonance number of the TE-strip, TE-rib and TM-strip waveguide approach. The resonances itself are shown in Fig.2.19.

Spec.	TE-strip	TE-rib	TM-strip
IL wavelength dependency (dB/nm)	0.085	0.021	0.072
ER wavelength dependency (dB/nm)	-0.26	-0.041	-0.167
RPR mean value (dB)	-12.9	-22.2	-19.7

Table 2.6: Wavelength dependency of IL and ER of the three waveguide approaches. Also the mean value over all peaks of the RPR is given.

from -5 to $-2\,\mathrm{dB}$, where as the TE-rib and TM-strip approach are much more stable. By fitting a linear curve, the general trend of the wavelength dependency becomes more visible. From these slopes, we find that the TE-rib approach has the smallest wavelength dependency with a value of $0.021\,\mathrm{dB/nm}$. Using the TM-strip approach, this slope is $3.4\times$ larger ($0.072\,\mathrm{dB/cm}$). The ring resonator using a TE-strip waveguide exhibits the largest wavelength dependency (and fluctuation on top of that) with a value of $0.085\,\mathrm{dB/cm}$. These values are also listed in Tab.2.6. A similar trend is found for the ER, as shown in Fig.2.20(b). Also for this property the TE-rib approach has the smallest wavelength dependency, followed by the TM-strip approach. In Fig.2.20(c), the wavelength dependency of the RPR is plot. From this figure, one can find that the RPR using the TE-strip approach is the largest of the three approaches with a mean value of $-12.5\,\mathrm{dB}$. Using a TM-strip approach this is reduced to a mean value of $-19.7\,\mathrm{dB}$. Again, the TE-rib approach has the best result with a mean RPR value of $-22.2\,\mathrm{dB}$, an improvement of almost $10\,\mathrm{dB}$ with respect to the TE-strip approach.

Note that these specifications are depending on two mechanisms: the cross coupling and the round trip loss. We found earlier that the round trip loss increases for longer wavelengths in the case of the TE-strip approach (Fig.2.6) and a similar behavior is expected for the other approaches. On the other hand, the cross coupling increases for longer wavelengths. Changing the physical waveguide (radius, width, height or cladding), the mode (wavelength or polarization) or the gap of the directional coupler, will influence these figures. However, we believe that this example represents well the general behavior given the fact that all three resonators have the same FSR (and thus the same effective length), and have the same configuration (i.e. perfect circular). Although the TE-rib approach has the smallest RPR and the smallest wavelength dependency, it is the TM-strip approach that has the best filter specifications. In this case the BW of both approaches is $31\,\mathrm{pm}$ around $1540\,\mathrm{nm}$ but the TM-strip approach has the best IL of $-1\,\mathrm{dB}$, which is $2\,\mathrm{dB}$ better than the TE-rib approach.

2.4.5 Conclusion

Two new approaches using less-confined modes to lower to overlap with the vertical sidewall roughness were extensively characterized in this section. We employed both a rib waveguide using the quasi-TE mode and a strip waveguide using the quasi-TM mode (in short: the *TE-rib* and the *TM-strip* approach) in a ring resonator and demonstrated a drastically improved filter performance. This improvement includes a reduced counter-directional coupling of the propagating light. As a consequence, no resonance splitting was visible and the reflected power ratio was reduced to lower levels for various configurations. In the case of a circular ring resonators having a FSR of $4\,\mathrm{nm}$, the mean RPR value dropped with almost $10\,\mathrm{dB}$ and $7\,\mathrm{dB}$ using respectively TE-rib and TM-strip waveguides instead of TE-strip waveguides.

The main drawback of using less-confined modes is the increased bend loss and possibly also substrate loss, that limits the designer to use this modes in bends with a minimum radius of $17 - 20\,\mu\mathrm{m}$. We have shown that the TE-rib approach shows smaller wavelength dependency with respect to strip waveguides. We also believe that each approach can be optimized even further, e.g. by using wider waveguide widths. An interesting example of lowering the loss of the TE-strip waveguides using $600\,\mathrm{nm}$ width is reported in [46].

2.5 Design flow & simulation

Any ring resonator design starts by answering the question 'what are the requirements?'. This could be typical filter requirements such as crosstalk, insertion loss and bandwidth but also mode volume, finesse and Q-factor. Additionally some application could require more robustness against fabrication variation or lower wavelength dependency of a certain filter specification. The most important limitation is typically the minimum free-spectral range which defines the circumference of the ring resonator. One should also determine the cladding of the waveguides which is typically defined by the application. E.g. oxide for a full-flow CMOS design, water or air for sensing applications or BCB for post-processing III-V on top of the ring resonator. Based on the requirements and limitations one should make a decision on the waveguide type, polarization, radius and gap. The simulation starts typically by determining the required coupling towards the ring resonator (κ^2), and the circumference of the ring resonator. For this purpose one can use equations (2.2) and (2.5) to calculate the spectrum of the ring resonator. At this point one needs to know the effective refractive index and group index (Eq.(2.7)). One can use a 2D mode solver to calculate the propagation characteristics and loss (Eq.(2.27)). The next step is to determine the physical dimensions of the directional coupler which is highly depending on the cladding, wavelength, waveguide dimensions, radius and maximum coupling length.

We start this section with the simulation of a directional coupler used to determine the cross coupling. Next, a matrix formalism is derived that can be used to calculate the analytical spectrum of a single and higher-order ring resonator. We end this section with a design exploration for a second-order ring resonator and the channel spacing calculation used to design a multi-ring demultiplexer.

2.5.1 Simulating coupling in a directional coupler

In some cases where one has a long coupling length (L$_c$) and the ring radius (R) is small, one can simplify the directional coupling section by neglecting the coupling in the bends. Then the coupling between two symmetric waveguides is easily calculated based on the phase difference between the two supermodes of the two waveguides, multiplied by the length of the coupling section L$_c$. One can use therefore a simple 2D mode solver, to calculate the difference in n$_{eff}$ between the even (n$_e$) and the odd (n$_o$) supermode. The effective (field) coupling between the two waveguides is then

$$\kappa = \sin\left(\frac{\beta_e - \beta_o}{2} L_c\right) = \sin\left(\frac{2\pi}{\lambda}\frac{n_e - n_o}{2} L_c\right) \tag{2.28}$$

Maximum coupling is then achieved when the argument of the sinus equals $\pi/2$ or when

$$L_c = \frac{\lambda}{2(n_e - n_o)} \tag{2.29}$$

.

The coupling strength between two symmetric waveguides depends on the wavelength, cladding, polarization and the actual waveguide dimensions. In Fig. 2.21(a), the effective refractive index of the even and odd supermode is shown in function of the gap for two different waveguide widths and polarization. The height of both strip waveguides is $220\,\mathrm{nm}$. Fig.2.21(b) shows that the coupling strength decreases exponentially for increasing gap. The coupling strength difference can vary a lot especially between different polarizations. The quasi-TM polarization is much less confined than the quasi-TE polarization due the physical asymmetry of the waveguide. For a waveguide width of $0.45\,\mu\mathrm{m}$ and waveguide gap of $200\,\mathrm{nm}$, this results in a 4 times larger coupling strength for TM then for TE. This difference becomes even larger for larger gaps. The effect of the waveguide width has a larger effect for the quasi-TE polarization than for the quasi-TM polarization. For a waveguide gap of $200\,\mathrm{nm}$ the coupling strength using the quasi-TE polarization is 0.038 for waveguide width of $0.5\,\mu\mathrm{m}$ and 0.06 for waveguide width of $0.45\,\mu\mathrm{m}$. This difference of almost 60% is again related to the mode confinement which is larger for a wider waveguide.

Using a (side and top) cladding with a lower refractive index, e.g. water n$_{eff}$ = 1.3 or air n$_{eff}$ = 1, the mode confinement in the silicon waveguide becomes larger and hence a lower coupling strength is expected. Using $450 \times 220\,\mathrm{nm}^2$ waveguide dimension and the quasi-TE polarization, the coupling strength between two symmetric waveguides with a gap of $200\,\mathrm{nm}$ is 80% smaller with an air cladding and

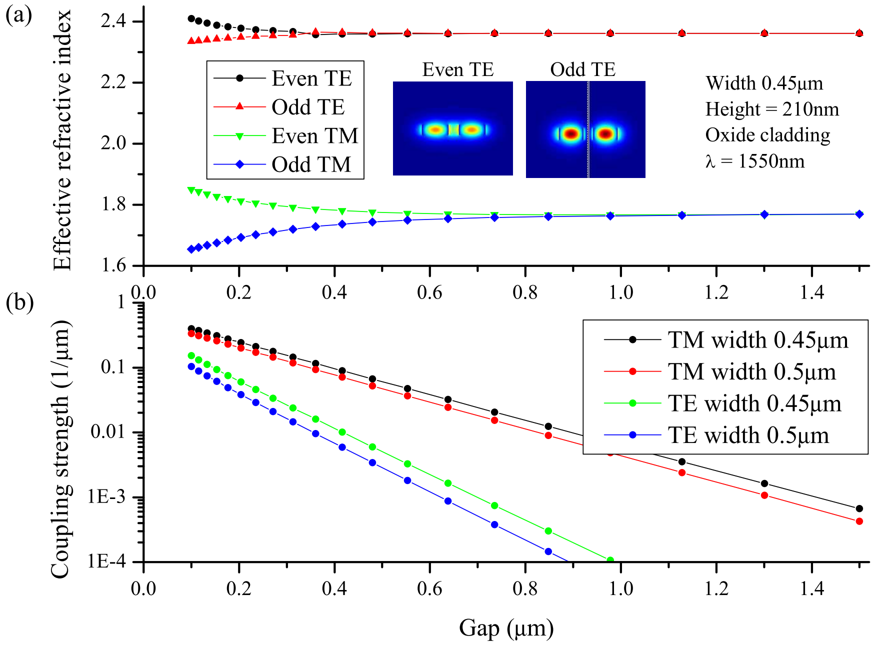

Figure 2.21: The calculation of the coupling strength (b) using the effective refractive index difference between the even and odd supermode (a) for different waveguide widths and polarization. In this case there is an oxide cladding and the height of the strip waveguides is 220nm.

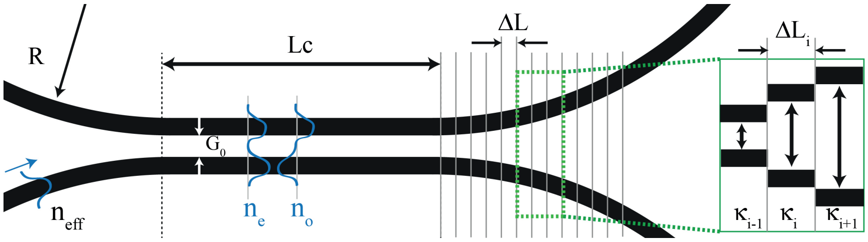

Figure 2.22: Illustration of how to calculate the coupling from a directional coupler with large bend sections.

14% smaller with an water cladding with respect to a full oxide cladding. Using a higher refractive index cladding (e.g. BCB n_{eff} = 1.54), the coupling is 11% increased.

As shown earlier, it can be advantageous to remove the straight coupling section and use circular rings. In that case, one typically uses a beam-propagation method or an eigenmode expansion method (e.g. FimmProp) to simulate the coupling. However, this is a rather time consuming job since a circuit designer needs several iterations between the required coupling and the resulting directional coupler physical dimensions. Therefore, a very simple and fast method has been developed in the course of this work to estimate the coupling from the bend section. It contains two steps: the first step is the simulation of the coupling strength ($\kappa[1/m]$) in function of gap using a 2D mode solver as shown in Fig.2.21(b) and the second step is to calculate the coupling for a certain directional coupler configuration.

This has been achieved treating the bend sections as a staircase of parallel waveguides with length ΔL as shown in Fig.2.22. We therefore neglect the fact that the mode in a bend is not equal to a mode in a straight waveguide. One can expect larger deviations for sharper bends.

The entrance coupling (κ_{bend}) is then the sum of smaller coupling sections with gap G_i and length ΔL_i as expressed in Eq.2.30.

$$\kappa_{\text{bend}} = \sum_i \kappa_i(G_i)\Delta L_i \tag{2.30}$$

The full coupling is then the sum of the coupling from the straight part (κ_{straight}) with gap (G_0) and length L_c and twice the coupling coming from a bend κ_{bend}.

$$\kappa = \sin(2\kappa_{\text{bend}} + \kappa_{\text{straight}}) = \sin\left(2\sum_i \kappa_i(G_i)\Delta L_i + \kappa_0(G_0)L_c\right) \tag{2.31}$$

In Fig.2.23, the resulting power coupling (κ^2) in function of ring radius between two symmetric strip waveguides with circular bends and no straight part (L_c = 0) is shown. Both a straight bus and a symmetrically curved bus waveguide are

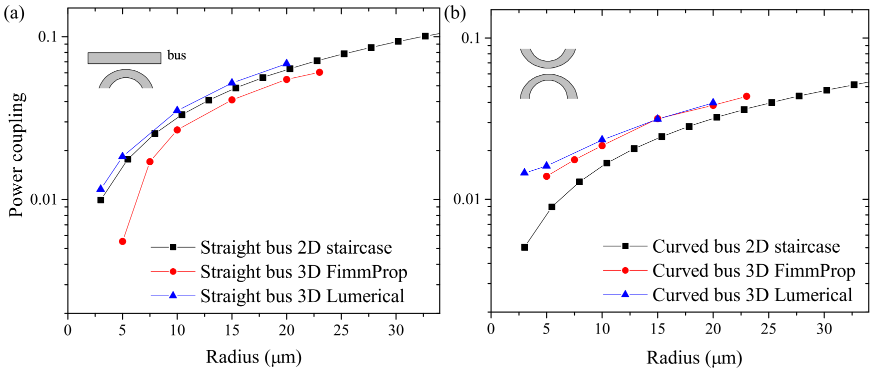

Figure 2.23: Power coupling between two symmetric strip waveguides (quasi-TE polarization) in function of radius, for both a straight (a) and curved (b) bus waveguide.

considered. Other parameters such as gap ($200\,\mathrm{nm}$), wavelength ($\lambda = 1550\,\mathrm{nm}$) and waveguide dimensions ($450 \times 220\,\mathrm{nm}^2$ with oxide cladding) are fixed. The calculated results using the 2D staircase approach are compared with the 3D eigenmode expansion tool from Photon Design (FimmProp) and a 3D FDTD tool from Lumerical. Since no approximations are made in the latter, we will refer to this as the most accurate one.

From Fig.2.23(a), it is seen that the 2D staircase approach for a straight bus waveguide matches very well with the Lumerical results. On the other hand, the FimmProp results are deviating increasingly for sharper bends. We find a different situation in Fig.2.23(b) for the calculation of the symmetrically curved bus waveguide. In this case, the 2D staircase approach are deviating largely from those calculated with Lumerical. The results from the 3D approaches (FimmProp and Lumerical) are matching very well. It turns out that the effective coupling is largely underestimated by the 2D staircase approach. This can be explained by the fact that the traveling modes are for both the ring and the bus pushed towards each other, resulting in a larger cross coupling. This effect is not taken into account using the 2D staircase approach that uses the coupling of straight waveguides. This seeming discrepancy between the well-matching results of a straight bus and the less-matching results of a curved bus waveguide can be explained as follows. First, also in the case of straight bus, the mode traveling in the ring waveguide is pushed towards the bus waveguide. This effect not only increases the effective coupling, as with using a curved bus, but it also changes the effective refractive index. This change is only for the ring waveguide and thus a small phase mismatch is introduced which lowers the effective coupling. According to Fig.2.23(b), these two effects cancel out with a well-matching result as a consequence. For larger bends, all three methods converge for both a straight and a curved bus. Then the 2D

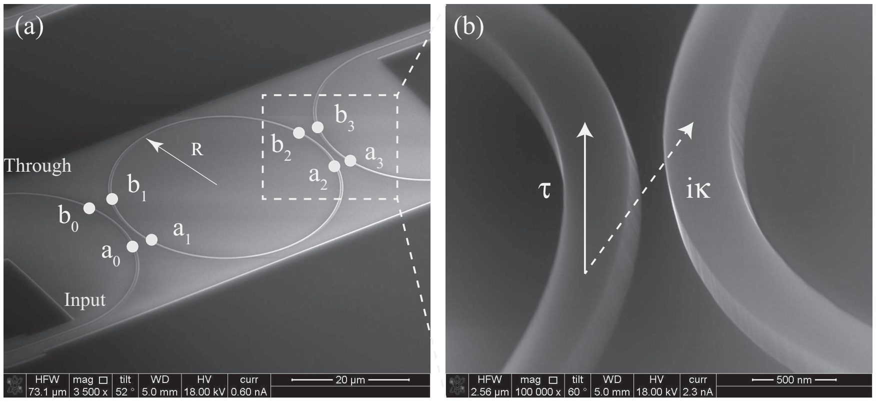

Figure 2.24: SEM picture of a (a) ring resonator with radius $20\,\mu\mathrm{m}$*, waveguide dimensions* $500 \times 220\,\mathrm{nm}^2$ *and (b) a directional coupler waveguide configuration used to couple a small portion of the bus light into the ring.*

staircase approach becomes superior due its fast computation time.

2.5.2 Simulating the spectrum of single and higher-order rings

Using the matrix formalism explained in [59], one can easily calculate the spectral characteristics from a first and higher-order ring resonator. Higher-order ring resonators offer a better trade-off between roll-off and insertion loss and are typically used when one requires a wide bandwidth and a steep roll-off filter characteristic [17]. The matrix formalism allows for an easy cascade of coupled ring resonators (also known as coupled resonator optical waveguides or CROWs [59]).

In Fig.2.24 (a), a SEM picture of circular ring resonator is shown with a zoom on the directional coupler in (b). The field at the input of the ring resonator is denoted as a$_0$ and the field after the directional coupler is denoted as b$_0$. The field that describes the portion of the light coupled to the ring is denoted as b$_1$ and consist out of $i\kappa a_0$ added with the field already inside the ring (τa_1). If the directional coupler has a certain coupling length, an extra phase difference $e^{i\beta L_c}$ is added with β the phase speed of the light defined as

$$\beta = \frac{2\pi}{\lambda n_{\text{eff}}}. \tag{2.32}$$

This results in the simple matrix relationship shown in Eq.(2.33) that connects the input fields of the directional coupler (a$_0$ and a$_1$) with the output fields (b$_0$ and b$_1$).

$$\begin{bmatrix} b_0 \\ b_1 \end{bmatrix} = \begin{bmatrix} \tau & i\kappa \\ i\kappa & \tau \end{bmatrix} e^{i\beta L_c} \begin{bmatrix} a_0 \\ a_1 \end{bmatrix} \tag{2.33}$$

One can then rearrange the Eq.(2.33) to obtain Eq.(2.34) such the relationship (described as matrix P) between the bus fields (a$_0$ and b$_0$) and the ring fields (a$_1$ and b$_1$) can be determined.

$$\begin{bmatrix} a_1 \\ b_1 \end{bmatrix} = \begin{bmatrix} -\frac{\tau}{i\kappa} & \frac{1}{i\kappa}\, e^{-i\beta L_c} \\ -\frac{\tau^2+\kappa^2}{i\kappa}\, e^{i\beta L_c} & \frac{\tau}{i\kappa} \end{bmatrix} \begin{bmatrix} a_0 \\ b_0 \end{bmatrix} = P \begin{bmatrix} a_0 \\ b_0 \end{bmatrix} \tag{2.34}$$

The relationship between one side of the ring (i.e. a$_1$ and b$_1$) and the other side of the ring (denoted as a$_2$ and b$_2$) is determined by a certain phase shift depending on the length of half the ring (L$_r$) and the attenuation a.

$$\begin{bmatrix} a_2 \\ b_2 \end{bmatrix} = \begin{bmatrix} 0 & ae^{i\beta L_r} \\ \frac{1}{a}e^{-i\beta L_r} & 0 \end{bmatrix} \begin{bmatrix} a_1 \\ b_1 \end{bmatrix} = Q \begin{bmatrix} a_1 \\ b_1 \end{bmatrix} \tag{2.35}$$

with L$_r$ the distance between a$_1$ and a$_2$, typically πR with R the radius of the ring. One can calculate the field propagation attenuation a from the (power) propagation loss of the waveguide A [dB/cm] as follows:

$$a = 10^{-AL_r 100/20} \tag{2.36}$$

where the factor 20 comes from the conversion from power to field attenuation and factor 100 from cm to m. The relationship between a$_2$ and b$_2$ and the output waveguide fields denoted as a$_3$ and b$_3$ is in the case of symmetrical coupling defined by matrix P. The field transmission from the bus (a$_0$ and b$_0$) to the output waveguide (a$_3$ and b$_3$) is then fully described as

$$\begin{bmatrix} a_3 \\ b_3 \end{bmatrix} = PQP \begin{bmatrix} a_0 \\ b_0 \end{bmatrix} = \begin{bmatrix} T_{[0,0]} & T_{[0,1]} \\ T_{[1,0]} & T_{[1,1]}. \end{bmatrix} \tag{2.37}$$

With no added signal (a$_3$ = 0) and unit input (a$_0$ = 1), the field at the through port (b$_0$) and drop port (b$_3$) is defined as

$$b_0 = -\frac{T_{[0,0]}}{T_{[0,1]}} \tag{2.38}$$

$$b_3 = T_{[1,0]} - \frac{T_{[0,0]}T_{[1,1]}}{T_{[0,1]}} \tag{2.39}$$

These equations are exactly the same as the analytic formulation given earlier in Eq.(2.5). However, the true elegance of this matrix formalism is that it can be extended very easily for higher-order ring resonators. With n the amount of coupled ring resonators the transmission matrix T describing the field relationship between input and output waveguide is then scribed as

$$T = (PQ)^n P. \tag{2.40}$$

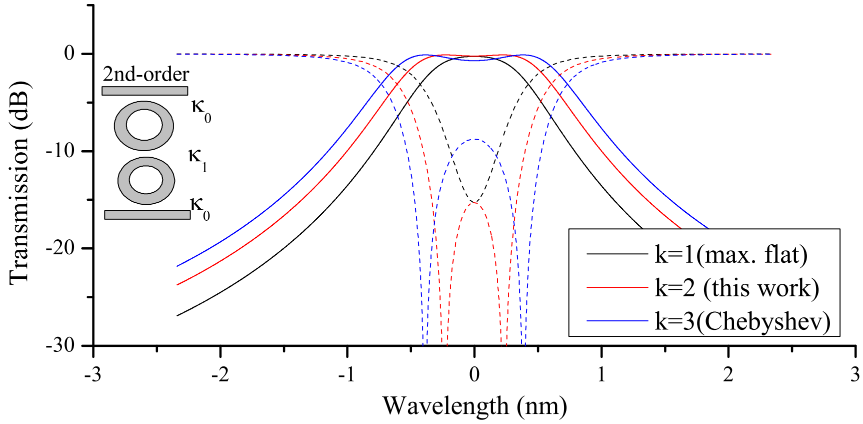

Figure 2.25: Applying different filter parameters conditions that relates κ_1 to κ_0 in a second-order ring resonator design. In this case $\kappa_0^2 = 0.35$ and the FSR = $9.3\,\mathrm{nm}$. A constant propagation loss of $8\,\mathrm{dB/cm}$ is assumed.

2.5.3 Second-order ring resonator design exploration

In this section, we explore the design space for second-order ring resonators. By varying the coupling parameters between the bus and the first ring (κ_0) and between the two inner rings (κ_1), one can achieve many different spectral shapes. The goal of this section is to create wide bandwidth filters. Early work on higher-order ring resonators reported in [17] translates general filter characteristics into coupling conditions that relates the different coupling parameters. This coupling condition for second-order ring resonators is listed in the following equation.

$$\kappa_1^2 = 0.25k\kappa_0^4 \tag{2.41}$$

When k=1, this equation resembles the *maximally flat* filter condition and for k=3 the (first order) *Chebyshev* filter condition, according to [17]. We plot the spectrum of a second-order ring resonator with $\kappa_0^2 = 0.35$ and FSR = $9.3\,\mathrm{nm}$ in Fig.2.25. Both coupling conditions are applied. A constant propagation loss of $8\,\mathrm{dB/cm}$ is assumed (based on some typical results as obtained in section 2.3).

From this figure, one can see that the maximally flat condition (k=1 in Eq.(2.41)) gives the most narrow bandwidth and a single resonance dip in the through transmission. Using the Chebyshev relationship (i.e. k=3 in Eq.(2.41)), the extinction ratio is degraded with more than $5, \mathrm{dB}$ and is showing two resonance dips. More important, a little dip is seen in the drop response which could cause a higher insertion loss. However, the 3dB BW is increased and is now almost double that of the case for k=1. We found that by taking k=2, an intermediate spectrum is found with an increased BW but without any dip in the drop response. Also the maximum level of the extinction ratio is equal to that of k=1. This response with k=2 is

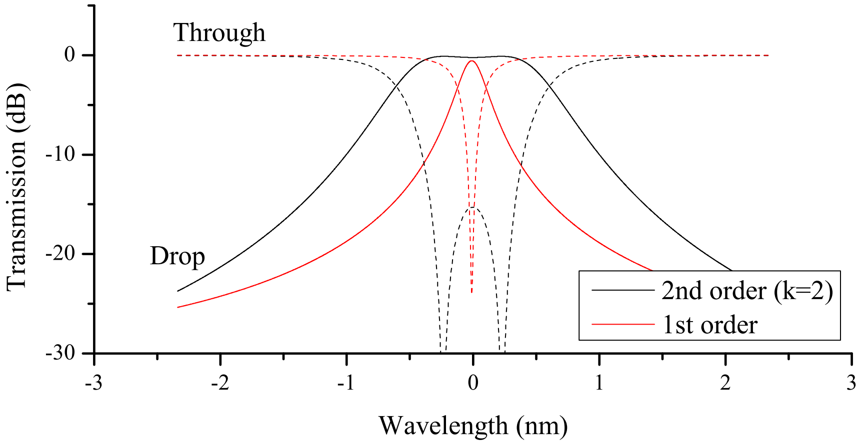

Figure 2.26: The drop and through transmission from a 1^{st} and 2^{nd}-order ring resonator. The FSR is for all designs $9.3\,\mathrm{nm}$.

Specification	κ_0^2	κ_1^2	BW_1 [nm]	BW_{10} [nm]	Roll off
1st order	0.073	-	0.14	0.7	0.2
2nd order	0.35	0.03	0.82	2	0.41

Table 2.7: Coupling parameters for a 1^{st} and 2^{nd}-order ring resonator design, FSR = $9.3\,\mathrm{nm}$. *Roll-off factor is defined as $\mathrm{BW}_1/\mathrm{BW}_{10}$.*

also shown in Fig.2.25.

In the following, a filter is designed with a constant drop level of $-25\,\mathrm{dB}$ at $300\,\mathrm{GHz}$ (or $2.3\,\mathrm{nm}$) away from the resonance wavelength. This specification is usually referred to as the crosstalk. The filter is implemented with first- and second-order ring resonators. Again, a constant propagation loss of $8\,\mathrm{dB/cm}$ is assumed. In Fig.2.26, the simulated drop and through transmission is shown. The FSR is $9.3\,\mathrm{nm}$. The coupling parameters are shown in Tab.2.7. The relationship between the κ_0 and κ_1 for the second order ring resonators is determined by Eq.(2.41) using k=2.

From Fig.2.26, it is clear that one can achieve a much wider bandwidth (BW) using a second-order ring resonator design, and this without sacrificing the dropping level at a certain spectral distance away from the peak (i.e. the crosstalk). For a first-order ring resonator design, we can achieve an 1dB BW (BW_1) of $0.14\,\mathrm{nm}$. This is much larger for second-order ring resonator ($0.82\,\mathrm{nm}$). One can also see that the roll-off (defined as ratio between BW_1 and BW_{10}) is doubled from 0.2 for a first-order to 0.41 for a second-order ring resonator.

2.5.4 Channel spacing calculation

By cascading ring resonators in series, one can create easily a demultiplexer where each ring resonator is responsible for dropping a certain channel. The channel spacing (CS) is defined as the spectral distance between the center wavelengths of two adjacent channels. One can shift the resonance of a ring resonator by changing the effective length of the optical path. In other words, one can change the effective refractive index of the resonating mode or the physical circumference of the ring resonator. In this work, we prefer to increase the circumference with ΔL to shift the resonance to a longer wavelength. In telecommunication, one typically uses a multiple of $100\,\mathrm{GHz}$ to define the wavelength grid. Depending on the exact center wavelength one can calculate the corresponding CS expressed in unit length, with f the frequency and c the speed of light:

$$\Delta\lambda = \frac{\Delta f}{f}\lambda = \Delta f\frac{\lambda^2_{\text{center}}}{c}. \tag{2.42}$$

Eq.(2.42) indicates that the CS expressed in ($\Delta\lambda$) is wavelength dependent. A channel spacing of $100\,\mathrm{GHz}$ at $1550\,\mathrm{nm}$ is $0.8\,\mathrm{nm}$. During this work we shifted our preferred wavelength range to slightly shorter wavelengths $1530\,\mathrm{nm}$, where the CS becomes $0.78\,\mathrm{nm}$. At $1310\,\mathrm{nm}$, a $100\,$GHZ-CS corresponds to a CS of $0.57\,\mathrm{nm}$. A closed-form expression to link a difference in circumference (ΔL) to a wavelength shift ($\Delta\lambda$) can be deduced starting from the difference in resonance condition expressed in Eq.(2.3).

$$\Delta\lambda = \lambda_2 - \lambda_1 = \frac{n_{eff}(\lambda_1)(L+\Delta L) - n_{eff}(\lambda_2)(L)}{m} \tag{2.43}$$

Using the definition of the group index (n_g), defined in Eq.(2.7), one can derive the following equation expressing ΔL as a function of wavelength and circumference.

$$\Delta L = \frac{n_g}{n_{eff}(\lambda)}\frac{\Delta\lambda}{\lambda}L = \frac{n_g}{n_{eff}(\lambda)}\frac{\Delta f\lambda}{c}L \tag{2.44}$$

One can ignore the wavelength dependency of n_{eff} and evaluate the expression based on the wavelength of the center channel. In that case ΔL is a constant. If the wavelength span becomes very large, one can evaluate ΔL for each intermediate wavelength λ_i, which is defined as the average wavelength between two channels ($\lambda_i = (\lambda_1 + \lambda_2)/2$).

In the following we derive all the parameters of a typical 4-channel demultiplexer with a channel spacing of $300\,\mathrm{GHz}$ around the wavelength of $1530\,\mathrm{nm}$. The FSR is chosen in such a way that there is no overlap between the first and last channel and is defined as $11.7\,\mathrm{nm}$ or $(4+1)\Delta\lambda$. Using Eq.(2.6), the required circumference can be calculated. Using a 2D mode solver, one finds a group index of 4.26 using a waveguide with dimensions $450 \times 210\,\mathrm{nm}$ and an oxide cladding

Channel	λ	L_c	G_0	G_1	FSR
	nm	μm	nm	nm	nm
1	1526.2	7.089	176	276	11.656
2	1528.5	7.154	178	278	11.66
3	1530.8	7.219	180	281	11.663
4	1533.1	7.284	182	283	11.666

Table 2.8: All the parameters of a typical 4-channel $300\,\mathrm{GHz}$*-spaced demultiplexer using 2nd-order ring resonators. The radius of* $5.21\,\mu\mathrm{m}$ *is kept constant and the waveguide dimension of both bus and ring waveguide is* $450 \times 210\,\mathrm{nm}$*. An oxide cladding is assumed.*

(around the center wavelength $1530\,\mathrm{nm}$). The circumference of the ring resonator is then $46.9\,\mu\mathrm{m}$. Using Eq.(2.3), one can calculate the resonance wavelength that corresponds with this circumference. Based on the coupling parameters required, a coupling length and radius is chosen in such a way that the radius is not too small (e.g. $R > 3\,\mu\mathrm{m}$) and the resulting gap is wide enough (e.g. $G_0 > 130\,\mathrm{nm}$). In this example we chose L_c to be $7\,\mu\mathrm{m}$ and the radius $5.21\,\mu\mathrm{m}$. Additionally, one can require that the first wavelength is fixed to a certain wavelength, e.g. $1526\,\mathrm{nm}$, and slightly change the circumference. In this example, we adjust the coupling length of the first channel to $7.089\,\mu\mathrm{m}$. Consequently, the FSR will be slightly off (in this example only $0.15\,\mathrm{nm}$). Once the channel center wavelengths are set, one can calculate $\Delta L = 130\,\mathrm{nm}$ using Eq.(2.44). In this example, the wavelength dependency of ΔL is very small and differences are smaller than the mask grid (i.e. $< 1\,\mathrm{nm}$). We implement this circumference difference as a $65\,\mathrm{nm}$ in coupling length (i.e. $\Delta L/2$). The resulting coupling lengths are listed in Tab.2.8. Note that the followed procedure is independent of the ring order.

In this example, we design a second-order ring resonator with a crosstalk below $-20\,\mathrm{dB}$ and minimized insertion loss. The coupling parameters κ_0^2 and κ_1^2 are respectively 0.38 and 0.072, and related by Eq.(2.41) using k=2. For each channel we calculate the right gap according the required power coupling. In this calculation, we take into account the resonance wavelength and the correct coupling length as listed in Tab.2.8. Note that the coupling strength is wavelength dependent but could be neglected when the wavelength range is small. Also, a mask grid of $1\,\mathrm{nm}$ is assumed here. Using a more coarse mask grid one introduces a detrimental error in resonance wavelength and coupling strength.

The resulting theoretical spectrum of the four drop ports is shown in Fig.2.27. In Fig.2.28, a typical as-measured spectrum is plot, demonstrating a good agreement with the simulated spectra shown in Fig.2.27. Note that the procedure used to design the component shown in Fig.2.28 was a simplified version of the design procedure that is presented in this section. However, the design parameters are very similar. The full design description and characterization of this component is extensively discussed in section 5.4 on page 5-7.

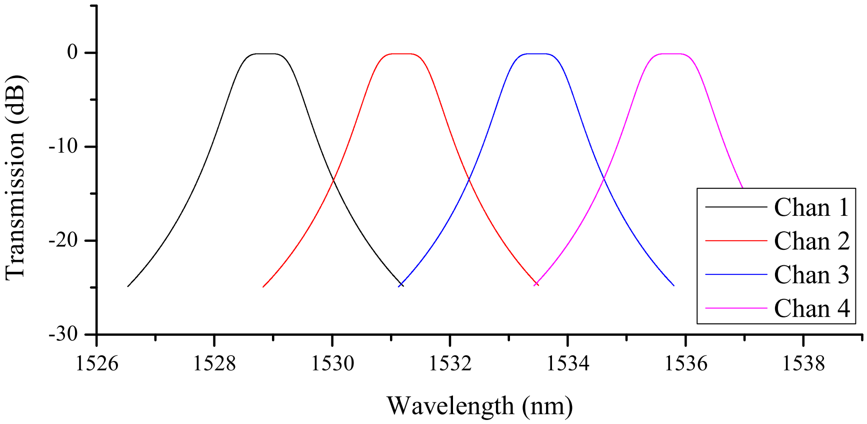

Figure 2.27: An as-simulated 4-channel 300 GHz*-spaced demultiplexer using 2nd-order ring resonators.*

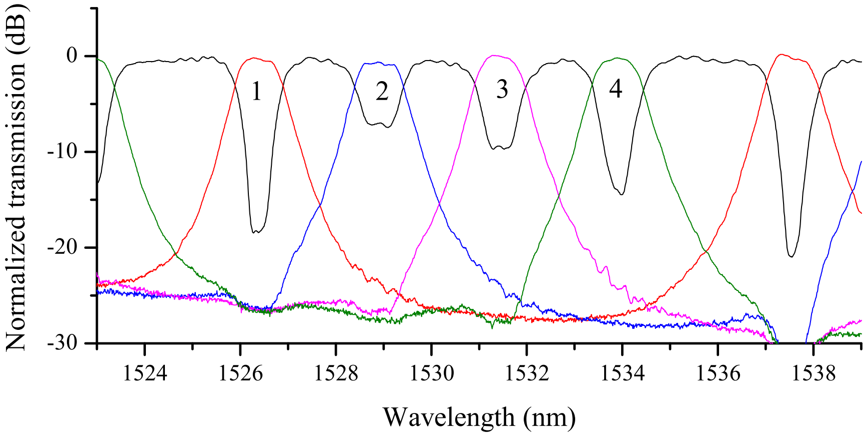

Figure 2.28: An as-measured 4-channel 300 GHz*-spaced demultiplexer using 2nd-order ring resonators.*

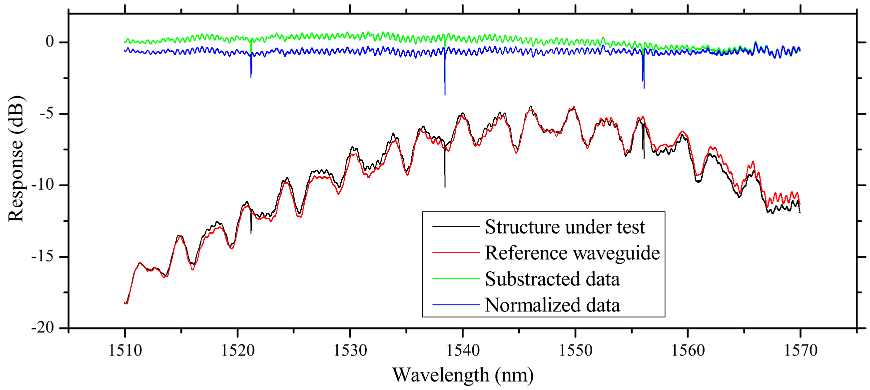

Figure 2.29: The procedure to normalize a typical ring transmission response.

2.6 Data processing

In Fig.2.29, a typical spectrum of a (under-coupled) ring resonator measured at the through port is shown and denoted as *structure under test*. The measured data has the typical Gaussian envelope of a fiber grating coupler, which is possibly distorted by a Fabry-Perot interference pattern. Using a simple ring structure, these reflections are typically coming from the grating couplers or from the mode mismatch between the chip and fiber. Using more complex structures, also reflections from the structure itself are expected. These patterns are making the data fitting more difficult and eventually less accurate. The strategy applied in this work is using a reference waveguide. This reference waveguide should have the same grating couplers and be located very close to the grating couplers from the structure under test. In Fig.2.29, the measured spectrum of a reference waveguide is shown as well. It can be seen that this reference waveguide has the same envelope and oscillations. If measured with the same resolution and span, one can easily subtract the reference from the through port. Possibly these spectra are deviating a bit, for a certain wavelength range. In this case the structure under test has a little higher transmission efficiency around $1530\,\mathrm{nm}$ and a little smaller at larger wavelengths around $1565\,\mathrm{nm}$. As a consequence the subtracted data is in this case slightly skewed but the Gaussian envelope and Fabry-Perot interference pattern are nicely removed. In a following step we fit the subtracted data to a second order function which will further remove the skewed response. To obtain the final *normalized* data, we make sure the maximum transmission is $0\,\mathrm{dB}$ by applying a last offset. The meaning of this last step is only to give the data a more physical understanding (there is no gain in the passive structure) and one should be careful to interpret this value correctly.

2.7 Polarization rotating coupler

This chapter ends with a novel ring resonator concept proposed and demonstrated during this work. The concept uses a polarization rotating asymmetrical directional coupler. Earlier, we have found that using the quasi-TM moded waveguide (TM-strip approach) a ring resonator has an improved performance. However, using the quasi-TE moded waveguide (TE-strip approach), one can make ultra-compact circuits due to small radiation loss in short bends. Therefore, we aim to combine the advantages of both polarizations: use quasi-TE polarized light for compact guiding of the light towards the ring resonator and quasi-TM polarized light in the ring to take advantage of the lower propagation loss and backscattering. This enables the realization of rings with a high Q-factor for e.g. applications in large and accurate sensor arrays. To make this polarization change possible one could use a separate polarization rotator in front of a ring resonator. However, this usually requires complicated fabrication steps and increases the footprint of the device. An elegant and simple solution for a polarization rotator is using an asymmetrical directional coupler similar as the one presented in [60] and [61], which is based on the existence of hybrid supermodes [62]. In this paper we go one step further and use this polarization rotating directional coupler in the coupling section of the ring resonator to excite the fundamental quasi-TM mode in the ring. The design rules on how a small transition loss and thus a ring with a high Q-factor can be achieved are explained. Experimental verification of the concept is provided. We demonstrate the operation principle with two AP ring resonators with radius $30\,\mu\text{m}$, working in the critically coupled regime with a quality factor of 31000 and in the under-coupled regime with a quality factor of 125000. This work has been published in IEEE Photonics Technology Letters [63].

2.7.1 Theory

To achieve a high Q-factor ring resonator using TM-polarized light, two conditions need to be fulfilled. The first condition is achieving efficient coupling from the fundamental quasi-TE mode (TE_{11}) in the bus waveguide to the fundamental quasi-TM mode (TM_{11}) in the ring waveguide and avoiding coupling to other modes. The second condition is that there should be a low loss of the excited TM_{11} mode of the ring waveguide at the coupler. In order to analyze the polarization conversion in a ring resonator, an AP ring resonator (radius = $30\,\mu\text{m}$) with an asymmetrical directional coupler such as presented in Fig.2.30 is used. There are two required levels of asymmetry in this directional coupler: 1) a different waveguide width for the bus and the ring and 2) an asymmetrical cladding. In such a vertically asymmetrical waveguide the second and the third eigenmode are hybrid [62] and are anti-crossing around $0.65\,\mu\text{m}$. In Fig.2.31(a), were the effective refractive index in function of waveguide width is plot, this anti-crossing is

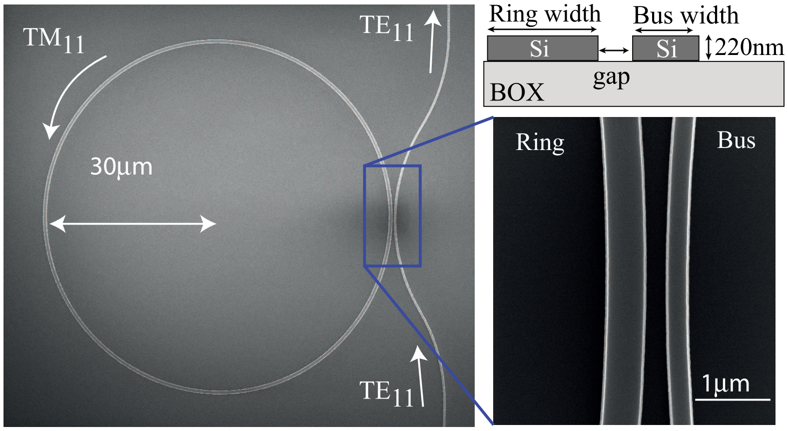

Figure 2.30: An AP ring resonator on SOI using a polarization rotating asymmetrical directional coupler. The fundamental quasi-TE mode in the bus is used to excite the fundamental quasi-TM mode using hybrid coupling.

clearly visible. By narrowing the bus waveguide, the TE$_{11}$ bus mode is almost phase matched with both hybrid modes and thus coupling is expected. This behavior is visible in Fig.2.31b, where the supermodes of the asymmetrical directional coupler in function of bus waveguide width are shown (gap = $100\,\mathrm{nm}$). The ring waveguide is fixed at $600\,\mathrm{nm}$. Since the mode overlap between two quasi-phase matched modes with the same polarization is larger than when they are of opposite polarization, the coupling from the TE$_{11}$ bus mode to the TE$_{21}$-like supermode is stronger than the coupling to the TM$_{11}$-like supermode. As the excited TE$_{21}$-like supermode travels further in the directional coupler and the gap becomes larger, it couples due to its hybrid nature rapidly to the fundamental TM$_{11}$ ring mode and only a small part evolves to the leaky TE$_{21}$ ring mode. The initially less excited TM$_{11}$-like supermode evolves to the TM$_{11}$ ring mode and slightly to the TM$_{11}$ bus mode. The supermode evolution of this non-adiabatic supermode taper is shown in Fig.2.32a and the corresponding field intensity is plotted in Fig. 2.32b, calculated using the rigorous fully-vectorial eigenmode expansion and propagation tool FimmProp (Photon Design).

To exploit this polarization rotating behavior, the power coupling to the different modes for different combinations of bus and ring waveguide widths is simulated for a $300\,\mathrm{nm}$ gap, shown in Fig. 2.33, where the power coupling from the TE$_{11}$ bus mode to the TM$_{11}$ and TE$_{21}$ ring mode and the TM$_{11}$ and TE$_{11}$ bus mode is shown. Note that for each combination the power coupling to the TE$_{11}$ ring mode is negligible due to a huge phase mismatch. From this figure, one can draw two intermediate conclusions for efficient polarization conversion. First, one can see that for each width of the ring waveguide maximum power coupling to

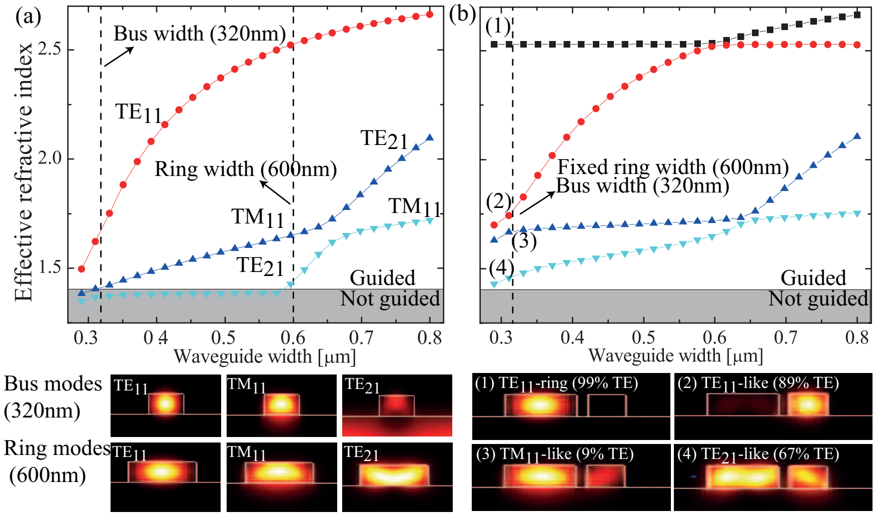

Figure 2.31: The effective refractive index (n_{eff}) of (a) the eigenmodes of an isolated silicon wire as a function of waveguide width and (b) the supermodes of two coupled asymmetrical silicon wires with gap $100\,\mathrm{nm}$ *as a function of the bus width and fixed ring width (*$600\,\mathrm{nm}$*). The waveguide height is* $220\,\mathrm{nm}$ *and operation wavelength is* $1550\,\mathrm{nm}$*. The mode profiles (intensity) are plotted for both configurations with bus width* $320\,\mathrm{nm}$ *and ring width* $600\,\mathrm{nm}$*.*

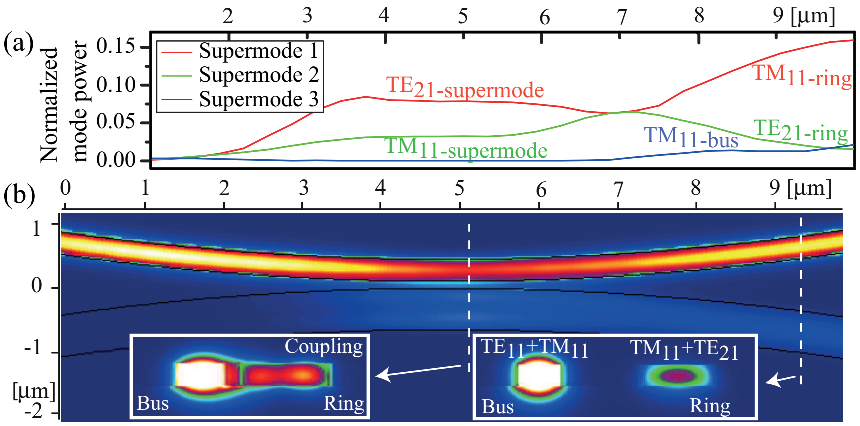

Figure 2.32: Supermode evolution (a) and intensity plot of the fields (b) in an asymmetrical directional coupler for a bus and ring waveguide width of respectively $0.32\,\mu\mathrm{m}$ *and* $0.6\,\mu\mathrm{m}$ *(*$100\,\mathrm{nm}$ *gap and* $30\,\mu\mathrm{m}$ *radius). The TE*$_{11}$ *bus mode is excited.*

the TM$_{11}$ ring mode is achieved for another bus waveguide width which confirms the corresponding phase matching condition extracted from the eigenmodes of an

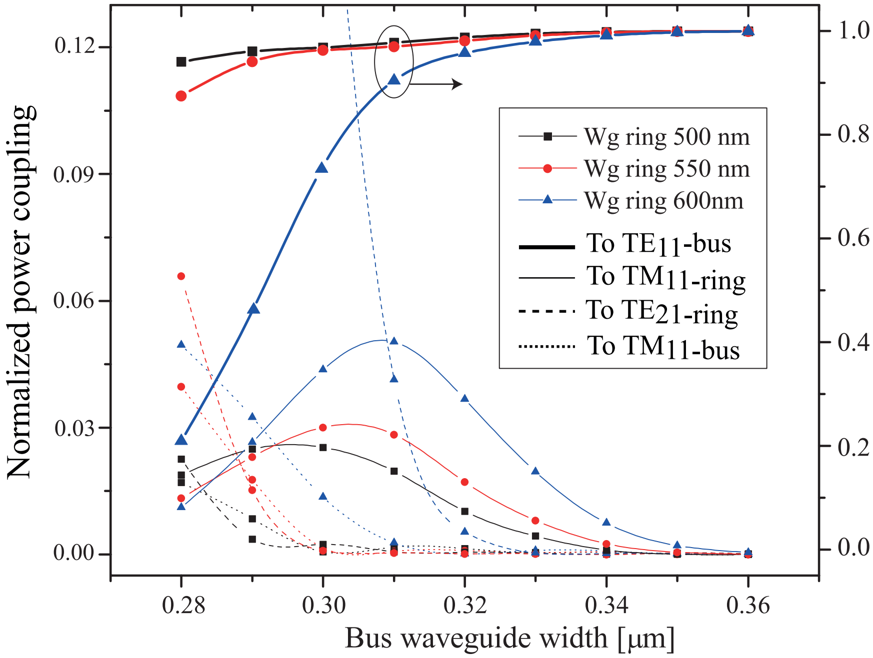

Figure 2.33: Power coupling from the TE$_{11}$ *bus mode towards the TM*$_{11}$ *and TE*$_{21}$ *ring mode and the TM*$_{11}$ *and the TE*$_{11}$ *bus mode as a function of varying bus width (*$300\,\mathrm{nm}$ *gap and* $30\,\mu\mathrm{m}$ *radius). Legend: the color and symbol of the curves explain the ring waveguide (wg) width and the line type explains to which mode the coupling occurs.*

isolated waveguide (Fig.2.31). Although the maximum power coupling occurs for a ring width of $0.6\,\mu\mathrm{m}$, this configuration also leads to the strong excitation of the leaky TE$_{21}$ ring mode and the leaky TM$_{11}$ bus mode. This can be prevented by selecting a wider bus waveguide width ($\geq 0.32\,\mu\mathrm{m}$) or a narrower ring waveguide width ($\leq 0.6\,\mu\mathrm{m}$).

The second condition to obtain a high Q-factor ring resonator is a low transition loss when the resonating TM$_{11}$ ring mode passes the directional coupler. Besides the expected (reciprocal) coupling from the TM$_{11}$ ring mode to the TE$_{11}$ bus mode, there is also coupling to the TM$_{11}$ bus mode and to the TE$_{21}$ ring mode which results in a transition loss. This is visualized in Fig.2.34a, where the power coupling to all these modes is plotted for an input TM$_{11}$ ring mode with a bus waveguide width of $320\,\mathrm{nm}$, $300\,\mathrm{nm}$ gap and a varying ring waveguide width between $0.5\,\mu\mathrm{m}$ and $0.6\,\mu\mathrm{m}$. From this figure one can deduce that the coupling towards the TM$_{11}$ bus mode becomes smaller using a wider ring waveguide, because of a higher phase mismatch with the $0.32\,\mu\mathrm{m}$ wide bus. On the other hand the coupling towards the TE$_{21}$ ring mode becomes larger when using a wider ring waveguide because of larger hybrid coupling as explained in Fig.2.31. The total

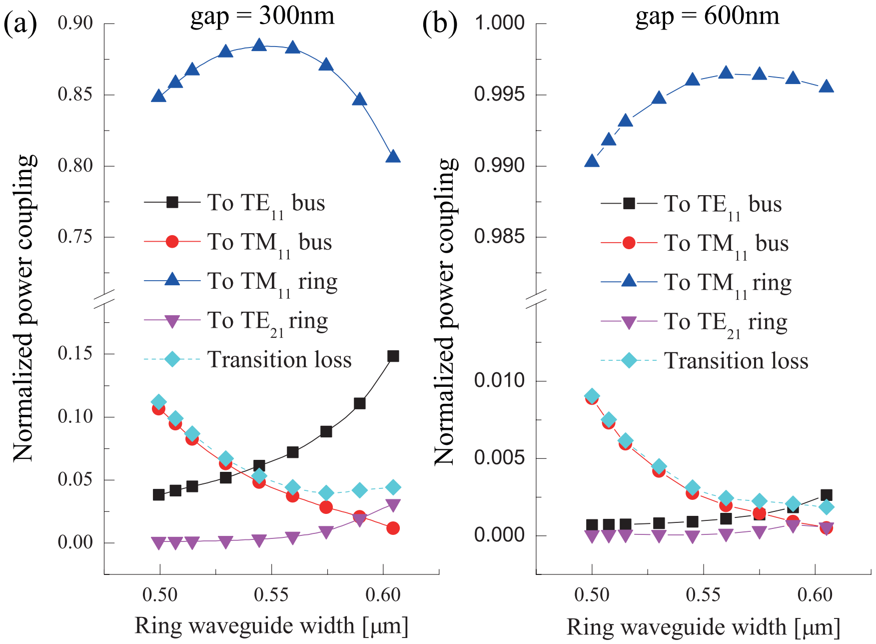

Figure 2.34: Power coupling in an asymmetric directional coupler from the TM$_{11}$ *ring mode (*$320\,\mathrm{nm}$ *bus width and* $30\,\mu\mathrm{m}$ *radius) for (a) gap* $300\,\mathrm{nm}$ *and (b) gap* $600\,\mathrm{nm}$*. For (a) the minimum transition loss occurs at a ring waveguide width of* $0.575\,\mu\mathrm{m}$ *which is a trade-off between the loss induced by phase mismatched coupling towards the TM*$_{11}$ *bus mode and the losses due to hybrid coupling towards the TE*$_{21}$ *ring mode.*

transition loss, defined as all the power that goes to another mode than the TE$_{11}$ bus mode and the TM$_{11}$ ring mode, is plotted in Fig. 2.34 as well, resulting in one optimum ring waveguide width around $0.575\,\mu\mathrm{m}$ for this configuration. For this width and gap the transition loss is $4.1\,\%$ which can be converted to a distributed loss of $9.6\,\mathrm{dB/cm}$ in a ring with $30\,\mu\mathrm{m}$ radius. Together with the waveguide propagation loss of $1.95\,\mathrm{dB/cm}$ [58], this ring resonator will have an intrinsic Q-factor of around 54300 or a critically coupled Q-factor of 27000. As it is clear from Fig.2.34a, the transition losses are relatively insensitive to a deviation in the ring width. The transition loss depends on the exact coupling from the bus to ring waveguide and can be improved by using a more adiabatic coupling section, e.g. a larger radius or a larger gap such as in Fig.2.34b where the transition loss is only $0.21\,\%$ for a gap of $600\,\mathrm{nm}$.

2.7.2 Experiments

The vertical asymmetry to create the hybrid coupling of the TM_{11} and TE_{21} mode is achieved using an air top-cladding. Both bus and ring waveguides were defined by a deep etch of $220\,\mathrm{nm}$. To facilitate the characterization of the device, grating couplers were added to the design using a $70\,\mathrm{nm}$ shallow etch step. These grating couplers are highly polarization dependent, with an extinction ratio of $50\,\mathrm{dB}$ and ensure only TE-polarized light is coupled in and out of the ring resonator. Light is guided with single-mode waveguides (width = $0.45\,\mu\mathrm{m}$) and tapered down to a width of $0.32\,\mu\mathrm{m}$ at the coupler of the AP ring resonator (radius of $30\,\mu\mathrm{m}$). Using s scanning electron microscope, the width of the ring waveguide is measured to be $0.56\,\mu\mathrm{m}$, which is slightly off the ideal waveguide width. A wavelength scan with $1\,\mathrm{pm}$ resolution is used to characterize the resonances between $1520\,\mathrm{nm}$ and $1540\,\mathrm{nm}$. The measured free spectral range (FSR) is $3.45\,\mathrm{nm}$ and corresponds to the resonating TM_{11} mode which has a lower group index ($n_g = 3.58$) than the TE_{11} mode ($n_g = 4.1$). Since all the resonances are very similar, their performance is reported as a mean value of the measured resonances. A critically coupled AP ring resonator with a mean extinction ratio of $-26.8 \pm 1.2\,\mathrm{dB}$, a mean Q-factor of 30858 ± 1836 and a mean finesse of 83 ± 5 is achieved using a $300\,\mathrm{nm}$ gap, which is plotted in Fig. 2.35a. This agrees well with the simulations. When the gap is increased to $600\,\mathrm{nm}$, the under coupled resonance shows a mean extinction ratio of $-2.1 \pm 0.2\,\mathrm{dB}$, a mean Q-factor of 124988 ± 9698 and a finesse of 335 ± 25.2 over the measured wavelength scan. This shows that the resonating mode has a lower effective propagation loss corresponding to a $1.32\,\%$ power transition loss as defined earlier (assumption of $1.95\,\mathrm{dB/cm}$ propagation loss). In Fig. 2.35b, an overlap of the resonances are plotted demonstrating the good uniformity.

2.7.3 Conclusion

A novel class of ring resonators is proposed which makes use of a polarization rotating asymmetrical directional coupling section. A critically coupled AP filter showing good performance was demonstrated. This ring resonator is expected to also be useful for a whole class of compact and high Q-factor applications, e.g. in large and accurate sensor arrays [64].

2.8 Conclusion

In this chapter we have given an overview of the state-of-the-art of the ring resonator. We have raised the problem of high reflection at resonance wavelength (RPR) next to the more generally known resonance splitting typically present in high-Q ring resonators. These two phenomena find their origin in the counter-directional coupling of the forward propagating light into backward propagating

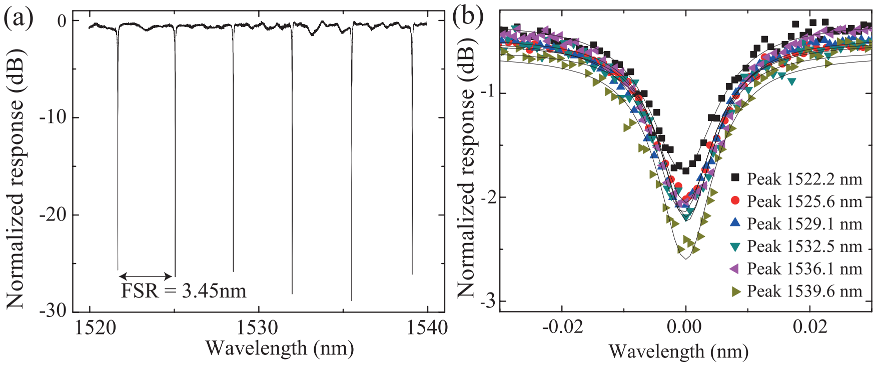

Figure 2.35: A TM$_{11}$ *resonating AP ring resonator (a) in the critically coupled regime with* $300\,\mathrm{nm}$ *gap (mean extinction ratio of* $-27\,\mathrm{dB}$ *and a mean Q-factor of* 31000*) and (b) in the under coupled regime with* $600\,\mathrm{nm}$ *gap (mean Q-factor of* 125000 *and a finesse of* 335*).*

modes due to overlap with the vertical sidewall roughness of strip waveguides. We have shown that this effect severely limits the performance of high-Q or narrowband ring resonators which are needed in this work, e.g. in chapter 4 as a ultra-dense WDM demultiplexer. Therefore, we came up with two new waveguide approaches with a smaller overlap with the vertical sidewall roughness. Both the TE-rib and the TM-strip approach were extensively characterized and optimized to significantly enhance the performance of standard TE-strip waveguides. The reduction in counter-directional coupling eliminates resonance splitting and lowers the high levels of reflected power with almost $10\,\mathrm{dB}$. Further we gave an overview of a typical ring resonator design flow and explained the design of higher-order ring resonators. These wide-band filters will extensively be used in chapter 5 and 6.

References

[1] B.E. Little, S.T. Chu, P.P. Absil, J.V. Hryniewicz, F.G. Johnson, F. Seiferth, D. Gill, V. Van, O. King, and M. Trakalo. *Very High-Order Microring Resonator Filters for WDM Applications*. IEEE Photonics Technology Letters, 16(10):2263–2265, October 2004.

[2] Fengnian Xia, Mike Rooks, Lidija Sekaric, and Yurii Vlasov. *Ultra-compact high order ring resonator filters using submicron silicon photonic wires for on-chip optical interconnects.* Optics express, 15(19):11934–41, September 2007.

[3] Sahnggi Park, Kap-Joong Kim, In-gyoo Kim, and Gyungock Kim. *Si microring MUX / DeMUX WDM filters*. Optics Express, 19(14):14627–14633, July 2011.

[4] M. Pantouvaki, M. Rakowski, P. Christie, P. Verheyen, G. Lepage, N. Van Hoovels, P. Absil, and J. Van Campenhout. *Comparison of Silicon Ring Modulators With Interdigitated and Lateral p-n Junctions*. IEEE Journal of Selected Topics in Quantum Electronics, 19(2):7900308–7900308, March 2013.

[5] Po Dong, Stefan F Preble, and Michal Lipson. *All-optical compact silicon comb switch.* Optics express, 15(15):9600–5, July 2007.

[6] Jaime Cardenas, Mark A Foster, Nicolás Sherwood-droz, Carl B Poitras, Hugo L, R Lira, Beibei Zhang, Alexander L Gaeta, Jacob B Khurgin, Paul Morton, and Michal Lipson. *Wide-bandwidth continuously tunable optical delay line using silicon microring resonators*. Optics Express, 18(25):26525–26534, 2010.

[7] Donald Adams, Greg Madejski, and Stefan Preble. *High-Q Shallow Etch Silicon Micro Resonators for Optical Delay*. In Photonics Conference (PHO), 2011 IEEE, volume 2, pages 871–872, 2011.

[8] K. De Vos, J. Girones, T. Claes, Y. De Koninck, S. Popelka, E. Schacht, R. Baets, and P. Bienstman. *Multiplexed Antibody Detection With an Ar-*

ray of Silicon-on-Insulator Microring Resonators. IEEE Photonics Journal, 1(4):225–235, October 2009.

[9] Muzammil Iqbal, Martin A Gleeson, Bradley Spaugh, Frank Tybor, William G Gunn, Michael Hochberg, Tom Baehr-jones, Ryan C Bailey, and L Cary Gunn. *Label-Free Biosensor Arrays Based on Silicon Scanning Instrumentation*. IEEE Journal of Selected Topics in Quantum Electronics, 16(3):654–661, 2010.

[10] Matthew Borselli. *High-Q Microresonators as Lasing Elements for Silicon Photonics*. PhD thesis, California Institute of Technology, 2006.

[11] J Van Campenhout, P Rojo Romeo, P Regreny, C Seassal, D Van Thourhout, S Verstuyft, L Di Cioccio, J-M Fedeli, C Lagahe, and R Baets. *Electrically pumped InP-based microdisk lasers integrated with a nanophotonic silicon-on-insulator waveguide circuit.* Optics express, 15(11):6744–9, May 2007.

[12] Alexander W Fang, Richard Jones, Hyundai Park, Oded Cohen, Omri Raday, Mario J Paniccia, and John E Bowers. *Integrated AlGaInAs-silicon evanescent race track laser and photodetector.* Optics express, 15(5):2315–22, March 2007.

[13] Thomas Van Vaerenbergh, Martin Fiers, Pauline Mechet, Thijs Spuesens, Rajesh Kumar, Geert Morthier, Joni Dambre, and Peter Bienstman. *Cascadable excitability in microrings*. Optics express, 20(18):18438–18452, 2012.

[14] John Heebner, Rohit Grover, and Tarek A. Ibrahim. *Optical Microresonators: Theory, Fabrication and applications*. Springer, 2008.

[15] Marco Masi, Régis Orobtchouk, Guofang Fan, Jean-marc Fedeli, and Lorenzo Pavesi. *Towards a Realistic Modelling of Ultra-Compact Racetrack Resonators*. Journal of Lightwave Technology, 28(22):3233–3242, 2010.

[16] W. Bogaerts, P. De Heyn, T. Van Vaerenbergh, K. De Vos, S. Kumar Selvaraja, T. Claes, P. Dumon, P. Bienstman, D. Van Thourhout, and R. Baets. *Silicon Microring Resonators*. Laser & Photonics Reviews, 6(1):47–73, 2012.

[17] B.E. Little, S.T. Chu, H.a. Haus, J. Foresi, and J.-P. Laine. *Microring resonator channel dropping filters*. Journal of Lightwave Technology, 15(6):998–1005, June 1997.

[18] C. Manolatou, M.J. Khan, S. Fan, P.R. Villeneuve, H.a. Haus, and J.D. Joannopoulos. *Coupling of modes analysis of resonant channel add-drop filters*. IEEE Journal of Quantum Electronics, 35(9):1322–1331, 1999.

[19] Jan Niehusmann, Andreas Vörckel, Peter Haring Bolivar, Thorsten Wahlbrink, and Wolfgang Henschel. *Ultrahigh-quality-factor silicon-on-insulator microring resonator*. Optics Letters, 29(24):2861–2863, 2004.

[20] Suresh Sridaran and Sunil a Bhave. *Nanophotonic devices on thin buried oxide Silicon-On-Insulator substrates.* Optics express, 18(4):3850–7, February 2010.

[21] Shijun Xiao, Maroof H Khan, Hao Shen, and Minghao Qi. *Modeling and measurement of losses in silicon-on-insulator resonators and bends.* Optics express, 15(17):10553–61, August 2007.

[22] Miloš A Popovic, Christina Manolatou, and Michael R Watts. *Coupling-induced resonance frequency shifts in coupled dielectric multi-cavity filters*. Optics express, 14(3), 2006.

[23] T J Kippenberg, S M Spillane, and K J Vahala. *Modal coupling in traveling-wave resonators.* Optics letters, 27(19):1669–71, October 2002.

[24] Jií Čtyroký, Ivan Richter, and Milan Šior. *Dual resonance in a waveguide-coupled ring microresonator*. Optical and Quantum Electronics, 38(9-11):781–797, January 2007.

[25] B E Little, J P Laine, and S T Chu. *Surface-roughness-induced contradirectional coupling in ring and disk resonators.* Optics letters, 22(1):4–6, January 1997.

[26] Matthew Borselli, Thomas Johnson, and Oskar Painter. *Beyond the Rayleigh scattering limit in high-Q silicon microdisks: theory and experiment.* Optics express, 13(5):1515–30, March 2005.

[27] F. Morichetti, a. Canciamilla, M. Martinelli, a. Samarelli, R. M. De La Rue, M. Sorel, and a. Melloni. *Coherent backscattering in optical microring resonators*. Applied Physics Letters, 96(8):081112, 2010.

[28] F Morichetti, A Canciamilla, C Ferrari, A. Melloni, D E E Dipartimento, and Politecnico Bari. *Backscattering in silicon photonic devices*. In CIO, pages 5–6, 2010.

[29] Francesco Morichetti, Antonio Canciamilla, Carlo Ferrari, Mario Martinelli, and Andrea Melloni. *Backscattering in silicon photonic waveguides and circuits*. In Proc. SPIE, volume 7943, pages 79430J–79430J–8, 2011.

[30] B.E. E Little and S.T. T Chu. *Estimating surface-roughness loss and output coupling in microdisk resonators.* Optics letters, 21(17):1390–2, September 1996.

[31] Francesco Morichetti, Antonio Canciamilla, and Andrea Melloni. *Statistics of backscattering in optical waveguides.* Optics letters, 35(11):1777–9, June 2010.

[32] Yurii Vlasov and Sharee McNab. *Losses in single-mode silicon-on-insulator strip waveguides and bends.* Optics express, 12(8):1622–31, April 2004.

[33] M Notomi, a Shinya, S Mitsugi, E Kuramochi, and H Ryu. *Waveguides, resonators and their coupled elements in photonic crystal slabs.* Optics express, 12(8):1551–61, April 2004.

[34] Wim Bogaerts, Vincent Wiaux, Dirk Taillaert, Stephan Beckx, Bert Luyssaert, Peter Bienstman, and Roel Baets. *Fabrication of Photonic Crystals in Silicon-on- Insulator Using 248-nm Deep UV Lithography*. IEEE Journal of Selected Topics in Quantum Electronics, 8(4):928–934, 2002.

[35] Wim Bogaerts, Pieter Dumon, Dries Van Thourhout, Dirk Taillaert, Patrick Jaenen, Johan Wouters, Stephan Beckx, Vincent Wiaux, and Roel Baets. *Compact Wavelength-Selective Functions in Silicon-on-Insulator Photonic Wires.* IEEE Journal of Selected Topics in Quantum Electronics, 12(6):1394–1401, 2006.

[36] Shankar Kumar Selvaraja, Patrick Jaenen, Wim Bogaerts, Dries Van Thourhout, Pieter Dumon, and Roel Baets. *Fabrication of Photonic Wire and Crystal Circuits in Silicon-on-Insulator Using 193nm Optical Lithography*. Journal of Lightwave Technology, 27(18):4076–4083, 2009.

[37] Shankar Kumar Selvaraja, Wim Bogaerts, Philippe Absil, Dries Van Thourhout, and Roel Baets. *Record Low-Loss Hybrid Rib / Wire Waveguides for Silicon Photonic Circuits*. In Group IV Photonics (GFP), 2010.

[38] Shankar Kumar Selvaraja, Peter De Heyn, Gustaf Winroth, Patrick Ong, Guy Lepage, Celine Cailler, Arnaud Rigny, Konstantin K Bourdelle, Wim Bogaerts, Dries Van Thourhout, and Joris Van Campenhout. *Highly uniform and low-loss passive silicon photonics devices using a 300mm CMOS platform*. In The Optical Fiber Communication Conference and Exposition (OFC) and The National Fiber Optic Engineers Conference (NFOEC) 2014, number 1, pages 3–5, 2014.

[39] Wim Bogaerts, Roel Baets, Pieter Dumon, Vincent Wiaux, Stephan Beckx, Dirk Taillaert, Bert Luyssaert, Joris Van Campenhout, Peter Bienstman, and Dries Van Thourhout. *Nanophotonic Waveguides in Silicon-on-Insulator Fabricated With CMOS Technology*. Journal of Lightwave Technology, 23(1):401–412, 2005.

[40] Pieter Dumon. *Ultra-Compact Integrated Optical Filters in Silicon-on-insulator by Means of Wafer-Scale Technology*. PhD thesis, Ghent University, 2007.

[41] Shankar Kumar Selvaraja. *Wafer-scale Fabrication Technology for silicon Photonic integrated Circuits*. PhD thesis, Ghent University, 2011.

[42] T. Barwicz and H.a. Haus. *Three-dimensional analysis of scattering losses due to sidewall roughness in microphotonic waveguides*. Journal of Lightwave Technology, 23(9):2719–2732, September 2005.

[43] Shankar Kumar Selvaraja, Wim Bogaerts, and Dries Van Thourhout. *Loss reduction in silicon nanophotonic waveguide micro-bends through etch profile improvement*. Optics Communications, 284(8):2141–2144, April 2011.

[44] Zhen Sheng, Daoxin Dai, and Sailing He. *Comparative Study of Losses in Ultrasharp Silicon-on-Insulator Nanowire Bends*. IEEE Journal of Selected Topics in Quantum Electronics, 15(5):1406–1412, 2009.

[45] V Van, Philippe P Absil, J V Hryniewicz, and P Ho. *Propagation Loss in Single-Mode GaAs AlGaAs Microring Resonators : Measurement and Model*. Journal of Lightwave Technology, 19(11):1734–1739, 2001.

[46] Shijun Xiao, Maroof H Khan, Hao Shen, Minghao Qi, and Main Campus. *Compact silicon microring resonators with ultra-low propagation loss in the C band.* Optics express, 15(22):14467–75, October 2007.

[47] Fengnian Xia, Lidija Sekaric, and Yurii a Vlasov. *Mode conversion losses in silicon-on-insulator photonic wire based racetrack resonators.* Optics express, 14(9):3872–86, May 2006.

[48] Chih-Wei Tseng, Chih-Wei Tsai, Kaung-Cheng Lin, Ming-Chang Lee, and Yung-Jui Chen. *Study of coupling loss on strongly-coupled, ultra compact microring resonators.* Optics express, 21(6):7250–7, March 2013.

[49] Michele Moresco, Marco Romagnoli, Stefano Boscolo, Michele Midrio, Matteo Cherchi, Ehsan Shah Hosseini, Douglas Coolbaugh, Michael R Watts, and Birendra Dutt. *Method for characterization of Si waveguide propagation loss.* Optics express, 21(5):5391–400, March 2013.

[50] J H Schmid, a Delâge, B Lamontagne, J Lapointe, S Janz, P Cheben, a Densmore, P Waldron, D-X Xu, and K P Yap. *Interference effect in scattering loss of high-index-contrast planar waveguides caused by boundary reflections.* Optics letters, 33(13):1479–81, July 2008.

[51] Francesco Morichetti, Andrea Melloni, and Mario Martinelli. *Effects of Polarization Rotation in Optical Ring-Resonator-Based Devices*. Journal of Lightwave Technology, 24(1):573–585, 2006.

[52] B.E. Little and S.T. Chu. *Theory of polarization rotation and conversion in vertically coupled microresonators*. IEEE Photonics Technology Letters, 12(4):401–403, April 2000.

[53] Tymon Barwicz, Miloš a. Popović, Fuwan Gan, Marcus S. Dahlem, Charles W. Holzwarth, Peter T. Rakich, Erich P. Ippen, Franz X. Kärtner, and Henry I. Smith. *Reconfigurable silicon photonic circuits for telecommunication applications*. In Alexis V. Kudryashov, Alan H. Paxton, and Vladimir S. Ilchenko, editors, Laser Resonators and Beam Control X, volume 6872, pages 68720Z–68720Z–12, February 2008.

[54] Miloš A Popović, Tymon Barwicz, Fuwan Gan, Marcus S Dahlem, Charles W Holzwarth, Peter T Rakich, Henry I Smith, Erich P Ippen, Franz X Kärtner, and Miloš A Popovi. *Transparent wavelength switching of resonant filters*. In CLEO, number c, pages 30–31, 2007.

[55] Sylvain Maine, Delphine Marris-morini, Laurent Vivien, Eric Cassan, Daniel Pascal, Suzanne Laval, Régis Orobtchouk, Bing Han, Taha Benyattou, Loubna El Melhaoui, and Jean-marc Fédéli. *High Q -Factor Microrings Using Slightly Etched Rib Waveguides*. Journal of Lightwave Technology, 27(10):1387–1391, 2009.

[56] Isa Kiyat, Atilla Aydinli, and Nadir Dagli. *High-Q silicon-on-insulator optical rib waveguide racetrack resonators.* Optics express, 13(6):1900–5, March 2005.

[57] Peter De Heyn, Diedrik Vermeulen, Thomas Van Vaerenbergh, Bart Kuyken, and Dries Van Thourhout. *Ultra-high Q and finesse all-pass microring resonators on Silicon-on-Insulator using rib waveguides*. In Proceedings of the 16th European Conference on Integrated Optics and Technical Exhibition (ECIO 2012), pages 1–2, 2012.

[58] P De Heyn, B Kuyken, D Vermeulen, W Bogaerts, and D Van Thourhout. *High-Performance Low-Loss Silicon-on-Insulator Microring Resonators using TM-polarized Light*. In The Optical Fiber Communication Conference and Exposition (OFC) and The National Fiber Optic Engineers Conference (NFOEC) 2011, page OThV, 2011.

[59] Fengnian Xia, Lidija Sekaric, Martin OBoyle, and Yurii Vlasov. *Coupled resonator optical waveguides based on silicon-on-insulator photonic wires*. Applied Physics Letters, 89(4):041122, 2006.

[60] Liu Liu, Yunhong Ding, Kresten Yvind, and Jørn M Hvam. *Silicon-on-insulator polarization splitting and rotating device for polarization diversity circuits*. Optics Express, 19(13):12646–12651, 2011.

[61] Daoxin Dai and John E Bowers. *Novel concept for ultracompact polarization splitter-rotator based on silicon nanowires.* Optics express, 19(11):10940–9, May 2011.

[62] K. Mertens, B. Scholl, and H.J. Schmitt. *New highly efficient polarization converters based on hybrid supermodes*. Journal of Lightwave Technology, 13(10):2087–2092, 1995.

[63] P. De Heyn, D. Vermeulen, D. Van Thourhout, and G. Roelkens. *Silicon-on-Insulator All-Pass Microring Resonators Using a Polarization Rotating Coupling Section*. Photonics Technology Letters, IEEE, 24(14):1176–1178, 2012.

[64] J-W. Hoste, S. Werquin, T. Claes, and P. Bienstman. *Conformational analysis of proteins with a dual polarisation silicon microring*. Optics Express, 22(3):2807, January 2014.

3

High-Performance Photodiodes Integrated on Silicon

In this chapter the goal is to fabricate a photodiode that can be integrated on a Si platform and detects high-speed signals between $10-40\,\mathrm{Gb/s}$ around $1550\,\mathrm{nm}$ as efficient as possible. As discussed in the introduction chapter, two attractive materials are available that can be integrated on silicon. First, the III-V compound semiconductors such as indium gallium arsenide (InGaAs), typically epitaxially grown on an InP wafer. By means of a heterogeneously die-to-die or die-to-wafer bonding technique, small areas of III-V material are integrated on top of a Si waveguide platform. An alternative for InGaAs is germanium (Ge) which can be monolithically grown on Si. In this chapter we will discuss both types of photodiodes regarding design, fabrication and characterization. The InGaAs p-i-n photodiodes are designed to be integrated with an in-band label extractor to convert the incoming label to the electrical domain as we will discuss in chapter 4. The Ge p-i-n photodiodes are to be integrated with the DWDM data demultiplexer terminating each WDM data channel as we will discuss in chapter 5 and 6.

We start this chapter by explaining the basic properties and design goals in section 3.1. The rest of the chapter is devoted to the design, fabrication and characterization of the evanescently-coupled InGaAs p-i-n photodiode in section 3.2 and the characterization of the butt-coupled Ge photodiodes in section 3.3.

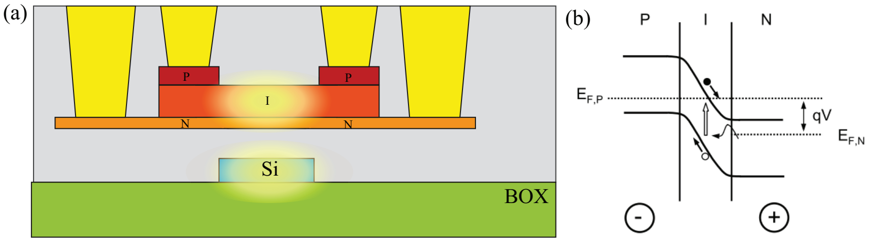

Figure 3.1: (a) The schematic cross-section of an evanescently coupled p-i-n photodiode heterogeneously integrated on a Si waveguide and (b) the band diagram of negative biased p-i-n.

3.1 Introduction and design goals

Most fundamental properties of photodiodes are extensively discussed in various text books (e.g. [1–4]). The concepts that are needed to describe the design goals and to understand the behaviour of photodiodes are briefly summarized in the following section.

3.1.1 Working principle

A schematic view of a heterogeneously-integrated photodiode on top of a Si waveguide is shown in Fig.3.1(a). This photodiode structure consists of thin epitaxially-grown layers of different lattice-matched III-V materials to form a so-called heterojunction. The intrinsically (i) doped absorbing layer is sandwiched between $p+$ and a $n-$ doped layers to form a vertical p-i-n junction. This intrinsic layer is depleted and a created electron-hole pair will be separated and drift towards the undepleted (doped) regions due to the internal electric field. The internal electric field can be increased by an externally applied voltage with an amount of qV: the so-called bias. This bias is causing the Fermi levels E_f to split and the excited carriers are now accelerated even more. This extra drift is necessary if one requires a fast responding photodiode. The working principle is shown in Fig.3.1(b). The mode propagating in the Si waveguide is evanescently coupled to the absorbing photodiode mode. A supermode of this coupled mode system demonstrating this coupling is superimposed on top of the schematic in Fig.3.1.

3.1.2 Own contributions

The two types of photodiodes (III-V and Ge) are discussed separately and use a slightly different design approach. In the following we give an overview of the contributed work.

InGaAs p-i-n photodiodes Both design and fabrication approach are based on earlier research work from colleagues Joost Brouckaert and Zhen Sheng. Their main contributions are summarized in [3, 5] and [6]. In [6], an evanescently coupled p-i-n photodiode with a responsivity of $1.1\,\mathrm{A/W}$ using the quasi-TE polarized mode is demonstrated. The dark current is around $50\,\mathrm{pA}$ for a reverse voltage of $3-5\,\mathrm{V}$. However, no results are given on the bandwidth of the device. In this work, the InGaAs p-i-n photodiode is optimized to be highly responsive and have a large bandwidth at the same time. The target was to reach a responsivity of $1\,\mathrm{A/W}$ and a bandwidth $> 10\,\mathrm{GHz}$. Furthermore, a low dark current and a good manufacturability is required. This photodiode is fabricated in the cleanroom of the photonics research group by means of a die-to-die heterogeneous BCB bonding technique [5, 7]. Own contributions are included in the optimization of the design, fabrication and high-speed characterization. The results are discussed in section 3.2.

Ge p-i-n photodiodes The design of the Ge p-i-n photodiode has been done by Joris Van Campenhout working at imec. This component has been fully fabricated in the $200\,\mathrm{mm}$ pilot line of imec [8]. Own contributions around this component are limited to characterization. This characterization gave some valuable feedback to improve the photodiode design among different generations. The results are discussed in section 3.3.

3.1.3 High responsivity

To enable a highly responsive photodiode, one needs a material that can absorb light efficiently at a given wavelength. In Fig.3.2, the wavelength dependency of this absorption coefficient is given. Materials with band gap wider than the energy of the photons are transparent (such as Si and InP) and no absorption occurs. InGaAs and Ge have a large absorption coefficient α of respectively $7820\,\mu\mathrm{m}^{-1}$ and $9000\,\mu\mathrm{m}^{-1}$ at $1550\,\mathrm{nm}$ [9]. For a certain photon energy per time unit incident on the absorbing layer (optical power P), there are $\frac{P}{E_p}$ photons with E_p the energy of a photon that can create an electron-hole pair. This process has an efficiency η. Each successful created and extracted electron-hole pair has the elementary charge q. The current flowing (electron charge q per time unit) is then described in Eq.3.1 in function of the optical input power P.

$$I = \frac{dQ}{dt} = \frac{\eta q \#\mathrm{photons}}{dt} = \eta q \frac{P}{E_p} = \eta \frac{\lambda q}{hc} P \tag{3.1}$$

The responsvity R is defined by Eq.3.2.

$$R = \frac{I}{P} = \eta \frac{\lambda q}{hc} \tag{3.2}$$

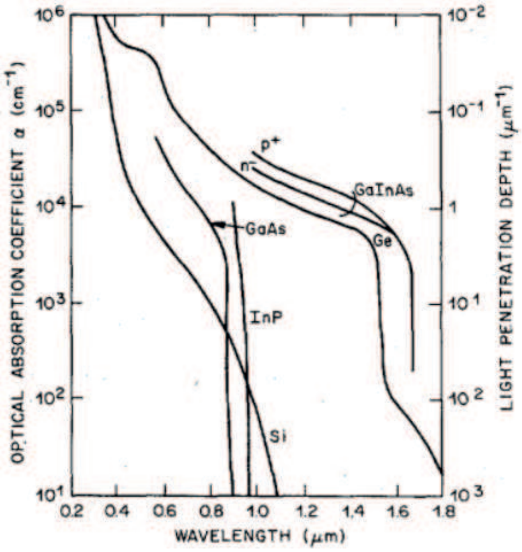

Figure 3.2: Dependence of absorption coefficient on wavelength for several materials, figure taken from [1]

Maximizing the efficiency η will hence maximize the responsivity. The maximum value of the responsivity (with $\eta = 1$) around $1550\,\mathrm{nm}$ is $1.25\,\mathrm{A/W}$. Using an evanescently coupled photodiode, the design optimization includes mainly the reduction of the mode overlap with the non-contributing absorption of the metal contacts and avoid carrier recombination in the undepleted regions.

3.1.4 Large bandwidth

Once created, each charge carrier needs to reach the metal contacts as fast as possible. The major limitations on the speed of a p-i-n photodiode is according to Bowers et.al. [1]:

1. The time it takes a carrier to drift across the depletion region
2. The time it takes carriers to diffuse out of undepleted regions
3. The time it takes to charge and discharge the inherent capacitance of the diode plus any parasitic capacitance
4. Charge trapping at heterojunctions.

The transit time of the depletion region is depending on the drift velocity of the carriers. This drift velocity is saturated when the electric field over the depletion thickness (t_i) is high enough. This requires the full depletion of the intrinsic layer by highly doped p and n-regions and possibly a reverse bias over the junction. This reverse bias determines the depletion thickness where as the intrinsic thickness (d_i) is determined by design and fabrication. One can then approximate the transit-time limited bandwidth as follows [4]:

$$f_t \approx \frac{3.5\overline{v}}{2\pi t_i} \tag{3.3}$$

with $\overline{v}$ the average carrier velocity. For InGaAs, values of $6.5 \times 10^6\,\mathrm{cm/s}$ and $4.8 \times 10^6\,\mathrm{cm/s}$ for respectively electron and holes have been reported in [10]. In Ge the electrons and holes have respectively a speed of 6 and $3 \times 10^6\,\mathrm{cm/s}$. The thinner the intrinsic thickness, the faster the transit time but the larger the capacitance (C_{pd}).

This capacitance determines the time it takes to charge and discharge the diode. The capacitance is formed between the two undepleted regions of the p-i-n diode. The magnitude of C_{pd} is calculated by

$$C_{pd} = \frac{k\epsilon_0 A}{t_i} \tag{3.4}$$

k the dielectric constant and ϵ_0 the free-space permittivity ($8.85 \times 10^{-12} F/m$). The dielectric constant k is for InGaAs 14.1 and for Ge 11.9. Typical values for the capacitance are between $10 - 500\,\mathrm{fF}$. The bandwidth limitation originating from this capacitance is inversely proportional to the RC product as follows:

$$f_{RC} = \frac{1}{2\pi R C_{pd}} \tag{3.5}$$

The resistance includes the metal/semiconductor interface as well as the $50\,\Omega$ load resistance.

Once the carriers drift in an undepleted region, the carriers are diffusing to the metal contacts. Typically this diffusion is fast in highly doped regions. Due to their large effective mass, *heavy* holes tend to be trapped at each heterojunction, especially at the InGaAs/InP junction [1]. The last two effects will not be taken into account because they contribution is negligible and the total bandwidth is then determined by the RC bandwidth (f_{RC}) and the transit bandwidth (f_t):

$$f_{3dB} \approx \sqrt{\frac{1}{\frac{1}{f_t^2} + \frac{1}{f_{RC}^2}}} \tag{3.6}$$

One says that a bandwidth of a photodiode is RC-limited if either R or C is so large that the transit time becomes less important. Typically this happens for photodiodes with a very thin depletion region where the transit time is very short. In the case of a thick depletion region, the bandwidth of the photodiode is said to be transit-time limited.

3.1.5 High sensitivity

In the absence of light the photodiode's dark or leakage current dominates. Generally, several effects contribute to the dark current with their actual magnitudes depending on the bias voltage, material properties, temperature and detector design. In summary, the dominant contributions are generation-recombination current in the depleted region, diffusion current from the undepleted p and n sides of the junction, tunneling current and surface leakage [1]. Depending on the structure and passivation technique, leakage current in the tens of picoamperes range has been achieved. In practice it is usually the fabrication quality that determines the dark current. If not well optimized, dark current values can reach easily several microamperes.

Dark current increases the total noise of the photodiode since both photocurrent (I_{pd}) and dark current (i_d) generates shot noise due to the statistical nature of the carrier transport and photon detection process. The mean square noise current originating from shot noise is given by

$$\langle i^2_{\text{shot}} \rangle = 2q(I_{pd} + I_d)\Delta f \tag{3.7}$$

with q the elementary charge and Δf the system's bandwidth. Together with the thermal noise (independent of the dark current and photocurrent), dark current degrades the signal-to-noise ratio (SNR). The thermal noise is depending on the temperature T and the (load) resistance R as

$$\langle i^2_{\text{th}} \rangle = \frac{4k_bT}{R}\Delta f \tag{3.8}$$

with k_b the Boltzmann constant. The maximum allowed level of dark current is depending on the required signal-to-noise ratio, limitations on the input power and the system's bandwidth.

$$\text{SNR} = \frac{I^2_{pd}}{\langle i^2_{\text{shot}} \rangle + \langle i^2_{\text{th}} \rangle} \tag{3.9}$$

3.1.6 Photodiode integration on Si

Three approaches are available to integrate photodiodes on a silicon platform: hybrid integration, epitaxial growth and bonding. One can find an extensive overview in [3]. In Fig.3.3, an overview of these three approaches is shown. Using the hybrid integration platform, a prefabricated photodiode is positioned above the silicon platform using a flip-chip technique. The attachment is provided by metal bumps. Hybrid integration is considered as a very matured process but is not suitable for large scale integration. The vertical coupling can be assisted by a grating coupler as shown in Fig.3.3 or a tilted mirror [11]. The design of the photodiode is optimized for vertical illumination.

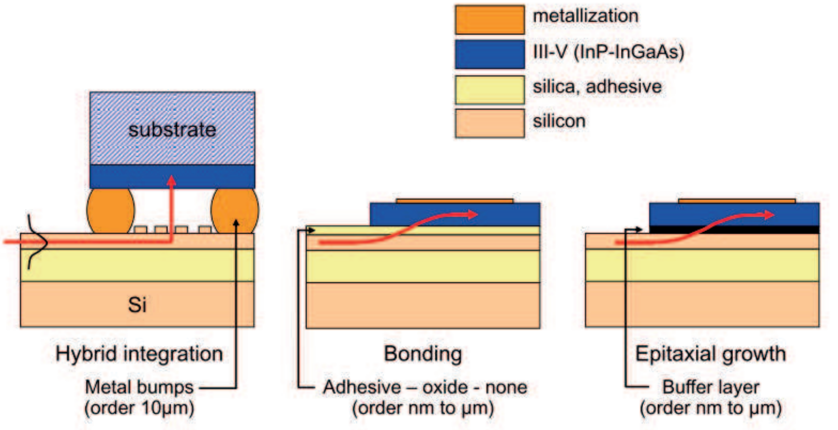

Figure 3.3: Three approaches for heterogeneous integration. From left to right - hybrid integration, bonding and epitaxial growth. Taken from [3]

A second approach is the direct epitaxial growth of InGaAs or Ge material on top of silicon. Typically the quality of the material is degraded due to the large lattice constant mismatch (around 7% for InGaAs-on-Si [3] and 4% for Ge-on-Si [12]). The direct growth of III-V material on top of Si has been limited to very small areas but recently progress has been shown in low-dark current selectively grown InGaAs photodiodes on Si [13]. More commonly, high-yield high-quality selectively grown Ge photodiodes on silicon are reported.

A third approach is die-to-wafer bonding as introduced earlier. Unprocessed III-V dies with the epitaxial layers facing down to the silicon are bonded very close to the waveguide. Most bonding techniques are based on direct bonding or adhesive bonding. In this work we use BCB (benzocyclobutene) as the bonding agent, a technique that has been developed in our own research group [14]. This process has the advantage that the material is not degraded and devices with the same performance as monolithically integrated photodiodes can be reached. Compared to hybrid integration, a much larger density can be reached using a bonding technique since lithographic techniques can be used to define the photodiodes after the bonding. Using a bonding technique, evanescent coupling is typically used to couple the light from the silicon waveguides into the absorption layer. We will use this approach to integrate InGaAs photodiodes on the silicon platform.

3.2 Evanescently-coupled InGaAs p-i-n photodiode

In this section we discuss the design, simulation and fabrication of an evanescently-coupled InGaAs photodiode. The design and simulation approach is generic and

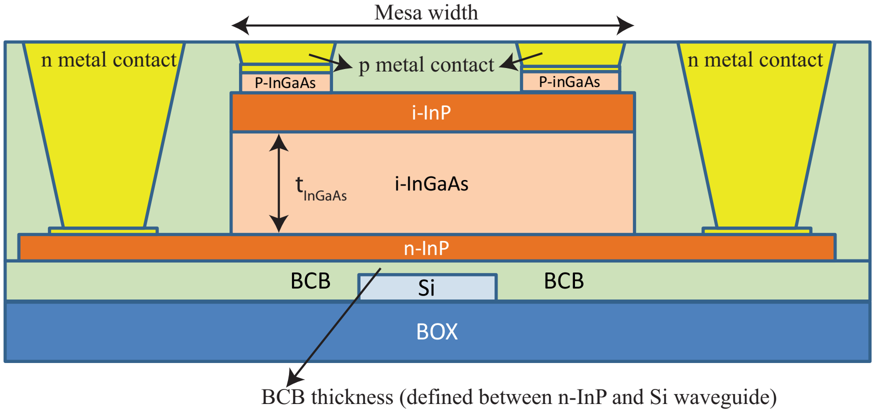

Figure 3.4: Schematic cross section of the evanescently-coupled photodetector (drawing not on scale).

can be used for other epitaxial material as well, e.g. using GaInAsSb as an absorption layer to be used at longer wavelengths ($2-2.5\ \mu$m) [15]. We start this section with the design overview and design parameters. Later, the simulation approach is discussed to optimize the bandwidth and responsivity. Then, the fabrication process is described. At the end of this section, the characterization and results are discussed.

3.2.1 Design

The schematic cross section of the proposed evanescenlty-coupled p-i-n photodiode is shown in Fig.3.4. It consist of an intrinsic InGaAs layer which is responsible for the absorption of the incoming light. The thickness of this absorption layer (t_{InGaAs}) is the most important parameter that determines the bandwidth and the responsivity as we will discuss later. To create a potential difference in this intrinsic layer, enabling the extraction of excited carriers, this layer must be sandwiched between a p-doped and a n-doped semiconductor layer. To form the mesa, and hence to enable contacting the n-layer from the top, an thin indium phosphide (InP) layer is used as the n-doped bottom layer. Using InP, we can use selective etching of InGaAs. For the top layer, a highly p-doped InGaAs layer is chosen to foresee an ohmic contact. As discussed in [6], an extra InP layer can be added between the intrinsic absorption layer and the p-doped InGaAs layer. This extra layer with a lower n_{eff} is used to decrease the mode overlap with the metal contacts and the non-contributing absorption in the p-doped InGaAs layers. Hence, this layer increases the efficiency η. Another measure to decrease the undesired absorption of the p-metal contacts is to split these contacts to the side of the photodiode. This configuration is referred to as a helmet configuration [6]. Note that by

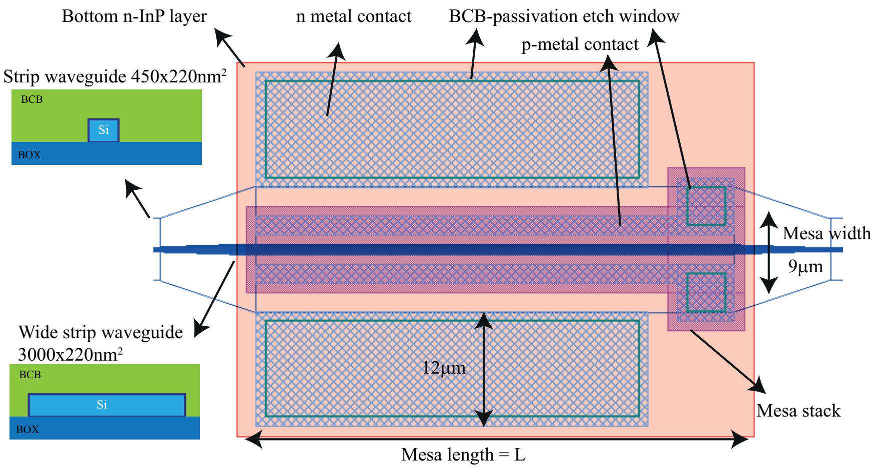

Figure 3.5: Top view of the proposed evanescently-coupled InGaAs photodetector.

splitting these p-contacts, the p-metal contact area is decreased. If the photodiode is RC-limited instead of transit-time limited, the increased series resistance causes the bandwidth to decrease.

In Fig.3.5 a top view of the proposed photodiode design is shown. First the strip waveguide ($450 \times 220\,\mathrm{nm}^2$) is adiabatically tapered to a broader waveguide ($1 - 3\,\mu\mathrm{m} \times 220\,\mathrm{nm}$). The width of this waveguide can be optimized and is an important parameter to excite the right mode in the photodiode as discussed later. Also the width of the detector mesa is relevant since it determines the capacitance. The spacing between the two p-metal contacts above the mesa is important to lower the overlap of the detector mode. On the other hand, using contact lithography, the minimum width of the p-metal contacts is $2\,\mu\mathrm{m}$ to ensure a well-defined lithography. In this work, the spacing is minimum $3\,\mu\mathrm{m}$. At the edges of the mesa another $1\,\mu\mathrm{m}$ offset is used to relax the alignment during lithography. This brings the total minimum width of the mesa to $9\,\mu\mathrm{m}$.

Also the length of the photodiode has an influence on the capacitance C as well as on the series resistance R. The longer the photodiode, the larger the contact area and thus the smaller the contact resistance. On the other hand, the longer the photodiode, the larger the capacitance. If the p-contact resistance is much larger than the load resistance and the n-contact resistance (which is typically the case), the RC product stays constant for a change in photodiode length. In the case of a small contact p-contact resistance, the shorter the detector length, the smaller the RC product. The length is of course also related to the desired responsivity and the attainable coupling strength. The longer the detector, the larger the responsivity (until all the light is absorbed). Hence, a strong coupling strength between the Si waveguide and the photodiode is necessary to limit the mesa length (L). At the end of the photodiode the mesa is broadened such that there is enough area to foresee a BCB opening (see fabrication).

3.2.2 Simulation

In this section an overview is given on how to optimize the photodiode design parameters for a high responsivity and a large bandwidth. The most important design parameters are

- $\mathbf{t}_{InGaAs}$: The thickness of the intrinsic layer
- $\mathbf{W}_{mesa}$: The width of the photodiode mesa
- $\mathbf{W}_{wg}$: The width of the silicon waveguide
- **L**: The mesa length

Optimizing the responsivity and the bandwidth at the same time is translated into a fast (small L) and efficient (high η) absorption and an optimized RC- and transit bandwidth (t_{InGaAs}). All height and width parameters are influencing the detector modes. Since the photodiode mesa has a rather large cross-section ($\approx 9 \times 1 \mu\mathrm{m}^2$), tens of modes can be excited, with each a different absorption coefficient (different overlap with the InGaAs layer) and efficiency (different overlap with the metal and the p-InGaAs layer).

2D simulation To gain insight in the absorption coefficient and efficiency of each mode, a (complex) 2D-mode solver is used to generate all the modes of the photodiode mesa. The modes are named based on their horizontal and vertical electric field lobes. E.g. TE 1-2, is the TE-polarized mode with one horizontal electric field lobe and two vertical electric field lobes. In Fig.3.6, three modes of the photodiode mesa are plot. In Fig.3.6, the simulation grid is shown with the i-InGaAs, n-InP and i-InP layers all $100\,\mathrm{nm}$ and the width of the mesa equal to $10\,\mu\mathrm{m}$. In Fig.3.6(b) the resulting fundamental detector mode (TE 1-1) is shown and in Fig.3.6(c) and (d) respectively the first and second order TE mode (TE 2-1 and TE 3-1). Note that there is no Si waveguide underneath the photodiode in this simulation. From this figure it can be seen that the mode overlap with the p-metal contacts (shown as white rectangles) is the smallest for TE 1-1. Both higher-order modes have an increased mode overlap with the p-metal contacts and will exhibit a smaller absorption efficiency η compared to TE 1-1. Also note that by placing the Si waveguide underneath the center (and not at the border) of the photodiode, the coupling strength between the fundamental TE-strip mode to the first order mode will be the minimized. This can be understood by noting that the TE 2-1 has a zero

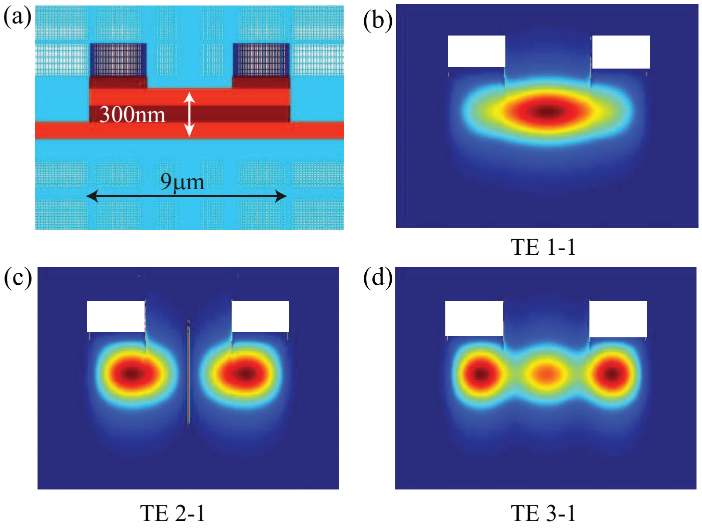

Figure 3.6: 2D mode simulation of the detector mesa modes (a) simulation grid (b) the fundamental TE mode (TE 1-1) (c) and (d) the horizontally first-order mesa mode (TE 2-1) and third -order mode (TE 3-1). The white rectangles are representing the metal contacts.

in the middle of the detector mesa and hence no mode overlap is present between these two modes. In other words, we need to make sure that the Si waveguide mode is coupled to the TE 1-1 detector mode and not to the higher-order modes without a zero in the center (i.e. TE 3-1, TE 5-1, TE 7-1). We found that this is possible by using wider silicon waveguides due to a better mode overlap. For more narrow waveguide widths, the coupling between the fundamental TE-strip mode and these higher-order modes is increased.

By increasing the InGaAs thickness, also vertically higher-order modes start to appear. It is found that these vertically higher-order modes that have only one lobe horizontally (e.g. TE 1-2) also have a very low mode overlap with the p-metal contacts. The higher the InGaAs thickness, the smaller the undesired absorption of the metal. In Fig.3.7, the n_{eff} of these detector modes are plot in function of the InGaAs thickness with the thickness of n-InP and i-InP both fixed at $100\,\mathrm{nm}$ and this for the TE and TM modes. The thicker the InGaAs the larger the n_{eff} of all the modes since there is a larger confinement in the mesa. Hence, one can expect that the dominant mode that will be excited by the Si waveguide mode will be different for each InGaAs thickness. To make this clear, the n_{eff} of both the quasi-TE and quasi-TM mode of a $3\,\mu\mathrm{m}$-wide silicon strip waveguide is shown as well in Fig.3.7. One can then choose a certain InGaAs height to find a phase matching between the waveguide and the detector mode. One can perform this optimization for one polarization only, or optimize the structure in such a way that

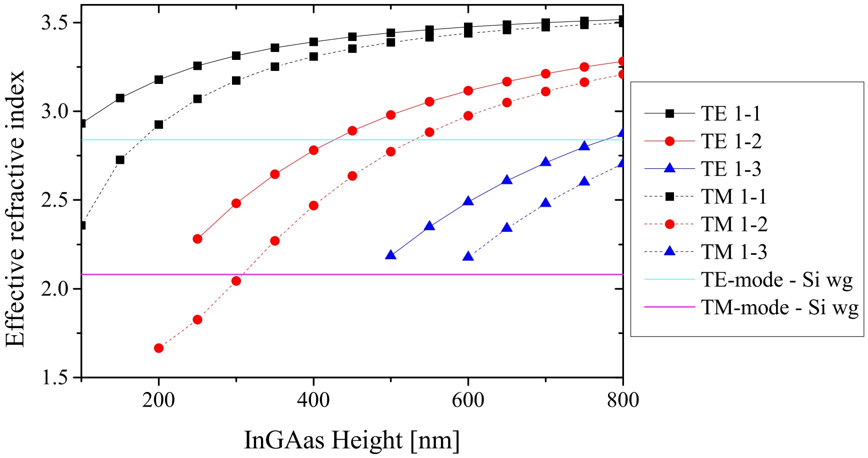

Figure 3.7: The effective refractive index of the detector modes with only 1 lobe horizontally in function of InGaAs thickness, both for TE and TM polarization. The n_{eff} of a $3\,\mu$m-wide strip is superimposed.

both polarizations will be detected. The actual coupling strength is more difficult to calculate since the fundamental detector mode can also couple to various other modes.

3D simulation Therefore, semi-vectorial 3D simulations (FimmProp) are used to calculate the absorption efficiency for both polarizations and this for a varying InGaAs height. The width of the Si waveguide is fixed at $3\,\mu\mathrm{m}$, as well as the mesa width and the p-contact width (respectively $10\,\mu\mathrm{m}$ and $2\,\mu\mathrm{m}$). The BCB thickness is $100\,\mathrm{nm}$. A typical simulation is shown in Fig.3.8, where one can see a side view of the simulated photodiode structure. Either a quasi-TE or a quasi-TM is excited in the Si waveguide. After $1\,\mu\mathrm{m}$ propagation, the photodiode structure starts and the waveguide mode couples vertically to the photodiode epitaxial structure. In Fig.3.8(a), the side view of detector simulation is shown for an InGaAs tickness of $750\,\mathrm{nm}$ and a quasi-TM mode as the input. One can find that after $10\,\mu\mathrm{m}$, nearly all the light has been absorbed. To understand the influence of the p-metal contacts, the same structure is simulated but now with only metal absorption (in the simulation, the absorption of the i-InGaAs layer is set to zero). This situation is shown in Fig.3.8(b).

From this figure, one can see the mode bouncing up and down between the vertically third-order mode (TM 1-3) in the photodiode and the quasi-TM strip waveguide mode. One can see that the intensity is slightly decreased after bouncing up and down a few times. This is partly due to the absorption of the p-metal contacts. Also some coupling is seen to horizontally higher-order detector modes.

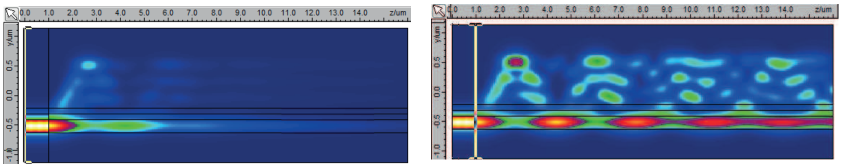
(a) InGaAs and metal absorption (b) Only metal absorption

Figure 3.8: Side view of a typical 3D FimmProp simulation in (a). (b) Same photodiode structure but only metal absorption.

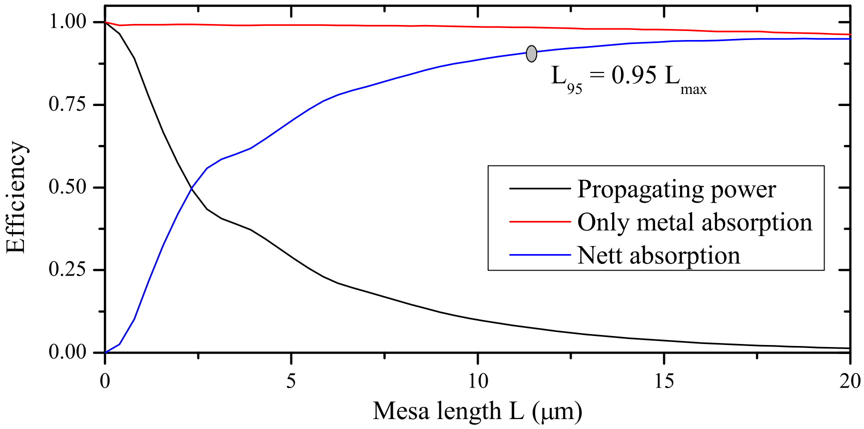

Figure 3.9: The propagation power and the nett absorption in function of the mesa length.

One can see that after $3\mu\mathrm{m}$ nearly all the light of the Si waveguide is propagating in the detector indicating a strong and fast coupling. By comparing the total optical power in function of length, for both situations (with and without InGaAs absorption), one can calculate the nett InGaAs absorption or the absorption efficiency η. This absorption efficiency in function of mesa length L is shown in Fig.3.9. From this figure, one can find that the maximum efficiency is 94%. We can use the length for where the maximum absorption is for 95% reached (noted as L_{95}) as a measure for the coupling strength. In this case L_{95} is only $11\,\mu\mathrm{m}$.

Influence InGaAs thickness on absorption length This simulation can be repeated for different InGaAs thicknesses ranging from $100\,\mathrm{nm}$ to $1\,\mu\mathrm{m}$. In Fig.3.10, the absorption length (L_{95}) in function of InGaAs thickness is plot and this for both the TE and TM mode as input of the Si waveguide. L_{95} ranges between $5\,\mu\mathrm{m}$ for the a TM mode with InGaAs thickness $900\,\mathrm{nm}$ and $60\,\mu\mathrm{m}$ using a $300\,\mathrm{nm}$ InGaAs thickness for a TE mode.

Fig.3.10(a) shows that the absorption length curves for TE and TM cross a

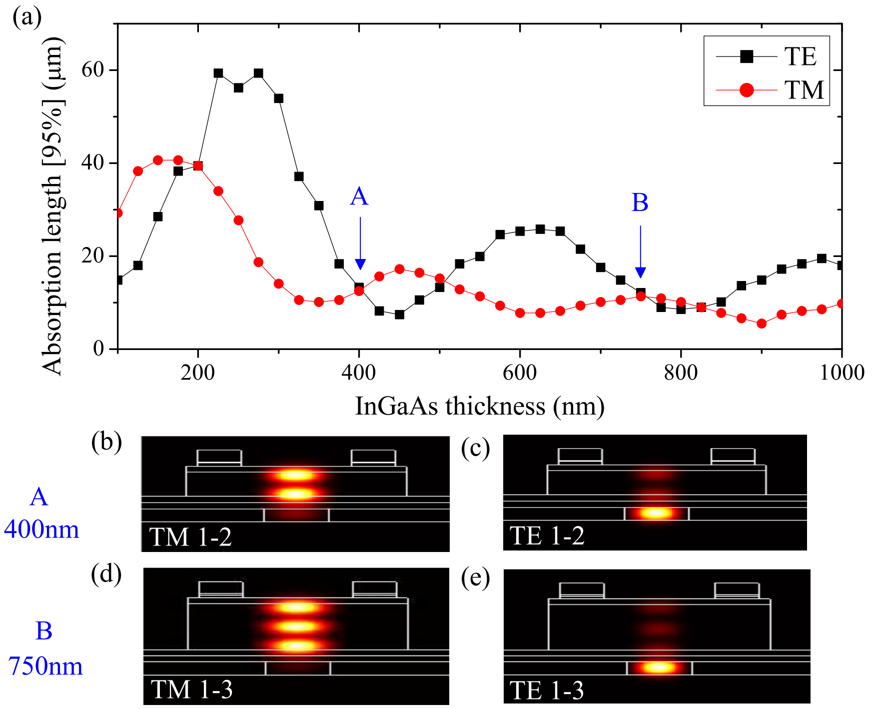

Figure 3.10: The absorption length (L_{95}) in function of InGaAs thickness and this for both the TE and TM Si waveguide mode.

few times. At these InGaAs thicknesses the absorption length is the same for TE and TM, which is interesting when optimizing the photodiode for two polarization simultaneously. At a thickness of $400\,\mathrm{nm}$ (case A), both the TM and the TE mode of the Si waveguide couple to respectively the TM 1-2 and the TE 1-2 mode, with mode profiles shown in Fig.3.10(b) and (c). The maximum efficiency η for TM and TE is respectively 97% and 94%. A similar case happens at a thickness of $750\,\mathrm{nm}$ (case B), where the coupling occurs between the TM 1-3 and TE 1-3 as shown in Fig.3.10(d) and (e). The maximum efficiency η for both TM and TE input equal to 96%. The resonant behavior is understood by the changing mode matching conditions.

Influence InGaAs thickness on the bandwidth Also the bandwidth (BW) of the photodiode mainly depends on the InGaAs thickness. As discussed before the BW of a photodiode is limited by a combination of the RC product and the transit-time limitation as shown in Eq.(3.6). In the following we will estimate the resulting BW in function of the InGaAs thickness. The total resistance is estimated by a serial contact pad resistance of $10\,\Omega$, a load of $50\,\Omega$ and the contact resistance. For this estimation we assume that the contact resistance is determined by the p-contacts only since these are the smallest in area (see Fig.3.5) with a width of $2\,\mu\mathrm{m}$. A contact resistivity of typically 0.1 to $1 \times 10^{-5}\Omega.\mathrm{cm}^2$ can be assumed in an optimized process environment, which would correspond to a total series resistance of $110 - 310\,\Omega$ for L = 5 $\mu\mathrm{m}$ and 72 $- 122\,\Omega$ for L = 20 $\mu\mathrm{m}$. However, in practice, larger contact resistances are observed, up to $1000\,\Omega$ and more. Therefore, we also consider the case where the contact resistivity is $10\times$ worse (k = $1 \times 10^{-4}\Omega.\mathrm{cm}^2$). With this contact resistance the series resistance for a detector with length 5 and $20\,\mu\mathrm{m}$ is respectively 560 and $185\,\Omega$. In Fig.3.11, the BW of these photodiodes is plot in function of the InGaAs thickness in the case of k = 1×10^{-5} and k = 1×10^{-4}. A top i-InP of $100\,\mathrm{nm}$ and a bottom n-InP layer of $50\,\mathrm{nm}$ is assumed. The width of the detector mesa is $13\,\mu\mathrm{m}$, which is slightly larger than the value used on the mask.

BW trade-off for normal p-contact resistivity Fig.3.11(a) illustrates the trade-off for a normal p-contact resistivity (k = 1×10^{-5}). As discussed before one can find the transit-time BW (f_t) decreases with $1/t_{InGaAs}$ and the RC BW (f_{RC}) increases linearly with t_{InGaAs}. The actual BW is determined by Eq.(3.6) and has a local maximum. At this InGaAs thickness (t_{max}), the bandwidth is maximized for a certain detector length. One can find that t_{max} is indeed very different for a detector length of 5 and 20 $\mu\mathrm{m}$, respectively $260\,\mathrm{nm}$ and $520\,\mathrm{nm}$. On the other hand, the actual required length of a photodiode is related by the absorption efficiency η and the absorption length L_{95} as shown in Fig.3.10, which is again depending on the InGaAs height. E.g. for L = $5\,\mu\mathrm{m}$, the t_{max} is $260\,\mathrm{nm}$. However, for this

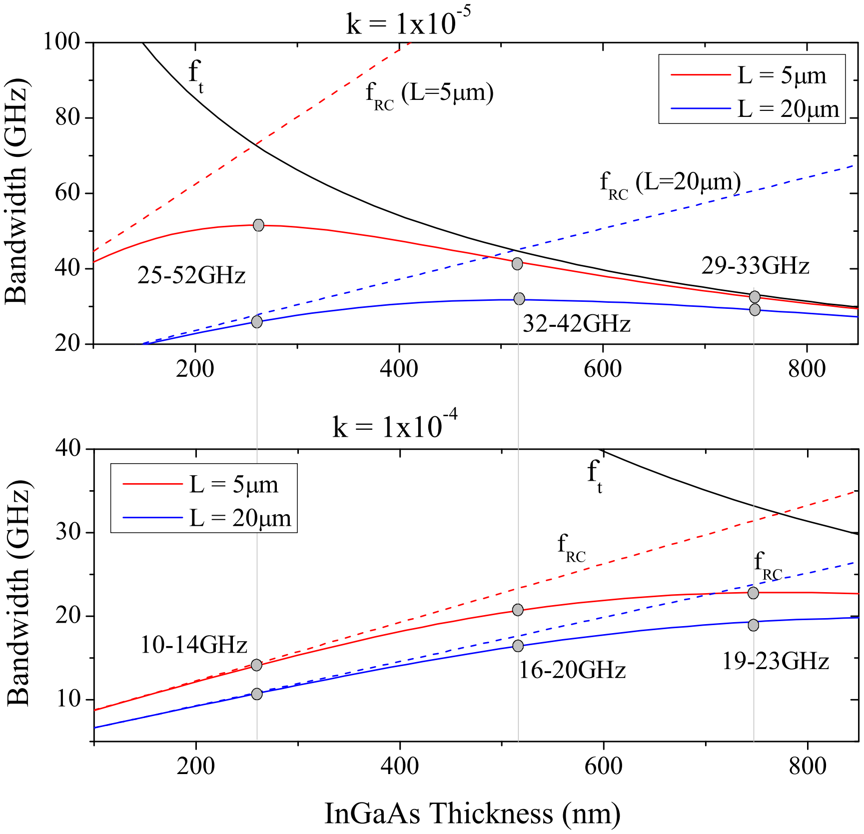

Figure 3.11: Bandwidth trade-off in function of InGaAs thickness with two p-contact resistivities (a) k = 1×10^{-5} *(b) k* = 1×10^{-4}*, with* f_t *the transit-time BW and* f_{RC} *the RC BW (*f_{RC}*). Width of the p-contacts is* $2\,\mu\mathrm{m}$*, the total width of the photodiode is* $13\,\mu\mathrm{m}$*. The top i-InP layer is* $100\,\mathrm{nm}$ *and the bottom n-InP layer is* $50\,\mathrm{nm}$*.*

thickness the required length L_{95} is $58\,\mu$m (assuming a BCB thickness of $100\,$nm). In other words, the bandwidth will be very high (i.e. $52\,$GHz) but the responsivity very low because the coupling strength to the photodiode is very weak. If one increases the length of the photodiode to $20\,\mu$m using the same InGaAs thickness, the BW drops to $25\,$GHz. For a L= $20\,\mu$m, t_{max} is found to be $560\,$nm, which corresponds to a maximum bandwidth of $32\,$GHz and to a $L_{95} < 20\,\mu$m for both the TE as the TM polarized mode (assuming a BCB thickness of $100\,$nm) and hence a better trade-off position is found. If one decreases the length of the photodiode to $5\,\mu$m the BW is increased to $42\,$GHz but the responsivity will be reduced.

BW trade-off for bad p-contact resistivity In Fig.3.11(b), the same situation is plot but now with an increased contact resistivity of k = 1×10^{-4}. This situation can happen in practice, when e.g. a larger contact resistance is observed due to a non-optimized process. One can find that the slope of f_{RC} is greatly reduced which moves the t_{max} positions for L = 5 and 20 μm to higher InGaAs thicknesses. Indeed, the BW of the photodiode with t_{InGaAs} equal to $260\,$nm has been reduced from $25 - 52\,$GHz to $10 - 14\,$GHz for L = 5 and $20\,\mu$m. In other words, this component is highly depending on the fabrication quality. This reduction in BW is much smaller for $t_{InGaAs} = 560\,$nm where the resulting BW is ranging between $16 - 20\,$GHz for respectively L = 5 and $20\,\mu$m. We found that by increasing the InGaAs thickness even more to $750\,$nm, the contact resistance dependency is even more reduced. This approach makes the design more robust against non-ideal contact resistivities. For this t_{InGaAs}, the bandwidth ranges between $18 - 31\,$GHz for a length of L = $20\,\mu$m and a varying contact resistivity. From Fig.3.10, one can find that with a length of $12\,\mu$m, the absorption efficiency is maximized and close to 1 (assuming a BCB thickness of $100\,$nm). Note that also the length dependency is decreased for higher InGaAs thickness. Increasing the length to $50\,\mu$m, using $t_{InGaAs} = 750\,$nm, the BW is still between $13 - 20\,$GHz depending on the resistivity. This way, the photodiode can be made longer to overcome BCB thickness variations.

3.2.3 Resulting parameters

The first generation, proposed by colleague Zhen Sheng, had a InGaAs thickness of $100\,$nm, optimized to excite the fundamental mode of the photodiode [6]. The length of the photodiode is $40\,\mu$m and a high responsivity of $1.1\,$A/W was achieved. The width of the Si waveguide was $3\,\mu$m. After re-fabrication, the bandwidth was found to be around $200\,$MHz. Using Fig.3.11(b) we can assuming that this is due to a bad p-contact resistivity. For this thin InGaAs thickness the capacitance is large ($260\,$fF) and the photodiode is fully determined by the RC constant. With a standard p-contact resistivity, the series resistance is estimated to be $122\,\Omega$.

This would results in a BW of $5\,\mathrm{GHz}$. In other words, the contact resistivity is 1×10^{-3}, $100\times$ worse than expected.

Besides optimizing the fabrication process, also the design has been adjusted to be more robust against higher contact resistivities. In the second generation, using the same architecture, the design was adjusted following the strategy explained in previous section. By increasing the InGaAs thickness to $700\,\mathrm{nm}$, the photodiode is believed to exhibit a smaller dependency on the contact resistivity. Note that this is slightly off the optimized InGaAs height of $750\,\mathrm{nm}$. The width of the SOI waveguide was varied between 1.1, 2 and $3\,\mu\mathrm{m}$, which is a trade-off between better phase matching and a faster coupling. The width needs to be wide enough to ensure primary coupling to the horizontal fundamental detector mode which has the lowest overlap with the p-metal contacts in comparison with horizontally higher-order detector modes. With a thin BCB layer of $100\,\mathrm{nm}$, all the light couples evanescently to the photodetector and gets fully absorbed by the InGaAs layer within $20\,\mu\mathrm{m}$. Because the BCB thickness can vary, the detector length is varied between $18 - 90\,\mu\mathrm{m}$ long. With this InGaAs height, the bandwidth is estimated to be $15 - 23\,\mathrm{GHz}$ for a contact resistivity of respectively $1 - 10 \times 10^{-5}$.

3.2.4 Fabrication

The fabrication starts with a BCB die-to-wafer bonding process. This process is described in [3], where one can also find more details about the various fabrication steps. After bonding the III-V die onto the patterned SOI substrate, the InP substrate was removed through a combination of mechanical grinding and chemical etching. Then, we free the alignment markers on the Si platform such that new alignment markers to align the contact mask for the following lithographic steps can be defined. This is shown in Fig.3.12(a). Then a pair of InGaAs/InP sacrificial layers was removed by chemical wet etching, exposing the p-InGaAs contact layer. After that, a Ti/Au p-metal contact is deposited as shown in Fig.3.12(b). This metal pattern was lithographically aligned to the underlying SOI waveguide. Subsequently, the p-InGaAs layer is etched through by using this p-metal contact layer as the etching mask. Then the detector mesa is defined by etching through the p-InP and i-InGaAs layers. The remaining n-InP layer was removed where it is not needed, e.g. on top of the access SOI waveguides and fiber grating couplers. An AuGe/Ni alloy is used to form an ohmic contact with n-InP. A $600\,\mathrm{nm}$-thick BCB dielectric layer was spin-coated on top of the whole device, and vias are opened down to the p- and n-metal contacts. An O_2 and SF_6 plasma etching process is used for this purpose. Finally, another Ti/Au metal alloy is prepared as the metal plugs as well as the probe pads. All the etching of the III-V materials was done with wet chemistry, in order to minimize the damage to the sidewalls. Fig.3.12(c) shows the top view of a fabricated device before the final metalization for plugs

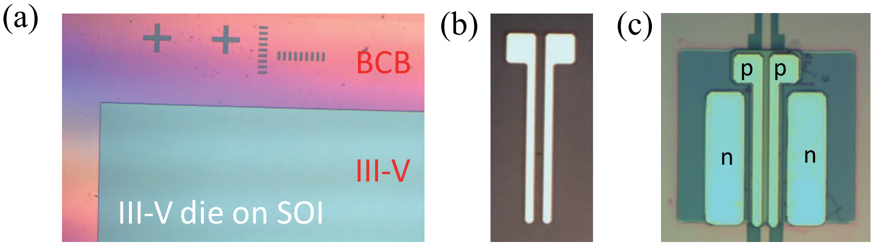

Figure 3.12: Microscope pictures of fabrication process of $40\,\mu\mathrm{m}$*-long InGaAs photodiode: (a) removing of the InP die on top of the SOI markers (b) first (p-)metal deposition which is used as a hard mask to define the helmet structure and (c) the resulting photodiode before the final metalization.*

and pads. In Fig.3.13, one can see a SEM picture of the as-fabricated InGaAs photodiode of the second generation.

3.2.5 Characterization

In this section, the evanescently coupled InGaAs p-i-n photodiode of the second generation is characterized. The responsivity of the detector was $1.06\,\mathrm{A/W}$ (quasi-TM) and $1.23\,\mathrm{A/W}$ (quasi-TE) respectively corresponding to an 85% and 98% efficiency for the $18\mu\mathrm{m}$ long detector ($10\,\mu\mathrm{m}$ mesa length) with $3\,\mu\mathrm{m}$ wide Si-waveguide. Increasing the length of the photodiode does not increase the responsivity. This indicates that the BCB-thickness is thin enough and all the light is absorbed as predicted in Fig.3.10. If the Si-waveguide width is decreased to $1.1\,\mu\mathrm{m}$, the efficiency is slightly lower for the TE polarization $(1.03\,\mathrm{A/W})$ due to coupling to horizontally higher-order modes. These higher-order modes have a larger overlap with the non-contributing metal absorption as simulated in previous section. The efficiency of the TM-polarized mode could be further increased by increasing the spacing between the p-contacts (e.g. to $5\,\mu\mathrm{m}$), but this will increase the capacitance of the photodiode. The dark current of the detector ranges between $3-5\,\mathrm{nA}$ for a bias voltage of $-3\,\mathrm{V}$. This bias is needed to work under high power illumination and/or at high speed, otherwise a zero bias is sufficient to reach the maximum responsivity. The dark current versus applied voltage is shown in Fig.3.14(a) for the different detector lengths. From the forward current one can estimate the series resistance by taking the derivative (dI(V)/dV). This series resistance is shown in Fig.3.14(b). One can observe that after rapid thermal annealing of the sample the series resistance drastically dropped with a factor of 4 to 5. Before annealing the resistance of a device with L = $20\,\mu\mathrm{m}$ is $870\,\Omega$, which would correspond to a p-contact resistance of 5×10^{-4}. After annealing the estimated p-contact resistance is 1×10^{-4}.

The measured capacitance versus detector length is shown in Fig.3.15 for an

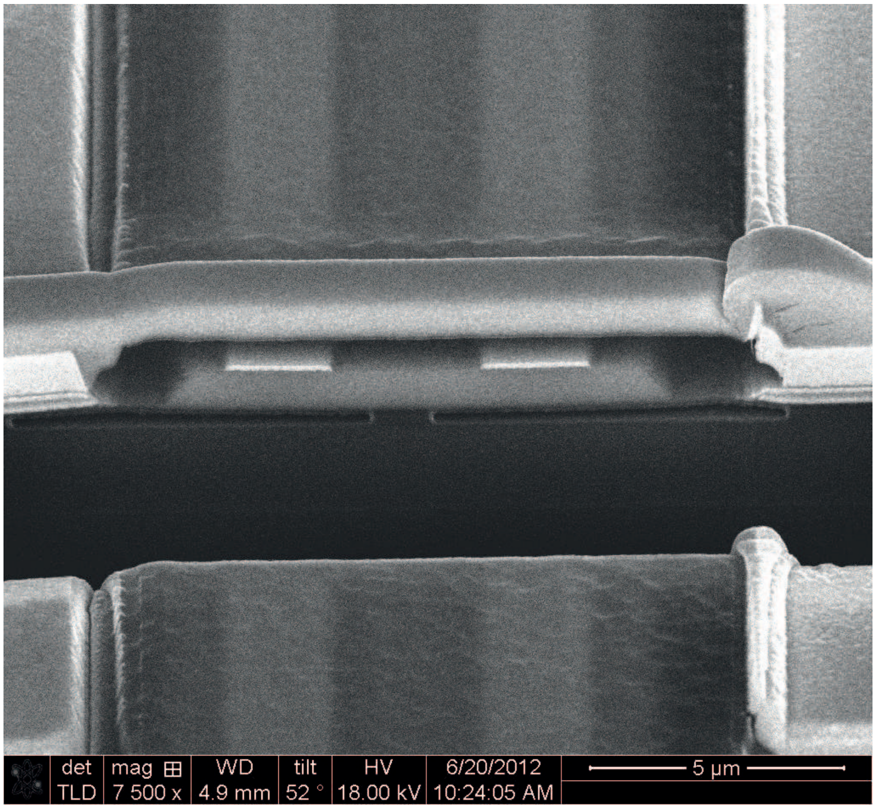

Figure 3.13: SEM picture of the as fabricated InGaAs photodiode (generation II). A FIB is used to make a cross-section of the photodiode after depositing a Pt mask on top of the photodiode.

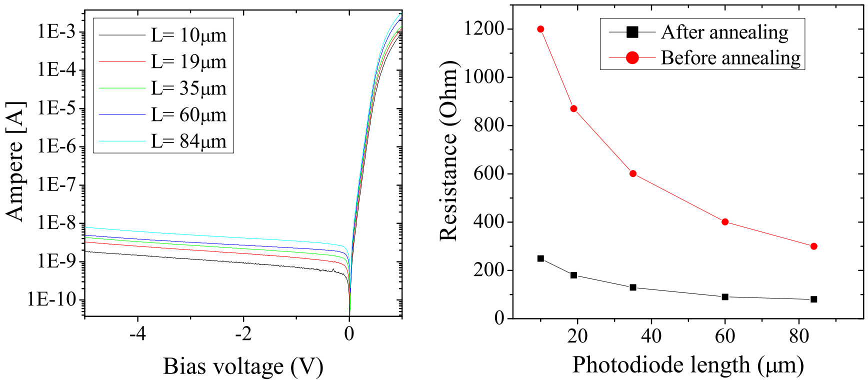

Figure 3.14: (a) Current versus voltage (IV) curve of the InGaAs p-i-n photodiodes for various lengths. (b) The extracted series resistance of the photodiodes before and after rapid thermal annealing. The series resistance lowers with a factor 4 to 5.

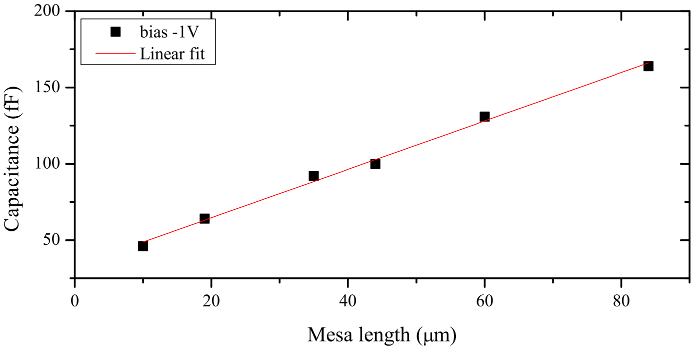

Figure 3.15: The observed capacitance versus detector length.

external bias of $-1\,\mathrm{V}$. Based on the resistance and the capacitance we can calculate the RC bandwidth to be around $3\,\mathrm{GHz}$ before annealing and $13\,\mathrm{GHz}$ after annealing. From Fig.3.11 one can find the transit-time bandwidth of photodiode to be $34\,\mathrm{GHz}$ and hence we can say that in both cases the BW of the photodiode is RC limited. Due to the large values of the series resistance, the bandwidth of the photodiode is independent of the length. If a larger reverse bias is applied, the bandwidth is expected to increase even further.

In the following we perform a large signal analysis. Therefore a $20\,\mathrm{GHz}$ modulator driven by a pulse pattern generator using a pseudo-random bit sequence (PRBS) signal of length $2^{31}-1$ was used. The wavelength is $1550\,\mathrm{nm}$, with an output power (end of fiber tip) of $3\,\mathrm{mW}$ and using a TE polarized mode. To visualize the response of the photodiode biased at $-5\,\mathrm{V}$, we use an electrical oscilloscope (Agilent 86100B). The setup configuration is shown in Fig.3.16. In

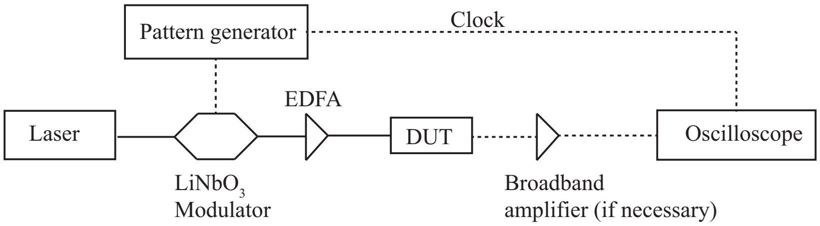

Figure 3.16: The setup configuration for a large signal analysis of the photodiode.

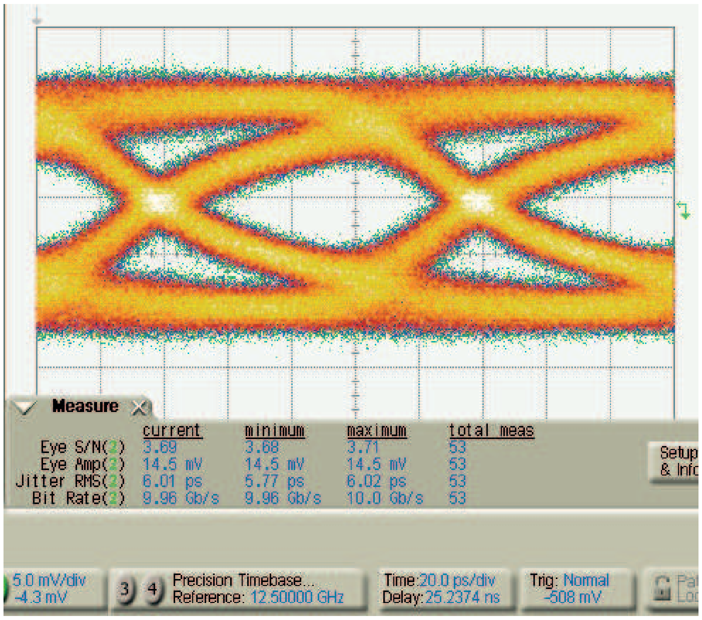

```
             current     minimum     maximum     total meas
  Eye S/N(2) 3.69        3.68        3.71        53
  Eye Amp(2) 14.5 mV     14.5 mV     14.5 mV     53
Jitter RMS(2) 6.01 ps    5.77 ps     6.02 ps     53
 Bit Rate(2) 9.96 Gb/s   9.96 Gb/s   10.0 Gb/s   53

5.0 mV/div   3 4 Precision Timebase...        Time:20.0 ps/div     Trig: Normal
-4.3 mV          Reference: 12.50000 GHz      Delay:25.2374 ns     -508 mV
```

Figure 3.17: $10\,\mathrm{Gb/s}$ *open-eye diagram of a* $20\,\mu\mathrm{m}$*-long InGaAs photodiode of generation II before rapid thermal annealing.*

Fig.3.17, a $10\,\mathrm{Gb/s}$ open-eye diagram is shown of a $20\,\mu\mathrm{m}$-long photodiode before rapid thermal annealing with length.

After thermal annealing, the response of the photodiode has been remeasured using a different setup (different lab). The modulator has a bandwidth of $12\,\mathrm{Gb/s}$ and is driven by an Anritsu pulse pattern generator (maximum BW $12.5\,\mathrm{Gb/s}$) using a PRBS signal with length $2^{31}-1$ and a $0.8\,\mathrm{V}$ output. The noise level on the $100\,\mathrm{GHz}$ Lecroy electrical oscilloscope is large ($7\,\mathrm{mV}$) and hence rather large input powers around $10-15\,\mathrm{mW}$ are needed to overcome the system noise. From Fig.3.18, an improved response is found with a very low BER of 75×10^{-12}. By comparing these results using a reference photodiode with a bandwidth of

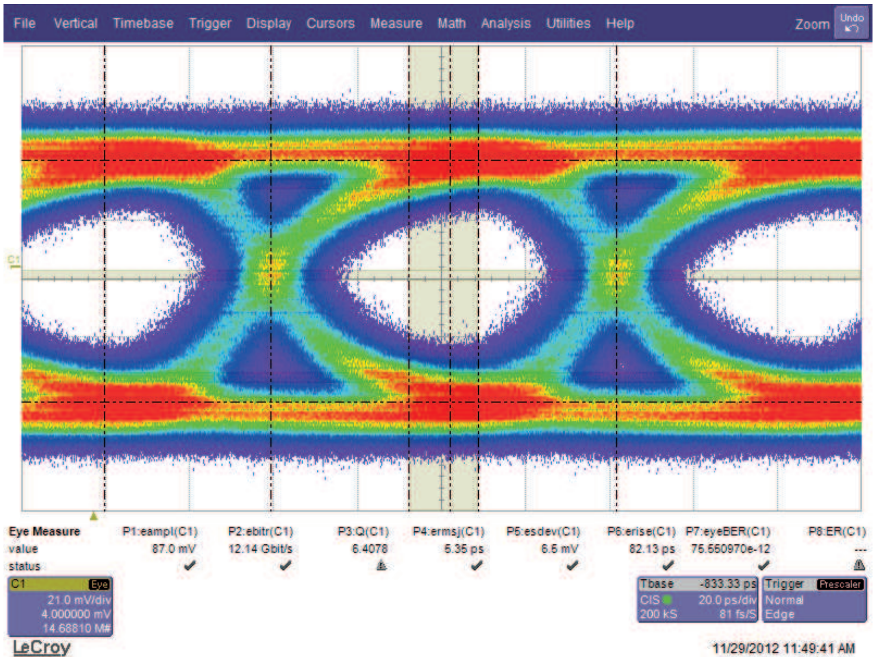

Eye Measure	P1:eampl(C1)	P2:ebitr(C1)	P3:Q(C1)	P4:ermsj(C1)	P5:esdev(C1)	P6:erise(C1)	P7:eyeBER(C1)	P8:ER(C1)
value	87.0 mV	12.14 Gbit/s	6.4078	5.35 ps	6.5 mV	82.13 ps	75.550970e-12	---
status	✓	✓	⚠	✓	✓	✓	✓	⚠

C1 Eye
21.0 mV/div
4.000000 mV
14.68810 M#

Tbase -833.33 ps
CIS 20.0 ps/div
200 kS 81 fs/S

Trigger Prescaler
Normal
Edge

11/29/2012 11:49:41 AM

Figure 3.18: $12\,\mathrm{Gb/s}$ *open-eye diagram of a* $20\,\mu\mathrm{m}$*-long InGaAs photodiode of generation II after annealing. A very low bit-error-rate is achieved (*75×10^{-12}*). Eye amplitude is* $87\,\mathrm{mV}$ *and the jitter* $5.3\,\mathrm{ps}$.

$100\,\mathrm{Gb/s}$, the jitter is found to be the same ($5.3\,\mathrm{ps}$). This indicates that the modulator and pulse pattern generator are limiting the maximum bandwidth of the photodiode in this setup.

The output current of the photodiode might not be large enough to sufficiently overcome the system noise typically present in high-speed oscilloscopes. This could happen when e.g. the responsivity is too low or the maximum input power is limited. Also higher input powers require larger bias voltage to overcome the internal drop of the electric field due to space charge effects [4]. The increase of bias could lead to higher dark current levels and a higher internal temperature. This higher temperature increases the dark current and the photodiode can be destroyed (thermal break-down). In that case, one could also add an electrical amplifier between the photodiode and the oscilloscope. However, typically extra noise is added and a careful noise trade-off is advised.

3.2.6 Outlook

At the end of this work, the design is once more improved (generation III). This photodiode is optimized for both a vertical (see Fig.3.3) and an evanescent cou-

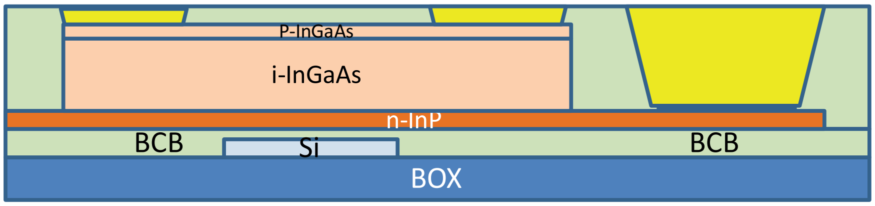

Figure 3.19: Design proposition for generation III. With an increased InGaAs thickness this epitaxial stack can act as a vertically and evanescently coupled photodiode. Compared to generation II, no i-InP sandwich layer is used to decrease the carrier transit time.

pling scheme. The main difference with generation II is the lack of a sandwich i-InP layer that was used to guide the optical mode away from the electrical contacts. The design proposal is shown in Fig.3.19 (only one n-contact is shown).

We found that for large InGaAs heights and using a TE-polarized mode, the overlap with the metal is very limited. By increasing the height of the InGaAs even further compared to generation II, we make this component even more transit-time limited and hence more robust against fabrication tolerances. We optimized the stack in such a way that for both coupling schemes a high bandwidth and high responsivity is achieved. This flexibility can be advantageous when one wants to integrate different types of photodiodes close to each other (or shared among different designers). Due to the increased InGaAs thickness, one could consider a full mesa-covering p-contact instead of a split p-contact. This increased p-contact area will further reduce the influence of contact resistivity on the BW of the photodiode. Furthermore, when a vertical coupling is used, this enlarged p-contact metal can act as mirror such that light, which is not absorbed after a single propagation through the InGaAs layer is bounced back.

In Fig.3.20, a 3D simulation to obtain the absorption length L_{95} in function of InGaAs thickness is shown. This is a similar simulation as shown earlier in Fig.3.9 but now for a InGaAs thickness starting from $700\,\mathrm{nm}$ up to $1300\,\mathrm{nm}$ and without the $100\,\mathrm{nm}$-thick i-InP layer. The maximum efficiency that is reached in denoted in the figure as a label. P-contacts are $2\,\mu\mathrm{m}$.

From Fig.3.20, the optimal thickness of the intrinsic layer is $1150\,\mathrm{nm}$. For this thickness, the responsivity is maximized and the absorption length is minimized for both polarizations. In an evanescently-coupled integration scheme, all the light is absorbed after $10\,\mu\mathrm{m}$ assuming a BCB thickness of $100\,\mathrm{nm}$. This would correspond to a responsivity of around $1.2\,\mathrm{A/W}$ and a 3-dB bandwidth of $25\,\mathrm{GHz}$. When used in a vertical coupling scheme, e.g. on top of a grating coupler, the responsivity is estimated to be $0.85\,\mathrm{A/W}$ with a bandwidth estimated between $13-17\,\mathrm{GHz}$. This calculation is without taking into account the insertion loss of the grating coupler.

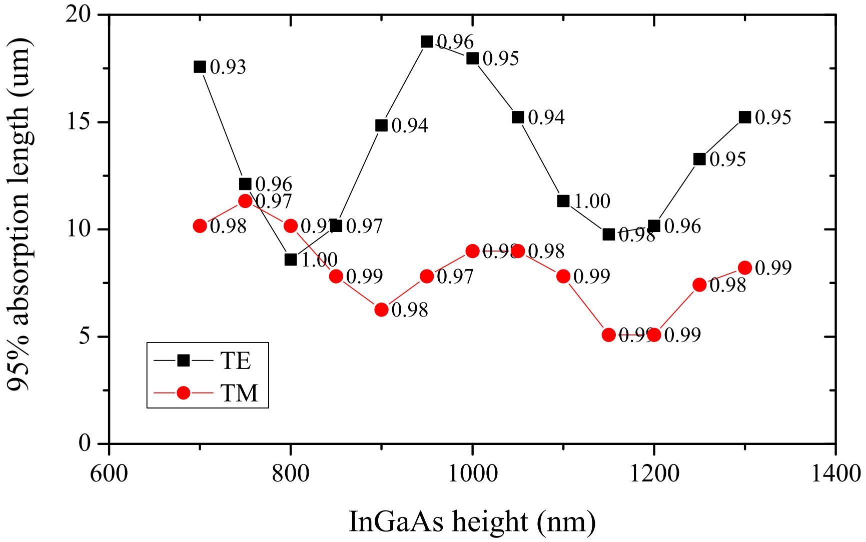

Figure 3.20: Design space for generation III photodiodes. The absorption length (L_{95}) *is plot in function of InGaAs thickness and this for both the TE and TM Si waveguide mode. A BCB thickness of* $100\,\mathrm{nm}$ *is assumed.*

3.3 Butt-coupled Ge p-i-n photodiodes

Two types of Ge photodiodes are investigated: a lateral and a vertical p-i-n photodiode. Germanium is monolithically grown on a shallowly etched waveguide such that light is almost directly incident on the photodiode. Therefore the photodiode is said to be butt coupled. The design and fabrication process have been fully developed by the iSIPP team of imec, with Joris Van Campenhout and Peter Verheyen as the two main contributors. The design is explained in [8] together with some preliminary characterization results. The design is optimized using similar trade-off techniques we have presented for InGaAs photodiodes in previous section. The process is fully CMOS compatible and is fabricated in the p-line of the $200\,\mathrm{mm}$ cleanroom of imec. A schematic and TEM picture of a lateral p-i-n photodiode is given in Fig.3.21(a) and (b). One can notice that the Ge is laterally overgrown, which helps to minimize the absorption of the metal contacts. In Fig.3.21(c), a top-view schematic of the laterial p-i-n photodiode is shown. A taper of deposited poly-Si on top of the Si waveguide is used to facilitate the butt coupling to the Ge region [8]. In a vertical p-i-n photodiode, the top p-metal contacts are in the middle of the Ge photodiode which reduces a bit the efficiency (see also Fig.3.21(d). The fabrication flow is covered in [16].

The responsivity of the photodiodes have been measured to be $0.6-0.8\,\mathrm{A/W}$ and is depending on the various parameters. Among other strategies, increasing the

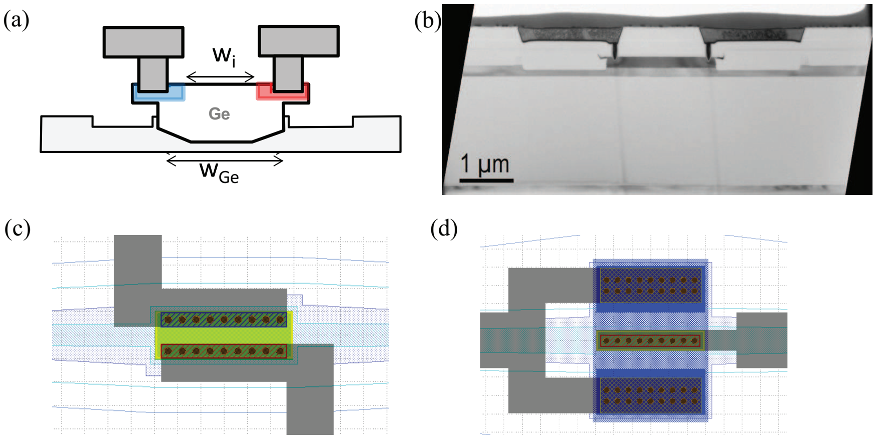

Figure 3.21: (a) A cross section and (b) a TEM picture of a lateral p-i-n Ge photodiode schematic. In (c) a top view of the lateral and (d) vertical p-i-n Ge design.

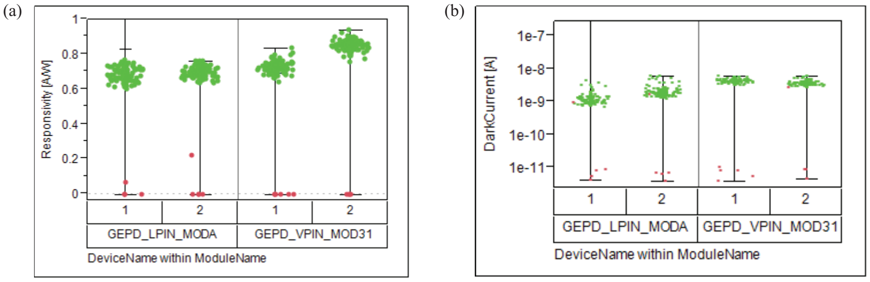

Figure 3.22: Wafer-level measurements of a lateral and vertical p-i-n Ge photodiode of the (a) responsivity and (b) the dark current.

thickness of Ge has been considered to decrease the effect of the metal contacts and improve the responsivity even further. Both photodiodes have a very low dark current ($1 - 10\,\mathrm{nA}$ at $-1.2\,\mathrm{V}$). This has been achieved by both optimizing the quality of the Ge and the design of the photodiode. One approach is to design the contacts in such a way that the electrical field is minimized at those edges were the quality of the Ge is the worst. Wafer-scale measurements illustrated in Fig.3.22 are showing a very high yield for both responsivity and dark current.

The bandwidth of the photodiodes has been characterized using a $50\,\mathrm{GHz}$ Lightwave network analyzer. S_{21}-parameters reveal a bandwidth of $22\,\mathrm{GHz}$ for a lateral p-i-n photodiode and a $> 50\,\mathrm{GHz}$ for a vertical p-i-n photodiodes using a bias voltage of $-2\,\mathrm{V}$. The bandwidth is for both photodiodes slightly reduced for a bias voltage of $-1\,\mathrm{V}$, respectively $18\,\mathrm{GHz}$ and $47\,\mathrm{GHz}$. We also found a clear influence of the amount of contacts on the top of the vertical p-i-n photodiode. The

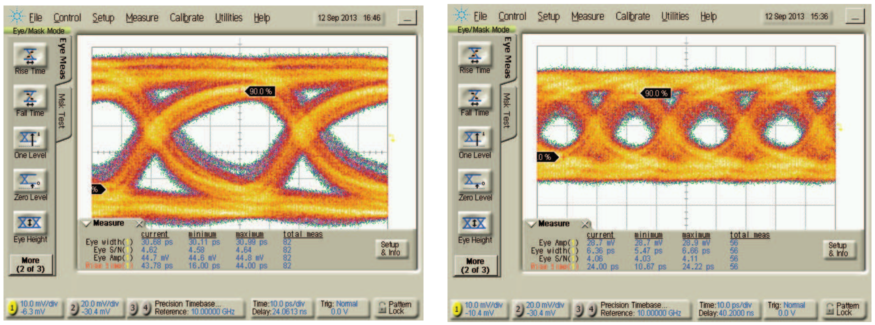

Measure	current	minimum	maximum	total meas
Eye width(1)	30.68 ps	30.11 ps	30.99 ps	82
Eye S/N(1)	4.62	4.58	4.64	82
Eye Amp(1)	44.7 mV	44.6 mV	44.8 mV	82
Rise time(1)	43.78 ps	16.00 ps	44.00 ps	82

1 10.0 mV/div -6.3 mV
2 20.0 mV/div -30.4 mV
3 4 Precision Timebase... Reference: 10.00000 GHz
Time: 10.0 ps/div Delay: 24.0613 ns
Trig: Normal 0.0 V

(a) Lateral p-i-n PD - 20 Gb/s

Measure	current	minimum	maximum	total meas
Eye Amp(1)	28.7 mV	28.7 mV	28.9 mV	56
Eye width(1)	6.36 ps	5.47 ps	6.66 ps	56
Eye S/N(1)	4.06	4.03	4.11	56
Rise time(1)	24.00 ps	10.67 ps	24.22 ps	56

1 10.0 mV/div -10.4 mV
2 20.0 mV/div -30.4 mV
3 4 Precision Timebase... Reference: 10.00000 GHz
Time: 10.0 ps/div Delay: 40.2000 ns
Trig: Normal 0.0 V

(b) Vertical p-i-n PD - 40 Gb/s

Figure 3.23: Eye diagram using a PRBS with length $2^7 - 1$ *and a bias voltage of* $-1\,\mathrm{V}$ *at (a)* $20\,\mathrm{Gb/s}$ *using a lateral and (b)* $40\,\mathrm{Gb/s}$ *using a vertical p-i-n photodiode.*

more contacts and hence a smaller spacing between them, the larger the bandwidth and the lower the responsivity. This can be understood by the fact that bandwidth is largely depending on the contact resistance of the p-contacts. An eye diagram showing the $20\,\mathrm{Gb/s}$ response of the lateral p-i-n photodiode with length $15\,\mu\mathrm{m}$ and a bias voltage $-1\,\mathrm{V}$ using a pseudo-random bit sequence (PRBS) of length $2^7 - 1$ is shown in Fig.3.23(a). Fig.3.23(b) shows the response of a $40\,\mathrm{Gb/s}$ PRBS signal using a vertical p-i-n photodiode with a length of $15\,\mu\mathrm{m}$ and a bias voltage of $-1\,\mathrm{V}$.

3.4 Conclusion

In this chapter we have reviewed the development of high-performance evanescently-coupled InGaAs and butt-coupled Ge photodiodes. Most of chapter was contributed to the design trade-off between responsivity and bandwidth for an InGaAs photodiode. Fabricated InGaAs photodiodes, heterogeneously integrated on Si, are showing promising results with very low dark current levels between $3 - 5\,\mathrm{nA}$ at high reverse bias voltages indicating a well-controlled wet etch process. A high responsivity between $1.06\,\mathrm{A/W}$ and $1.23\,\mathrm{A/W}$ for respectively a quasi-TM and quasi-TE mode is achieved. With this efficiency levels (respectively 89% and 98%), these photodiodes are the best in class. The bandwidth has been improved from a poor (RC-limited) $200\,\mathrm{MHz}$ to open-eye diagrams at $12\,\mathrm{Gb/s}$. This improvement is partly due to an improved p-contact resistivity but also due to an improved design. This design is optimized to exhibit a smaller dependency to a varying contact resistivity. By reducing this dependency, the bandwidth of the photodiode becomes less RC-limited and more transit-time limited. Another consequence is that this photodiode becomes less depending on the exact length of the photodiode. The possibility to increase the length decreases the influence of the exact BCB thickness to the overall responsivity. A new design is proposed with an increased flexibility and robustness that exhibit a high responsivity and a high bandwidth both using a vertical and evanescent coupling scheme.

Monolithically-grown butt-coupled Ge photodiodes are also characterized regarding responsivity, dark current and bandwidth. Results (summarized in section 3.3) are showing promising results with a $50\,\mathrm{GHz}$ bandwidth and wafer-scale measured dark current levels of below $10\,\mathrm{nA}$ as the main highlight. Further investigation is devoted to increase the responsivity. By increasing the bias voltage up to several volts, one can create an avalanche effect of high energetic electrons. These avalanche photodiodes (APD) could have an internal gain of $10\,\mathrm{dB}$ and could significantly increase the sensitivity of a receiver.

References

[1] John E Bowers and Charles A Burrus. *Ultrawide-band long-wavelength p-i-n photodetectors*. Journal of Lightwave Technology, 5(10):1339–1350, 1987.

[2] Antoni Rogaiskia and Computer Science. *Narrow gap semiconductor photodiodes*. Optoelectronics and High-Power Lasers & Applications, 3287:2–13, 1998.

[3] Joost Brouckaert. *Integration of photodetectors on silicon photonic integrated circuits (PICs) for spectroscopic applications*. PhD thesis, Ghent University, 2010.

[4] Andreas Beling and Joe C Campbell. *Photodetectors*. In Key Devices in Fibre Optics, volume 161, pages 1–52. Springer New York, 2012.

[5] Joost Brouckaert, Gunther Roelkens, Dries Van Thourhout, and Roel Baets. *Thin-Film IIIV Photodetectors Integrated on Silicon-on-Insulator Photonic ICs*. Journal of Lightwave Technology, 25(4):1053–1060, April 2007.

[6] Zhen Sheng, Liu Liu, Joost Brouckaert, Sailing He, and Dries Van Thourhout. *InGaAs PIN photodetectors integrated on silicon-on-insulator waveguides.* Optics express, 18(2):1756–61, January 2010.

[7] G. Roelkens, J. Brouckaert, D. Van Thourhout, R. Baets, R. Notzel, and M. Smit. *Adhesive Bonding of InPInGaAsP Dies to Processed Silicon-On-Insulator Wafers using DVS-bis-Benzocyclobutene*. Journal of The Electrochemical Society, 153(12):G1015, 2006.

[8] J Van Campenhout, M Pantouvaki, P Verheyen, H Yu, P De Heyn, G Lepage, W Bogaerts, and P Absil. *Silicon-Photonics Devices for Low-Power , High-Bandwidth Optical I / O*. In Advanced Photonics Congress (OSA - 2012), 2012.

[9] Mathieu Rouviere, Mathieu Halbwax, Jean-Luc Cercus, Eric Cassan, Laurent Vivien, Daniel Pascal, Michel Heitzmann, Jean-Michel Hartmann, Daniel Bouchier, and Suzanne Laval. *Integration of germanium waveguide photodetectors for optical intra-chip interconnects*. Proceedings of SPIE, 5453:142–149, September 2004.

[10] Andreas Beling and Joe C Campbell. *InP-Based High-Speed Photodetectors*. Journal of Lightwave Technology, 27(3):343–355, 2009.

[11] Z Zhang, N Mettbach, C Zawadzki, D Schmidt, W Brinker, J Wang, N Keil, and N Grote. *Hybrid Integration of Optical Polymer Waveguides and 25 GHz Photo Detector Arrays*. In ECIO 2010, page WeG7, 2010.

[12] Solomon Assefa, Fengnian Xia, Stephen W Bedell, Ying Zhang, Teya Topuria, Philip M Rice, and Yurii a Vlasov. *CMOS-integrated high-speed MSM germanium waveguide photodetector.* Optics express, 18(5):4986–99, March 2010.

[13] Andrew W. Poon, Shaoqi Feng, Yu Li, Yu Geng, and Kei May Lau. *All-silicon and epitaxially grown III-V-on-silicon photodetectors for on-chip optical interconnection applications*. Proc. SPIE 8628, Optoelectronic Integrated Circuits XV, (86280E), 2013.

[14] Gunther Roelkens. *Heterogeneous III-V/Silicon Photonics: Bonding Technology and Integrated Devices*. PhD thesis, Ghent University, 2007.

[15] Nannicha Hattasan, Alban Gassenq, Laurent Cerutti, Jean-baptiste Rodriguez, Eric Tournié, and Gunther Roelkens. *Heterogeneous Integration of GaInAsSb p-i-n Photodiodes on a Silicon-on-Insulator Waveguide Circuit*. IEEE Photonics Journal, 23(23):1760–1762, 2011.

[16] Peter Verheyen, Guy Lepage, Joris Van Campenhout, Marianna Pantouvaki, Philippe Absil, Peter De Heyn, Wim Bogaerts, Pieter Dumon, and Shankar Selvaraja. *Co-integration of Ge detectors and Si modulators in an advanced Si photonics platform*. In Photonics Europe (SPIE), pages 8431, 843114, 2012.

4

In-band label extraction for all optical packet switching

In this chapter we demonstrate in-band label extraction from very high speed ($40-160\,\mathrm{Gb/s}$) optical data packets using narrowband silicon ring resonators. Based on the information encoded in the label, a switch will then route the optical packet to the right direction. An efficient label extraction is an important step to all-optical packet switching. All-optical or transparent networks have many advantages with respect to electrical switched networks as there is no need anymore to convert the whole data into the electrical domain at each node. The label extraction must be scalable in terms of the number of possible addresses but must also fit in a system which can be scaled to large number of ports (in and output) and this at minimized latency.

High performance narrowband ring resonators and highly responsive photodiodes, both covered separately in the previous two chapters, are our two building blocks to create a photonic integrated WDM-label extractor in silicon. By cascading these narrowband ring resonators, an ultra-dense wavelength division multiplexing (UDWDM) demultiplexer is formed.

We start this chapter by reviewing several techniques to extract a label. The design, fabrication and characterization is explained in section 4.2. The UDWDM demultiplexer was then employed in system experiments that were performed in the COBRA labs of the Eindhoven University of Technology (TU/e) of Prof. Harm Dorren using the expertise of Jun Luo, Nicola Calabretta and Stefano Di Lucente. Two system experiments are discussed at the end of this chapter. In section 4.3, an in-band label using four wavelengths is error-free extracted from $160 Gb/s$ optical packets. In the last section (4.4), $40\,\mathrm{Gb/s}$ optical packets were used to demonstrate the combination of a dense WDM data demultiplexer and an in-band label extractor.

4.1 Introduction

Several techniques to extract an optical label have been researched over the last 20 years. We start this section by comparing the in-band label technique to other alternatives. Next, we discuss the position of the envisioned label extractor in an all-optical packet switch.

4.1.1 In-band label technique

One can add an address (containing the forwarding information) to an optical bit stream (the *payload*) in various ways. One can make a strict distinction between serial and parallel processed address extraction. In the following we will discuss both classes.

Serial processing Following a typical structure of an IP packet, a popular method is to encode the address in a bit stream in front of the payload [1–6]. Usually this technique is referred to as time-division multiplexing (TDM) and the address as the *header*. One can encode the address in a synchronous or asynchronous way. Synchronous read-out of the header requires ultra-fast electronic processing. Asynchronous headers (header at a lower speed than the payload) makes the header much longer with respect to the payload and consequently lowers the throughput. To synchronize the receiver, one typically also needs some synchronization bits. Long guard times are needed to effectively erase the header and not distort the payload. Ultra-fast all-optical header recognition methods have been proposed to minimize these limitations by extracting the address in the same (optical) physical layer and thus making the switch completely all-optical [4]. Non-linearities in semiconductor optical amplifiers (SOA) are a common way to correlate a header with an address in a predefined routing table. A good overview of these techniques can be found in [6–8]. Complete routing experiments were demonstrated, e.g. a $160\,\mathrm{Gb/s}$ optical packet switch over a $110\,\mathrm{km}$ field installed fiber in [4] using optical flip-flops as memory element. However most techniques are rather limited in scalability due to their large number of optical components, long guard times and exponential latency for larger routing tables. A significant smaller routing table has been achieved and thereby solving partly the scalability issue using pulse-position modulation technique [6]. However long guard times are still present.

Parallel processing To maximize the send time for the payload, parallel processing techniques [9–12] were invented where the address is encoded along or within the payload and not in series as in the case of TDM. This eliminates guard times and thus latency. A good overview of these techniques can be found in [10, 13] and typically allow asynchronous (low-speed) processing of the labels and consume potentially therefore less power. However, among these techniques one can note that the label is still encoded in the time domain. It consumes extra time to synchronize, read, buffer and process the information before sending a control signal to the switch [13]. This processing time can be much longer than the payload itself which is not acceptable, e.g. it takes $200\,\mathrm{ns}$ to recognize the label for a $75\,\mathrm{ns}$ long $160\,\mathrm{Gb/s}$ payload [13].

To fully minimize the latency coming from address extraction, also the label processing can be performed in parallel instead of in series. This has been proposed and demonstrated first in [14], where parallel coded multiple label wavelengths are used to encode the address. These optical labels are transmitted in-band, in other words, within the signal bandwidth of the payload to maximize the spectral efficiency. These labels are transmitted using separate transmitters which is the main drawback of this technique since this adds extra power consumption and component cost. The labels are extracted using narrowband optical filters and can be processed immediately. The labels are used as a binary code to encode the address. With N labels or N wavelengths one can route the incoming payload to 2^N addresses. More addresses will not increase the label processing time. A very low latency (time to process and send a control signal to the switch) of $< 3\,\mathrm{ns}$ has been achieved in [14] to switch between 64 addresses (using 6 labels). One should note that $3\,\mathrm{ns}$ is still a very long time to optically buffer the payload. This long delay could eventually prevent a photonic integrated solution [15]. Using a long spiral using SOI waveguides, a $3\,\mathrm{ns}$ delay corresponds to a $30\,\mathrm{cm}$ delay line. With a typical loss of $3\,\mathrm{dB/cm}$, this would result in a total insertion loss of $90\,\mathrm{dB}$, which is not practical. However, waveguide losses are still improving, e.g. using a more advanced $300\,\mathrm{mm}$ platform waveguide losses are reduced to $0.45\,\mathrm{dB/cm}$. In this case a $30\,\mathrm{cm}$ delay line would only add $13.5\,\mathrm{dB}$ of insertion loss. Using rib waveguides, the propagation loss is further decreased to $0.27\,\mathrm{dB/cm}$ [16] with only $8.1\,\mathrm{dB}$ total insertion loss. However, one should minimize this processing time as much as possible since the total power consumption and hence the scalability is highly depending on the loss of this delay line. Furthermore, an extra power penalty can be expected from this high loss.

The duration of the labels is the same as the total length of the payload. As a consequence the optical label has a much smaller bandwidth than the payload and the detection becomes straight forward by using low-speed low-noise receivers (one says the label detection is asynchronous [14]). This in-band label technique is visualized in Fig.4.1 where four wavelengths are used which could encode 16

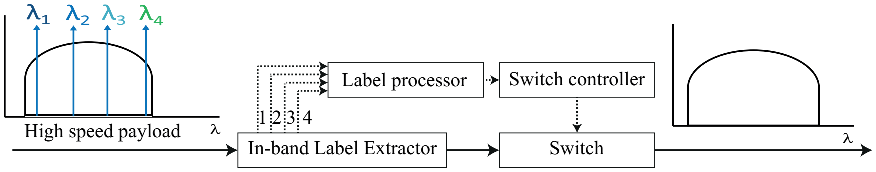

Figure 4.1: In-band label technique using 4 parallel coded multiple in-band wavelengths.

addresses in total. The label extractor extracts then these four wavelength and sends them to the label processor/switch controller. If the available optical bandwidth is limited one can easily increase the number of addresses through the use of RF tone coding [13]. With M different RF tones one can encode $2^{N\times M}$ addresses. The main drawback is the increase in processing latency by $7\,\mathrm{ns}$ which could prevent a fully photonic integrated solution as discussed earlier. Still, one should improve the processing time of the switch both to keep the latency small but also to not degrade the payload due to a high on-chip insertion loss. In the following we will position the envisioned label extractor in an all-optical packet switch.

4.1.2 A modular all-optical packet switch

Packets entering the OPS are labeled with forwarding information to properly configure the switch and set the packet destination. A novel modular wavelength division multiplexed (WDM) optical packet switch architecture using parallel multiplexed coding together with an in-band optical label technique has been proposed and demonstrated both numerically and experimentally by the COBRA group of the TU/e [13, 17]. This architecture will be used in this chapter. The essential parts are explained in the following but for a full description one is referred to [17].

In this architecture (shown in Fig.4.2(a)), there are N clusters of M server racks (with N and M arbitrary numbers) which can send information to each other. The information of all the servers is synchronized and wavelength division multiplexed. Each server rack in a certain cluster has a certain wavelength channel (M WDM packets denoted as λ_1 ... λ_M). Each cluster has one physical optical fiber to the optical switch module. The optical switch module has for each cluster a separate WDM optical module. Each module forwards the M WDM packets to N output ports, based on the information encoded in the optical label. Such an optical module is shown in Fig.4.2(b). In each of those optical modules, the M WDM packets are demultiplexed, e.g. by an arrayed waveguide grating (AWG), and each packet enters a $1 \times N$ optical switch module. This optical switch consists of a label extractor and a $1 \times N$ switch. The output port of the switch is set by a centralized switch controller. The centralized controller will make sure there is only one chan-

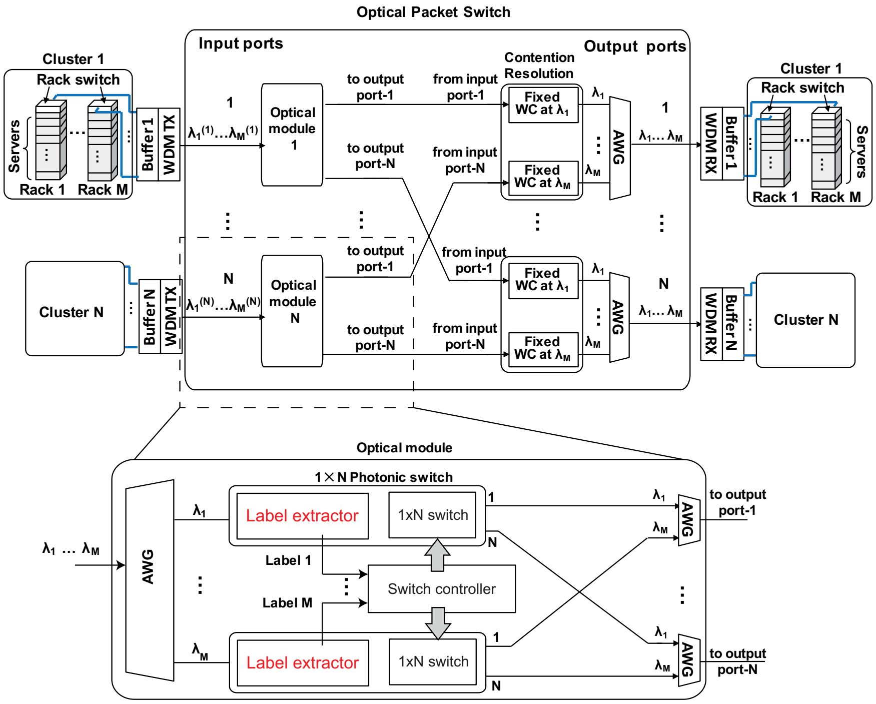

Figure 4.2: Example of a modular WDM optical packet switch architecture, demonstrated both numerically and experimentally in [13, 17].

nel going to the same destination port. If there is more than one WDM packet for a certain output port, a re-transmit request can be send to the server from which the transmitted packet was blocked. This means that contention occurs only for channels from the same input port. At the output port contention between channels coming from different input ports is prevented by the fixed wavelength conversion (WC). This allows the optical packet switch to have a modular architecture in which the optical modules are exact copies. The fixed WC can be based on cross-gain modulation in a semiconductor optical amplifier (SOA) (e.g. [3]). In [18], the experimental results for an 8×8 OPS optical module with forwarding operation of 8 input WDM channels at $40\,\mathrm{Gb/s}$ to 8 output ports with a record low latency of $25\,\mathrm{ns}$ were shown. A large optical packet switch with N=64 and M=64 (in total 4096 ports) has been numerically investigated in [17], showing a total throughput of $50\,\mathrm{Tb/s}$ and sub-microsecond latency.

4.2 Label extractor - Design & fabrication

To drastically decrease the size, unit cost and power consumption of the proposed OPS and to be able to compete with power efficient electronic switches, integration of the different optical building blocks is absolutely necessary. In [13] an optical packet switch built using integrated InP 1×4 optical wavelength-space switching modules was shown to exhibit a reduced power consumption but still used a discrete and bulky optical label processor. Enabling the proposed spectral-efficient in-band labeling requires narrowband filters to extract the low-speed labels from a high-speed payload. This filter could be an integrated ring resonator as was demonstrated in [19] were signals at $160\,\mathrm{Gb/s}$ were successfully switched. In that demonstration a single $\mathrm{Si_3N_4}$ ring resonator ring followed by an external arrayed waveguide grating was used to extract an in-band label consisting of two wavelengths.

In this work we demonstrate a four-wavelength in-band label extractor consisting of cascaded narrowband ring resonators implemented in a SOI waveguide platform. A higher-index contrast system such as SOI confines the light more strongly and hence allows smaller bending radii. In general, this allows fabricating narrowband filters with larger FSR. It also permits a higher integration density compared to lower-index contrast systems such as those based on InP or SiN based systems which is essential when scaling to larger port numbers. In Fig.4.3, a schematic of the design is shown. A label consisting of four in-band wavelengths is extracted by four cascaded narrowband ring resonators and converted into the electrical domain. The narrow bandwidth of the ring resonators enables the possibility to place the labels anywhere in the payload band which is an important improvement with earlier experiments.

In the framework of the ICT-BOOM project (running from 2008-2012), sev-

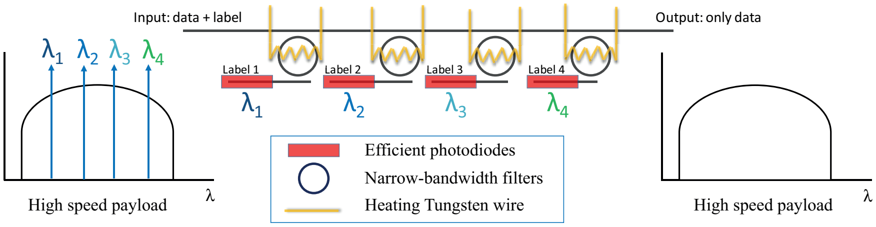

Figure 4.3: Schematic of the proposed 4 in-band label extractor.

Channel spacing	$0.1\,\mathrm{nm}$
Crosstalk (XT) [dB]	$\leq -20\,\mathrm{dB}$
Free spectral range (FSR)	$> 5\,\mathrm{nm}$
PD Responsivity	$1.1\,\mathrm{A/W}$
PD Dark Current	$\leq 5\,\mathrm{nA}$

Table 4.1: Specifications of UDWDM 4-channel InGaAs receiver.

eral design goals were set at the beginning of the project. The label extractor was described as an ultra-dense wavelength division multiplexing (UDWDM) demultiplexer with a very narrow channel spacing of $0.1\,\mathrm{nm}$ and a crosstalk below $-20\,\mathrm{dB}$. The free spectral range (FSR) of the ring resonators is set to be $> 5\,\mathrm{nm}$ such that only one resonance per filter is present within the $20\,\mathrm{dB}$ band of the payload (modulated at $160\,\mathrm{Gb/s}$). The photodiodes (PD) should have small dark current ($< 5\,\mathrm{nA}$) and have an high responsivity (R = $1.1\,\mathrm{A/W}$). The bandwidth of the photodiodes should be larger than $1\,\mathrm{GHz}$ but faster bandwidth would enable the switching of shorter packets. The specifications are listed in Tab.4.1.

The rest of the section about the design and fabrication of the label extractor is structured as follows. We start by discussing the full fabrication strategy in section 4.2.1. To place the achieved results in the right context, some preliminary work from PhD colleague Shen Zhen between 2008-2009 is reported in section 4.2.2 which has been a very useful starting point for the rest of the work. Next, the first generation of the UDWDM label extractor is discussed in section 4.2.3. Although the results were not sufficient, specific problems could be detected. New design strategies have led to the successful results of generation II, which are extensively reported in section 4.2.4 and partly published in [20].

4.2.1 Fabrication flow

The UDWDM demultiplexer was fabricated at imec on a $200\,\mathrm{mm}$ SOI wafer with $2\,\mu\mathrm{m}$ buried oxide (BOX) and $220\,\mathrm{nm}$ top c-Si layer. Two silicon patterning steps were carried out in which respectively $70\,\mathrm{nm}$ and $220\,\mathrm{nm}$ of the c-Si layer were locally etched to define fiber-grating couplers as well as the ring filter and the

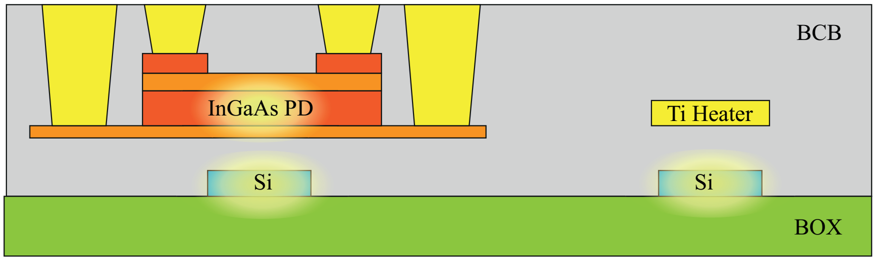

Figure 4.4: Overview fabrication strategy: schematic cross-section of the InGaAs photodetector (PD), titanium (Ti) heater, and silicon (Si) waveguides.

access waveguides. The evanescently coupled InGaAs photodiodes are integrated on the Si platform using an adhesive bonding technique, post-processed in the cleanroom facility of our group. The BCB thickness is chosen to be between $100 - 200\,\mathrm{nm}$ to maximize the coupling strength between the Si waveguide and the photodiode. Detailed processing details of the photodiodes can be found in chapter 3.

In Fig.4.4 one can find a cross-section of the InGaAs p-i-n photodiode heterogeneously integrated on top of the Si waveguides. The heaters consist of Ti/Au alloy (respectively $120\,\mathrm{nm}$ and $10\,\mathrm{nm}$) deposited on a $0.6 - 1.5\,\mu\mathrm{m}$ thick BCB layer to avoid optical absorption of the optical mode. The heater module is processed after the photodiode module. The final BCB opening and metal contacting is combined for the heaters and photodiodes.

4.2.2 Generation 0

The work described in this section was carried out by PhD colleague Zhen Sheng. To meet the narrow bandwidth goals set by the BOOM project, very small coupling between the bus and ring waveguides of the ring resonator is required. Assuming a waveguide propagation loss of $3\,\mathrm{dB/cm}$, the design goals (Tab.4.1) can be met with first order ring resonators with a radius of $17\,\mu\mathrm{m}$ and a 1% power coupling between bus and ring. The first-order ring resonators using the TE-strip waveguide were marked by serious wavelength-dependent resonance splitting [21]. A typical spectrum of a 4-channel UDWDM demultiplexer with random resonance splitting is shown in Fig.4.5(a). One can notice an insertion loss (IL) ranging from $-12.5\,\mathrm{dB}$ to $-18\,\mathrm{dB}$. Channel 3 seems to have even a higher IL but is probably due to the close spectral proximity of channel 2. In Fig.4.5(b), the best out of four resonances is shown. The asymmetric shape of the resonance is due to a bad characterization (too much optical power) and the resulting XT of $-15\,\mathrm{dB}$ reported in [21] is therefore wrong. In Fig.4.5(c), typical resonance splitting is shown (channel 2). We can conclude that even for peaks with no resonance split-

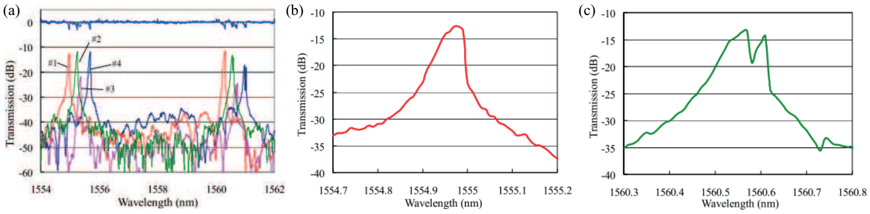

Figure 4.5: Generation 0: preliminary work around UDWDM implemented with first order ring resonators. Data taken from Zheng Sheng [21]. Unacceptable high IL and wavelength dependent resonance splitting has been detected.

ting, the IL is unacceptably high. Notice that the four ring resonators are exact copies from each other but the resonances are up to $0.7\,\mathrm{nm}$ away from each other. Therefore heaters will be necessary to tune the resonances to the expected spectral position. Titanium heaters were fabricated on top of the first-order ring resonator and a tuning efficiency of $0.04\,\mathrm{nm/mW}$ has been realized. However the maximum wavelength shift was $1.6\,\mathrm{nm}$, which is not enough to sweep over the whole FSR of $5\,\mathrm{nm}$. The photodiode itself has been fabricated and characterized separately from the demultiplexer chip. The responsivity has been measured to be $1.1\,\mathrm{A/W}$, also reported in [22]. However, a poor bandwidth of $600\,\mathrm{MHz}$ was found which is probably due to a high series resistance coming from a non-optimized process.

4.2.3 Generation I

Generation 1 (2009-2010) of the label extractor tries to solve the problems that were detected during the characterization of generation 0. A full characterization of generation I, i.e. the spectrum of the resonances tuned on the right spectral position is missing due to several design and processing problems as discussed further.

Design improvements To solve the high IL and low XT detected in generation 0 devices, second-order ring resonators were designed for their better trade-off between IL and XT with respect to first-order ring resonators. The new SOI design consists out of 22 slightly different 4-channel demultiplexers anticipating for different propagation losses in the ring resonators. For a $3\,\mathrm{dB/cm}$ waveguide propagation loss, the power coupling between bus and ring has been designed to 3.2% and between the two rings 0.029%. With a radius of $19\,\mu\mathrm{m}$ this results in a gap of respectively $255\,\mathrm{nm}$ between bus and ring waveguide and $550\,\mathrm{nm}$ between the two rings. The demultiplexers were designed in such a way that they could be characterized with a fiber array with a pitch of $250\,\mu\mathrm{m}$. A microscope picture of a fabricated device is shown in Fig.4.6(a), with a focus on one of the heaters

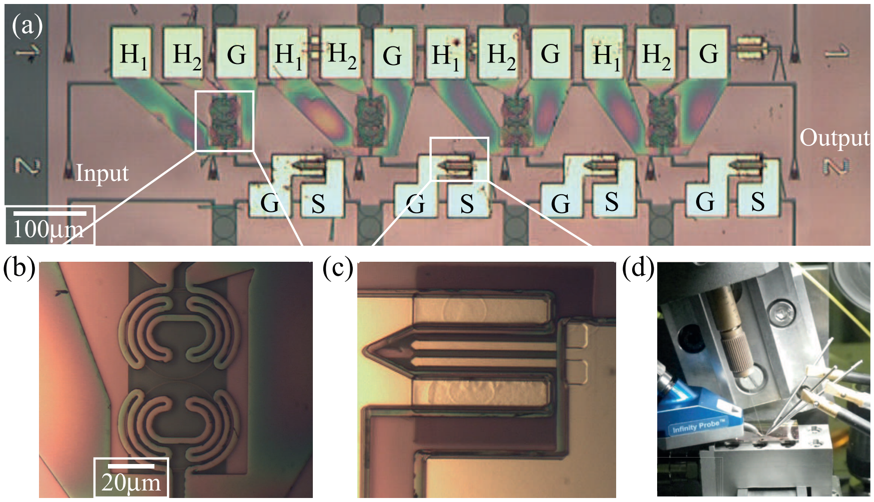

Figure 4.6: Microscope picture of the fabricated UDWDM label extractor (generation I), with a zoom-in on the double heater structure (b) and the photodiode in (c). A picture of how to measure this device is shown in (d).

(b) and the photodiode (c). Each second-order ring resonator has separate heating element for each ring resonator. Contact pads are labeled with H1, H2 and G, respectively annotating the two heater control signals ($H_{1/2}$) and the common ground (G). Practically, two heaters for one filter requires many driving signals and one needs a probe card to measure them simultaneously. A picture of a typical setup is shown in Fig.4.6(d), with a Cascade SG high-speed probe to measure the response of the photodiode and three DC probes to control the heaters separately.

Design problem: lack of test structures This design (mask set PICSOI31) was taped out only 2 months after the start of this work and was marked with many but typical shortcomings. First, test structures that can be characterized using a single fiber (instead of a fiber array) is much more flexible, which could have greatly helped the characterization of this design. We also forgot a reference photodiode positioned close to demultiplexer design, which is necessary to quantify the responsivity correctly.

Fabrication problem: BCB non-uniformity At that time bonding of a III-V die was performed manually, i.e. with manual and thus difficult to control pressure. In Fig.4.7(a), a microscope picture during fabrication is shown. The photodiodes are already defined but not yet the contact pads and most of the III-V die is etched away. From this figure a clear color variation is detected which corresponds to a change in BCB thickness. Using a small knife, BCB has been removed next to

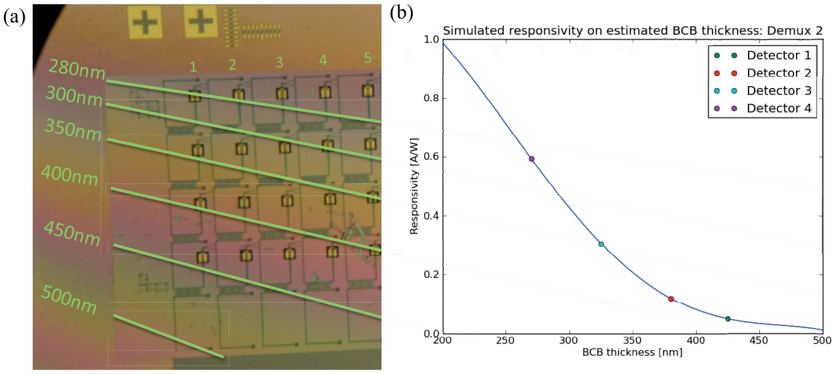

Figure 4.7: Illustration of the non-uniformity of the BCB layer. This is a microscope picture taken before the processing of the photodiode contact pads.

the sample. Using a profilometer we could measure the BCB thickness variation with respect to the underlying Si layer as labeled in Fig.4.7. A well-controlled BCB thickness is essential for a uniform photodiode responsivity. In Fig.4.7(b), the responsivities of the fabricated photodiodes from device number 2 are simulated based on this BCB thickness variation. The estimatated BCB thickness of respectively detector 1 is $425\,\mathrm{nm}$ and $270\,\mathrm{nm}$ resulting in an estimated responsivity of $0.05\,\mathrm{A/W}$ and $0.6\,\mathrm{A/W}$. This would result in approximately $10\,\mathrm{dB}$ lower response for channel 1 than for channel 4 which is unacceptable.

Photodiode problem: high series resistance Investigation of the forward IV curve showed that the photodiodes are marked by a very large series resistance of around $15\,k\Omega$. This corresponds to contact resistance of $0.08\,\Omega\mathrm{cm}^2$ which makes the bandwidth of the photodiode RC limited between $10 - 200\,\mathrm{MHz}$. Normal contact resistances are expected to be several orders of magnitude smaller $(10^{-5}\Omega\mathrm{cm}^2)$. The lack of test structures prohibited us to characterize the responsivity of the multiple photodiodes of the demultiplexer. The dark current of adjacent photodiodes is shown in Fig.4.8(a) and is below $5\,\mathrm{nA}$ at $-0.75\,\mathrm{V}$. However, it is clear from this graph that the dark current varies a lot between the different photodiodes and that the fabrication has a rather bad yield.

Filter characteristics In Fig.4.8(b), a typical optical-to-electrical (OE) spectrum of a single channel is shown (demultiplexer number 2 as shown in Fig.4.7). The integrated Ti heaters are used to optimize the channel response. H_1 and H_2 indicate the voltages applied to the two heaters of the double ring filter as explained in Fig.4.6. Because this is the last channel of the four cascaded second-order ring filters, some distortion from the previous channels can be expected. When no

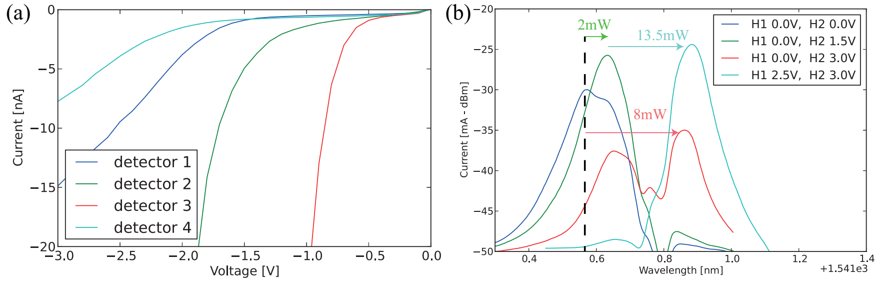

Figure 4.8: (a) Dark current curves of the measured photodiodes and (b) the OE response of channel 4 for different heater voltages.

voltage is applied (i.e. H_1=$0\,\mathrm{V}$ and H_2=$0\,\mathrm{V}$), one can see that the resonance is showing some splitting. This can be explained by the fact that both resonances of the second-order ring resonator are a little bit detuned from each other. In this case the deviation is rather limited but can be very large as well. E.g. a very local and small air void can arise during BCB planarization causing the resonances to detune severely. Applying $1.5\,\mathrm{V}$ to H_2, shifts one of the two resonances by $100\,\mathrm{pm}$ and increases the response with $5\,\mathrm{dB}$. This voltage corresponds to $2\,\mathrm{mW}$ power consumption and thus an efficiency of $0.05\,\mathrm{nm/mW}$ is achieved to shift one ring resonator. The resulting XT (right side) is $-14.2\,\mathrm{dB}$ at a channel spacing of $0.1\,\mathrm{nm}$. Increasing the voltage on H_2 to $3\,\mathrm{V}$, the shift is $0.35\,\mathrm{nm}$ and the power consumption is $8\,\mathrm{mW}$. Applying now $2.5\,\mathrm{V}$ to H_1, the entire resonance is shifted $0.25\,\mathrm{nm}$. The efficiency of the whole heater is thus $0.025\,\mathrm{nm/mW}$. Assuming a responsivity of $0.6\,\mathrm{A/W}$, the insertion loss of the filter is estimated to be $15\,\mathrm{dB}$. Part of this loss could come from the integrated heaters being situated too close to the optical waveguide.

Conclusion An overview of the results is listed in Tab.4.2. Many lessons can be drawn regarding design (demultiplexer test structures, ring resonators and photodiode) and fabrication (dark current yield and BCB uniformity). Different strategies to solve this problems are discussed in the next section (generation II).

4.2.4 Generation II

Due to the many problems that generation I encountered, we decided to start with a new Si circuit design. The design breakthrough to realize narrowband ring resonators (discussed in chapter 2) is implemented in generation II of the label extractor. Also, an improved contact mask with many test structures and an improved III-V to BCB die bonding technique were used. Results coming from this design were accepted as a contributed talk at the Asian Photonics Conference (2012) in

Specification	Design goal	Achievement
Channel spacing [nm]	0.1	-
Crosstalk (XT) [dB]	≤ -20	-15
Insertion loss (IL) [dB]	< 5	$10 - 15$
Free spectral range (FSR) [nm]	> 5	5
PD Responsivity [A/W]	1.1	$0.05 - 0.6$
PD Dark current [nA]	$\leq$	Highly varying
PD Bandwidth	1 GHz	$10 - 200$ MHz
Heater efficiency [nm/mW]	-	0.025

Table 4.2: Specifications and achievements of Generation I UDWDM 4-channel InGaAs receiver.

Guangzhou, China.

Ring design improvements Due to the lack of proper test structures, we could not fully investigate the cause of the high insertion loss of the narrowband second-order ring resonators. However, it was clear from a measurement point of view that second-order ring resonators where highly unpractical, especially when they are cascaded, because it requires the fine tuning of 8 heaters.

As explained in chapter 2, a more elegant solution to reach the filter specification is to use the quasi-TM mode instead of the quasi-TE mode. The use of the TM lowers significantly the backscattering on the surface roughness on the vertical sidewalls of the Si waveguide. It has been showed in chapter 2 that the TM-strip waveguide approach effectively decreases backscattering and makes resonances free of wavelength-dependent resonance splitting. This enabled us to use first-order ring resonators instead of second-order ring resonators and reaches the required narrowband behaviour. An alternative is to use the quasi-TE mode in a partially etched rib waveguide (TE-rib). Also this approach allows to lower the overlap with vertical sidewall roughness and has been proven to enable narrowband filters (chapter 2). In both cases the waveguide confinement decreases, requiring somewhat higher bend radii and hence limiting the free spectral range to $4.5 - 5\,\mathrm{nm}$.

The design and characterization is fully explained in chapter 2. Here, we shortly describe the demultiplexer design used in this generation. The TM-strip approach requires a waveguide dimension of height $220\,\mathrm{nm}$ and width $500\,\mathrm{nm}$ and the ring resonator is designed to have a gap between the bus and ring waveguide of $900\,\mathrm{nm}$ and a radius of $23\,\mu\mathrm{m}$. For the TE-rib approach the waveguide is defined using a partial etch of $70\,\mathrm{nm}$, the height of the rib is $220\,\mathrm{nm}$ and the width is $600\,\mathrm{nm}$. The coupling length of the racetrack ring resonator is $4\,\mu\mathrm{m}$ and the radius is $24\,\mu\mathrm{m}$. The gap between bus and ring waveguide is $550\,\mathrm{nm}$. All ports of the ring are tapered to strip waveguides to allow compact guiding of the light.

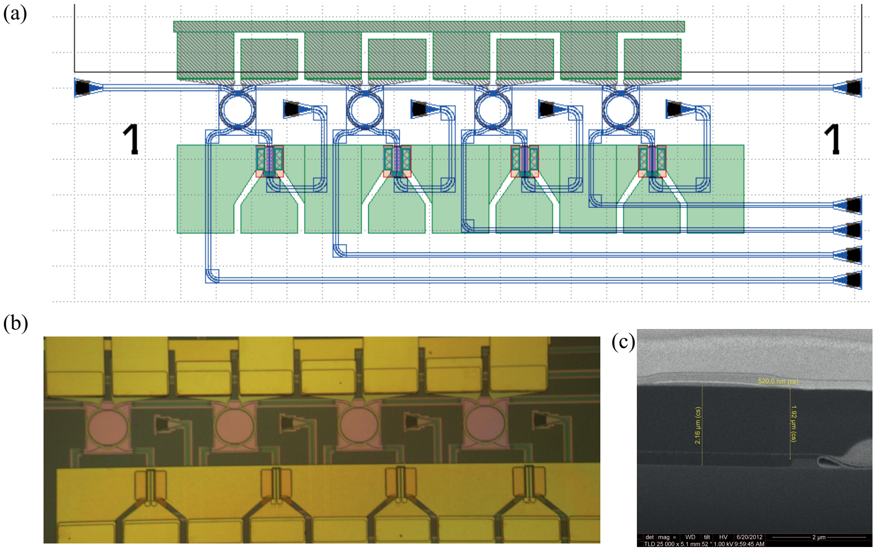

Figure 4.9: Design schematic and microscope picture of the integrated label extractor.

Photodetector improvements Since the origin of the high internal resistance was initially unknown, we have tried to tackle the problem in several ways. From a fabrication point of view, the process flow was adapted to minimize the chance of contamination of the surface prior to metal deposition to ensure a good metal to semiconductor contact and alloy formation. Also from a design point of view the III-V epitaxial layers were adapted to ensure the photodetector is more transit time limited than RC limited (as covered in chapter 3). This could enhance the bandwidth uniformity and at the same time improve the fabrication tolerances.

BCB uniformity improvement The cause of this problem originated in the way the III-V dies were attached to the SOI die. It was decided to switch from a manual based to a machine based bonding process. This helped to obtain more uniform bonding thicknesses and hence a uniform photodiode responsivity. This technique has been developed and optimized by PhD colleagues Stevan Stancovic and Shahram Keyvaninia [23]. Machine based bonding not only increased the uniformity of the BCB thickness but also allowed a thinner bonding thickness ($< 50\,\mathrm{nm}$ in comparison with $\pm 250\,\mathrm{nm}$ typically achieved for manual bonding) without decreasing the bonding yield. The thinner bonding thickness increases the coupling strength between waveguide and photodetector and thus allow shorter photodetector. Shorten the length of the photodetector lowers the total capacitance but increases the total resistance, leaving us with the same intrinsic RC.

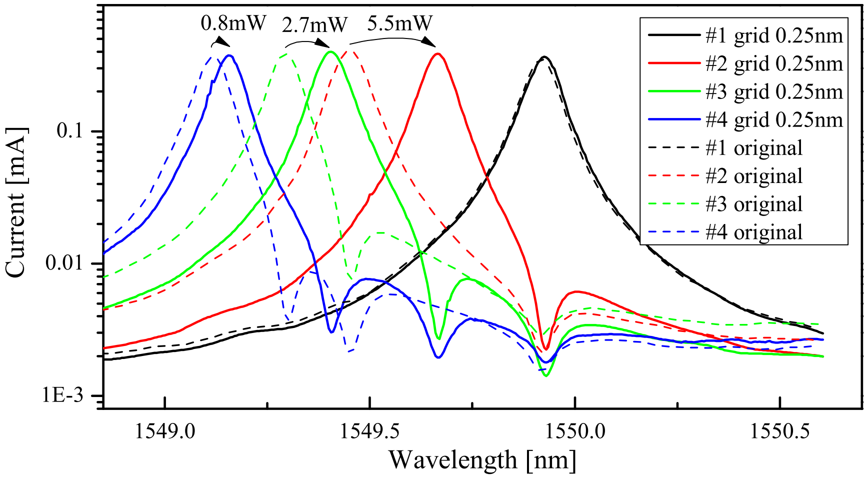

Figure 4.10: The optical-to-electrical spectrum of a four-channel UDWDM using a TE-rib approach with channels tuned on a $0.2\,\mathrm{nm}$ *grid and a crosstalk* $< -15\,\mathrm{dB}$ *XT.*

Optical-to-electrical spectrum - TE rib approach Devices fabricated using the TE-rib approach were characterized on a fully integrated chip and the resulting optical-to-electrical spectrum is shown in Fig.4.10. The filters are tuned to a uniform $0.25\,\mathrm{nm}$ grid with a resulting $-15\,\mathrm{dB}$ XT. Although this result is not meeting the specifications of $-20\,\mathrm{dB}$ XT on a grid of $0.1\,\mathrm{nm}$, this result is still very promising and a huge improvement with respect to generation I. Further improvements include the removal of the straight waveguide in the directional coupler of the ring, which decrease the ring performance as demonstrated in Fig.2.18 on page 2-37. The on-chip efficiency is $0.4\,\mathrm{A/W}$ and the external efficiency of the label extractor is $0.13\,\mathrm{A/W}$. The heater efficiency for the TE-rib ring resonators is $36\,\mathrm{pm/mW}$ and for this device $9\,\mathrm{mW}$ is needed to tune the heaters on the right grid.

Optical-to-optical spectrum - TM strip approach The TM-strip approach is optically characterized showing very good filter characteristics: a crosstalk on the $0.1\,\mathrm{nm}$ UDWDM grid of $-17\,\mathrm{dB}$ ($\mathrm{XT}_{0.1}$), a $20\,\mathrm{dB}$-bandwidth (BW) of $0.3\,\mathrm{nm}$ and an insertion loss (IL) of only $3\,\mathrm{dB}$, which is shown in Fig.4.11. The heaters are performing inefficient ($5.3\,\mathrm{pm/mW}$) because of the low confinement in the Si-waveguide and the thick BCB spacer layer ($> 1.9\,\mu\mathrm{m}$). This is an important drawback of the TM-strip approach but could be resolved using alternative approaches for heater integration, e.g. by using side heaters as demonstrated in the next chapters. The FSR of the filter (for both approaches) is $5\,\mathrm{nm}$.

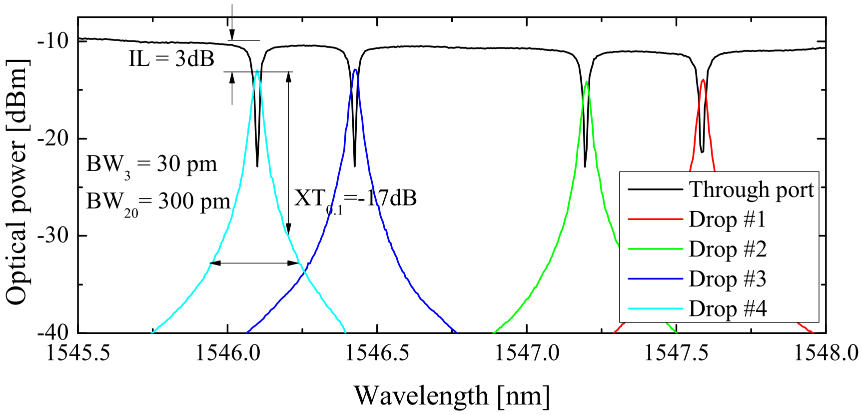

Figure 4.11: The optical-to-optical TM-strip approach with no post-processing. Filters exhibit excellent filter characteristics.

Photodiode response The detector was characterized for both polarizations as a standalone component and in a demultiplexer configuration. The responsivity of the detector is $1.06\,\mathrm{A/W}$ (quasi-TM) and $1.23\,\mathrm{A/W}$ (quasi-TE) respectively corresponding to an 85% and 98% efficiency. The dark current of the detector ranges between $3-5\,\mathrm{nA}$ for a bias voltage of $-3\,\mathrm{V}$ which is a huge improvement with respect to earlier generations. This bias is needed to work under high power illumination and/or at high speed, otherwise a zero bias is sufficient to reach the maximum responsivity. In section 3.2 - Fig.3.18, a $12\,\mathrm{Gb/s}$ open-eye diagram of this photodiode (after annealing the contacts) is shown.

Conclusion In Tab.4.3, a full overview of the achieved results has been listed. The second generation is marked by a very good improvement regarding ring characteristics with the best performance achieved by the TM-strip approach, a thin and highly uniform BCB thickness due to machine bonding, highly responsive and low dark current high-speed photodiodes.

4.2.5 Packaging

The goal is to package the UDWDM receiver with four high-speed trans-impedance amplifiers (TIA). The packaging design and assembly has been performed at the Fraunhofer Institute for Reliability and Microintegration (IZM) with the expertise of Tolga Tekin and his colleagues. The wire bonding is performed at the Fraunhofer Institute HHI by Detlef Pech. The TIA's were provided by Lars Zimmerman from IHP).

The demultiplexer design from generation II is first further optimized for pack-

Spec	Goal	GenI	GenII TM-strip	GenII TE-rib
CS [nm]	0.1		0.1	0.25
XT [dB]	≤ -20	-15	-17	-15
IL [dB]	< 5	10 – 15	3	5
FSR [nm]	> 5	5	5	5
PD R [A/W]	1.1	0.05 – 0.6	1.1	1.25
PD DC [nA]	≤ 5	High	3 – 5	3 – 5
PD BW [GHz]	1	< 0.2	10	10
Eff [nm/mW]	-	0.025	0.005	0.036

Table 4.3: Specifications and achievements of generation 1 and 2 (GenI/II) of the UDWDM 4-channel InGaAs receiver. Following abbreviations are used for the photodiode (PD) responsivity (R), dark current (DC) and bandwidth (BW) and heater efficiency (Eff).

aging purposes. In the packaging process flow, a relatively large fiber array (V-groove technology) is used to align the optical fiber to the SOI fiber coupler. Therefore we need an extension of the power lines (heaters) and high-speed coplanar waveguide lines (photodetectors) over several millimeters. Few extra post-processing steps are introduced. First, an extra planarization layer of BCB is used that will act as an insulation layer between the two metal layers. Vias through the BCB are defined by normal lithography and a dry-etch step is used to open these vias. The long metal connecting lines are defined by lithography and an thick layer of gold (Au) is deposited. After metal lift off, the UDWDM is ready to be packaged. A $2\,\mathrm{cm} \times 2\,\mathrm{cm}$ ceramic sub mount has been designed according to our SOI chip size. The extended coplanar waveguides of the photodiode array and the 5 signal lines from the heaters are wire bonded to this ceramic sub mount design. An overview of the fully packaged UDWDM label extractor is shown in Fig.4.12 with in (a) a top view and (b) from a birds-eye perspective a zoom on the SOI chip. Four integrated $10\,\mathrm{Gb/s}$ TIA's are integrated on top of the same sub mount. The effective impedance is converted from an estimated $20\,\Omega$ of the coplanar waveguides, to a $50\,\Omega$ standard input impedance of the TIA, using a coplanar stub. This impedance matching is narrowband and optimized for a bandwidth of $1\,\mathrm{Gb/s}$. Each TIA has a differential output (SMA connector).

To control the on-chip heaters, 5 DC bias lines are provided: 1 common ground and 4 signal lines to control the 4 heaters. Each TIA is controlled by several bias voltages to control the jitter, bias and gain.

The primary reason to use a TIA is to have a higher output voltage. In the following we will estimate the efficiency of the whole package. Due to time constraints we were not able to test the sample before the fiber array was attached. What follows is an estimation based on reference structures from a different chip. The photodiodes using a TM polarization are estimated to have an internal responsivity of $1.08\,\mathrm{A/W}$. With a fiber coupler loss of $-6\,\mathrm{dB}$, the external efficiency of

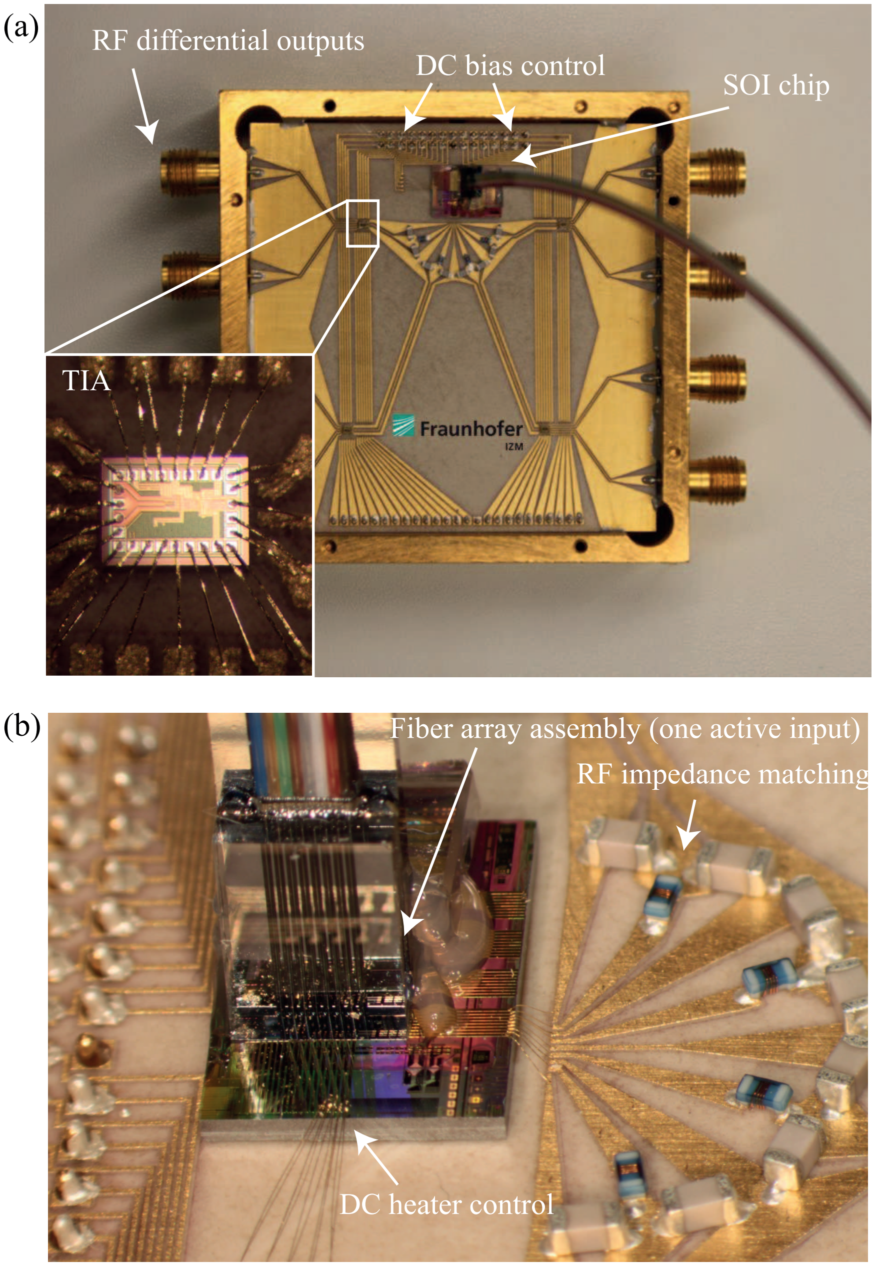

Figure 4.12: Picture of the packaged label extractor. (a) Top view (b) zoom in on the chip.

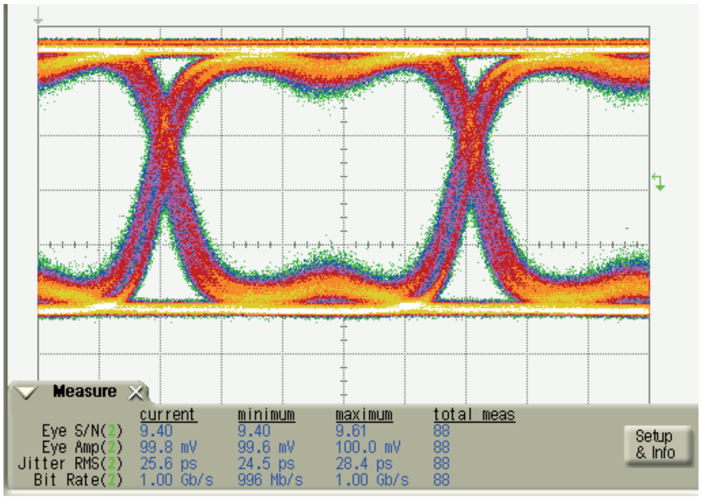

	current	minimum	maximum	total meas
Eye S/N(2)	9.40	9.40	9.61	88
Eye Amp(2)	99.8 mV	99.6 mV	100.0 mV	88
Jitter RMS(2)	25.6 ps	24.5 ps	28.4 ps	88
Bit Rate(2)	1.00 Gb/s	996 Mb/s	1.00 Gb/s	88

Figure 4.13: The electrical open-eye diagram of one wavelength of the label.

the TM photodiode is $0.275\,\mathrm{A/W}$. The IL of the ring resonators is estimated to be $-5\,\mathrm{dB}$ and thus the total responsivity is estimated to be $0.09\,\mathrm{A/W}$. In Fig.4.13, a clear open-eye diagram of a label modulated at $1\,\mathrm{Gb/s}$ is shown.

The large signal analysis is performed using a $20\,\mathrm{GHz}$ modulator driven by a 2^{31-1} pulse. The eye amplitude is $100\,\mathrm{mV}$ but the on and off levels are saturated around this value. An optical input of $8.5\,\mathrm{dBm}$ ($7.08\,\mathrm{mW}$) is used and thus an external efficiency of $0.35\,\mathrm{A/W}$ has been achieved. By comparing this with the (estimated) external responsivity of $0.09\,\mathrm{A/W}$ achieved without the TIA integration, we can conclude the TIA showed gain of almost a factor 4. Increasing the bit rate to $2\,\mathrm{Gb/s}$ resulted in a nearly closed eye diagram due to the narrowband impedance matching circuit between the SOI chip and the TIA. Note that only one channel is shown. That is because the TIAs were very difficult to drive, and the results shown in Fig.4.13 were only achieved after pushing the TIAs to the limits. Testing of the other channels ended in a device failure.

4.2.6 Conclusion

An ultra-dense WDM demultiplexer with $0.1\,\mathrm{nm}$ and $0.25\,\mathrm{nm}$ channel spacing was designed using the TM-polarization with strip waveguides and using the TE-polarization with rib waveguides to improve the filter characteristics using standard waveguides. From a technological point of view, huge improvements in the quality and reliability of the processing of the heterogeneously integrated InGaAs photodetectors were achieved with the following milestones:

1. 99% III-V/BCB bonding yield

2. $50\,\mathrm{nm}$ thick BCB layer with high uniformity
3. $10\times$ decrease in series resistance and PD bandwidth

This results in very promising device performances. The InGaAs photodetector is heterogeneously bonded on a SOI platform and has a very good efficiency for both TM and TE polarization, respectively $1.05\,\mathrm{A/W}$ and $1.25\,\mathrm{A/W}$.The dark current is low ($< 5\,\mathrm{nA}$ for $-3\,\mathrm{V}$). A successful packaging the UDWDM with a TIA array showed a clearly open-eye diagram at $1\,\mathrm{Gb/s}$ with an overall external efficiency of $0.35\,\mathrm{A/W}$.

The performance of such an UDWDM demultiplexer acting as an in-band label extractor for all-optical packet switching is investigated in the next section (section 4.3). We packaged the demultiplexer initially to ease the system experiments since in that case no optical setup or electrical probes were needed anymore. However, the problems with the failure of some of the integrated TIAs forced us to use optical-to-optical demultiplexers, without III-V or heater integration. Using the integrated photodiodes to convert the optical labels to the electrical domain without an integrated TIA is giving a worse signal-to-noise ratio in system experiment than using the optical-to-optical chip variant and having the opto-electronic conversion externally performed by a low-noise photoreceiver.

4.3 A four-channel in-band label extractor for 160 Gb/s optical packets

In this section, a four-channel UDWDM is used to extract a label consisting of four wavelengths from $160\,\mathrm{Gb/s}$ optical packets. This experiment is performed in the COBRA labs of the Eindhoven University of Technology (TU/e) of Prof. Harm Dorren using the expertise of Jun Luo, Nicola Calabretta and Stefano Di Lucente. The ring resonators are using the low-loss and less-confined quasi-TM mode and can be used to create resonances with a bandwidth as narrow as $17\,\mathrm{pm}$. This TM-strip waveguide approach has been extensively characterized in section 2.4.3. The performance of the ring regarding insertion loss, extinction ratio and BW is shown to have a large influence on the quality of the extracted label and forwarded payload and a trade-off between different devices and parameters is studied. The minimum required label power relative to the payload to reach a certain bit-error rate is also investigated. We found that this power depends on the spectral position of the label with respect to the center of the payload. The following results were submitted for publication in Journal of Lightwave Technologies.

To explore the effect of the bandwidth of the ring resonator, the gap between the bus and ring waveguide was swept between $0.65\,\mu\mathrm{m}$ and $1.1\,\mu\mathrm{m}$. All four rings were designed equally but due to some local non-uniformity the resonances of the

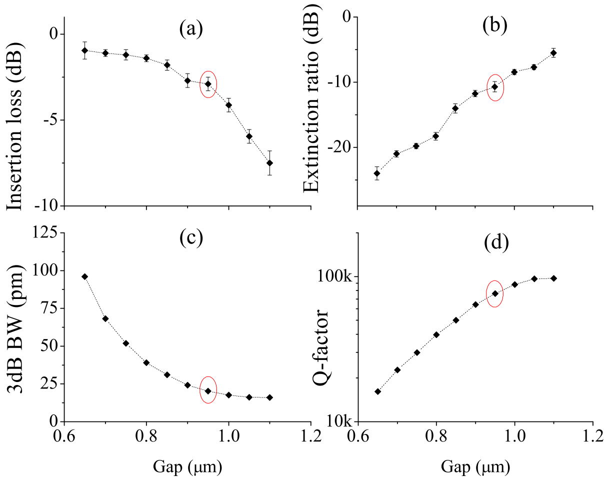

Figure 4.14: Overview of the main characteristics of the ring resonators, with (a) the insertion loss, (b) the extinction ratio, (c) the 3dB bandwidth (BW) and (d) the Q-factor, all as function of the gap width. For a larger gap, the insertion loss and Q-factor increase, while the extinction ratio and bandwidth decrease. The performance parameters for the chosen device with gap $0.95\,\mu\mathrm{m}$ *are denoted with a circle.*

ring resonator are not overlapping. The quasi-TM mode is particularly sensitive to height deviations of the silicon waveguide due to its tight vertical confinement of the electrical field.

We start this section with the characterization of the ring resonator and discussing how the different filter specifications change in function of the bus-to-ring waveguide coupling. Then, using the optimized ring resonators, we demonstrate the extraction of four in-band labels from a $160\,\mathrm{Gb/s}$ payload.

4.3.1 Characterization of the ring resonator

The label extractor was characterized using a tunable laser with a resolution of $1\,\mathrm{pm}$ centered around $1550\,\mathrm{nm}$. Fig.4.14 shows how the main characteristics of the label filter vary as function of the bus-to-ring waveguide gap, with (a) the insertion loss (IL), (b) the extinction ratio (ER) defined by the drop power at resonance with respect to off resonance, (c) the $3\,\mathrm{dB}$ BW and (d) the Q-factor.

These results show that there is a trade-off between efficiency of the label extraction and power penalties induced on the forwarded payload. To minimize the power penalty on the payload the ring resonators with the smallest bandwidth are preferred since these will erase the smallest amount of signal power of the payload. In Fig.4.15, the effect of the resonance bandwidth on the payload is investigated. The BER of the payload with a fixed input power versus the Q-factor of the four

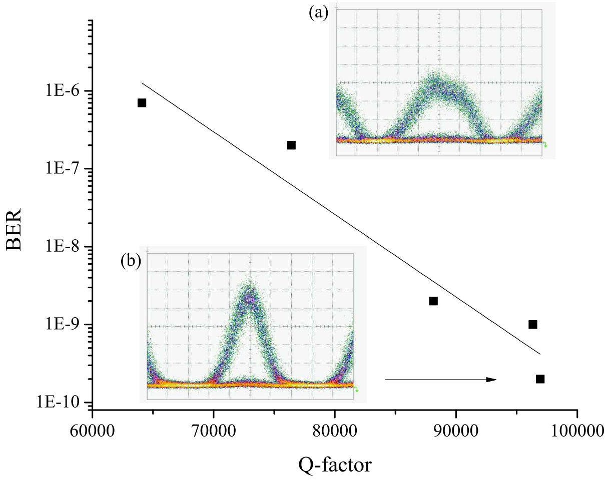

Figure 4.15: The relationship between the BER of the payload and the bandwidth (Q-factor) of the four label extractors. The power of the payload is kept constant and received as $-9\,\mathrm{dBm}$*. The larger the Q-factor, the less signal power of the payload is erased and thus the better the BER.*

rings is plotted. The full setup is explained in the following section (section 4.3.2). Note that no labels were added to the payload in this case. The resonance wavelengths of the ring resonators are different for each device but all of them are close to the center of the payload and none of them is overlapping with another. One can see that the BER of the payload is indeed improving drastically for increasing Q-factor as expected, which is the result of both a smaller ER and a more narrow BW for the higher Q-factor devices.

Another positive effect of using ring filters with a smaller bandwidth is the decreasing fraction of the payload that is found in the dropped label, resulting in an improved optical signal to noise ratio for constant label and payload input power. However, at the same time the IL becomes larger (Fig.4.14a) exceeding $5\,\mathrm{dB}$ for a gap $\geq\ 1.05\,\mu\mathrm{m}$. This can be understood from the fact that the light is longer in the ring before it can exit the ring and therefore exhibits more attenuation due to waveguide losses. For the same reason also the ER is smaller for narrowband ring resonators. This results in more power of the label remaining in the payload and thus potentially lowers the quality of the payload.

Based on these figures of merit, we choose to use the device with ring resonators with gap of $0.95\,\mu\mathrm{m}$ to perform a system test. The spectral characteristics of this label extractor are shown in Fig.4.16. The FSR is $5.5\,\mathrm{nm}$, the IL is between $2.5-3.5\,\mathrm{dB}$ depending on the channel and the ER is $10\,\mathrm{dB}$. The non uniformity between the channels IL and ER is most likely coming from small deviations in waveguide losses. The quality factor (Q) of each ring resonator is around 76000,

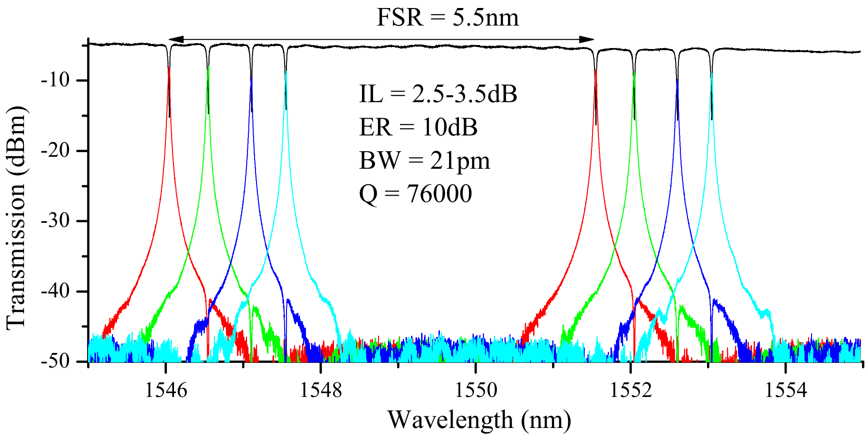

Figure 4.16: Filter characterization of the 4-channel label extractor based on high-Q ring resonators using the quasi-TM mode.

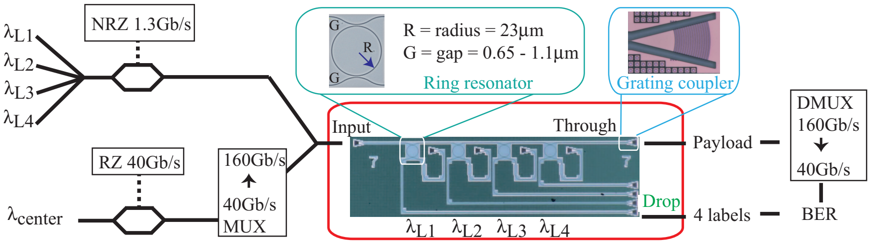

Figure 4.17: The setup consisting of label and payload creation, coupled together into the DUT. After label extraction the payload is demultiplexed to $40\,\mathrm{Gb/s}$ for BER measurements.

corresponding with a $3\,\mathrm{dB}$ BW of $21\,\mathrm{pm}$.

4.3.2 Label extraction experiment

The experimental setup employed is shown in Fig.4.17. The small bandwidth of the filters requires a stable temperature which is ensured by a temperature-controlled chip stage. The spectrum of the label extractor input signal consisting of a $160\,\mathrm{Gb/s}$ modulated payload and four labels modulated at $1.3\,\mathrm{Gb/s}$ is shown in Fig.4.18(a). The payload is generated by time-quadrupling a $40\,\mathrm{Gb/s}$ data stream consisting of 256 return-to-zero bits into a $160\,\mathrm{Gb/s}$ data stream using a passive pulse interleaver. Each pulse has a duration of $1.5\,\mathrm{ps}$ resulting in a $20\,\mathrm{dB}$ bandwidth of the payload $5\,\mathrm{nm}$. The center wavelength of the payload is $1552.2\,\mathrm{nm}$ and has a total input power of $3.7\,\mathrm{dBm}$.

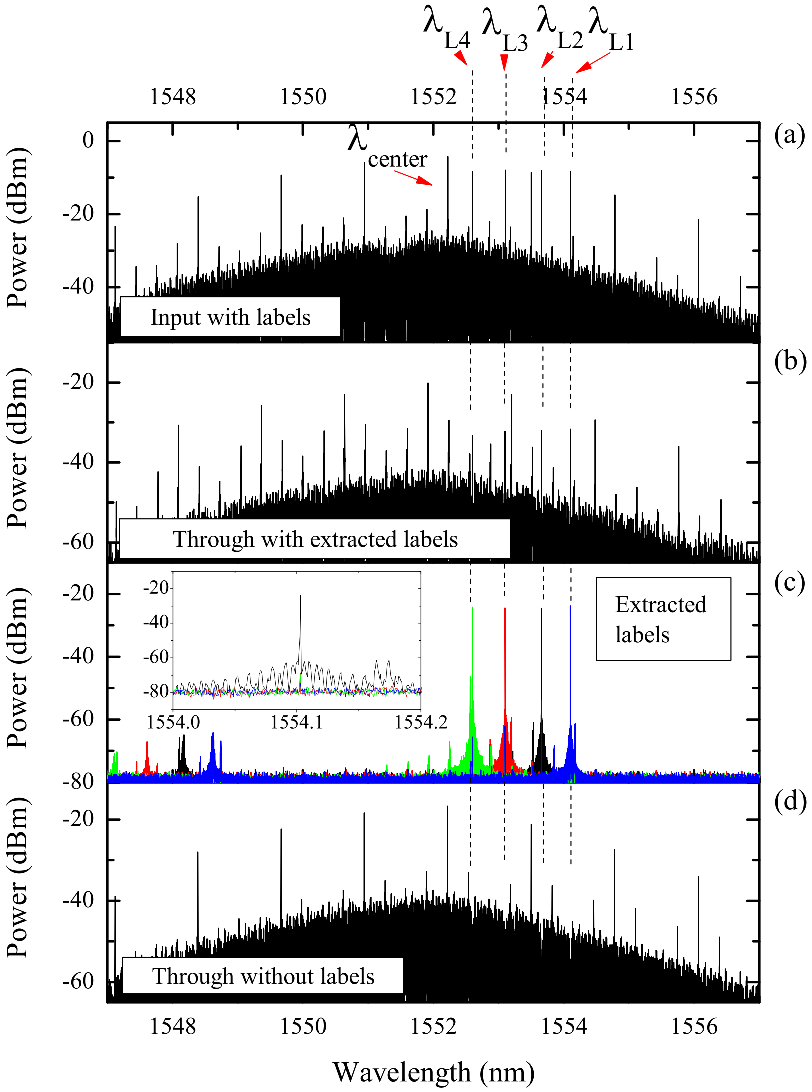

Figure 4.18: Optical spectra from the input and output ports of the label extractor with in (a) the input spectrum of the label extractor consisting of a $160\,\mathrm{Gb/s}$ *modulated payload signal centered at* $1552.2\,\mathrm{nm}$ *and four* $1.3\,\mathrm{Gb/s}$ *modulated label signals, placed in-band close to* λ_{center} *of the payload and the output spectra of (b) the through port and (c) the four drop ports containing the WDM label. In (d) the through port of the label extractor of only the payload as input (no label).*

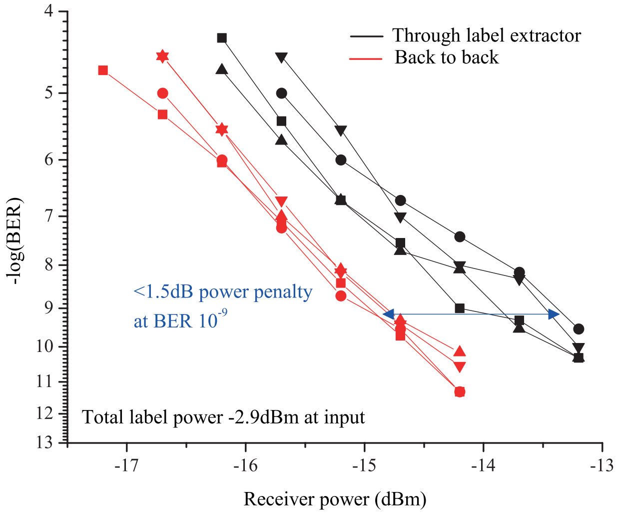

Figure 4.19: Bit-error rate measurements of the payload after label extraction. The power penalty introduced compared with the payload without labels before the device (denoted as back-to-back) is less than $1.5\,\mathrm{dB}$.

The four labels are generated with four tunable continuous-wave lasers and are placed right on the resonances of the ring filters, with wavelengths as denoted in Fig.4.18(a). The power of each label is set to $-8.9\,\mathrm{dBm}$ making the total label power equal to $-2.9\,\mathrm{dBm}$. At this power level, the payload after label extraction is error free (error rate = 10^{-9}). The output spectrum of payload after label extraction, measured at the through port of the cascaded ring filters, is shown in Fig.4.18(b). Each label is dropped by $\approx 10\,\mathrm{dB}$ with respect to the payload, which corresponds to the ER of the ring resonator plotted in Fig.4.14. In Fig.4.18(d), the output spectrum of the payload is shown without the WDM label. The total output power of the payload is $-9.2\,\mathrm{dBm}$ at the through port of our device, showing a total IL of $12.9\,\mathrm{dB}$. We can contribute most of the loss to the grating couplers.The output spectra measured at the drop ports of the ring filters are plotted in Fig.4.18(c). Each WDM-label signal has an amount of noise coming from the payload signal. One can see that the amount of noise is larger for label 4, which is located just next to the center of the payload ($0.4\,\mathrm{nm}$) than for label 1, located $1.9\,\mathrm{nm}$ away from the center. One can also see a smaller amount of noise at shorter wavelengths coming from the adjacent resonances of the ring filters. The quality of the payload after label extraction is assessed through a bit-error rate measurement of the four demultiplexed $40\,\mathrm{Gb/s}$ signals and is compared with the case where the payload without labels is sent directly to the receiver (denoted as back-to-back). The results are shown in Fig.4.19. One can see that the power penalty introduced by the label extractor is $< 1.5\,\mathrm{dB}$. This power penalty partly results from the fact

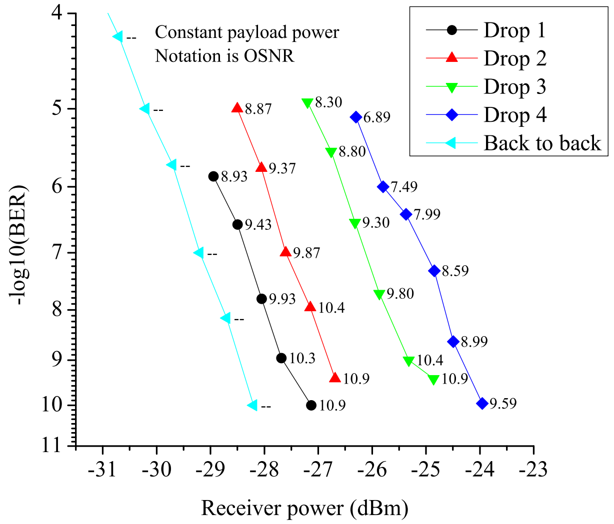

Figure 4.20: Bit-error rate measurements of the four labels compared with the input condition of the label (back-to-back). The power of the payload is kept constant to provide more insight based on the optical signal-to-noise ratio (OSNR). Label 1 has a smaller power penalty then label 4 due to its spectral position further away from the center of the payload.

that some signal power of the payload is filtered out when passing through the label extractor and partly from the four labels which are not perfectly removed and therefore are adding an extra noise floor to the payload.

The quality of the four in-band labels after extraction from the payload is evaluated as well and compared to the input condition of the label, denoted as back-to-back in Fig.4.20. To provide more insight, only the power of the label is changed while keeping the power of the payload constant. Since the signal bandwidth of the label modulated at $1.3\,\mathrm{Gb/s}$ is small ($3\,\mathrm{dB}$ BW of $7.2\,\mathrm{pm}$), no distortion is expected from the ring resonator with a $3\,\mathrm{dB}$ BW of $21\,\mathrm{pm}$. In other words, the optical lifetime of the signal in the ring is short enough to not affect the signal quality of the label. The only noise is coming from the fraction of the payload passing through to the drop port. Increasing the power of the payload therefore decreases the optical signal-to-noise ratio (OSNR) and thus the bit error rate (BER). This ratio is defined by the amount of label power divided by the payload power both measured separately at a certain drop port of the label extractor and is denoted explicitly for each data point in Fig.4.20. The difference in spectral position with respect to the center wavelength of the payload has a clear impact on the power penalty of the different labels. Label 1, which is further away from the center wavelength, only has a power penalty of approximately $1\,\mathrm{dB}$ while label 4, which

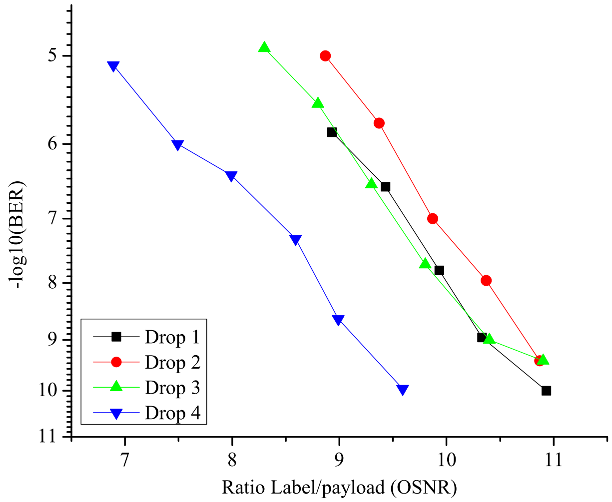

Figure 4.21: The bit-error rate versus the optical signal-to-noise ratio (OSNR) for the different labels, each for different payload and label power. Label 1, 2 and 3 are following a similar trend, where as label 4 has a slightly different trend due to close spectral distance to the center of the payload.

is near the center of the payload, has the largest power penalty of $4\,\mathrm{dB}$. One can also see that an OSNR close to 11 is a necessary condition to achieve error-free (EF) operation of the label (i.e. error rate = 10^{-9}), independent from the spectral position of the label. An exception is label 4, where the OSNR required for EF operation is only 9.5, which is probably due to the fact that this label is very close to the center of the payload.

The relationship between the BER and the OSNR is plotted in a different way in Fig.4.21, where one can indeed see that label 1, 2 and 3 are following the same trend while label 4 is shifted. The power of each label can now be adjusted depending on the spectral distance away from the center wavelength and on the required BER. The spectra of the EF received labels are plotted in Fig.4.22 with input powers of $-10.1\,\mathrm{dBm}$, $-9.6\,\mathrm{dBm}$, $-7.4\,\mathrm{dBm}$ and $-5.9\,\mathrm{dBm}$ for respectively label 1, 2, 3 and 4. This brings the total power of the 4-channel label to $-1.89\,\mathrm{dBm}$ which is $1\,\mathrm{dB}$ more than the total label power used initially to assess the quality of the payload. Fig.4.22 also shows the eye diagrams of the four different labels at EF operation, plotted on the same scale, where label 4 has indeed the largest noise level.

If the system requires smaller label input powers, e.g. due to power limitations, one can shift the resonances with respect to the payload and work at lower power penalties for the labels.

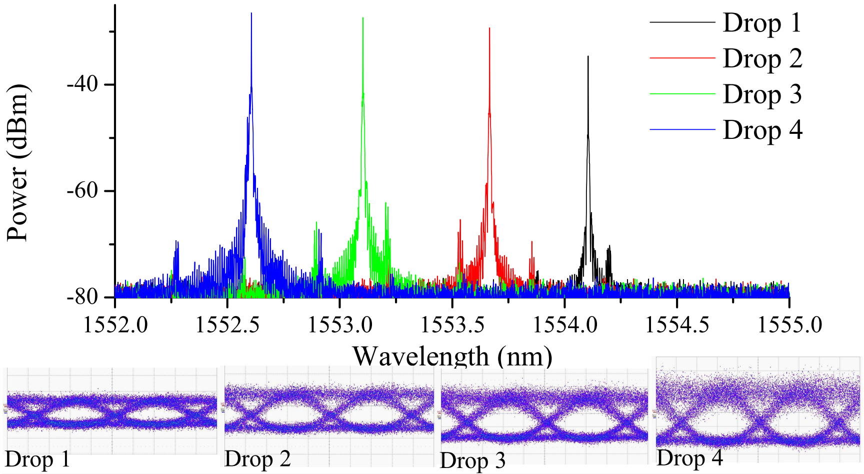

	Drop 1	Drop 2	Drop 3	Drop 4
Label input power (dBm)	-10.1	-9.6	-7.4	-5.9
Total output power (dBm)	-27.5	-26.9	-24.8	-23.9
Payload output power (dBm)	-38.4	-37.9	-36.1	-34
OSNR (Power label/payload)	10.93	10.87	10.9	9.6

Figure 4.22: The spectra of the four received labels at error free (BER = 10^{-9}) condition. The signal power of the different labels before and after the chip are denoted in the table, as well as the received amount of payload per label channel and the resulting optical signal-to-noise ratio (OSNR).

4.3.3 Conclusion

In this section an in-band label extractor based on narrowband silicon ring resonators using the low-loss quasi-TM mode was investigated. A trade-off between different ring resonator designs regarding relevant filter specifications such as insertion loss, extinction ratio and bandwidth is made. The selected device consisting of four cascaded ring filters with an insertion loss of $3\,\mathrm{dB}$, and extinction ratio of $10\,\mathrm{dB}$ and a bandwidth of $21\,\mathrm{pm}$, was shown to be able to extract four in-band labels modulated at $1.3\,\mathrm{Gb/s}$ from a $160\,\mathrm{Gb/s}$ payload. The quality of the payload as well as the quality of the four labels was evaluated showing error free operation at $< 1.5\,\mathrm{dB}$ power penalty for the payload. The power penalty of the label depends on the exact spectral position with respect to the center of the payload and ranges between $1\,\mathrm{dB}$ and $4\,\mathrm{dB}$ in our study. It has been shown before that filter position can be tuned using integrated heaters [20]. This gives the designer the freedom to optimize the exact spectral position of the labels based on system requirements regarding bit-error rate, power limitations, amount of labels etc. Positioning extra labels further from the center will not add extra distortion to the payload and lower label powers can be used. The amount of labels can then further be multiplied by using several RF tones [17, 24] making this label approach flexible and scalable in terms of amount of labels.

4.4 Demultiplexer for 40Gb/s optical packets and in-band label extractor

In this section we demonstrate a compact integrated $40\,\mathrm{Gb/s}$ packet demultiplexer integrated with a single in-band label extractor. One can either add extra wavelength labels [24] and/or modulate this one label with RF tones [17] to create up to 32 addresses. The $4\times$ lower bit rate of the payload with respect to the previous section makes it relatively more difficult to position a narrowband filter within the spectrum of the payload. That is because relatively more payload power is dropped due to a smaller payload spectral bandwidth. The desired functionality is realized using a $32 \times 200\,\mathrm{GHz}$ AWG filter followed by a ring resonator using a TE-strip approach. The potential advantage of using the TE-rib approach instead of the TM-strip approach is a more efficient (top) heater as has been shown in section 4.2.4. Experimental results confirmed a channel crosstalk lower than $18\,\mathrm{dB}$ and error-free operation with less than $0.5\,\mathrm{dB}$ penalty after the AWG and the label extractor filtering. Also the label, modulated at $1.3\,\mathrm{Gb/s}$ has been error-free detected after the label extracted with a power penalty of $0.5\,\mathrm{dB}$. The chip was designed by colleague Andrea Trita (based on the AWG simulation expertise of Shibnath Pathak [25]). The following results were accepted for a contributed talk at the European Conference and Exhibition on Optical Communication (ECOC)

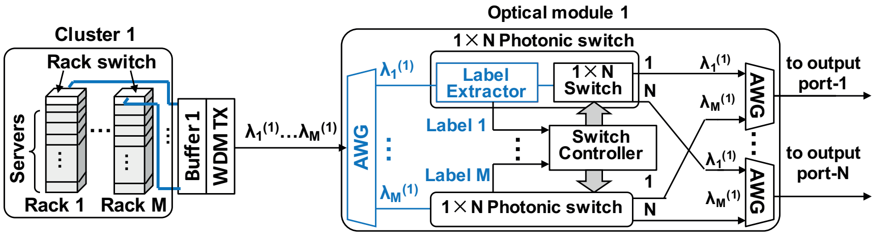

Figure 4.23: Architecture of the modular WDM OPS with in blue the demonstrated functionality in this work.

2013 in London [26]. In fig.4.23, the presented functionality is shown in blue.

4.4.1 Design

The label extracting ring resonator must be narrowband in order to not distort the payload and to minimize the crosstalk of the payload on the label as been shown in previous section 4.3. The ring resonator is using the TE-rib waveguide approach as discussed extensively in section 2.4.2. To realize the rib, a shallow etch step of $70\,\mathrm{nm}$ is used. This etch step is also used to realize input and output fiber grating couplers as well as the star-coupler of the AWG [25, 27]. An AWG consist of two free propagation regions (which are known as star-couplers) and an array of waveguides with successive increment of length. We used shallowly etched (or rib) waveguide apertures as inputs and outputs of the star-couplers to reduce the reflections. To design the $32 \times 200\,\mathrm{GHz}$ AWG, 90 waveguides were used in the array. A microscope picture can be found in the inset of Fig.4.24. The radius of the ring resonator is $35\,\mu\mathrm{m}$ which corresponds to a free spectral range (FSR) of $2.92\,\mathrm{nm}$. This FSR is large enough to avoid any extra distortion of the incoming payload. The waveguide width of the ring resonator is $450\,\mathrm{nm}$ and the gap between bus and ring waveguide is $600\,\mathrm{nm}$. A microscope picture can be found in the inset of Fig.4.25. In section, we have seen that rib waveguides using broader waveguides $(650 - 700\,\mathrm{nm})$ have smaller bend and propagation losses which will improve the performance of the ring resonator further.

4.4.2 Device characterization

Both components were characterized first isolated from each other. In Fig.4.24, the optical spectrum of the isolated AWG is plotted. The center channel insertion loss is small $(-1.2\,\mathrm{dB})$ and the $1\,\mathrm{dB}$ bandwidth (BW) is wide $(0.56\,\mathrm{nm})$. With a roll-off factor (defined as the ratio of the $1\,\mathrm{dB}$ BW over the $10\,\mathrm{dB}$ BW) of 0.33, and a crosstalk below $-18\,\mathrm{dB}$, this filter exhibits an appropriate channel response to successful demultiplex $40\,\mathrm{Gb/s}$ signals. The spectrum of the isolated ring res-

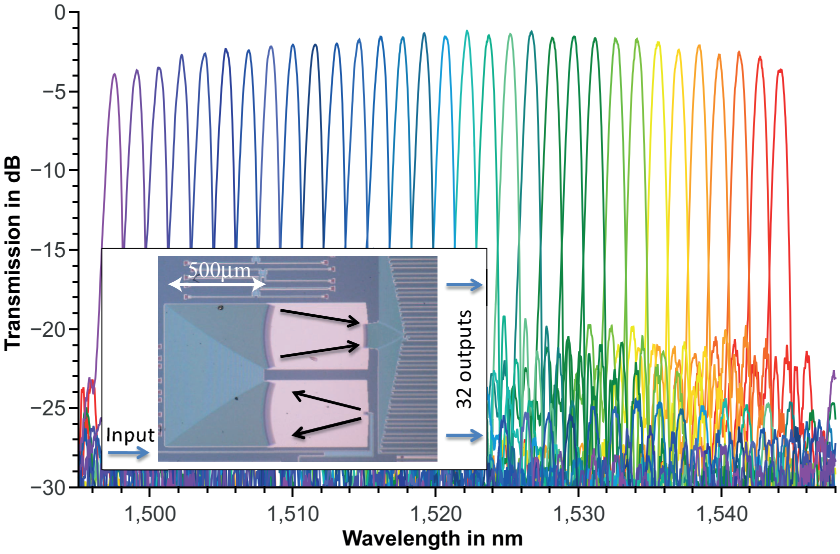

Figure 4.24: Optical spectrum of the isolated 32x200 GHz AWG (courtasy of Shibnath Pathak). In the inset a microscope picture of the AWG (courtasy of Andrea Trita).

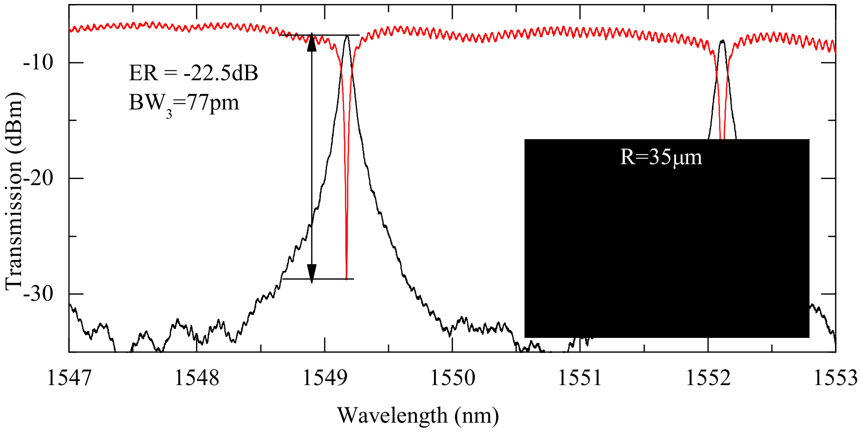

Figure 4.25: Spectrum of the isolated ring resonator.

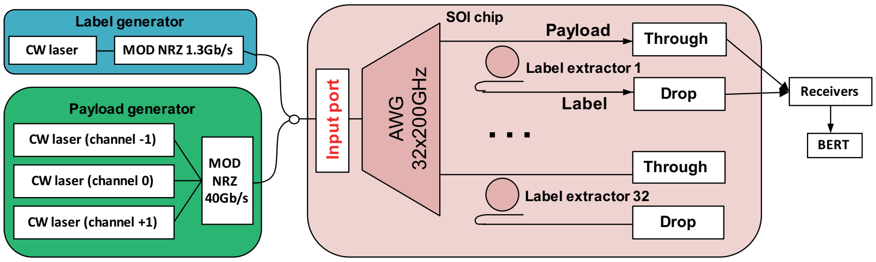

Figure 4.26: Schematic of the experimental setup

onator is plotted in Fig.4.25. The extinction ratio (ER) of the through port is large ($-22.5\,\mathrm{dB}$) and the IL for the drop small ($< 0.5\,\mathrm{dB}$). The $3\,\mathrm{dB}$ bandwidth (BW) is narrow ($77\,\mathrm{pm}$). In principle the BW of this ring resonator could have been much smaller when a smaller bus-ring coupling was used. However, the decrease in BW will go at the expense of an increased IL and a decreased ER and a well-considered trade-off should be made.

4.4.3 Label extraction experiment

Fig.4.26 shows the experimental setup employed to demonstrate the packet demultiplexer and label extractor. The system is evaluated as follows. Three carrier wavelengths ($1548.16\,\mathrm{nm}$, $1549.67\,\mathrm{nm}$ and $1551.15\,\mathrm{nm}$) are modulated at $40\,\mathrm{Gb/s}$ and combined with one label modulated at $1.3\,\mathrm{Gb/s}$ at $1549.08\,\mathrm{nm}$. The power of a single payload channel is $1.8\,\mathrm{dBm}$ and the label is transmitted at a power of $-6\,\mathrm{dBm}$, $8\,\mathrm{dB}$ smaller than the payload. The input spectrum of the experiment is plotted in Fig.4.27(a). The goal of our experiment is to successfully demultiplex the center payload channel (0) from two adjacent payload channels (denoted as -1 and 1), and to extract the in-band label of the middle payload without distorting the payload itself.

In the following we evaluate the spectrum at the through port (Fig.4.27(b)) and the drop port (4.27(c)) of the cascaded ring resonator, both using a tunable laser (blue) and the input spectrum shown in Fig.4.27(a).

In Fig.4.25(b), the spectrum of the through port of the ring resonator is shown, presenting the demultiplexed payload without label. Indeed, one can see that both adjacent payload channels are successfully dropped with an ER of respectively $-20.4\,\mathrm{dB}$ and $-17.6\,\mathrm{dB}$. The label has an extra $-23\,\mathrm{dB}$ drop with respect to the power of payload 0, which is the combination of the ER of the ring and the IL of the AWG. This is more clear if one looks at the cascaded device characteristic using a tunable laser (blue overlay curve). The total IL of payload 0 is $14.8\,\mathrm{dB}$ which includes the IL of both input and output fiber grating couplers (each $\approx 6\,\mathrm{dB}$), waveguide losses ($1\,\mathrm{dB}$) and the (center) IL of the AWG ($1.8\,\mathrm{dB}$).

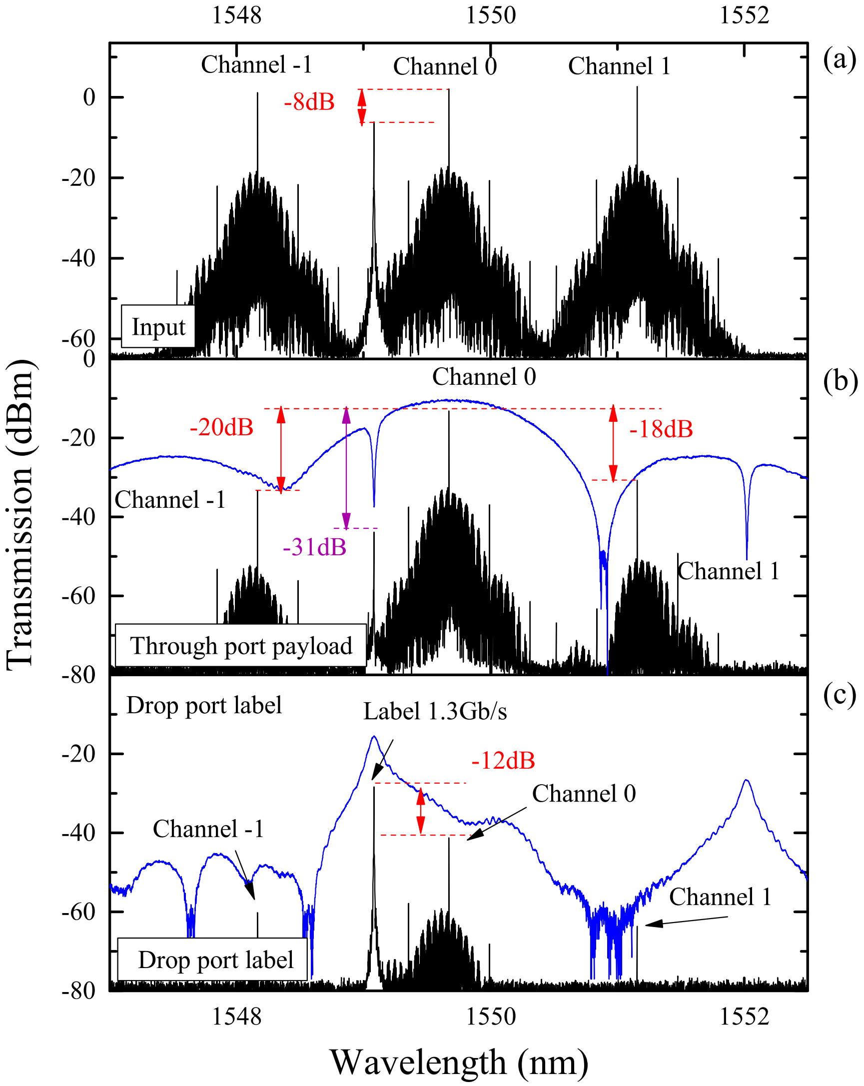

Figure 4.27: Three transmission spectra (sharing the same wavelength axis) of (a) the input of our experiment with three payloads modulated at 40 Gb/s *with one label modulated at* 1.3 Gb/s *(b) the through port of the ring resonator cascaded behind the AWG with channel -1 and 1 dropped with at least* -18 dB *and (c) the drop port of the ring resonator where the power ratio between label and payload is* 12 dB.

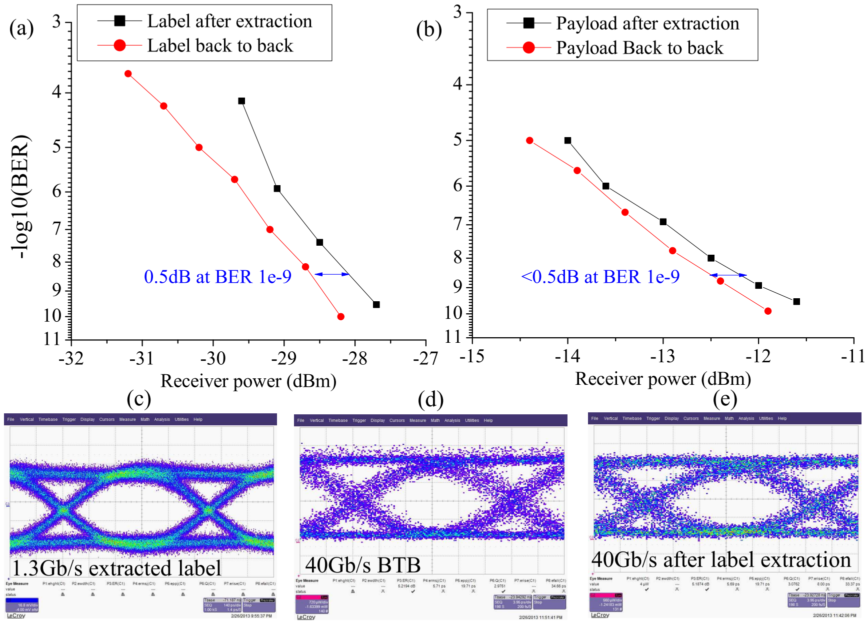

Figure 4.28: BER curves of (a) the extracted $1.3\,\mathrm{Gb/s}$ *label and (b) the forwarded* $40\,\mathrm{Gb/s}$ *payload, both back-to-back and after the label extraction. Only a very low penalty is detected for both label and payload. In (c) the error-free open-eye diagram of extracted label. The error-free open-eye diagram of (d) the back-to-back payload and (e) after label extraction.*

In Fig.4.25(c), the spectrum of the drop port of the ring resonator is shown, presenting the extracted label output. Also in this graph, both a tunable laser (shown in blue) and the system input (shown in black) are used to characterize the system. One can find a $12\,\mathrm{dB}$ power ratio between the label and the payload of channel 0, predicting a good optical signal to noise ratio of the label.

To evaluate the transmission quality of both payload and label, a BER curve is for both plotted in Fig.4.28(a) and (b) respectively. One can notice for both signals error free operation with only a small power penalty of $< 0.5\,\mathrm{dB}$ compared with the back-to-back situation (not through the SOI chip).

4.4.4 Discussion

Using Fig.4.25(b) and (c), the position of the label with respect to the payload could be further optimized. In this case, the spectral label position is $0.58\,\mathrm{nm}$ away from the center wavelength of the payload which results in good extinction ratios and very limited distortion. One can play with this relative position by using the integrated Ti heater. If we make the label offset smaller, e.g. because extra label wavelengths are needed, the signal ratios will change. From a label perspective, a larger amount of payload will be present in the label and to keep the optical signal to noise ratio constant, the label input power should be increased. At the same time also the absolute power of the extracted label will increase, because of the decreased suppression of the AWG channel response. From a payload perspective, a smaller offset of the label wavelength causes a relatively larger distortion of the payload. The general effect of a filter with a bandwidth of $6\,\mathrm{GHz}$ or $50\,\mathrm{pm}$ on the quality of $40\,\mathrm{Gb/s}$ payloads is investigated in [13]. For a label offset smaller than $20\,\mathrm{GHz}$ or $0.12\,\mathrm{nm}$, a significant distortion on the payload is noticed [13]. Based on this information we could decrease the label offset approximately $0.3\,\mathrm{nm}$ without distorting the payload.

The label extractor itself has a very large ER of $-22.5\,\mathrm{dB}$, which results in a total ER of $-31\,\mathrm{dB}$ at a label spectral offset of $0.58\,\mathrm{nm}$. This high ER gives the ring resonator designer the room to decrease the BW further but at the expense of a higher IL of the ring resonator (and thus a lower label output). However, decreasing the BW of the ring resonator could even further decrease the impact on the payload and a smaller label offset can be used. By using a smaller label offset, the cascaded IL of the label is drastically improved due to decreased IL of the AWG channel response.

4.4.5 Conclusion

We demonstrated a compact SOI-integrated $32 \times 200\,\mathrm{GHz}$ AWG followed by a narrowband ring resonator to establish the demultiplexing of three $40\,\mathrm{Gb/s}$ payloads and the extraction of the in-band optical label, both with power penalty of $< 0.5\,\mathrm{dB}$. This result is promising for the realization of a compact large port-count and low-latency photonic integrated optical packet switch. We have discussed possible system improvements based on spectral offset of the label with respect to the payload. The channel spacing of $200\,\mathrm{GHz}$ is relatively a bit broad for $40\,\mathrm{Gb/s}$ and one could decrease the channel spacing down to $100 - 150\,\mathrm{GHz}$.

4.5 Conclusion and outlook

In this chapter we investigated an integrated label extractor on SOI based on high performance ring resonators and photodiodes. The tremendous progress in the quality of both building blocks enabled us to successfully fabricate a four-channel UDWDM demultiplexer with high-speed optical-to-electrical conversion which could be used as label extractor. Two systems tests in collaboration with the COBRA group of the TU/e have shown the feasibility of ultra-compact SOI components as a potential low-cost solution in large port low latency all-optical packet switches.

References

[1] J M Martinez, F Ramos, and J Marti. *All-optical packet header processor based on cascaded SOA-MZIs*. Electronics Letters, 40(14):8–9, 2004.

[2] F. Ramos, E. Kehayas, J.M. M Martinez, R. Clavero, J. Marti, L. Stampoulidis, D. Tsiokos, H. Avramopoulos, J. Zhang, N. Chi, P. Jeppesen, N. Yan, I.T. Tafur Monroy, a.M.J. M J Koonen, M.T. T Hill, Y. Liu, H.J.S. J S Dorren, R Van Caenegem, D. Colle, M. Pickavet, B. Riposati, P.V. Holm-Nielsen, and R. Van Caenegem. *IST-LASAGNE: towards all-optical label swapping employing optical logic gates and optical flip-flops*. Journal of Lightwave Technology, 23(10):2993–3011, October 2005.

[3] Y. Liu, J. M. Martinez, J. Herrera, R. Clavero, F. Ramos, a. M. J. Koonen, J. Marti, and H. J. S. Dorren. *Demonstration of an all-optical routing decision circuit*. Proceedings of SPIE, 6783(2):67832Q–67832Q–6, 2007.

[4] J. Herrera, O. Raz, E. Tangdiongga, Y. Liu, H. C. H. Mulvad, F. Ramos, J. Marti, G. Maxwell, a. Poustie, M. T. Hill, H. de Waardt, G. D. Khoe, a. M. J. Koonen, and H. J. S. Dorren. *160-Gb/s All-Optical Packet Switching Over a 110-km Field Installed Optical Fiber Link*. Journal of Lightwave Technology, 26(1):176–182, 2008.

[5] Jianji Dong, Xinliang Zhang, Songnian Fu, Jing Xu, P. Shum, and Dexiu Huang. *Ultrafast All-Optical Signal Processing Based on Single Semiconductor Optical Amplifier and Optical Filtering*. IEEE Journal of Selected Topics in Quantum Electronics, 14(3):770–778, 2008.

[6] H. Le-Minh, Z. Ghassemlooy, W.P. Ng, and M.F. Chiang. *All-optical router with pulse-position modulation header processing in high-speed photonic packet switching networks*. Engineering and Technology, 3(3):465–476, 2009.

[7] Daniel J. Blummental, Bengt-Erik Olsson, Giammarco Rossi, Timothy E. Dimmick, Lavanya Rau, Milan Masanovic, Olga Lavrova, Roopesh Doshi, Olivier Jerphagnon, John E Bowers, Volkan Kaman, Larry A Coldren, and John Barton. *All-Optical Label Swapping Networks and Technologies*. Journal of Lightwave Technology, 18(12):2058–2075, 2000.

[8] Harm J. S. Dorren, M.T. Hill, N. Calabretta, R. Geldenhuys, and G.D. Khoe. *All-optical header processing and optical buffering for optical packet switching networks*. In Proceedings of SPIE, volume 5626, pages 123–136. Spie, 2005.

[9] Naoya Wada, Gabriella Cincotti, Satoshi Yoshima, Nobuyuki Kataoka, and Ken-ichi Kitayama. *Characterization of a Full Encoder / Decoder in the AWG Configuration for Code-Based Photonic Routers Part II : Experiments and Applications*. Journal of Lightwave Technology, 24(1):113–121, 2006.

[10] A M J Koonen, Ni Yan, J J Vegas Olmos, Idelfonso Tafur Monroy, Christophe Peucheret, Erik Van Breusegem, and Evi Zouganeli. *Label-Controlled Optical Packet Routing Technologies and Applications*. IEEE Journal of Selected Topics in Quantum Electronics, 13(5):1540–1550, 2007.

[11] N. Chi, J. Zhang, and P. Jeppesen. *All-optical subcarrier labeling based on the carrier suppression of the payload*. IEEE Photonics Technology Letters, 15(5):781–783, May 2003.

[12] Ian M White, Matthew S Rogge, Kapil Shrikhande, and Leonid G Kazovsky. *A Summary of the HORNET Project : A Next-Generation Metropolitan Area Network*. IEEE Journal of Selected Areas In Communications, 21(9):1478–1494, 2003.

[13] Jun Luo, Stefano Di Lucente, Abhinav Rohit, Shihuan Zou, Kevin A Williams, Harm J S Dorren, and Nicola Calabretta. *Optical Packet Switch With Distributed Control Based on InP Wavelength-Space Switch Modules*. IEEE Photonics Technology Letters, 24(23):2151–2154, 2012.

[14] Wenrui Wang, N Calabretta, T Ditewig, F Gomez Agis, S Zhang, O Raz, E Tangdiongga, and H J S Dorren. *Scalable Optical Packet Switching at 160 Gb / s Data Rate*. In Proc. Ecoc 2009, number 1, pages 2009–2010, 2009.

[15] N. Calabretta, H. Jung, E. Tangdiongga, and H. Dorren. *All-Optical Packet Switching and Label Rewriting for Data Packets Beyond 160 Gb/s*. IEEE Photonics Journal, 2(2):113–129, April 2010.

[16] W Bogaerts and S K Selvaraja. *Compact Single-Mode Silicon Hybrid Rib/Strip Waveguide With Adiabatic Bends*. IEEE Photonics Journal, 3(3):422–432, June 2011.

[17] S Di Lucente, J Luo, R Pueyo Centelles, A Rohit, S Zou, K a Williams, H J S Dorren, and N Calabretta. *Numerical and experimental study of a high port-density WDM optical packet switch architecture for data centers.* Optics express, 21(1):263–9, January 2013.

[18] J Luo, S Di Lucente, J Ramirez, and N Calabretta. *Low Latency and Large Port Count Optical Packet Switch with Highly Distributed Control*. In OFC/NFOEC 2012 - 2012 Conference on Optical Fiber Communication and the National Fiber Optic Engineers Conference, pages 2–4, 2012.

[19] N. Calabretta, P. J. Urban, D. H. Geuzebroek, E. J. Klein, H. de Waardt, and H. J. S. Dorren. *All-Optical Label Extractor/Eraser for In-Band Labels and 160-Gb/s Payload Based on Microring Resonators*. IEEE Photonics Technology Letters, 21(9):560–562, May 2009.

[20] Peter De Heyn, Steven Verstuyft, Shahram Keyvaninia, Andrea Trita, and Dries Van Thourhout. *Tunable 4-Channel Ultra-Dense WDM Demultiplexer with III-V Photodiodes Integrated on Silicon-on-Insulator*. In Asia Communications and Photonics Conference (ACP - 2012), pages 8–10, 2012.

[21] Zhen Sheng, Liu Liu, Sailing He, Dries Van Thourhout, and Roel Baets. *Silicon-on-insulator microring resonator for ultra dense WDM applications*. 2009 6th IEEE International Conference on Group IV Photonics, pages 122–124, September 2009.

[22] Zhen Sheng, Liu Liu, Joost Brouckaert, Sailing He, and Dries Van Thourhout. *InGaAs PIN photodetectors integrated on silicon-on-insulator waveguides*. Optics express, 18(2):1756–61, January 2010.

[23] S. Keyvaninia, M. Muneeb, S. Stanković, P. J. Van Veldhoven, D. Van Thourhout, and G. Roelkens. *Ultra-thin DVS-BCB adhesive bonding of III-V wafers, dies and multiple dies to a patterned silicon-on-insulator substrate*. Optical Materials Express, 3(1):35, December 2012.

[24] S Di Lucente, P De Heyn, J Luo, D Van Thourhout, H J S Dorren, and N Calabretta. *160 Gb/s Optical Packet Switch Module Employing SOI Integrated Label Extractor*. In The 18th OptoElectronics and Communications Conference (OECC2013) / Photonics in Switching 2013 (PS2013), pages 5–6, 2013.

[25] Shibnath Pathak, Dries Van Thourhout, and Wim Bogaerts. *Design trade-offs for silicon-on-insulator-based AWGs for (de)multiplexer applications*. Optics letters, 38(16):2961–4, August 2013.

[26] P De Heyn, J Luo, A Trita, S Pathak, S Di Lucente, H Dorren, and N Calabretta. *A Compact Integrated 40Gb / s Packet Demultiplexer and Label Extractor on Silicon-on-Insulator for an Optical Packet Switch*. In The 39th European Conference and Exhibition on Optical Communication, number 1, pages 1–3, 2013.

[27] Shibnath Pathak, Michael Vanslembrouck, Pieter Dumon, Dries Van Thourhout, and W. Bogaerts. *Optimized Silicon AWG With Flattened Spectral Response Using an MMI Aperture*. Journal of Lightwave Technology, 31(1):87–93, 2013.

5

Dense wavelength division demultiplexing Ge receivers

Using multiple wavelengths on a single optical link (wavelength-division multiplexing or WDM) to effectively increase the bandwidth is a widely used approach in long-haul communication for more than 2 decades. In this chapter we explore the adoption of WDM in highly-confined Si photonics for receivers for short to intermediate-reach communication ($< 2\,\mathrm{km}$). For these applications, a low cost and low-power consumption are the primary requirements. Si photonics offers this low-cost requirement and its availability to create compact structures can improve the power consumption as well.

In this chapter we explore WDM in Si as a first approach to increase the aggregate bandwidth per fiber. We demonstrate a polarization-insensitive 5-channel dense WDM (DWDM) receiver with $300\,\mathrm{GHz}$ ($2.34\,\mathrm{nm}$) channel spacing around $1540\,\mathrm{nm}$ wavelength and high-speed ($20\,\mathrm{Gb/s}$) Ge photodiodes to terminate each channel. An aggregate bandwidth of $100\,\mathrm{Gb/s}$ is hereby reached.

We start this chapter by discussing the system specifications of an intra data center optical interconnect (OI) in section 5.1 and how these specifications are translated in WDM component specifications in section 5.2. Several challenges of WDM in Si regarding manufacturability and control are given in section 5.4. In the rest of the chapter we discuss the design of a 4 and 5-channel $300\,\mathrm{GHz}$ demultiplexer and characterize extensively their manufacturability based on wafer-scale measurements. In the next chapter, we investigate the bandwidth-scalability of this component with respect to an increased amount of channels and several strategies to lower the consumption.

5.1 System specifications

Typically standarized pluggable modules (e.g. SFP) are used for an OI with a transmitter and receiver subassembly inside. Today's maximum (one way) bandwidth per module in data center OI has just reached $100\,\mathrm{Gb/s}$. Examples are the 100GBASE-SR10 in the IEEE 802.3bm Ethernet standard with a data rate per channel of $10\,\mathrm{Gb/s}$ or the Enhanced Data Rate in the Infiniband standard. The Ethernet bandwidths for the next and future generation optical interconnects are targeting $400\,\mathrm{Gb/s}$ and $1.6\,\mathrm{Tb/s}$. As explained in section 1.4, scaling the bandwidth and reach using today's parallel multi mode fiber is limited by the increasing fiber cost and available front panel area. Therefore the present need in data centers and supercomputers for a compact, low-cost and bandwidth-scalable approach using single mode fiber is very high.

Several approaches to fulfill these requirements have been demonstrated in a PIC implementation ranging from a simple 4-lane parallel single mode (PSM4) [1] fiber implementation to more dense 1-lane solutions such as space-division multiplexing (SDM) [2], pulse-amplitude modulation (PAM), or wavelength-division multiplexing (WDM) [3, 4]. Each approach has its own advantages regarding specific system requirements such as power consumption, chip area, operating temperature range, cost, reach and bandwidth scalability. We believe that WDM offers the most promising path for bandwidth scalability and chip area. However, WDM is also the most vulnerable to temperature variations and limited fabrication tolerances, such as waveguide dimensional control (see also section 5.3). These system specifications are translated into WDM component specifications in the following section.

5.2 WDM component specifications

Power-consuming heating elements are typically used to compensate for the detrimental shifts in center wavelength of a WDM channel coming from temperature and fabrication variations. As explained in section 1.7.2, the use of a coarse WDM grid (CWDM) with a wide channel spacing of $20\,\mathrm{nm}$ or $2500\,\mathrm{GHz}$ is therefore advantageous since the transceiver can work uncontrolled for varying temperature and relaxes the fabrication tolerance of the filters. This drastically decreases the power consumption and reduces operation costs and complexity. However, the required bandwidth ($> 80\,\mathrm{nm}$) is incompatible with the bandwidth of a grating coupler ($30\,\mathrm{nm}$). Therefore, we prefer a more aggressive approach using denser channel spacings. A channel spacing of $300\,\mathrm{GHz}$ is chosen and found to offer

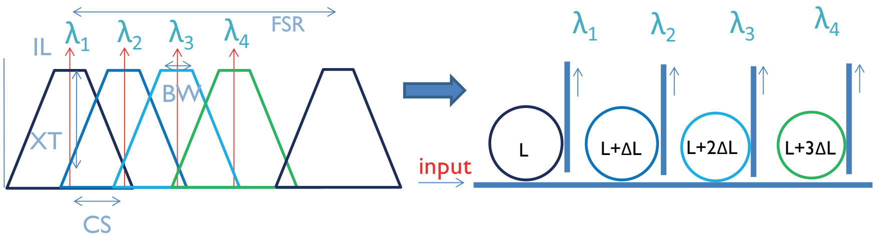

Figure 5.1: Abstract design of a WDM demultiplexer based on cascaded Si rings. Typical filter specifications are denoted in the figure.

a good compromise between channel density and filter robustness. A collective heater is used to compensate for wafer-level variations or ambient temperature drifts, which reduces the complexity of dynamic tuning. Additionally, the channel response is polarization insensitive such that a change in polarization between transmitter and receiver is allowed.

As discussed in earlier chapters, filters realized with ring resonators using a high-index contrast platform such as silicon-on-insulator (SOI) can be made very compact, and can be designed with large free-spectral ranges (FSR). By cascading several ring resonators one can create easily a scalable demultiplexer. By introducing a circumference difference (ΔL) between the adjacent rings one can achieve a desired shift between the center of the filters. This shift is called channel spacing (CS) as illustrated in the Fig.5.1. Other typical filter specifications are illustrated as well such as crosstalk (XT) which is defined per channel as the ratio between the detected level of its own channel and the next channel, insertion loss (IL) and the $1\,\mathrm{dB}$ and $3\,\mathrm{dB}$ bandwidth (BW). The free-spectral range (FSR) should be larger than the amount of channels multiplied with the CS. The ability of the Si photonics platform to achieve ring resonator filters with a large FSR will allow to maximize the amount of channels and thus the aggregate bandwidth.

The Si photonics based transceiver we envision is illustrated in Fig.5.2. An external laser array feeds the cascaded Si photonic integrated ring modulators. A single mode fiber connects the transmitter package and the receiver package. At the receiver side, the incoming optical WDM signal is demultiplexed in separate signals and converted into the electrical domain with the use of photodiodes. The current of the photodiodes is converted in a high level, digital voltage signal with a CMOS transimpedance amplifier (TIA) followed by a linear amplifier (LA). The CMOS circuit for the modulator drivers and TIA/LA could be monolithically integrated on top of the Si photonics, wire-bonded next to the Si chip or flip-chipped on top of the Si chip.

The aim of this chapter is to make this photonic component commercially viable and therefore many challenges need to be addressed. For WDM enabled Si

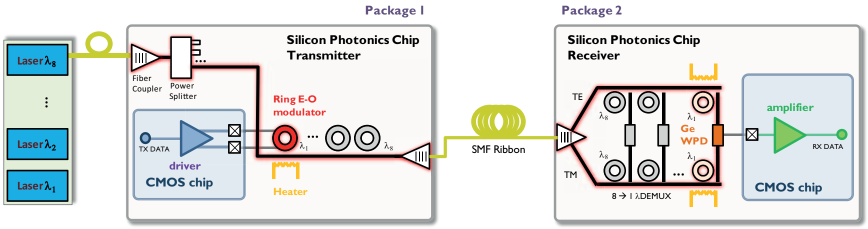

Figure 5.2: A silicon photonics link.

photonic transceivers, the comprehensive list of challenges are achieving a low insertion loss (IL) and low channel crosstalk (XT), polarization insensitivity, compact footprint, low power consumption, robustness against temperature variations, simple dynamic control, high bandwidth and a high-yield manufacturability. In the following list we will explain the different challenges in a bit more detail.

- **Low IL** will increase the sensitivity of the full receiver. The total IL consists of fiber-to-chip coupling loss, waveguide loss and filter insertion loss. The first one is typically the largest one, especially in this work, and ranges between $5 - 6\,\mathrm{dB}$. However, researchers have demonstrated fiber grating couplers with $1.2\,\mathrm{dB}$ IL [5] using e-beam lithography or $2.7\,\mathrm{dB}$ using 248-nm optical lithography. Since our components are very compact, waveguide losses are typically $< 1\,\mathrm{dB}$. The typical filter IL can vary between $0.5 - 4\,\mathrm{dB}$. In this work, the target for the filter IL is below $1\,\mathrm{dB}$.

- **Low XT** between the channels is necessary to preserve the quality of the received signal (BER). In this work we pursue a XT $\leq -20\,\mathrm{dB}$.

- **Polarization insensitive** circuits will cope with a polarization change between the transmitter and receiver side which could lead to large IL if a circuit is optimized for one polarization. One can make a polarization independent circuit but that is very difficult on SOI because of the asymmetric waveguides ($220\,\mathrm{nm} \times 450\,\mathrm{nm}$). Alternatively one can apply a polarization-diversity scheme [6, 7].

- **Compact footprint, thermal robustness and low power consumption.** Ring-based WDM components have been demonstrated with a considerably smaller footprint [8] compared to other filter implementations such as arrayed waveguide gratings (AWG), echelle gratings or Mach-Zehnder interferometer (MZI) based lattice filters. The fundamental limit of the channel footprint of a ring resonator is the ring radius. The smaller the radius, the more compact the filter. Typically, a certain racetrack length (see chapter 2) is introduced in order to fulfill the power coupling requirements. Increasing the order of the filter also increases the area. Besides enabling high

# WDM channels	4, 8, 16, 32	Thermally robust & pol. insensitive	
Channel spacing	$\mathrm{M} \times 100\,\mathrm{GHz}$	Channel heater power	≤ 2 mW
Insertion loss	$\leq 1\,\mathrm{dB}$	Channel footprint	$\leq 5000\,\mu\mathrm{m}^2$
Crosstalk XT	$\leq -20\,\mathrm{dB}$	Channel bandwidth	$20 - 30$ GHz

Table 5.1: Proposed WDM filter specifications

integration density and thus low unit cost, the compactness of ring-based filters enables low-power thermal tuning. Thermally robust ring resonators are difficult to achieve without active compensation and are therefore typically combined with integrated heaters to compensate for wafer-scale variations and ambient temperature variations.

- **Simple dynamic control** is necessary since dynamic temperature variations can shift the center wavelength of the ring resonator filters. The advantage of implementing a demultiplexer with ring resonators is that each channel response can be tuned separately and independently from each other. The control of a large amount of heaters can be become cumbersome and power hungry which could eventually limit the scalability. In this chapter we will propose a simplified heater control.

- **High bandwidth** can be achieved in two ways. The first one is to use a larger amount of channels but due to the limited bandwidth of a grating coupler, the channel spacing (or the channel density) should then scale as well. The second way is to maximize the bandwidth per channel by maximizing the bandwidth of the photodiode. The actual $1\,\mathrm{dB}$ bandwidth of the filter should be large enough for the incoming signal to pass the filter without signal degradation.

- **Design for manufacturing** to achieve a component with a high yield in such a way that it can cope with various fabrication variations, within a device bus also wafer-to-wafer or lot-to-lot.

These WDM component specifications are listed in Tab.5.1. In the next section we discuss the technological challenges related to the Si photonics platform.

5.3 Challenges for WDM in Si

As discussed earlier, an important requirement of photonic component is the manufacturability. In other words, if one designs a ring resonator according to certain filter specifications, how good is this translated on the wafer and with which yield or spread on the filter specifications.

One of the major challenges for realizing manufacturable compact WDM optical devices in silicon is the sensitivity of these components to variations in waveguide dimensions. Waveguide perturbations due to fabrication variations directly influence the shape of the resonance as well as the resonance wavelength of each channel. Using typical Si waveguides (quasi-TE mode), one can expect a $100 - 125\,\mathrm{GHz}$ wavelength shift for a $1\,\mathrm{nm}$ change in waveguide width and nearly the double for $1\,\mathrm{nm}$ shift in height [9, 10]. These detrimental shifts can cause the channel responses to overlap which can result in a bad crosstalk between these channels and an increased insertion loss. Both effects are investigated in section 5.4 '*Design for manufacturability*'. Dimension variations include linewidth variations during lithographic pattern definition as well as thickness variations of the top silicon layer of the SOI stack. Waveguide dimension variations can be present both at the device scale ($1 - 100\,\mu\mathrm{m}$), chip scale ($1 - 20\,\mathrm{mm}$), wafer scale (up to $200\,\mathrm{mm}$) and wafer-to-wafer or lot-to-lot. A good overview is given in [10].

A second challenge is the high thermo-optic coefficient of Si, which makes silicon wavelength-selective devices highly sensitive to temperature variations. One can expect a wavelength shift of $12\,\mathrm{GHz}$ (or $100\,\mathrm{pm}$ at $1550\,\mathrm{nm}$) per Kelvin, independent of the kind of filter. The ambient temperature can vary between $25 - 95°C$ [11] and hence induces a wavelength shift of $7\,\mathrm{nm}$ or $840\,\mathrm{GHz}$. Therefore we need a way to make our components robust towards ambient temperature variations. Overall two approaches are known. The first one is active compensation with the use of an integrated heater but this consumes power. Furthermore, one needs a sensing mechanism to detect the temperature and the corresponding wavelength shift and a control circuit to regulate the heater. An alternative way is realizing an athermal component which does not consume power. The former can be achieved by either using an overlay with a material of opposite thermo-optic coefficient. This has been demonstrated using a polymer overlay but this is not CMOS compatible [12, 13]. A CMOS-compatible athermal ring resonator coupled to balanced Mach-Zehnder interferometer has been demonstrated in [14, 15] by compensating the temperature induced phase shift in the parallel arm of the MZI. However, this approach has been proven to be stable only for a small temperature range and increases the area consumption drastically. Another important drawback of both compensation approaches is the need for narrow waveguides which will decrease the tolerance to dimensional waveguide variations. An alternative is recently been shown in [16], where a CMOS-compatible material TiO_2 is used as an overlay on top of broader waveguides. However, this material degrades with high temperatures needed for e.g. the annealing of Ge, which makes it incompatible within a photonic CMOS process flow.

Individual channel control has been demonstrated on a WDM filter array with a $200\,\mathrm{GHz}$ grid in [17, 18]. In this way one can combine active compensation for both device-level and wafer-level waveguide perturbations, as well as (dynamic) ambient temperature variations. However, as mentioned earlier, this can become complex and power hungry for demultiplexers with a large amount of channels as every channel needs its own control signal. Therefore we introduce a new idea called ’*collective tuning*’ in section 5.5, where all heaters are collectively controlled instead of individually. Hence, collective tuning would only use a single thermal control circuit for the whole demultiplexer. Important is that the heating is uniform for each channel and that the heater works efficiently to minimize the power consumption. A full characterization is made in 5.5.2. A direct drawback of having only one control pad, is that we lose the ability to tune for device-level waveguide perturbations. Therefore we will explore the flat-top behaviour of second-order ring resonators to overcome device-level (or local-scale) waveguide perturbations. A full performance characterization of a collectively tuned four-channel demultiplexer using first-order and second-order ring resonator is given in section 5.5.3.

The third and last challenge which we will address in this chapter is polarization insensitivity. The asymmetry of the $450\,\mathrm{nm} \times 220\,\mathrm{nm}$ silicon-on-insulator SOI waveguides makes it practically impossible to design a ring resonator for both polarizations simultaneously without performance degradation. Therefore a polarization-diversity scheme is preferred, for which one can use either a polarization beam splitting grating coupler cascaded with a polarization rotator [19] or use a 2-dimensional grating coupler [20] to make a polarization-diversity scheme [6, 7]. This is addressed in section 5.7 where a polarization-insensitive $5 \times 20\,\mathrm{Gb/s}$ receiver is demonstrated.

5.4 Design for manufacturability

Waveguide dimension variations will have an influence on the coupling factor between bus and ring waveguide and hence directly influence the shape of the spectral response of the individual channel. Therefore we start this chapter by investigating typical channel specifications such as $1\,\mathrm{dB}$ bandwidth, crosstalk and insertion loss based on wafer-scale measurements and this for first- and second-order ring resonators.

Fabrication variations also influence the resonance wavelength of the ring resonator. We separate this discussion in local variations and global variations. Local variations happen on device scale, in other words within the demultiplexer. This can cause the adjacent channel responses of the cascaded ring resonators to overlap with each other resulting in a high crosstalk. Resonance wavelength variations can be separated in a variation of the average channel spacing and a variation of the individual channel position with respect to the average channel spacing. On the other hand, global variations (that are happening on wafer scale) are responsible for shifting the whole filter comb (i.e. all the channels simultaneously) away from its desired wavelength grid. Higher-order ring resonators can suffer from an extra variation, namely the variation between the resonances of the different resonators. This effect is more difficult to quantify but one can easily detect these variations as discussed later.

To fully understand the performance of the receiver regarding manufacturability, we start in section 5.4.3 by investigating the individual channel response of a four-channel demultiplexer. We compare the performance of first- and second-order ring resonators. Wafer-scale trends of the spectral shape, center wavelength position and the relation to their position on the wafer are examined. A comprehensive channel spacing analysis (section 5.4.4) will learn us how tolerant each filter design is against device-scale fabrication related non-uniformities. From this investigation it will be clear that the main problem of designing a filter based on ring resonators on a Si platform is not the spectral shape but the variation of the center wavelength of the filter with respect to the other adjacent filters.

5.4.1 Design

The channel spacing is designed to fit a dense WDM grid with a spacing of $300\,\mathrm{GHz}$ or $2.4\,\mathrm{nm}$ at $1550\,\mathrm{nm}$. The free spectral range (FSR) is designed to be $12\,\mathrm{nm}$ in such a way that at least four channels can fit within the FSR. The rings have a racetrack shape and are implemented with a $9\,\mu\mathrm{m}$ coupling length (L_c) and a $5\,\mu\mathrm{m}$ radius (R). A small increase (Δ) in round-trip length of the ring (L) is used to establish the shift in resonance wavelength $\lambda_{\mathrm{center}}$ according to the defined channel spacing (CS) using following formula.

$$\Delta L = \frac{n_g}{n_{eff}} \frac{CS}{\lambda_{\mathrm{center}}} L \tag{5.1}$$

with the group index n_g equal to 4.3 and effective refractive index n_{eff} equal to 2.43. In this design $\Delta L = 150\,\mathrm{nm}$ which is implemented through an added $75\,\mathrm{nm}$ in both racetracks of the ring. The very small increase in coupling strength could be compensated with a $1.5\,\mathrm{nm}$ change in gap, which is not implemented due to the $5\,\mathrm{nm}$ mask grid resolution. Both ring resonators are designed to have a $-20\,\mathrm{dB}$ roll off at one channel spacing ($2.4\,\mathrm{nm}$) away from their center resonance wavelength. The second-order ring resonator has more design freedom and is optimized for a maximized (flat-top) bandwidth at the drop ports.

In Fig.5.3, a schematic view of the designed four-channel demultiplexer is shown with the typical design parameters. The ring resonators are cascaded with a $50\,\mu\mathrm{m}$ spacing. The above channel requirements result in a desired bus-ring waveguide power coupling of 0.08 for the first-order ring resonator and a bus-ring and ring-ring waveguide power coupling of respectively 0.32 and 0.04 for the second-order ring resonator. Using a $450\,\mathrm{nm}$ wide and $220\,\mathrm{nm}$ thick waveguide with oxide cladding for both the bus and ring this results in a bus-ring gap (G) of

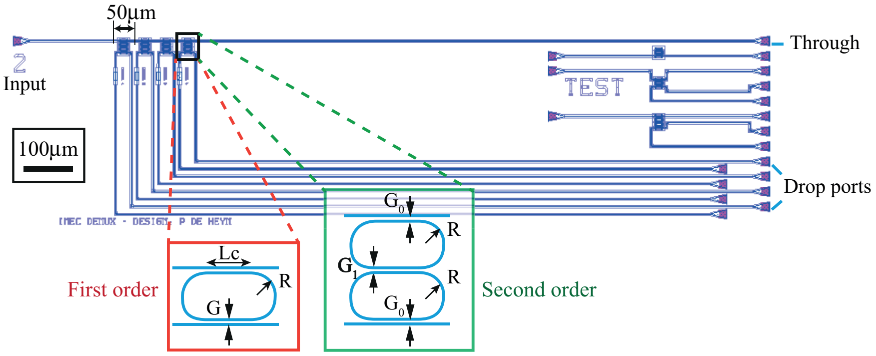

Figure 5.3: Schematic of a single-polarization four-channel demultiplexer. Insets are illustrating the 1$^{\mathrm{st}}$ and 2$^{\mathrm{nd}}$ order ring resonator design parameters.

$295\,\mathrm{nm}$ for the first-order ring resonator and a bus-ring (G_0) and a ring-ring gap (G_1) of respectively $205\,\mathrm{nm}$ and $340\,\mathrm{nm}$ for the second-order ring resonator. The above coupling and gap values are simulated using techniques which are explained in section 2.5 on page 2-42. Note that we assumed a propagation loss of $2\,\mathrm{dB/cm}$ during the simulation which is underestimating the typical roundtrip loss by a factor of 4. In 2.5 on page 2-42, the full design flow of a demultiplexer design has been discussed.

5.4.2 Characterization methodology

Both receiver designs are characterized using a tunable laser with a wavelength step size of $10\,\mathrm{pm}$, centered around $1550\,\mathrm{nm}$. The spectral responses are normalized by subtracting the Gaussian-like spectrum of the fiber grating couplers, which are extracted from fitting the off-resonance data of the through port response. Measurements are performed using an automated alignment procedure assuring a reproducible fiber-to-chip coupling in a temperature-controlled environment. Because the coupling of the ring resonators is wavelength dependent, filter characteristics are all measured preferably around the same wavelength. Due to fabrication variations, the center wavelength of the filter bank is varying over the wafer by more than one FSR. Therefore the analysis is done on four adjacent resonances with the first channel situated around $1540\,\mathrm{nm}$.

5.4.3 Individual channel response

In Fig.5.4(a) and (b), one can see the typical spectral response of the first and second channel of a 4-channel WDM filter implemented with respectively first and second-order ring resonators. The $3\,\mathrm{dB}$ bandwidth (BW) of the second-order

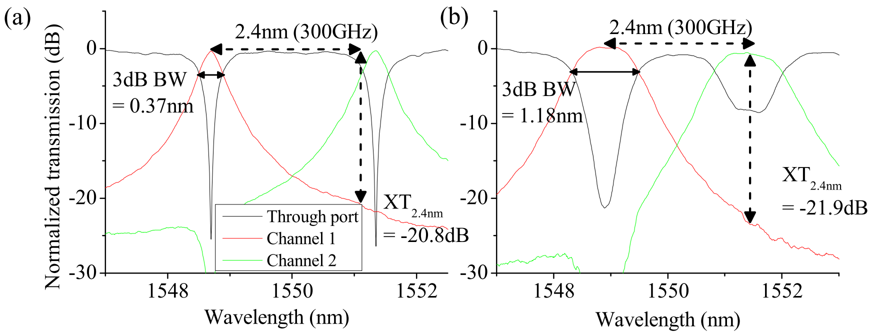

Figure 5.4: First- versus second-order ring resonator response. Designed to have a crosstalk below $-20\,\mathrm{dB}$ *at* $2.4\,\mathrm{nm}$.

	first order			second order		
Specification	mean	P10	P90	mean	P10	P90
$1\,\mathrm{dB}$ BW	0.22	0.2	0.24	0.87	0.8	0.94
$3\,\mathrm{dB}$ BW	0.43	0.38	0.47	1.27	1.17	1.37
XT at 2.4nm	-20.4	-21.3	-19.5	-21.4	-22.8	-20.3
IL	-0.45	-0.63	-0.25	-0.38	-0.76	-0.01

Table 5.2: Filter performance. Mean and both percentiles (10^{th}, 90^{th}) *are based on the mean value of the 4 channels.*

ring resonator is indeed much larger ($3\,\mathrm{dB}$ BW = $1.18\,\mathrm{nm}$) than that of the first-order ring ($3\,\mathrm{dB}$ BW = $0.37\,\mathrm{nm}$) whereas the crosstalk (XT) is for both channels better than $-20\,\mathrm{dB}$. A small misalignment between the resonances of the two ring resonators forming a second-order ring resonator can cause large fluctuations in extinction ratio (ER) of the through response. This effect is clearly visible in Fig.5.4(b) showing an ER difference of more than $10\,\mathrm{dB}$ between channel 1 and 2. This misalignment explains the slightly larger IL ($\approx 1\,\mathrm{dB}$) of channel 2 with respect to channel 1. We investigated nominally identical devices on different dies across the wafer and the statistics (mean, 10^{th} and 90^{th} percentiles) based on the mean value of the 4 channels (device mean) are listed in Tab.5.2. One can see that the device using second-order ring resonators has slightly better mean values but a higher spread regarding XT and IL. The larger spreading is explained by the possible misalignment between two ring resonators forming a second-order ring resonator. This adds an extra dimension of variation and thus a larger spread on the channel is expected.

In Fig.5.5, we plot the insertion loss (IL) of only the receiver's worst channel (largest IL) instead of the mean value listed in Tab.5.2. From these two wafer plots it is clear that this worst channel depends on local non-uniformities because there

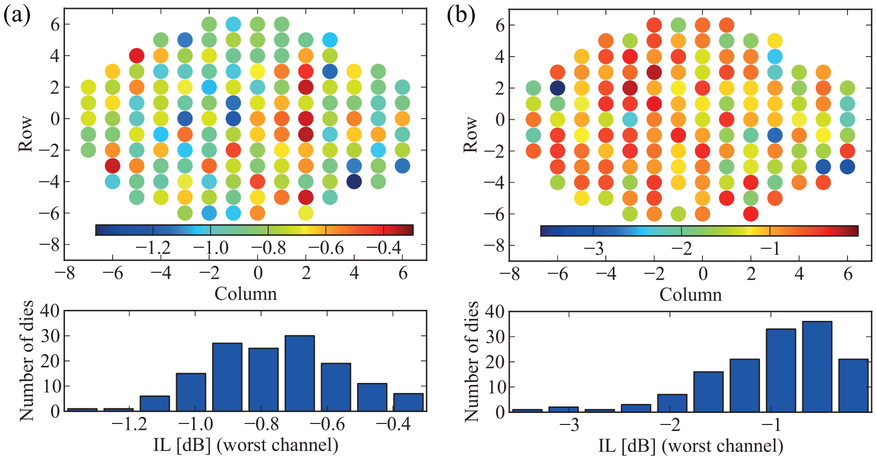

Figure 5.5: Insertion loss (IL) of the receivers worst channel employed with (a) first-order and (b) second-order ring resonators, both in function of the receivers position on the wafer and in a device-count histogram.

is not a clear wafer-scale trend visible. From the device-count histogram one can see that the receiver's worst channel using the second-order ring resonator has a larger spread and more skewed distribution of the IL than when first-order ring resonators are used.

In the following we investigate the absolute position of the center wavelength of the different channels, where we use the first channel as a reference for the whole filter comb. In Fig.5.6(a), the center wavelength of this first channel in function of its position on the wafer and a corresponding device-count histogram are plotted. As explained in the section 5.4.2, the analyzed resonance wavelength is chosen within 1 FSR around the arbitrary chosen wavelength $1540\,\mathrm{nm}$. It can be seen from this figure that the center wavelength is uniformly distributed between the arbitrary chosen selection borders which means that the variation between two positions of the wafer can differ with more than 1 FSR. To create more insight in these wafer-scale variations, the same data is plotted with a different selection procedure in Fig.5.6(b). This selection procedure is based on the assumption that the difference in center wavelength between two identical designed devices on adjacent dies must be smaller than half a FSR which results in a continuous variation of the center wavelength in function of its position on the wafer. From the corresponding histogram one can notice that the maximum variation is reaching $30\,\mathrm{nm}$ which is more than twice the FSR. Expelling the outliers with the shortest wavelength, which are corresponding with devices on the edge of the wafer, one finds a reduced variation of $23\,\mathrm{nm}$. This wafer-scale variation can partially be explained by small thickness variations of the waveguide layer within a SOI wafer where

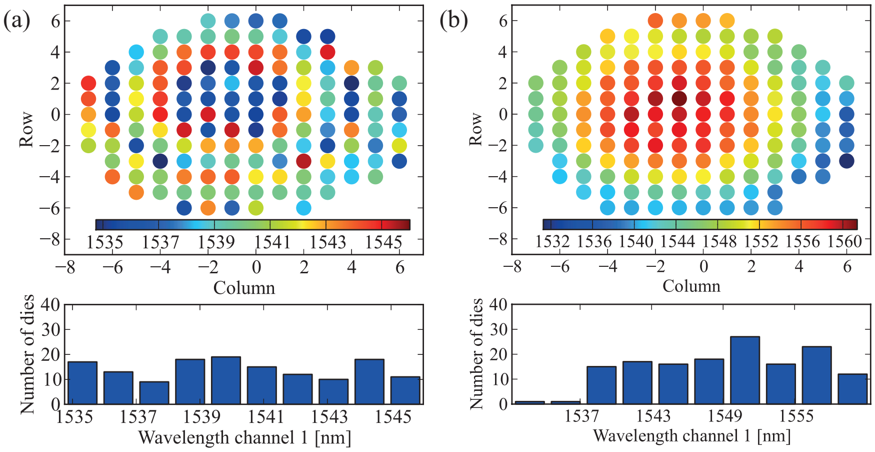

Figure 5.6: The center wavelength of the first channel in function of its position on the wafer and a corresponding device-count histogram created with two selection procedures: (a) within 1 FSR around $1540\,\mathrm{nm}$ *(b) assuming only small die-to-die shifts to create a more continuous variation.*

approximately $1\,\mathrm{nm}$ difference in thickness results in a $2\,\mathrm{nm}$ wavelength shift. In the following (section 5.5) the collective heater, which will be used to compensate for these wafer-scale variations, is characterized.

5.4.4 Channel spacing analysis

Local variations at the device scale are typically much smaller ($\leq 1\,\mathrm{nm}$) than the global variations found across a full wafer ($\approx 10\,\mathrm{nm}$ and higher) but can still cause adjacent channels to overlap with each other resulting in a large XT between these channels. An important characteristic of a good WDM filter is a predictable and constant spacing between the center wavelength of adjacent channels. Especially when using a collective heater where these inter-channel deviations cannot be compensated, this deviation must be smaller than e.g. half the $1\,\mathrm{dB}$ bandwidth to keep the insertion loss tolerable. To quantify this channel spacing variability, we perform a linear regression analysis by fitting the absolute resonance position of the 4 channels (plotted in Fig.5.7(a)) as function of their channel number. This fit is plotted in Fig.5.7(b) and denoted as ‘fit optimized slope’. The slope of this fit is then the device-optimized channel spacing (CS) and is in this case equal to $2.6\,\mathrm{nm}$. In Fig.5.7(c) the residuals representing the relative deviations away from the CS are plotted, which are in this example $\leq 0.2\,\mathrm{nm}$. We repeat this analysis with a linear fitting with a fixed slope equal to the designed value of the CS (i.e. $2.4\,\mathrm{nm}$). Using this fitting we expect larger deviations but this will better match the performance in a practical situation where the CS should equal the incoming

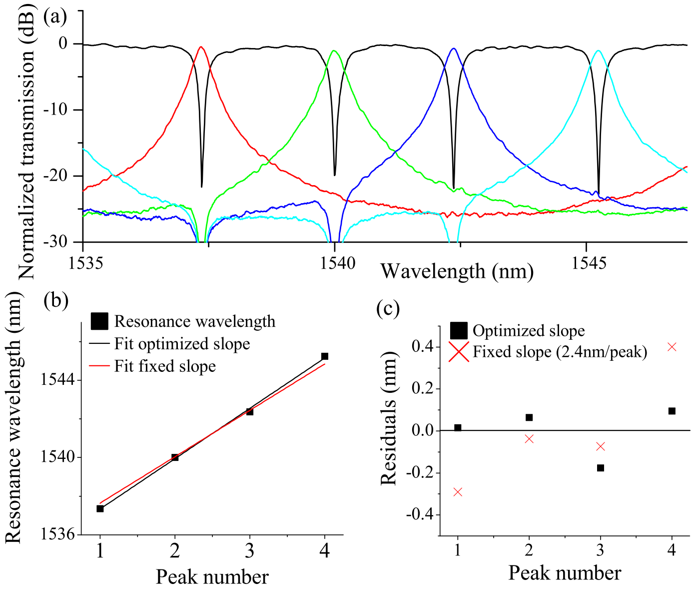

Figure 5.7: A typical channel spacing analysis with (a) the normalized response of a 4-channel WDM filter (first-order ring resonators). In (b) the absolute position of the resonances is plotted in function of the peak number. After fitting, the residuals are calculated and plotted in (c). Two fits are made, one where the slope is optimized for this particular device, and one with a fixed slope for all devices measured on the wafer.

channel grid, defined in the design phase of the component. In this way the largest deviation goes up to $0.4\,\mathrm{nm}$. At this point one can distinguish two issues. First, the optimum channel spacing from this device is not the designed one and second, the maximum deviation ($0.4\,\mathrm{nm}$) is exceeding the $3\,\mathrm{dB}$ BW of our first-order ring resonator. We repeat this analysis for all first-order ring resonators on a full wafer studying the CS on waferscale.

Channel spacing deviation In Fig.5.8(a), the device-optimized channel spacing is plotted in function of its position on the wafer. The figure shows that the channel spacing is not following any clear wafer trend. This indicates that the variation of the channel spacing ($3\sigma = 0.36\,\mathrm{nm}$ or $14\,\%$) is rather caused by local (or device-level) fabrication variations. If one plots a device-count histogram, one can see that the mean channel spacing is $2.54\,\mathrm{nm}$, or $0.14\,\mathrm{nm}$ off from our design value of $2.4\,\mathrm{nm}$. We believe that this deviation can partly be compensated by design, e.g. a better calibration of the group and effective refractive index used in the calculation of the incremental circumference of the ring resonators (see equation 5.1).

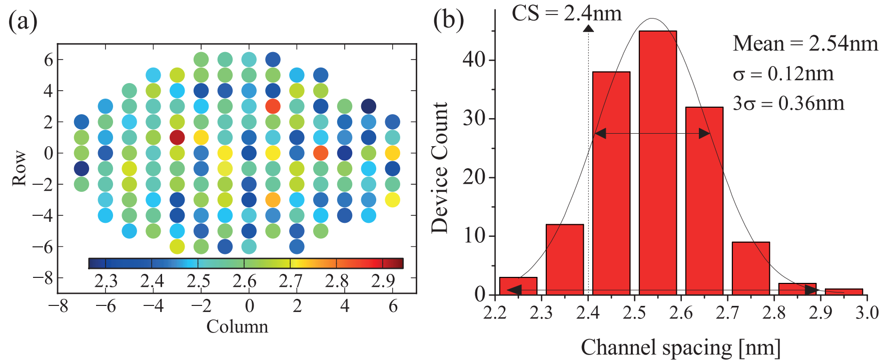

Figure 5.8: Channel spacing investigation. (a) CS in function of its position on the wafer (b) device-count histogram a mean value of $2.54\,\mathrm{nm}$*, which is a bit off the designed value of* $2.4\,\mathrm{nm}$*.*

	σ	3σ	min	1%	10%	90%	99%	max
CS $2.4\,\mathrm{nm}$	0.29	0.86	-0.9	-0.69	-0.36	0.36	0.63	0.84
CS $2.54\,\mathrm{nm}$	0.26	0.7	-0.95	-0.52	-0.31	0.3	0.56	0.7
Opt. CS	0.19	0.58	-0.85	-0.44	-0.25	0.24	0.5	0.63

Table 5.3: The true deviations of a desired spectral position relative to the CS in numbers

Deviations from the channel spacing In this paragraph we investigate the deviations away from the as-designed and device-optimized channel spacing. All the resonances of the 142 measured 4-channel demultiplexers using first-order ring resonators are considered (568 resonances in total). Their true deviation away from their desired spectral position (calculated for both channel spacing analyses) is plotted in Fig.5.9(a), where each deviation from a certain resonance is plotted as a little dot. The distribution of these deviations follows a Gaussian profile and the various percentiles are illustrated in the figure using a box-plot representation on top of the distribution plot. These percentile values as well as the σ and 3σ values are listed in Tab.5.3. To complete the investigation, we also add the statistical values of the true deviations when using the wafer-optimized fixed channel spacing. Based on Fig.5.8, this CS is $2.54\,\mathrm{nm}$. This distribution compensates for the small design offset, discussed in the previous section, and is thus giving a true representation of how well one can design four ring resonators on a certain spectral position for a given technology (i.e. mask and lithography). Even with an improved design one cannot improve these numbers. The maximum deviation goes up to $0.95\,\mathrm{nm}$ away from the relative desired spectral position but in general one can expect deviations up to $0.7\,\mathrm{nm}$ (3σ). Based on the 3σ value, an improvement with respect to the relative deviations away from the as-designed CS ($2.4\,\mathrm{nm}$) of $0.16\,\mathrm{nm}$ is found.

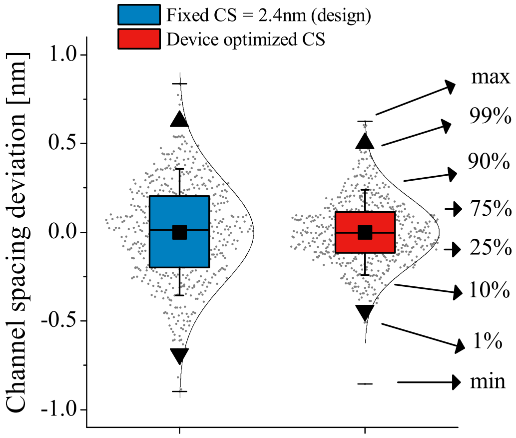

Figure 5.9: The true deviations of the desired spectral position relative to the CS, illustrated with a distribution and box plot.

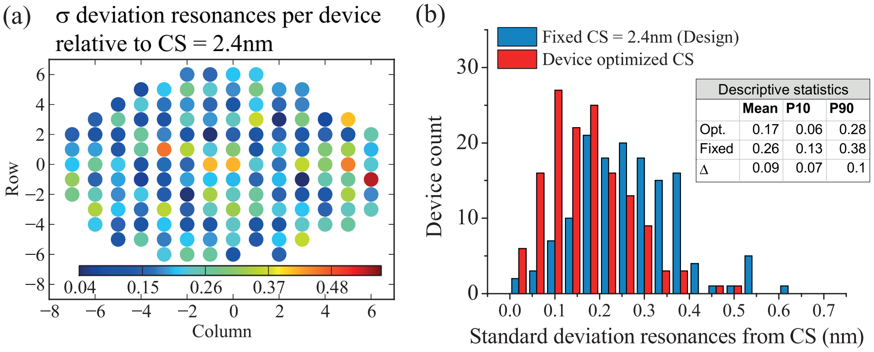

Descriptive statistics

	Mean	P10	P90
Opt.	0.17	0.06	0.28
Fixed	0.26	0.13	0.38
Δ	0.09	0.07	0.1

Figure 5.10: (a) A wafer mapping of the σ value of the deviation away from the fixed as-designed CS in function of its wafer position.

By wrapping the 4 residuals from a certain fitting (as shown in Fig.5.7(c)) in a single number by taking the standard deviation (σ), we can subdivide each device based on the standard deviation of the relative deviations. This is plot in Fig.5.10(a) by using a wafer map, where once again no clear wafer trend is noticed (e.g. larger deviations at the side of the wafer) for the σ value of the deviations away from the fixed as-designed CS. In Fig.5.10(b), two device-count histograms for this standard deviation of the resonance deviation, calculated with both fitting analyses, are plotted. As expected the device-optimized CS gives smaller deviations with a wafer-mean value of $0.17\,\mathrm{nm}$, compared to the $0.26\,\mathrm{nm}$ calculated with the more realistic method of a fixed as-designed CS.

5.4.5 Conclusion

This section investigated the manufacturability of a 4-channel demultiplexer using first and second-order ring resonators. We found that the spectral shape of both resonator designs is very well translated on a fabricated device resulting in tight specifications of the measured channel responses on wafer-level. By investigating the relative spectral position with respect to the desired position, we found that wafer-mean channel spacing was a bit off with respect to the designed one ($2.54\,\mathrm{nm}$ with respect to designed $2.4\,\mathrm{nm}$). We quantified these deviations using three different channel spacings, i.e. the fixed as-designed CS, the fixed wafer-mean CS and the device-optimized CS. Using these techniques we could differentiate between different effects. The resulting 3σ values are respectively quantified as 0.86, 0.7 and $0.56\,\mathrm{nm}$.

Let us assume that the demultiplexer is further optimized and the wafer-mean CS is $2.4\,\mathrm{nm}$. Then 99.7% of the resonances has a channel spacing deviation of $\leq 0.7\,\mathrm{nm}$. In a worst case scenario, when two adjacent channels have an opposite deviation (towards each other) of $0.7\,\mathrm{nm}$, there is still $1\,\mathrm{nm}$ left between the resonances. However, one can expect a huge degradation in IL and XT since the two channels are largely overlapping. Note that this is a very unlikely case. Using a denser channel spacing of $200\,\mathrm{GHz}$ ($1.6\,\mathrm{nm}$) the minimum channel spacing with this channel spacing variation is reduced to only $0.2\,\mathrm{nm}$ and large degradations become much more likely. A channel spacing $\leq 200\,\mathrm{GHz}$ using this technology are therefore considered too aggressive, especially when the CS is not yet optimized. In the following we investigate further how robust our $300\,\mathrm{GHz}$-spaced WDM filter designs are against these CS deviations.

5.5 Collective tuning

As discussed earlier, the deviation of the absolute position of the filter bank (quantified to be larger than one FSR in Fig.5.6) needs to be corrected, either by a temperature controlled (TEC) submount or by using a more effective on-chip integrated heater that only heats the filter area. In the case of an on-chip heater, typically individual heaters are used to control the individual resonances [18], which makes the actual control of this filter complex. In this section, we investigate the feasibility of using a collective integrated heater to thermally control a four-channel demultiplexer with a channel spacing of $300\,\mathrm{GHz}$. The efficiency and the wafer-level uniformity of this collective heater is characterized in section 5.5.2. However, as discussed earlier, the collective integrated heater cannot compensate for the relative deviation of the channel's center wavelength with respect to the adjacent channels within a device. Any channel spacing variation will have direct consequences on the performance of the receiver when locked in a fixed channel

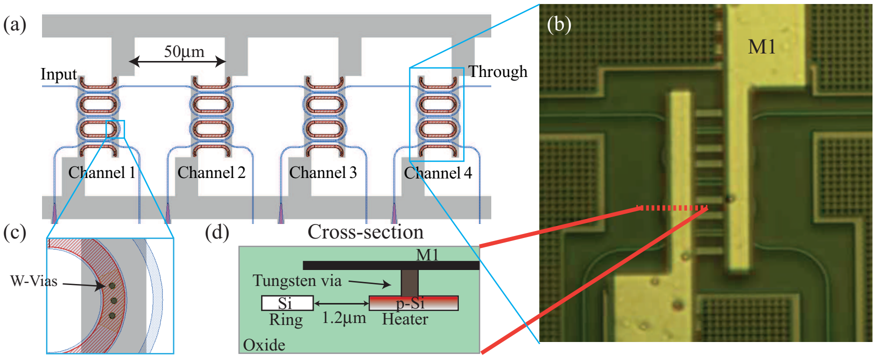

Figure 5.11: A robust 4-channel WDM demultiplexing filter based on collectively tuned silicon ring resonators with (a) design schematic (Sipp08), (b) microscope picture of the filter and heater, (c) zoom on the design of 1 ring resonator and p-doped silicon resistor and (d) cross-section of the ring waveguide and heater structure.

grid of $300\,\mathrm{GHz}$ or $2.4\,\mathrm{nm}$. A profound comparison is made between the robustness of a WDM filter using a first-order and second-order ring resonator design. The consequences on the IL and XT of the receiver's worst channel are discussed in section 5.5.3, defining the robustness of our design against fabrication related non-uniformities on device scale. The following results were published in Journal of Lightwave Technology [21].

5.5.1 Fabrication

The heaters were implemented as highly p-type doped, $1\,\mu\mathrm{m}$-wide silicon resistors, located at $1.2\,\mu\mathrm{m}$ away from the inner edge of the ring waveguides. Local silicide and a CMOS-like tungsten/copper back-end are used to contact the heaters. A design schematic and microscope picture of one channel of a 4-channel WDM filter using second-order ring resonators with a collective heater is given in Fig.5.11.

5.5.2 Thermal tuning

A large thermal tuning range and low corresponding energy consumption are important for the realization of a tunable WDM receiver. In addition, a collective heater should distribute the heat uniformly over all the channels. These metrics are calculated by tracking the resonance red-shifts while applying a voltage to the heater. This is shown in Fig.5.12(a) and (b) where this red-shift for different applied heater powers is plotted for designs using respectively first-order and second-order ring resonators. For the sake of clarity only the first channel is plotted but the denoted power consumption and heater efficiency is calculated for the

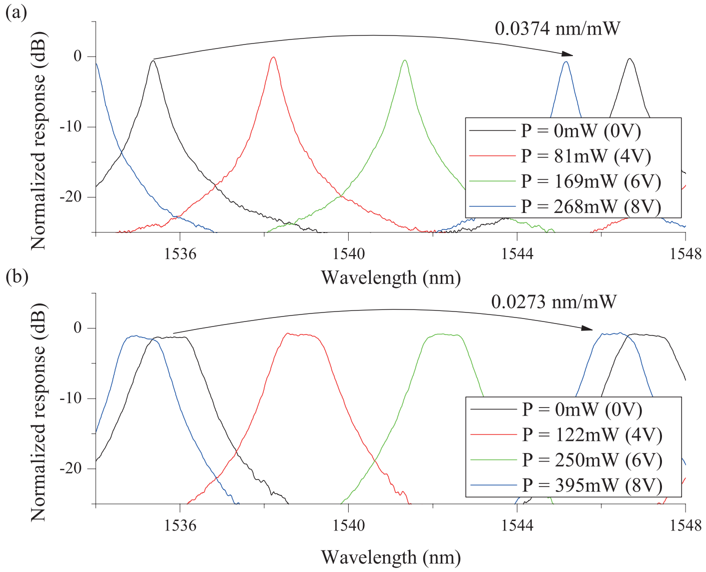

Figure 5.12: Thermal tuning of the spectral response of one channel of a 4-channel WDM filter using (a) first-order and (b) second-order ring resonators. Tuning efficiencies indicated in the figure are for the whole filter bank.

whole filter bank.

Tuning efficiency The collective tuning efficiency is $0.0374\,\mathrm{nm/mW}$ for the design with first-order ring resonators which is $37\,\%$ more efficient then when implemented with second-order ring resonators ($0.0273\,\mathrm{nm/mW}$). This difference is explained by the larger heated area in the latter case. In Fig.5.13 the relative shift expressed in function of power consumption is plotted for all four channels. From this figure it can be seen that each channel has an equal efficiency and thus a very good local heater uniformity is achieved. Efficiency measurements were taken on a full wafer. The mean shift of all 4 channels is used to plot a device-count histogram for the power consumption needed for a full FSR shift in Fig.5.14. From this plot it is clear that there is also a very good uniformity on wafer level perceived, indicating a well defined resistor using highly p-doped silicon strip next to the optical waveguide (see Fig.5.3). Wafer-mean heater efficiency is for WDM filter design using first-order ring resonators (1RR) $0.028\,\mathrm{nm/mW}$ and for second-order ring resonators (2RR) $0.038\,\mathrm{nm/mW}$, both with a very small spread, indicating a well defined resistor used as the heater. Based on the wafer-mean values, it takes on average $296\,\mathrm{mW}$ for 1RR and $407\,\mathrm{mW}$ for 2RR to tune the 4-channel WDM filter over a full FSR (calculated for each device separately but on average $11.35\,\mathrm{nm}$). For one channel this corresponds to $74\,\mathrm{mW/FSR}$ for the filter design using 1RR

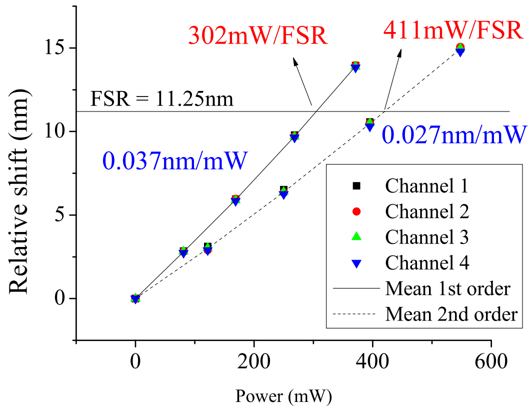

Figure 5.13: The relative tuning of a 4-channel filter bank using first or second-order MRRs in function of the applied power to all four channels collectively, consuming respectively 302 mW *and* 411 mW *to tune a full free spectral range (π-phase shift for one filter is respectively* 38 mW *and* 51 mW*).*

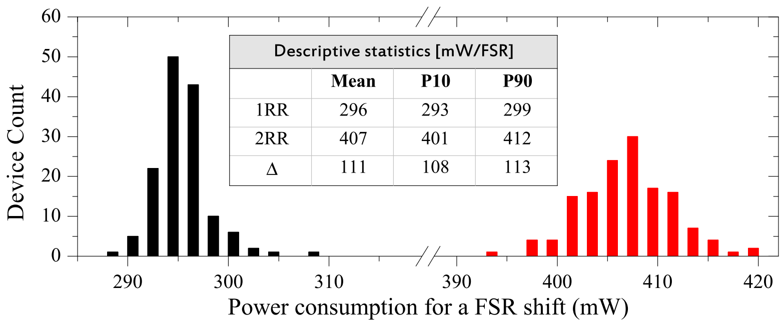

Descriptive statistics [mW/FSR]

	Mean	**P10**	**P90**
1RR	296	293	299
2RR	407	401	412
Δ	111	108	113

Figure 5.14: Device-count histograms of the power consumption for a FSR shift of all the channels.

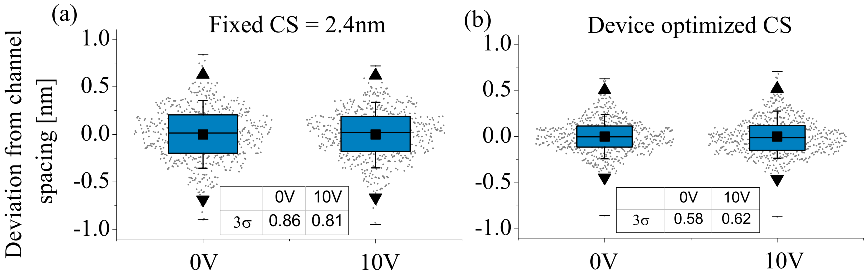

Figure 5.15: The channel spacing deviation is measured and compared for two heater voltages ($V = 0\,\mathrm{V}$ and $V = 10\,\mathrm{V}$) showing no degradation in channel spacing error.

and $101\,\mathrm{mW/FSR}$ using 2RR. These values are comparable with other reported values, e.g. $89\,\mathrm{mW/FSR}$ in [17]. As demonstrated in [22], these efficiencies can drastically be improved using a top-side silicon undercut-etching technique, resulting in a $2.4\,\mathrm{mW/FSR}$.

Local heater uniformity The local heater uniformity, or in other words the ability of a heater to distribute the heat uniformly over all the channels, is investigated based on the channel spacing deviation. If the collective heater would not be uniform, the channel spacing deviation could become worse, with a degraded performance of the collectively tuned demultiplexer as a direct consequence. Therefore, we take the channel spacing deviation as a figure of merit to investigate the local heater uniformity.

In Fig.5.15, a comparison is made between the channel spacing deviation between an unheated device ($\mathrm{V} = 0\,\mathrm{V}$) and a heated device ($\mathrm{V} = 10\,\mathrm{V}$). The wavelength shift between the heated and the unheated heater status is more than a full FSR (which can be seen from Fig.5.12(b)). All the resonances of the 142 measured four-channel WDM filter using first-order ring resonators are considered (568 resonances in total). Their true deviation from the channel spacing is plotted (fixed as designed and device-optimized CS as explained in Fig.5.7). On top of these deviations, a boxplot is used to visualize the distribution of the data better. By investigating the deviation change away from the fixed-as-designed CS (Fig.5.15(a)), one can see that the deviations became slightly smaller (3σ from $0.86\,\mathrm{nm}$ to $0.81\,\mathrm{nm}$), indicating that the channel spacing of the heated WDM filter became closer to the desired one (i.e. as designed). Indeed, a shift of the wafer-mean channel spacing is detected, moving from $2.54\,\mathrm{nm}$ to $2.5\,\mathrm{nm}$. To eliminate the effect of a changed channel spacing, we also investigate the deviations from the device-optimized CS, shown in Fig.5.15(b). One can see from this figure that these deviations became slightly larger. This trend can now safely be devoted to the non-uniformity of the heater (3σ from $0.58\,\mathrm{nm}$ to $0.62\,\mathrm{nm}$). However these changes

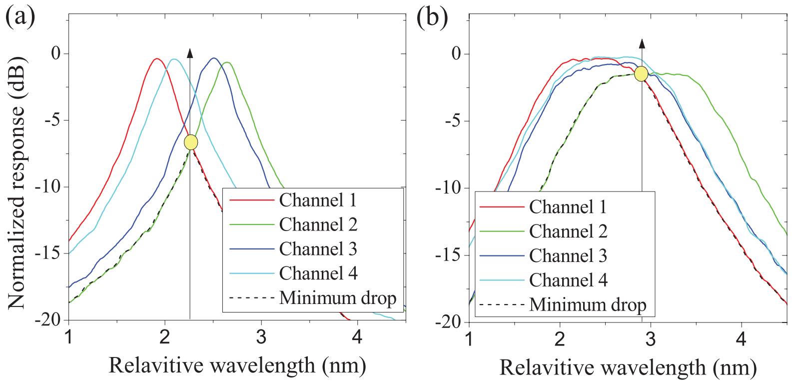

Figure 5.16: Numerically shifted responses of all channel resonances, each shifted with a multiple of the designed channel spacing on top of each other for (a) 1RRs and (b) 2RRs. In this way one easily detects deviations of the designed channel spacing. Based on this curve the optimum position of the receiver grid is easily derived based on the maximum of the moving minimum of all four channels (dashed line).

are very small and we can conclude that the employed integrated collective heater has an excellent local heater uniformity.

5.5.3 IL and XT performance using collective tuning

To test how tolerant both receivers are to lock into a fixed channel grid of $300\,\mathrm{GHz}$ or $2.4\,\mathrm{nm}$, we numerically shift the measured responses of all 4 channel resonances with an appropriate multiple of the designed channel spacing on top of each other. This way, the impact of device-scale variations of the relative resonance frequencies away from their ideal spectral position are easily detected. The result is plotted in Fig.5.16(a) and (b), respectively for a 1RR and 2RR design. It can be seen that for a 1RR design, the channel spacing deviation can be much larger than the $3\,\mathrm{dB}$ BW. For a 2RR design, a better result regarding filter overlap is found due to their broader resonance shape.

Next, the collective tuning of the resonances of the ring resonators is emulated by choosing the best position of the receiver grid which is determined by the minimization of the IL of the worst channel. This procedure is also illustrated in Fig.5.16 where the dashed line is the moving minimum response of all four drop channels. The maximum of this curve overlaps by definition with the minimum IL of the worst channel, which is determining the overall performance of the receiver. The resulting IL and XT of all the channels can then be calculated and is denoted in Fig.5.17, where also the laser grid with a $300\,\mathrm{GHz}$ grid spacing is plotted as a dashed arrow. In this example, both receivers channel 1 and 2 have the largest IL and are thus the channels that are limiting the performance of the

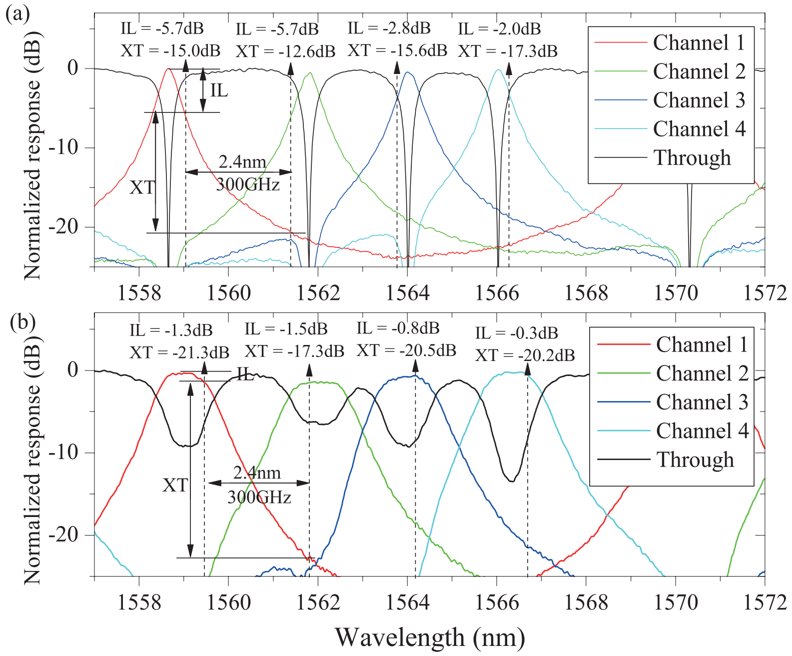

Figure 5.17: The typical normalized spectral response of a 4-channel WDM filter implemented with (a) 1RRs and (b) 2RRs. The channel responses are collectively tuned to an optimum position where the insertion loss (IL) of the worst channel is minimized. The resulting IL and crosstalk (XT) per channel when collectively tuned and operated with four 300 GHz*-spaced lasers (dashed arrows) is denoted in the figure as well.*

receiver. We compare both receivers (using first and second-order ring resonators) based on their worst channel. This results in an IL of $-5.7\,\mathrm{dB}$ and XT of $-12.6\,\mathrm{dB}$ using first-order ring resonators, which makes the design using second-order ring resonators superior against device-scale resonance variations with an IL of only $-1.47\,\mathrm{dB}$ and XT of $-17.3\,\mathrm{dB}$. To validate our findings, we measured the same two designs on all 146 dies of a $200\,\mathrm{mm}$-wafer and compared both receivers on their degraded IL and XT when collectively locked on a fixed laser grid with a $300\,\mathrm{GHz}$ spacing. In Fig.5.18, a histogram of the IL and XT is shown for the worst channel of each design, together with the mean, 10^{th} and 90^{th} percentiles. From this figure it is clear that by using second-order ring resonators superior characteristics regarding IL and XT are perceived. This is not only true for the average value but also the spread of these metrics (10^{th} and 90^{th} percentiles) is smaller. This superior performance can be devoted to the flat-top filter behavior of a second-order ring resonator design. As shown in the inset tables of Fig.5.18, the wafer-mean value of the IL is $-6.09\,\mathrm{dB}$ using first-order ring resonators, which is $4.7\,\mathrm{dB}$ larger than the design using second-order ring resonators, which has

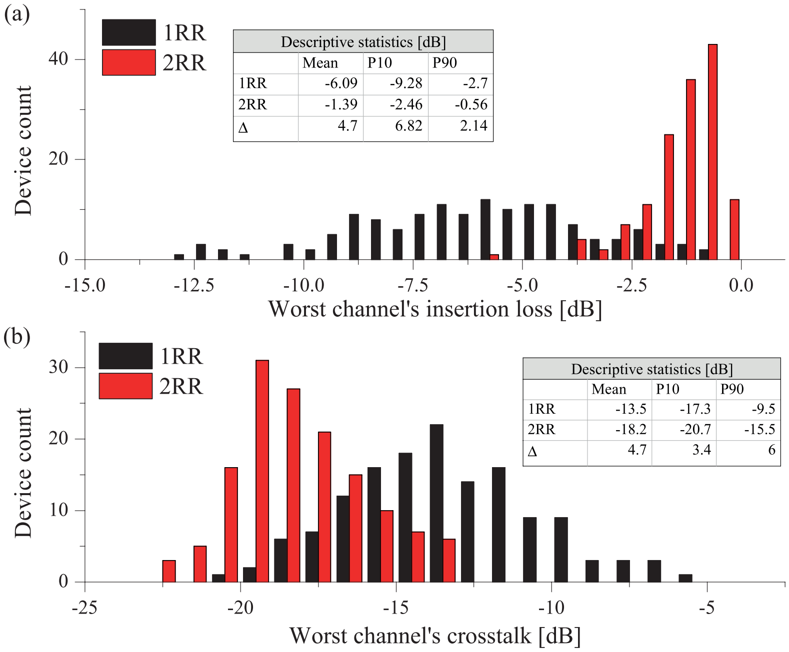

Figure 5.18: Device-count histogram of (a) insertion loss and (b) crosstalk of the worst channel of the 4-channel receiver using 1RRs and 2RRs when the filter is collectively tuned. The 2RRs are much more robust against device level non-uniformities influencing the CS between the channels. In the inset table the mean, 10^{th} and 90^{th} percentiles are given as well.

a wafer-mean IL of only $-1.39\,\mathrm{dB}$. Also for XT we found an improvement of $4.7\,\mathrm{dB}$ using second-order ring resonators (wafer-mean XT = $-18.2\,\mathrm{dB}$) with respect to the poor wafer-mean XT of $-13.5\,\mathrm{dB}$ using first-order ring resonators.

5.5.4 Discussion on power consumption heater

To gain insight in how much power one needs to lock a receiver grid to an incoming laser grid, we can use the knowledge of the previous section where the actual position of the filter bank around a certain wavelength is uniformly distributed. Independent of the actual operation temperature, one can expect in a worst case scenario the need to tune the receiver filter grid up to a full FSR to lock it to an incoming laser grid. If each channel of the receiver will handle a bit rate of $20\,\mathrm{Gb/s}$ (following the reasoning of [23]), this would mean a worst-case power consumption of $3.7\,\mathrm{pJ/bit}$ using first-order ring resonators and a $5.07\,\mathrm{pJ/bit}$ using second-order ring resonators . Note that this is a worst-case scenario, on average one device will consume half of this power (corresponding to only half a FSR as the average tuning shift). This is far from the 2015 energy target for tunable WDM filters of $30\,\mathrm{fJ/bit}$ [23] or reported values of $15\,\mathrm{fJ/bit}$ [24] using underetched waveguides and flexible wavelength registration. With the latter technique, one only has to shift the receiver comb over maximum one channel spacing instead of a full FSR. In that case the FSR should be exactly a $M \times \Delta\lambda$. This and several other ideas to drastically improve the power consumption are discussed extensively in the following chapter (6.3) on page 6-5.

5.5.5 Conclusion

In this section we have demonstrated a robust 4-channel WDM demultiplexing filter using collective tuning. The flat-top response of second-order multi-ring filters is exploited to overcome the wafer- and device-scale irregularities on channel spacing and channel bandwidth arising from fabrication non-uniformity. The improved filter response enables a thermal control mechanism based on collective tuning to track the wavelengths of a WDM laser source on a specified channel grid. After collective tuning with integrated heaters, the 4-channel second-order filter exhibits a worst-channel insertion loss of $-1.39\,\mathrm{dB}$ and a crosstalk of $-18.2\,\mathrm{dB}$ (wafer-level average), an improvement of $4.7\,\mathrm{dB}$ on both metrics over first-order filters. The required power consumption of such a collectively tuned 4-channel WDM filter using with 2RRs can reach up to $406\,\mathrm{mW/FSR}$ (wafer-level average) to tune over a full FSR. This relatively low efficiency is expected to increase by an order of magnitude, when proven techniques on removing of the substrate are applied (e.g. [22]). Some initial results on applying the technique to these structures can be found in section 6.3.4 in the following chapter. This reduced complexity for thermal control will likely reduce the power and footprint overhead of the required CMOS control circuits, which will be beneficial when scaling to higher channel counts.

5.6 Simple thermal control

The optimization of the receiver based on the minimization of the worst-channels IL should be implemented on chip such that no manual control is needed for the heaters controlling the absolute wavelengths of the filter bank. Furthermore this optimization should be dynamic, since ambient and on-chip temperatures can vary in time.

5.6.1 Tuning strategy

Although easy to visualize, this optimization scheme would require tapping off some power of the dropped channels and process these n signals from a n-channel

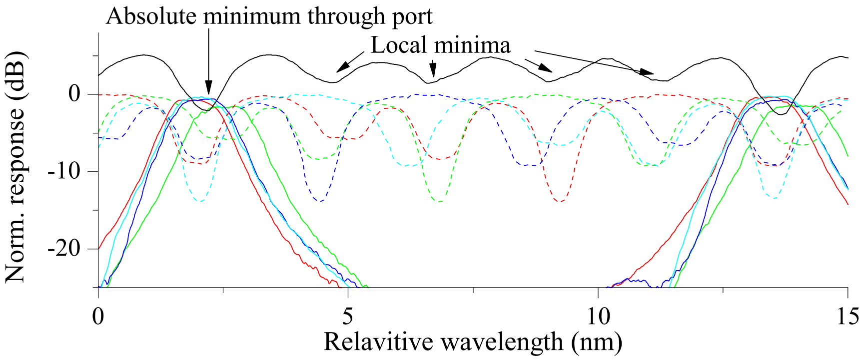

Figure 5.19: Normalized response of the with a multiple of the channel spacing shifted resonances for a 4-channel WDM filter filter employed with second-order ring resonators.

WDM filter simultaneously. This will not only require twice as much photodiodes, and thus space, but also some computing power. A much easier and elegant optimization method is based on the WDM filters single through port instead of the 4 drop ports and would thus only need one extra photodiode. The photodiode terminating the optical through port will detect the sum of the parts of the 4 input signals which were not dropped by the preceding cascaded filters. An algorithm can then locate a minimum of this signal in function of heater driving signal, which will corresponds with a receiver grid position where the maximum power of all input signals were dropped. In the following we will compare the exact method based on the information of the 4 drop ports with the estimation based on the through port. The four-channel WDM filter using second-order ring resonators presented in previous section 5.3 is used as our device under test.

5.6.2 The estimated optimum position

In the following we investigate whether the estimated optimum position based on the minimum of the through port matches with the exact optimum position extracted based on the multiple signals coming from the drop ports. Therefore, we transform once more the frequency response of Fig.5.17 by shifting all channel resonances with a multiple of the designed channel spacing on top of each other. We do this also for the corresponding through port responses. This is shown in Fig.5.19 for a four-channel WDM filter using second-order rings. The sum of the input signals detected at the through port (black line in Fig.5.19), resembles the incoming signal to our (hypothetical) control circuit. From Fig.5.19, one can see that there is only one absolute minimum over a full FSR, which is close to the optimum position of the resonances. Besides the absolute minimum, there are several local minima in between the two absolute minima. This can be understood

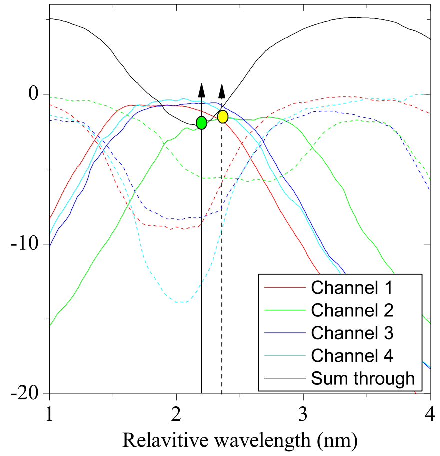

Figure 5.20: Zoom on the resonances, also plotted in Fig.5.19, showing the good estimation of the receivers best spectral position based on the through port.

by the fact that the FSR is designed to be $(n+1) \times CS$ for an n-channel WDM filter with CS the channel spacing. In this way it is possible to ensure that each channel is correctly directed (e.g. incoming channel 1 directed to outgoing channel 1), which would not be possible if the FSR is $n \times \delta\lambda$. In the latter case there will be a n times an absolute minimum and then the decision circuit could not distinguish between the different positions. At the other hand, this strategy can then still be used when flexible wavelength registration can be afforded [24]. If the resonance deviations with respect to the CS is too large, a local minimum could become an absolute minimum but then only 3 out of 4 channels are locked properly. As a consequence, one of the channels of the receiver is not detecting anything, and the other channels are directed wrongly (e.g. incoming channel 1 directed to outgoing channel 2). In Fig.5.20, a zoom in of Fig.5.19 is plotted. We represent the incoming 4-channel $300\,\mathrm{GHz}$ spaced input with one arrow (overlap of the four equally spaced input wavelengths). The optimum position according to the minimum of the through channel method is denoted with a solid arrow and according to maximum of the moving minimum of the four drop channel responses with a dashed arrow. The yellow and green dot are representing the corresponding WDM filter's worst channel IL. Even though the device-level resonance deviation is relatively large for channel 2 (green), the optimum position of the receivers grid is nicely determined by the sum at the through port. The reason for this robustness is the fact that the stop band of the through port is relatively broad. Using a first-order ring resonator would result in a very narrow stop-band, and the proposed strategy would initially fail due to the large device-level resonance deviations.

	XT [dB]		IL [dB]	
grid position	mean	worst	mean	worst
estimated	-18.1	-7.7	-1.6	-6.7
exact	-18.3	-13.5	-1.3	-5.5
Δ	-0.02	-7.2	-0.3	-1.2

Table 5.4: Worst channels performance quantified in a wafer-mean and wafer-worst values when collectively tuned to the incoming grid based on estimated and exact method.

5.6.3 Comparison between the exact and estimated position

The degradation between the two methods is clear by comparing the worst channels IL for respectively the through channel estimation method and the exact method based on the drop channels by comparing the green and yellow dot. Using second-order ring resonators, the degradation is only small (in this case only $0.5\,\mathrm{dB}$). We verify our findings with wafer-scale measurements.

For only 6 of the total 142 measured four-channel WDM filters usings second-order ring resonators, the estimation method failed. This can be explained due to the flat-bottom characteristic of the pass band. For the following investigation we discard the 6 wrongly optimized devices of that data set. The performance of the remaining devices are shown in Tab.5.4, listing the worst channels IL and XT based on the introduced estimation method or the exact method. From this table, one can find that the mean receivers degradation when the estimated method with respect to the exact method is very small. However, one can find that the worst XT of all devices on the wafer has been increased with $7\,\mathrm{dB}$ and the worst IL decreased with $1.2\,\mathrm{dB}$. Over all we can safely state that the estimation method based on the through port could be used as an elegant alternative to the exact method.

5.6.4 Implementation

In the following we discuss briefly a possible implementation of this feedback control loop. First, the component is initiated during a calibration phase. In this phase the power of the heater control signal is increased linearly in such a way that the filter bank is shifted for a full FSR. Using an analog to digital convertor the signal detected at the through port of the component is sampled and stored in an on-chip logic. An electronic circuit finds the minimum of this curve and the corresponding power and applies this power then to the heater. After this calibration phase the ambient temperature can change in time and the control circuit operates then in a tracking phase. In this phase, the control port is slowly sampled (for a low power consumption) and its value is compared to the minimum value stored before. If the power difference exceeds a certain threshold, the circuit can perform a short optimization phase where the applied power is changed only over a small range, e.g.

one channel spacing, to detect the local minimum. The time that it takes to perform the heater sweep is limited by the heater time constant of the ring resonator configuration. This time constant is highly depending on the heating insulation and hence the heater efficiency. The better the efficiency the slower the heater time constant. This time constant has been measured using a Mach-Zenhder interferometer by colleague Masood in [25] and varies between 20-200 μs depending on the heater efficiency.

5.6.5 Conclusion

We have demonstrated the working principles of an simple thermal control strategy. The minimum response of the through port is used as an estimation for the optimum receiver's position. This strategy would only require a single photodiode terminating the single through port of the cascaded resonators and could offer an alternative to the more complex optimization that analyzes the response of each channel separately. A drastic simplified decision circuit with only one input signal could then drive the collective heater. This strategy finds its success in the robustness of the second-order ring resonators due to device-level non-uniformities. Only a small degradation is found in the WDM filter performance by using the proposed estimation method with respect to the more exact method used in previous section.

5.7 Polarization-insensitive 5-channel 20 Gb/s DWDM Ge receiver

In this section we extend the results of previous sections by using a 2-dimensional grating coupler (2D GC) [20] to decouple the two orthogonal polarization states of a single mode fiber on chip. Each polarization state has its own filter bank. In other words, each WDM channel consists out of two separate ring filters. Each decoupled channel is terminated with a single germanium (Ge) high-speed lateral PIN photodiode. The following results were submitted to OFC 2014. A schematic of the presented polarization-diversified DWDM Ge receiver design is shown Fig.5.21. The amount of channels is slightly increased to five which gives the system designer the freedom to use this channel as separate clock signal or as an extra channel transmit information.

5.7.1 Design

The designed filter array consists of two parallel identical arms with each five cascaded second-order (racetrack) ring resonators at a channel spacing of $300\,\mathrm{GHz}$ or $2.34\,\mathrm{nm}$. The ring radius is $4\,\mu\mathrm{m}$ and the coupling length $6.8\,\mu\mathrm{m}$ resulting in

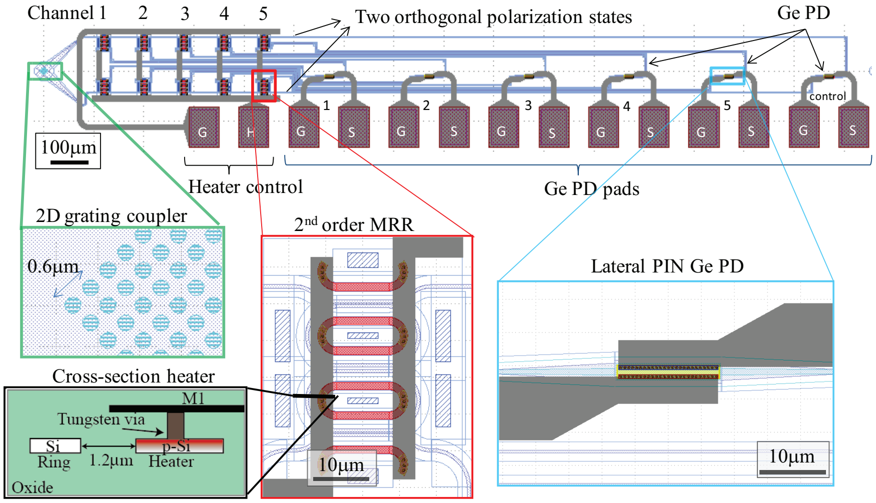

Figure 5.21: Schematic of a polarization-diversified DWDM receiver with five cascaded second-order ring resonators, p++ doped Si heaters and Ge PDs.

a FSR of $14\,\mathrm{nm}$. The channel spacing is achieved by a small increase in coupling length of $55\,\mathrm{nm}$ between two adjacent filters (circumference increase of $110\,\mathrm{nm}$). The bus-to-ring power coupling is 0.34 and ring-to-ring power of 0.055 which corresponds with a bus-to-ring gap of $178\,\mathrm{nm}$ and a ring-to-ring gap of $293\,\mathrm{nm}$. The wavelength dependency of the coupling is taking into account by adjusting the gap for each channel. The design is made on a $1\,\mathrm{nm}$ grid, an improvement compared to previous sections (5.4 and 5.5) where a mask resolution of $5\,\mathrm{nm}$ was used. The resulting crosstalk between the different channels is designed to be $-20\,\mathrm{dB}$. The details of the Si p++ doped heaters used can be found in Section 5.5.1. Total device footprint is $1.7\,\mathrm{mm} \times 0.28\,\mathrm{mm}$ but can easily be decreased to $1.1\,\mathrm{mm} \times 0.28\,\mathrm{mm}$ when the detector pad pitch is decreased to $50\,\mu\mathrm{m}$ instead of $100\,\mu\mathrm{m}$ as used now. Scaling this component to 10 channels would result in a total component size ≈ 40 times smaller than reported in [19] for an arrayed waveguide grating based filter. Each channel is terminated with a lateral PIN germanium photodiode with an intrinsic width of $0.75\,\mu\mathrm{m}$ and a length of $15\,\mu\mathrm{m}$.

5.7.2 Opto-electronic performance

The presented receiver is characterized using two orthogonal polarization states. The external fiber-referenced channel responsivity for each channel using a wavelength resolution of $0.1\,\mathrm{nm}$ is shown in Fig.5.22(a). The performance metrics are listed in Tab.5.5. The input 2D grating coupler has an insertion loss (IL) of $6.5\,\mathrm{dB}$. The germanium photodiodes have a very low dark current of around $8\,\mathrm{nA}$ at $2\,\mathrm{V}$

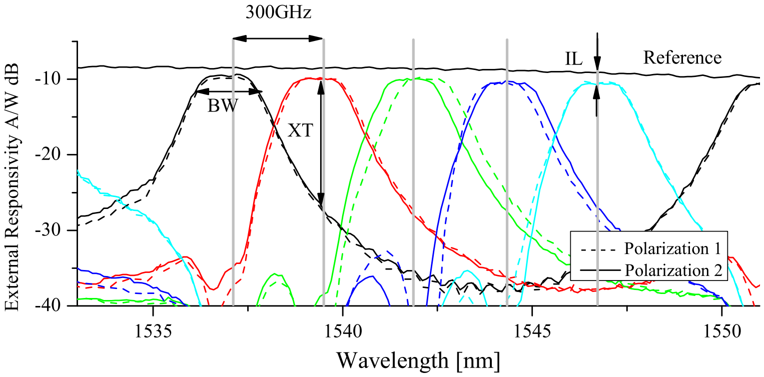

Figure 5.22: The fiber-referenced responsivity spectrum of the as-fabricated 5-channel WDM Ge receiver for both polarizations (solid/dashed lines). Details wafer: P123298-D05

Responsivity	$0.1\,\mathrm{A/W}$
1 dB BW	$1.2\,\mathrm{nm}$
XT [dB]	$\leq -15\,\mathrm{dB}$
IL 2D GC	$6.5\,\mathrm{dB}$
IL filter	$1.2\,\mathrm{dB}$
PD responsivity	$0.61\,\mathrm{A/W}$
Dark current	$\leq 8\,\mathrm{nA}$

Table 5.5: OE specifications of a as-fabricated 5-channel WDM Ge receiver. Specifications are valid for both polarization states. Details wafer: P123298-D05

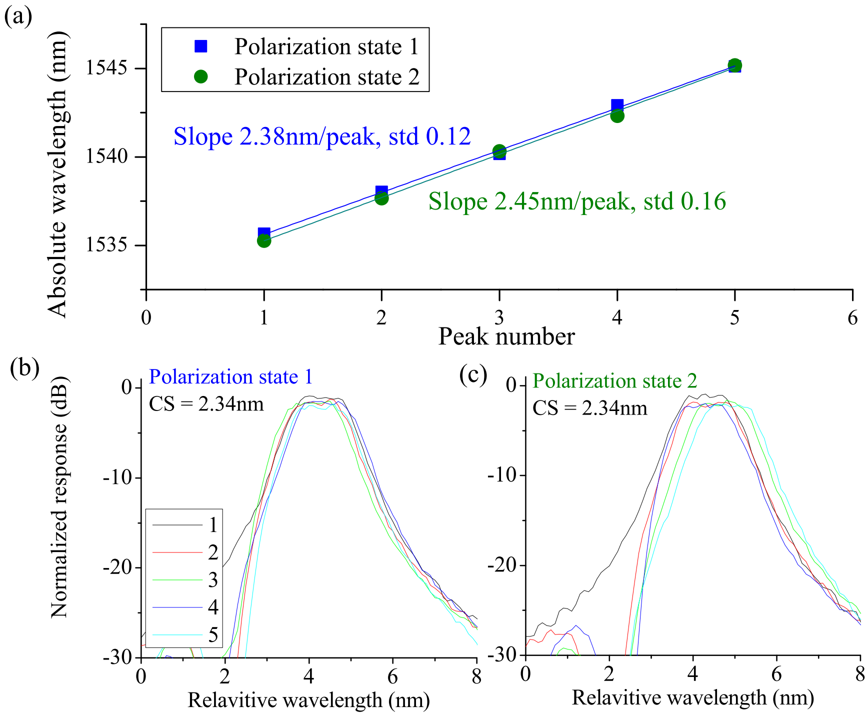

Figure 5.23: The center wavelength of the channels of polarization states in function of their channel number (a) and the overlaid channel responses for polarization state 1 (b) and polarization state 2 (c). Details wafer: P130315 D08

reverse bias and a responsivity of $0.61\,\mathrm{A/W}$ resulting in a reference responsivity of $0.14\,\mathrm{A/W}$ (Fig.5.22). The IL of the ring resonator filters is about $1.2\,\mathrm{dB}$, bringing the overall fiber-referenced responsivity to $0.1\,\mathrm{A/W}$. The polarization dependence of the IL is very small ($\leq\ 0.5\,\mathrm{dB}$) and the maximum crosstalk (XT) between the 5 channels is $-15\,\mathrm{dB}$ (between channel 3 and 4).

5.7.3 Channel spacing analysis

To enable collective tuning, a uniform channel spacing is necessary as explained in 5.4.4. Having a separate demultiplexer arm for each polarization state increases the need on a well controlled channel spacing, especially on device level. We have investigated this on a different device (but same design) than shown in Fig.5.22. A channel spacing (CS) analysis is performed on a OE demultiplexer for two polarization states, illustrated in Fig.5.23(a), where the center wavelengths of the adjacent channels are plotted in function of their channel number. Fitting these absolute wavelengths for each polarization state learns us that the CS of polarization state 1 is $2.38\,\mathrm{nm}$ whereas the CS of polarization state 2 is larger ($2.45\,\mathrm{nm}$), which is a rather large difference for two demultiplexers separated $100\,\mu\mathrm{m}$ away from each other. To visualize this effect, we overlay the OE responses of a all channels according to the designed $300\,\mathrm{GHz}$ channel spacing (or $2.34\,\mathrm{nm}$), as shown in Fig.5.23(b) for polarization state 1 and (c) for polarization state 2. Indeed, one can notice a walk-off of the center wavelength for polarization state 2, due to the larger as designed CS. One should notice at this point that the optimum position of the wavelength comb, defined by e.g. the minimization of the IL of the worst channel, is different for both polarization states. A polarization change would thus require a new optimization using the collective heater. However, the broad $1\,\mathrm{dB}$ BW $1.2\,\mathrm{nm}$ of the individual channel responses can readily cope with this large channel spacing walk-off and no degradation of IL is found. With 5-channel $300\,\mathrm{GHz}$ spaced input signal, this receiver exhibits a worst channel performance of $-1.96\,\mathrm{dB}$ insertion loss (with respect to the reference waveguide) for polarization state 1 and $-2.22\,\mathrm{dB}$ for polarization state 2. In these conditions the worst channels crosstalk is $-15.3\,\mathrm{dB}$ and $-16.8\,\mathrm{dB}$ for respectively polarization state 1 and 2.

5.7.4 High-speed performance

The bandwidth of the photodiodes is characterized using a $50\,\mathrm{GHz}$ Lightwave Network Analyzer. The normalized transmission s21-parameters for all five channels are shown in Fig.5.24 demonstrating a $3\,\mathrm{dB}$ BW ranging between $20\,\mathrm{GHz}$ and $26\,\mathrm{GHz}$ at $2\,\mathrm{V}$ reverse bias. At smaller bias voltages the BW is measured $13.5\,\mathrm{GHz}$ at $0.5\,\mathrm{V}$ and $18.5\,\mathrm{GHz}$ at $1\,\mathrm{V}$ reverse bias. The same photodiode is also characterized using a pseudo-random bit sequence with a length of 2^7-1 at $20\,\mathrm{Gb/s}$ at $2\,\mathrm{V}$ reverse bias. No electrical amplification is used to visualize the received signal on an oscilloscope and therefore a rather large optical input power of $11.5\,\mathrm{dBm}$ is used. In Fig.5.24, the resulting eye diagram is showing a clearly open eye at $20\,\mathrm{Gb/s}$.

This measurement has been repeated in a later stage of writing the manuscript using a better characterization equipment. Using the N1045 60GHz remote sampling head from Agilent, we could improve the performance of the photodiodes due to a lower noise level. In Fig.5.25, the electrical eye diagrams at $20\,\mathrm{Gb/s}$ (bias $-2\,\mathrm{V}$) are shown with a very uniform performance with a signal-to-noise ratio (SNR) of 7.0. This SNR resembles the Q-factor of the eye-diagram and corresponds to BER of 10^{-12}. The polarization, fiber position and fiber angle are fixed for all channels. Note that an uniform channel spacing of $2.4\,\mathrm{nm}$ is used with a uniform resulting eye amplitude variation between $8-10.7\,\mathrm{mV}$. Also in this figure, one can find the optical input using a PRBS signal with length $2^{15}-1$. Input power is $13\,\mathrm{dBm}$.

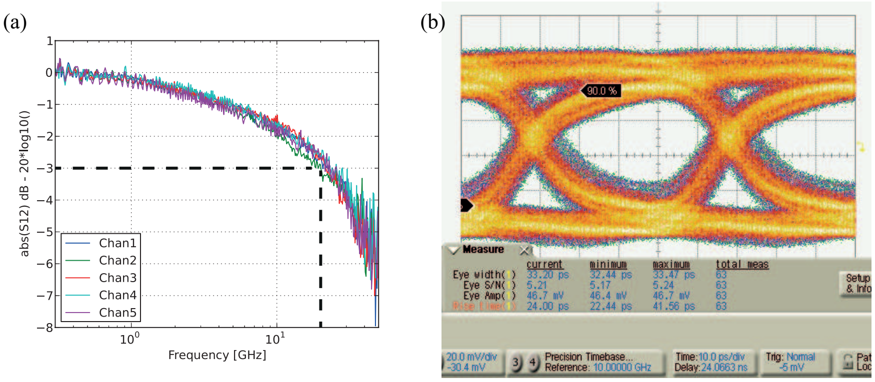

```
              current    minimum    maximum    total meas
Eye width(1)  33.20 ps   32.44 ps   33.47 ps   63
  Eye S/N(1)  5.21       5.17       5.24       63
  Eye Amp(1)  46.7 mV    46.4 mV    46.7 mV    63
Rise time(1)  24.00 ps   22.44 ps   41.56 ps   63
```

Figure 5.24: Open-eye diagram at $20\,\mathrm{Gb/s}$*, PRBS length* $2^7 - 1$ *at* $-2\,\mathrm{V}$ *bias. Input power* $11.5\,\mathrm{dBm}$.

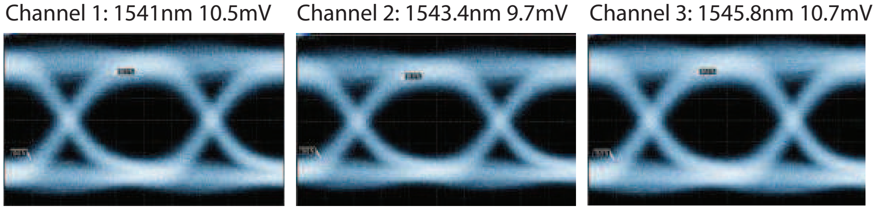
Channel 1: 1541nm 10.5mV
Channel 2: 1543.4nm 9.7mV
Channel 3: 1545.8nm 10.7mV

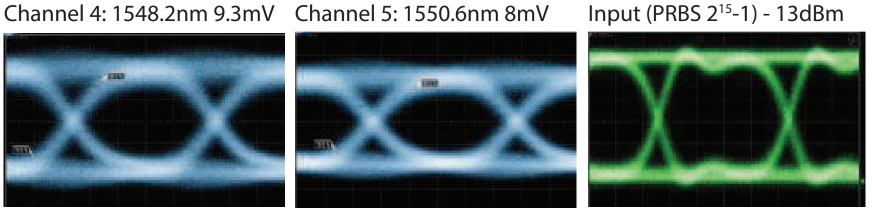
Channel 4: 1548.2nm 9.3mV
Channel 5: 1550.6nm 8mV
Input (PRBS 2^{15}-1) - 13dBm

Figure 5.25: Uniform eye diagrams of 5 channel Ge receiver with signal-to-noise ratio (SNR) of 7.0. The eye amplitude is varying between $8 - 10.7\,\mathrm{mV}$. *A uniform channel spacing of* $2.4\,\mathrm{nm}$ *is used.*

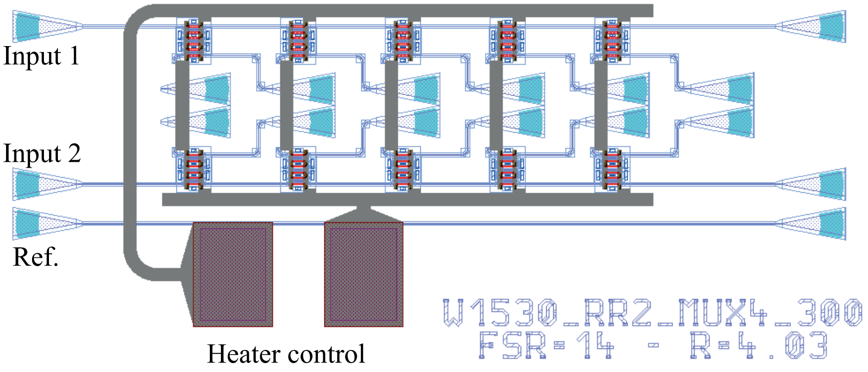

Figure 5.26: Optical (OO) test structure used for wafer-scale manufacturability test.

Specification	Mean	P10	P90
1 dB BW [nm]	1.17	1.16	1.2
3 dB BW [nm]	1.59	1.56	1.62
XT at CS [dB]	-18.8	-19.2	-18.3
IL [dB]	-1.12	-1.5	-0.73
λ 1 [nm]	1529	1525	1532

Table 5.6: Wafer scale mean values of the channel responses of an OO test structure.

5.7.5 Design for manufacturability

Wafer-scale measurements were performed on a purely optical test structure containing the same filter array but having two separate one-dimensional input grating couplers for TE polarization only and no Ge-detectors, as shown in Fig.5.26.

In Tab.5.6, the mean value and percentiles of the main characteristics of the individual channel responses are listed for 72 devices showing very uniform wafer-scale performance. The 1-dB and 3-dB bandwidth (BW) is tightly confined between $1.17\,\mathrm{nm}$ and $1.59\,\mathrm{nm}$. The mean crosstalk and insertion loss of a channel response is respectively $-18.8\,\mathrm{dB}$ and $1.2\,\mathrm{dB}$.

The wafer-scale channel spacing analysis (CS) is performed for both polarization states separately such as illustrated for a single opto-electronic (OE) device in Fig.5.23. The variation of the optimum channel spacing is plotted in Fig.5.27 for both polarization states. Remarkable is the difference between both polarization states which corresponds with earlier findings on the channel spacing analysis on the OE device. Polarization state 1 (resembling with the upper arm of the OO test structure) has a mean CS value which is slightly smaller than polarization state 2 ($2.31\,\mathrm{nm}$ versus $2.33\,\mathrm{nm}$). Note that these CS values correspond much better with the designed CS value of $2.34\,\mathrm{nm}$ with respect to earlier designs (e.g. Fig.5.8 on

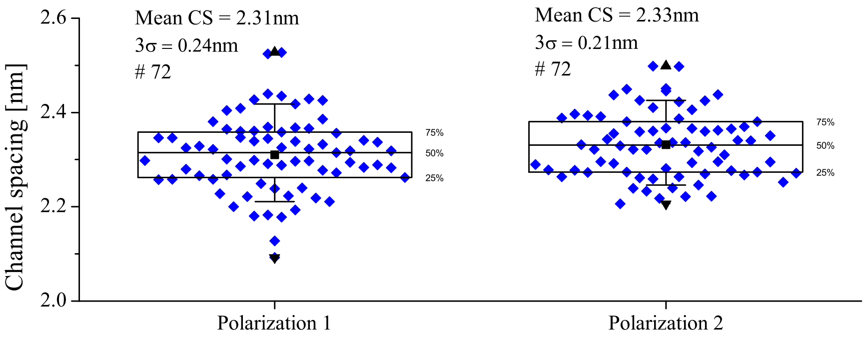

Figure 5.27: A wafer-scale CS analysis on the OO test structure, for both polarizations.

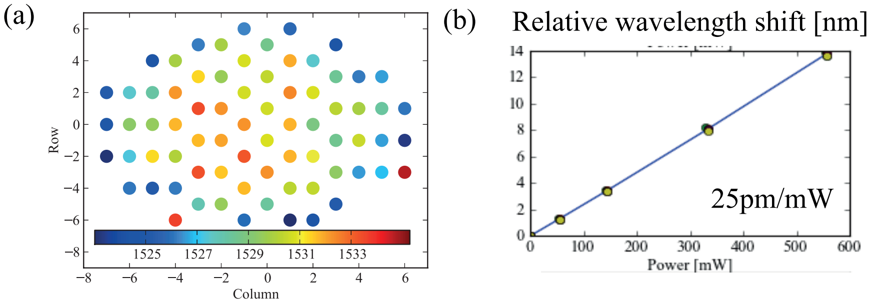

Figure 5.28: (a) The central wavelength the first channel (λ_1) relative to its position on the wafer and (b) the relative wavelength shift of the 5 channels in function of applied power to the collective heater.

page 5-14). Also the $3\,\sigma$ spread is smaller for polarization state 2 ($0.21\,\mathrm{nm}$ versus $0.23\,\mathrm{nm}$). With respect to the earlier generation of demultiplexers (single polarization 4-channel $300\,\mathrm{GHz}$ CS) the $3\,\sigma$ variation of $0.36\,\mathrm{nm}$ is significantly reduced (see Fig.5.8 on page 5-14).

Collective tuning will be used to overcome wafer-scale waveguide non-uniformity which causes the receiving comb to shift in center wavelength. This detrimental shift is characterized in Fig.5.28(a) where the center wavelength of channel 1 is plotted in function of its position on the wafer. As listed in 5.6, 80% of the devices is lying within $7\,\mathrm{nm}$ of the wafer mean value of $1529\,\mathrm{nm}$ showing a good within-wafer waveguide uniformity. Especially when one compares these values with the earlier generation of devices (quantified in Fig.5.6 on page 5-12), where a $23\,\mathrm{nm}$ wavelength variation was shown. This good uniformity lowers the maximum required tuning range and thus the power consumption.

Specification	Mean	Min	P10	P90	Max
XT Pol. 1 [dB]	-16.9	-20.1	-19.1	-14.3	-12.8
XT Pol. 2 [dB]	-16.7	-20.1	-19.1	-14.6	-11.9
IL Pol. 1 [dB]	-1.87	-6.51	-2.37	-1.14	-0.95
IL Pol. 2 [dB]	-1.73	-3.8	-2.22	-1.11	-0.92

Table 5.7: Wafer-scale OO performance of XT and IL for both polarization states (Pol. 1/2) of 5-channel demultiplexer with a 300GHz CS.

5.7.6 Thermal tuning

To characterize the integrated heaters used for collective tuning, we use the optical test structure, where an additional substrate removal step was used to improve the efficiency (discussed extensively in section 6.3.4 on page 6-8). The relative shift of the resonances of all five channels in function of applied power is shown in Fig.5.28(b), showing an efficiency of $25\,\mathrm{pm/mW}$ resulting in $142\,\mathrm{mW}$ for a full FSR ($14\,\mathrm{nm}$) tuning, calculated per channel. This efficiency is likely to be improved by optimizing the heater design (e.g. distance between heater and waveguide), which will be covered as well in section 6.3.4. A tight uniformity over all channels of the heater tunability is obtained, which is essential for collective thermal control.

5.7.7 Worst channels insertion loss and crosstalk

From a system point of view one is more interested on the over-all system performance crosstalk (XT) and insertion loss (IL). As before, an continuous wave input of 5 equally spaced wavelengths ($300\,\mathrm{GHz}$) is assumed to be the input of our system. The performance of the WDM filter is determined by its worst-channel performance. The wafer-scale measurements (72 devices) were used to calculated the worst-channel XT and IL, listed for the mean, minimum (min), P10, P90 and maximum (max) value in Tab.5.7. From this table, we can clearly state that this demultiplexer design is indeed polarization insensitive, or at least that both polarization arms are performing equally good. The mean worst-channel XT is $-16.7\,\mathrm{dB}$ and the 90% of the devices has a worst-channel XT better than $-14.3\,\mathrm{dB}$. The maximum crosstalk of all the 72 devics is $-11.9\,\mathrm{dB}$. The mean worst-channels IL is around $1.8\,\mathrm{dB}$, but only 10% of the devices have a worst-channels IL below $-2.22\,\mathrm{dB}$.

5.7.8 Conclusion

We demonstrated in this section a 5-channel DWDM Ge receiver array with a highly responsive (fiber-referenced $0.1\,\mathrm{A/W}$), polarization-insensitive and uniform channel response with crosstalk better than $-15\,\mathrm{dB}$. The photodiode signal bandwidth is larger than $20\,\mathrm{GHz}$, having a $20\,\mathrm{Gb/s}$ open-eye diagram at $2\,\mathrm{V}$ reverse bias while having a low dark current of $8\,\mathrm{nA}$. The integrated collective heater shows uniform heating and an efficiency of $24.7\,\mathrm{pm/mW}$. In addition a high manufacturability and yield is demonstrated based on wafer-scale measurements, with mean worst-channels XT of $-16.7\,\mathrm{dB}$ and a mean worst-channels IL of $1.8\,\mathrm{dB}$.

5.8 Conclusion

In this chapter we addressed four challenges of WDM optical devices based on ring resonators: manufacturability, collective tuning, simple thermal control and polarization insensitivity.

A 4-channel $300\,\mathrm{GHz}$ WDM filter using first- and second-order ring resonators is showing very good manufacturability (section 5.4) resulting in tight specifications of the measured channel responses on wafer-level. This indicates a well controlled fabrication. However, a comprehensive channel spacing analysis shows a 3σ device-scale resonance variation of $0.7\,\mathrm{nm}$ or $87.5\,\mathrm{GHz}$ as a technology limitation. On component level this would require the use of individual heaters with a complex control.

In section 5.5 we have demonstrated a robust 4-channel WDM filter using collective tuning. The flat-top response of second-order ring filters is exploited to overcome the wafer- and device-scale irregularities on channel spacing and channel bandwidth arising from fabrication non-uniformity. The improved filter response enables a thermal control mechanism based on collective tuning to track the wavelengths of a WDM laser source on a specified channel grid. After collective tuning with integrated heaters, the 4-channel second-order filter exhibits a worst-channel insertion loss of $-1.39\,\mathrm{dB}$ and a crosstalk of $-18.2\,\mathrm{dB}$ (wafer-level average).

To ease the optimization method of finding the IL-optimized spectral position of the WDM filter, we investigated in section 5.6 a simplified decision circuit using a single photodiode terminating the single through port of the cascaded ring resonators.

We ended this chapter in section 5.7 with a promising demonstration of a 5-channel DWDM Ge receiver array with a highly responsive (fiber-referenced $0.1\,\mathrm{A/W}$), polarization-insensitive and uniform channel response with crosstalk better than $-15\,\mathrm{dB}$. With a uniform bandwidth of $20\,\mathrm{GHz}$, each channel could handle a data rate of $28\,\mathrm{Gb/s}$. We showed an open eye-diagram at $20\,\mathrm{Gb/s}$ which demonstrates a $100\,\mathrm{Gb/s}$ aggregate bandwidth.

In the next chapter we will investigate the bandwidth scalability of WDM components in Si and several strategies to lower the power consumption of the integrated heaters.

References

[1] *Luxtera's 4x28Gbs transceiver using PSM4.*, 2013.

[2] A M J Koonen, Haoshuo Chen, Henrie P A Van Den Boom, and Oded Raz. *Silicon Photonic Integrated Mode Multiplexer and Demultiplexer*. IEEE Photonics Technology Letters, 24(21):1961–1964, 2012.

[3] C R Doerr, L Chen, L L Buhl, and Y Chen. *Eight-Channel SiO / Si N / Si / Ge CWDM Receiver*. IEEE Photonics Technology Letters, 23(17):1201–1203, 2011.

[4] Long Chen, Christopher R. Doerr, Larry Buhl, Yves Baeyens, and Ricardo a. Aroca. *Monolithically Integrated 40-Wavelength Demultiplexer and Photodetector Array on Silicon*. IEEE Photonics Technology Letters, 23(13):869–871, July 2011.

[5] Xia Chen, Chao Li, Christy K Y Fung, Stanley M G Lo, and Hon K Tsang. *Apodized Waveguide Grating Couplers for Efficient Coupling to Optical Fibers*. IEEE Photonics Technology Letters, 22(15):1156–1158, 2010.

[6] Wim Bogaerts, Dirk Taillaert, Pieter Dumon, Dries Van Thourhout, Elroy Pluk, and B V Genexis. *A polarization-diversity wavelength duplexer circuit in silicon-on-insulator photonic wires*. Optics Express, 15(4):1335–1344, 2007.

[7] Yunhong Ding, Liu Liu, Christophe Peucheret, Jing Xu, Haiyan Ou, Kresten Yvind, Xinliang Zhang, and Dexiu Huang. *Towards Polarization Diversity on the SOI Platform*. IEEE Photonics Technology Letters, 23(23):1808–1810, 2011.

[8] Wim Bogaerts, Shankar Kumar Selvaraja, Pieter Dumon, Joost Brouckaert, Katrien De Vos, Dries Van Thourhout, and Roel Baets. *Silicon-on-Insulator Spectral Filters Fabricated With CMOS Technology*. IEEE Journal of Selected Topics in Quantum Electronics, 16(1):33–44, 2010.

[9] Pieter Dumon. *Ultra-Compact Integrated Optical Filters in Silicon-on-insulator by Means of Wafer-Scale Technology*. PhD thesis, Ghent University, 2007.

[10] Shankar Kumar Selvaraja. *Wafer-scale Fabrication Technology for silicon Photonic integrated Circuits*. PhD thesis, Ghent University, 2011.

[11] Solomon Assefa, Huapu Pan, Steven Shank, William M J Green, Alexander Rylyakov, Clint Schow, Marwan Khater, Swetha Kamlapurkar, Edward Kiewra, Carol Reinholm, Teya Topuria, Philip Rice, Christian Baks, and Yurii Vlasov. *Monolithically Integrated Silicon Nanophotonics Receiver in 90nm CMOS Technology Node*. In OFC/NFOEC 2013 - 2013 Conference on Optical Fiber Communication and the National Fiber Optic Engineers Conference, page OM2H.4, 2013.

[12] Jie Teng, Pieter Dumon, Wim Bogaerts, Hongbo Zhang, Xigao Jian, Xiuyou Han, Mingshan Zhao, Geert Morthier, and Roel Baets. *Athermal Silicon-on-insulator ring resonators by overlaying a polymer cladding on narrowed waveguides.* Optics express, 17(17):14627–33, August 2009.

[13] Jong-Moo Lee, Duk-Jun Kim, Ho-Kyun Ahn, Sang-Ho Park, Junghyung Pyo, and Gyungock Kim. *Temperature-Insensitive Silicon Nano-Wire Ring Resonator*. OFC/NFOEC 2007 - 2007 Conference on Optical Fiber Communication and the National Fiber Optic Engineers Conference, pages 1–3, March 2007.

[14] Biswajeet Guha, Bernardo B C Kyotoku, and Michal Lipson. *CMOS-compatible athermal silicon microring resonators.* Optics express, 18(4):3487–93, February 2010.

[15] Sarvagya Dwivedi, Herbert D'heer, and Wim Bogaerts. *A Compact All-Silicon Temperature Insensitive Filter for WDM and Bio-Sensing Applications*. IEEE Photonics Technology Letters, 25(22):2167–2170, November 2013.

[16] Feng Qiu, Andrew M. Spring, Feng Yu, and Shiyoshi Yokoyama. *Complementary metaloxidesemiconductor compatible athermal silicon nitride/titanium dioxide hybrid micro-ring resonators*. Applied Physics Letters, 102(5):051106, 2013.

[17] Xuezhe Zheng, Ivan Shubin, Guoliang Li, Thierry Pinguet, Attila Mekis, Jin Yao, Hiren Thacker, Ying Luo, Joey Costa, Kannan Raj, John E Cunningham, and Ashok V Krishnamoorthy. *A tunable 1x4 silicon CMOS photonic wavelength multiplexer/demultiplexer for dense optical interconnects.* Optics express, 18(5):5151–60, March 2010.

[18] Xuezhe Zheng, Ivan Shubin, Guoliang Li, Ying Luo, Namseok Park, Jin Yao, Hiren Thacker, Jin-hyoung Lee, Kannan Raj, John E. Cunningham, and Ashok V. Krishnamoorthy. *1 8 Si ring Mux/DeMux with ultra-low tuning*

power. In Group IV Photonics (GFP), 2013 IEEE 10th International Conference on, volume 3, page WC3, 2013.

[19] Long Chen, Christopher R Doerr, and Young-kai Chen. *Polarization-Diversified DWDM Receiver on Silicon Free of Polarization-dependent Wavelength Shift*. In OFC/NFOEC 2012 - 2012 Conference on Optical Fiber Communication and the National Fiber Optic Engineers Conference, volume 1, page OW3G7, 2012.

[20] Dirk Taillaert, Harold Chong, Peter I Borel, Lars H Frandsen, Richard M De La Rue, and Roel Baets. *A Compact Two-Dimensional Grating Coupler Used as a Polarization Splitter*. IEEE Photonics Technology Letters, 15(9):1249–1251, 2003.

[21] Peter De Heyn, Jeroen De Coster, Peter Verheyen, Guy Lepage, Marianna Pantouvaki, Philippe Absil, Wim Bogaerts, Joris Van Campenhout, and Dries Van Thourhout. *Fabrication-Tolerant Four-Channel Wavelength-Division-Multiplexing Filter based on Collectively Tuned Si Microrings*. Journal of Lightwave Technology, 31(16):3085–3092, 2013.

[22] Po Dong, Wei Qian, Hong Liang, Roshanak Shafiiha, Dazeng Feng, Guoliang Li, John E Cunningham, Ashok V Krishnamoorthy, Mehdi Asghari, and Xin Wang. *Thermally tunable silicon racetrack resonators with ultralow tuning power.* Optics express, 18(19):20298–304, September 2010.

[23] a.V. Krishnamoorthy, H. Schwetman, P. Koka, I. Shubin, and J.E. Cunningham. *Computer Systems Based on Silicon Photonic Interconnects*. Proceedings of the IEEE, 97(7):1337–1361, July 2009.

[24] Ashok V Krishnamoorthy, Xuezhe Zheng, Guoliang Li, Jin Yao, Thierry Pinguet, Attila Mekis, Hiren Thacker, Ivan Shubin, Ying Luo, Kannan Raj, and John E Cunningham. *Exploiting CMOS Manufacturing to Reduce Tuning Requirements for Resonant Optical Devices*. IEEE Photonics Journal, 3(3):567–579, 2011.

[25] Adil Masood, Marianna Pantouvaki, Guy Lepage, Peter Verheyen, and Joris Van Campenhout. *Comparison of heater architectures for thermal control of silicon photonic circuits*. In Group IV Photonics (GFP), 2013 IEEE 10th International Conference on, page ThC2, 2013.

6

Si DWDM scaling

In this last chapter we describe several strategies to scale the Si ring-based DWDM receiver towards a higher performance. The objective is to improve the design and fabrication technology for a lower power consumption and larger bandwidth receiver. These two aspects are vital to enable future Ethernet-based OI bandwidths of $400\,\mathrm{Gb/s}$ to $1.6\,\mathrm{Tb/s}$.

We start in section 6.2 to explore on how an advanced CMOS fabrication can improve the channel spacing variation and hence the performance of the DWDM receiver. Next in section 6.3, we focus on lowering the power consumption needed to tune the receiving DWDM grid to the incoming external laser grid. Several strategies to improve the heater design are presented as well as a lower-power consuming design variation of the polarization-diversified demultiplexer. In section 6.4, we explore the bandwidth scalability of demultiplexers with a larger amount of channels and/or a denser channel spacing. We end this chapter by exploring DWDM demultiplexers in the o-band (wavelength $1310\,\mathrm{nm}$).

6.1 Device naming convention

We use the following convetion to name the different designs in a simple and short way: RR*[i]* F*[j]* M*[k]* *[l]*, with *i* the order of the ring resonator filter used, *j* the FSR [nm], *k* the amount of channels and *l* the channel spacing [GHz]. Example: RR4 F12 M8 100 is an eight-channel demultiplexer using a fourth-order ring resonator filter with a FSR of $12\,\mathrm{nm}$ and a channel spacing of $100\,\mathrm{GHz}$. This device

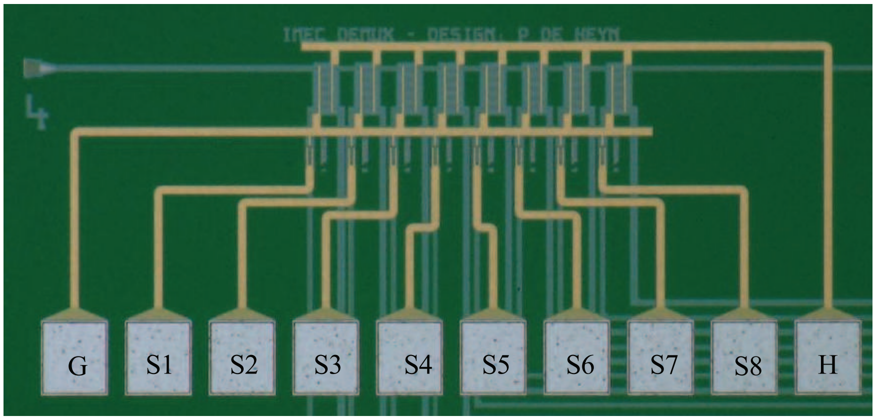

Figure 6.1: Microscope picture of RR4 F12 M8 100: an 8-channel $100\,\mathrm{GHz}$ *spaced demultiplexer using* 4^{th}*-order ring resonators.*

with integrated collective heater and vertical p-i-n Ge photodiodes is shown in Fig.6.1.

6.2 Improved fabrication technology

Using an advanced $300\,\mathrm{mm}$ CMOS platform, a better fabrication control and smaller tolerances are expected due to the use of a new generation of fabrication tools. An overview of this fabrication technology is given in [1]. Apart from a record-low propagation loss of $0.5\,\mathrm{dB/cm}$ (submitted to OFC in [2]), we expect that the local waveguide variation will improve as well. The following study has been partly published in [2] but is extended in this section with a worst channels investigation and a discussion on mask-related effects. In order to analyze the improvement between two different wafers and technologies in a correct manner, we copied the designs of one mask without any adjustments. Also the same mask grid of $5\,\mathrm{nm}$ is used. In the following, wafer-scale measurements are used to compare the performance of RR1/2 F12 M4 300. In total we measured 141 devices on a $200\,\mathrm{mm}$ wafer and 69 devices on a $300\,\mathrm{mm}$ wafer.

6.2.1 Local waveguide variation

As discussed earlier, local- and wafer-scale fabrication variations will both influence the channel spacing (as the best fit between the adjacent resonances) and the resonance deviation away from this channel spacing. Each wafer has an optimum channel spacing, where the resonance deviations relative to this fixed channel spacing measured on all the dies are minimized. This is visualized in Fig.6.2, where

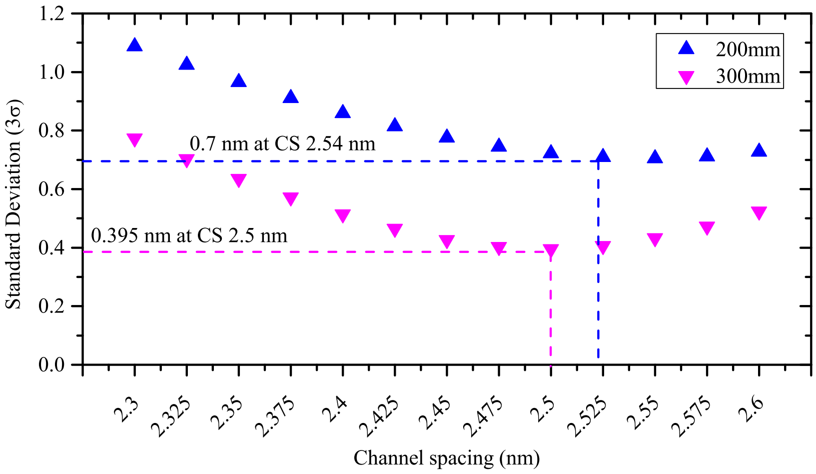

Figure 6.2: Standard deviation (3σ value) of the deviations in function of channel spacing.

the $3\,\sigma$ value of all resonance deviations with respect to a fixed CS is plotted for both wafers using RR1 F12 M4 300. For this $200\,\mathrm{mm}$ wafer (same data as used in the channel spacing analysis 5.4.4 on page 5-12), the smallest deviations are found by using a CS of $2.54\,\mathrm{nm/channel}$, which is indeed the wafer-mean CS. The $3\,\sigma$ value of these deviations is $0.7\,\mathrm{nm}$. Repeating the same analysis on the same device on a $300\,\mathrm{mm}$ wafer, we find a minimum $3\,\sigma$ value of $0.395\,\mathrm{nm}$ for a CS of $2.5\,\mathrm{nm/channel}$, which is a huge improvement of 44%.

6.2.2 Worst channel’s analysis

This improved variation is clearly visible in a worst channels analysis of a four-channel second-order demultiplexer (RR2 F12 M4 300). Using four $300\,\mathrm{GHz}$ (or $2.4\,\mathrm{nm}$) channel spaced inputs, the demultiplexer is collectively tuned until the insertion loss of the worst channel is minimized. The worst crosstalk (XT) of all the channels is then calculated for all the dies on a wafer fabricated on a $200\,\mathrm{mm}$ and $300\,\mathrm{mm}$ platform. A device-count histogram visualizing the improvement in the worst channels XT is shown in Fig.6.3. Not only the spread is drastically improved but also a general improvement in worst channels XT is clearly visible. In Tab.6.1, this improvement is quantified in numbers. We found a mean improvement of $3.4\,\mathrm{dB}$ and the 90^{th} percentile ($P90$ or 90% of all device are better than this value) made a drastic improvement of $4.6\,\mathrm{dB}$. In the same table, also the worst channels insertion loss (IL) is listed. Also there a clear improvement is present,

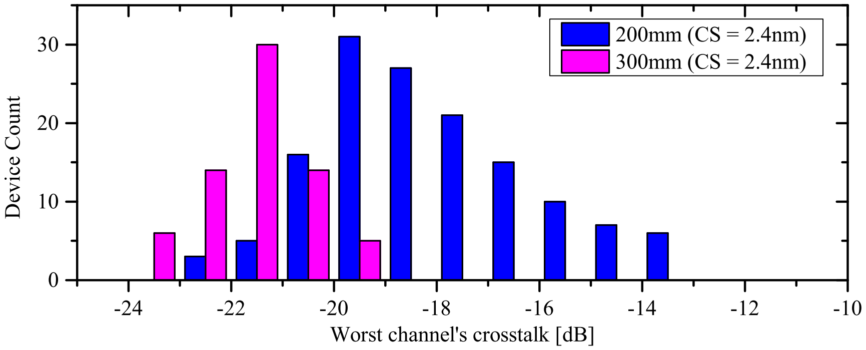

Figure 6.3: Device count histogram of the worst channel's XT of a RR2 F12 M4 300 fabricated on a $200\,\mathrm{mm}$ *and a* $300\,\mathrm{mm}$ *platform.*

	XT at CS 2.4nm			IL at CS 2.4nm		
Platform	mean	P10	P90	mean	P10	P90
300mm	-21.6	-22.9	-20.1	-1.21	-1.67	-0.39
200mm	-18.2	-20.6	-15.5	-1.39	-2.46	-0.57
Δ	3.4	2.3	4.6	0.18	0.78	0.18

Table 6.1: Crosstalk of the worst channel of RR2 F12 M4 300.

especially in the 10^{th} percentile ($P10$ or 10% of all devices are better than this value) where an improvement of $0.78\,\mathrm{dB}$ is noticed.

6.2.3 Mask-related effects

Having an exact copy of a mask design and this with the same mask grid (i.e. $5\,\mathrm{nm}$) for both platforms allows us to investigate mask-related effects on the channel spacing deviation and hopefully exclude the effect of fabrication. These mask-related effects mainly counting for discretization errors in the definition of the waveguide width. For the following investigation, we used a four-channel demultiplexer using first-order ring resonators (*RR1 F12 M4 300*). To minimize the effect of different fabrication conditions (e.g. the height of the wafer, or the bias of the etch dose), we use the wafer-optimized channel spacing (i.e. $2.5\,\mathrm{nm}$ for the $300\,\mathrm{mm}$ wafer and $2.54\,\mathrm{nm}$ for the $200\,\mathrm{mm}$ wafer). For each device, we collect the channel number that has the largest deviation from this wafer-optimized channel spacing and is visualized in a device-count histogram in Fig.6.4. In this figure, we see that for both platforms the second channel is consistently the channel with the largest deviation. The similar behavior between the two fabrication platforms indicates that this effect is a mask-related effect. A possible explanation could be that the $5\,\mathrm{nm}$ grid size snaps the bends of the ring in such a way that the resonance

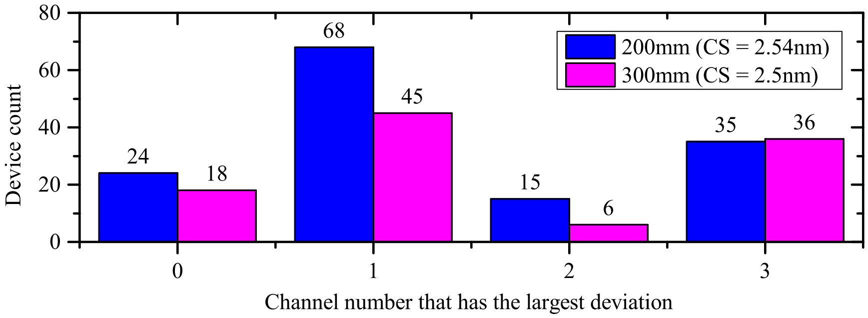

Figure 6.4: Device-count histogram of the channel numbers which have the largest deviations relative to the wafer-optimized channel spacing.

of the ring is shifted. An investigation on a device using a $1\,\mathrm{nm}$ grid and a $5\,\mathrm{nm}$ grid could, preferably fabricated on the same platform, confirm these findings. One can safely assume that shifting from a $5\,\mathrm{nm}$ grid to a $1\,\mathrm{nm}$ grid will improve the performance of demultiplexers fabricated on the $300\,\mathrm{mm}$ platform even more.

6.2.4 Case study: 100GHz channel spacing on 300mm

Initial investigation of an 8-channel demultiplexer with a narrow channel spacing of $100\,\mathrm{GHz}$ or $0.8\,\mathrm{nm}$ (device *RR2 F12 M8 100*) is showing an excellent result when fabricated on a $300\,\mathrm{mm}$ platform. A typical spectrum is shown in Fig.6.5 for both fabrication platforms. Although a wafer-level measurement can quantify the general improvement between both fabrication methods regarding the fabrication of this device, it is clear by comparing these two spectra that a narrow channel spacing of $100\,\mathrm{GHz}$ can be successfully achieved using a $300\,\mathrm{mm}$ platform. The FSR of $12\,\mathrm{nm}$ is large enough to cascade a few more channels. In this way we could extend this design without any problem to a 14-channel $100\,\mathrm{GHz}$ spaced demultiplexer.

6.3 Improved power consumption

To improve the power consumption, five ideas are discussed. First we start with an alternative architecture using a bidirectional WDM design where each polarization state is using the same channel filters. Second, a systematic method using flexible wavelength registration originally presented in [3] is discussed. Further more we quantify the efficiency improvement coming from an improved waveguide control using an advanced $300\,\mathrm{mm}$ CMOS platform. Based on the first experimental results of a local substrate removal step for ring resonators, several heater design improvements are presented. At last, we discuss the feasibility of using

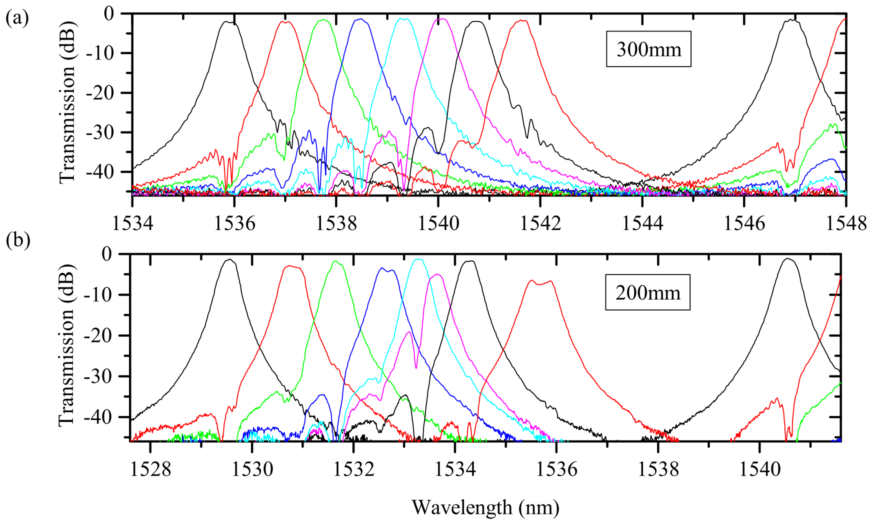

Figure 6.5: An 8-channel demultiplexer with a 100 GHz *channel spacing (RR2 F12 M8 100) fabricated on (a) a* 300 mm *and (b) a* 200 mm *platform.*

larger-FSR ring resonators to reduce the power needed for a certain wavelength shift introduced by waveguide variations. The filter performance metrics of these larger-FSR designs using a collectively tuned heater are also discussed.

6.3.1 Bidirectional WDM design

The polarization insensitive design used in this chapter is achieved by using a two-dimensional grating coupler (2D GC) where each polarization state has its own demultiplexer arm. In the bus waveguide the light is unidirectional and a control PD at the end of both arms is capturing all the light which has not been filtered by the channels. A schematic of this architecture is visualized in Fig.6.6(a). The drawback of this architecture is the fact that each channel needs two ring resonator filters and thus that the heater power consumption needed to tune this device is doubled. A possible solution is shown in Fig.6.6(b), where a bidirectional architecture is presented. For both polarization states, the same channel filter is used. A control PD to optimize the receivers position (section 5.6), can not be used anymore. However, a certain channel could be used as a control system, visualized in grey in Fig.6.6(b). The exact spectral position of this channel is not important as long as there is no overlap between the control filter and the other channels. The control circuit of the heater will then maximize the response of this control PD, which is terminating the control filter. The heater efficiency of this control filter should be equal to the other channel filters to enable collective tuning. Using this

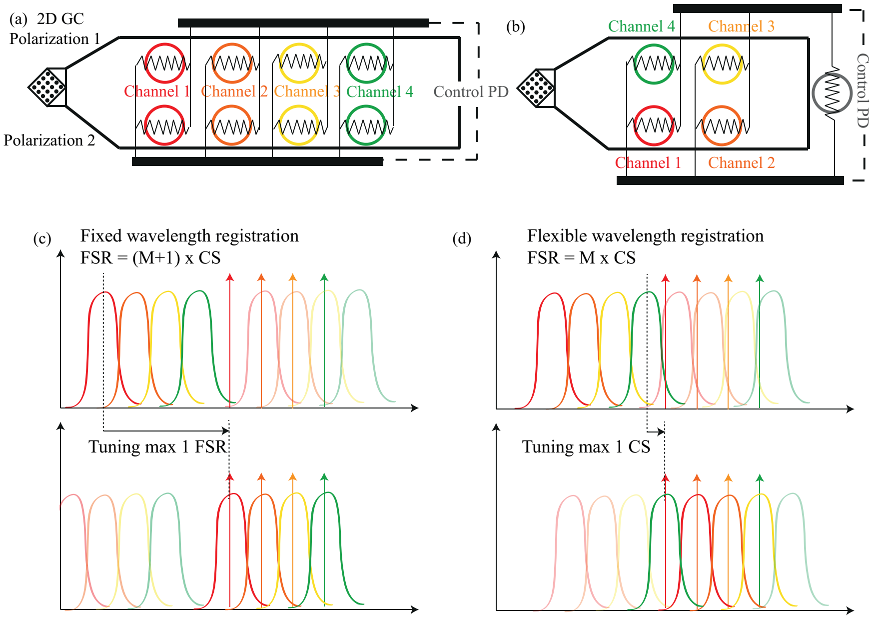

Figure 6.6: The unidirectional polarization insensitive design with a control PD (b) a bidirectional design reducing the power consumption by a factor of two. An illustration of (a) a fixed and (b) a flexible wavelength registration.

architecture, the power consumption is reduced by a factor of two.

To minimize the delay between the different polarization states one should minimize the distance between the first and last channel. Assuming a minimum distance of $50\,\mu\mathrm{m}$ between two channels, the maximum channel separation of a 5 channel demultiplexer is the $200\,\mu\mathrm{m}$. At a very fast bit rate of $50\,\mathrm{Gb/s}$, the delay is then $2\,\mathrm{ps}$ which is only a fraction of the bit length of $20\,\mathrm{ps}$.

6.3.2 Flexible wavelength registration

Using a fixed wavelength registration, the receivers channel 1 must be aligned with channel 1 of the transmitter, as visualized in Fig.6.6(c). A consequence is that the required wavelength shift of the heater can be up to a full FSR or a full 2π phase shift which leads to large power consumptions. To easily recognize channel 1 of the receiver, the FSR is chosen to be $(M+1)\times CS$ with M the amount of channels. Using a control photodiode (PD) at the end of the bus waveguide (as illustrated in Fig.6.6(a)) we can find the optimum position of the receivers comb as explained in section 5.6. Using a flexible wavelength registration, the maximum tuning range is reduced to only one channel spacing (CS) as illustrated in Fig.6.6(d). This idea was initially proposed in [3]. The registration must be done at system start up, and can eventually be performed on software level depending on the exact system (and may thus not be applicable). It is then required to design the FSR exactly to be $M \times CS$ with M the amount of channels, which requires a good extraction of the group index. The power reduction is inversely proportional to the amount of channels and can therefore be greatly improved.

6.3.3 Improved waveguide control

Especially the wafer-scale waveguide variations can cause the filter comb to shift easily more than $20\,\mathrm{nm}$, as shown in Fig.5.6. The exact reason for this large variation is still under investigation. However, an improved $3\,\sigma$ variation of $9-10\,\mathrm{nm}$ using a $200\,\mathrm{mm}$ fabrication technology and $3\,\sigma$ value of $6.1\,\mathrm{nm}$ in [2] using a $300\,\mathrm{mm}$ platform has been shown. The latter proposes the width variation to be the main cause of the wavelength variation. In [4], one argues that the primary driver of resonant frequency variation is the silicon thickness to explain resonance variations of $1\,\mathrm{THz}$ (or $8\,\mathrm{nm}$) using microdisks fabricated on a 6-inch SOI wafer (height $0.35\,\mu\mathrm{m}$). A smaller variation lowers the maximum range to tune the resonances, at least when a fixed wavelength registration system is used (see previous paragraph). More research on the exact cause of this waveguide variations and more measurements on different wafers can quantify further improvements and the possible power reduction.

6.3.4 Improved heater design

By locally removing the substrate underneath the heaters and the ring resonators, an important heat sink can be removed. This technique, typically referred as 'undercut' or 'UCUT', has shown a heater improvement with a factor of 10, having a record efficiency of $2.4\,\mathrm{mW/FSR}$ [5]. In that work, a Ti (titanium) top heater is used, $1.2\,\mu\mathrm{m}$ separated from the waveguide. Using top heaters, one can bring the undercut trenches closer to the optical waveguide then by using side heaters. A cross-section of an undercut heater structure is shown in Fig.6.7. One can clearly see that the silicon substrate has been removed underneath the buried oxide layer (BOX) but still some substrate is left, e.g. underneath the coupling section where two silicon waveguides are coming together as shown in Fig.6.7.

An overview of various DWDM demultiplexer and their design parameters used in this experiment are given in Tab.6.2 and referred to as DWDM generation I.

In the following table (Tab.6.3, we show the results of the heater efficiency (mW per FSR per channel) with and without UCUT on DWDM generation I demultiplexers. In Fig.6.8, one can see the different design schematics of the UCUT vias (visualized as yellow rectangles) applied to these four demultiplexers. The largest improvement has been achieved on structure RR2 F12 M4 300, with an

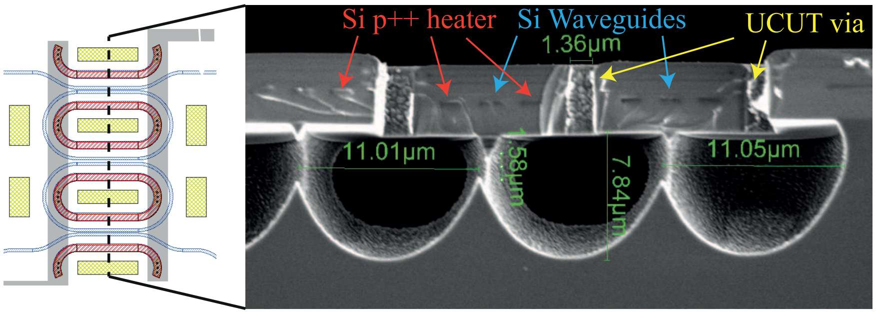

Figure 6.7: Schematic and cross-section of the local substrate removal (UCUT).

Nr.	Label	Δ L μm	BW$_3$ nm	K$_0$	K$_1$	G$_0$ μm	G$_1$ μm
1	RR1 F12 M4 300	0.15	0.32	0.08	-	0.294	-
2	RR2 F12 M4 300	0.15	1.1	0.32	0.04	0.205	0.275
3	RR1 F21 M4 500	0.14	0.56	0.08	-	0.235	-
4	RR2 F21 M4 500	0.14	1.9	0.32	0.04	0.149	0.340

Table 6.2: Design parameters DWDM demultiplexers of generation I for wavelengths around $1550\,\mathrm{nm}$ *and waveguide width* $0.45\,\mu\mathrm{m}$*. Device 1 and 2 have* $L_c = 9\,\mu\mathrm{m}$ *and* $R = 5\,\mu\mathrm{m}$*, devices 3 and 4 have* $L_c = 5\,\mu\mathrm{m}$ *and* $R = 3\,\mu\mathrm{m}$*.*

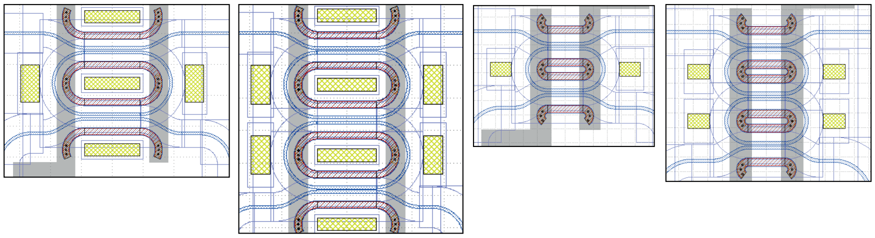
RR1 F12 M4 300 RR2 F12 M4 300 RR1 F21 M4 500 RR2 F21 M4 500

Figure 6.8: Undercut schematic DWDM demultiplexers of generation I. All figures are on shown on the same scale.

Label	mW per FSR per channel		Improvement
	No UCUT	With UCUT	
RR1 F12 M4 300	74	31	$2.4\times$
RR2 F12 M4 400	101	36	$2.8\times$
RR1 F21 M4 500	115	92	$1.25\times$
RR2 F21 M4 500	182	115	$1.5\times$

Table 6.3: UCUT efficiency improvement on the DWDM demultiplexers of generation I. Wafer details: no UCUT P112819-D18, with UCUT P121154-D16.

	Label	L_c μm	R μm	BW_3 nm	K_0	K_1	G_0 μm	G_1 μm
1	RR2 F14 M5 300	6.9	4	1.5	0.34	0.05	0.178	0.293
2	RR2 F9 M5 200	13.9	5	1	0.34	0.05	0.238	0.358
3	RR2 F16 M9 200	4.9	4	1	0.23	0.018	0.17	0.322
4	RR2 F23 M9 300	2.2	3	0.7	0.13	0.0055	0.132	0.318

Table 6.4: Overview DWDM devices of generation II for wavelengths around $1530\,\mathrm{nm}$. *Waveguide width of* $0.45\,\mu\mathrm{m}$.

UCUT efficiency improvement of $2.8\times$. The small circumference of the two right devices (RR1/2 F21 M4 500), is making the use of an undercut in the middle of the ring practical impossible since the distance between an UCUT via and the Si heater should be kept at least $1\,\mu\mathrm{m}$. From Tab.6.3, one can see that the efficiency improvement is indeed the largest for RR1/2 F12 M4 300. This could be explained by the fact that these two structures have an UCUT via in the middle of the ring. Another reason could be found in another heat sink: the M1 layer. For structures RR1/2 F12 M4 300, with a long coupling length of $9\,\mu\mathrm{m}$, the relative density of M1 above the ring is practically half that of structures RR1/2 F21 M4 500 with a coupling length of $5\,\mu\mathrm{m}$. Both effects, lower M1 layer density and an extra middle UCUT via, could be the reason why the effect on the UCUT efficiency improvement with respect to no UCUT step is doubled. A possible way to overcome the lack of space in the middle of a small ring to have an extra UCUT via is by using Ti top heaters as has been done in [5]. We also found that the UCUT efficiency improvement is slightly larger using a second-order ring resonator.

At this point it is not clear how we could improve the effect of an UCUT on the heater efficiency further, besides using larger rings, which is not desirable since that limits our design space due to a smaller FSR. The same analysis has been performed on the polarization-diversified DWDM structures (generation II) using their optical-to-optical test structures, shown in Fig.5.28. All design parameters of generation II DWDM devices are listed in Tab.6.4 and a schematic view of their ring structures is shown in Fig.6.9.

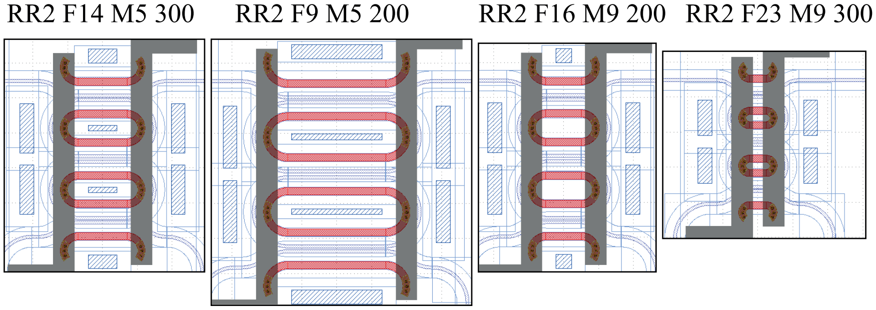

Figure 6.9: Undercut schematic of DWDM devices of generation II. All drawings are on the same scale.

Label	mW per FSR per channel		Improvement
	No UCUT	With UCUT	
RR2 F14 M5 300	206	142	1.44×
RR2 F9 M5 200	194	102	1.9×
RR2 F16 M9 200	201	165	1.21×
RR2 F23 M9 300	184	-	-

Table 6.5: UCUT efficiency improvement for the DWDM devices of generation II. Wafer details: no UCUT P130315-D08, with UCUT P122512-D10.

The UCUT vias (visualized as blue rectangles) are applied where possible according to the design rules. Again, there was no space available in the middle of the ring for devices RR2 F16 M9 200 and RR2 F23 M9 300, with respectively a FSR of $16\,\mathrm{nm}$ and $23\,\mathrm{nm}$.

In Tab.6.5, the heater efficiencies (expressed in mW per FSR per channel) are listed for the different devices. Comparing with results from generation I (listed in Tab.6.3), one finds that the power one needs to tune a channel a full FSR is roughly doubled. This is understood by the fact that each channel consists out of two ring resonators filters as shown in Fig.6.6(a). The actual improvement on the power consumption due to UCUT is for all structures smaller than $2\times$ with respect to the UCUT improvement achieved using the generation I demultiplexers. This could partly be explained by design. The design rule regarding the spacing between the UCUT via and the M1 layer is in the generation II designs slightly larger than in the generation I designs (respectively $2\,\mu\mathrm{m}$ versus $1.5\,\mu\mathrm{m}$). A cross section of these structures would reveal if the process had a similar effect as shown in Fig.6.7. More important at this point is the heater efficiency improvement due to undercut for the different structures. From Tab.6.5 one can see that RR2 F9 M5 200, with the smallest FSR ($9\,\mathrm{nm}$) and the longest L_c, has the largest improvement (up to $1.9\times$). Devices with a larger FSR (RR2 F14 M9 200 and RR2 F16 M9 200) have

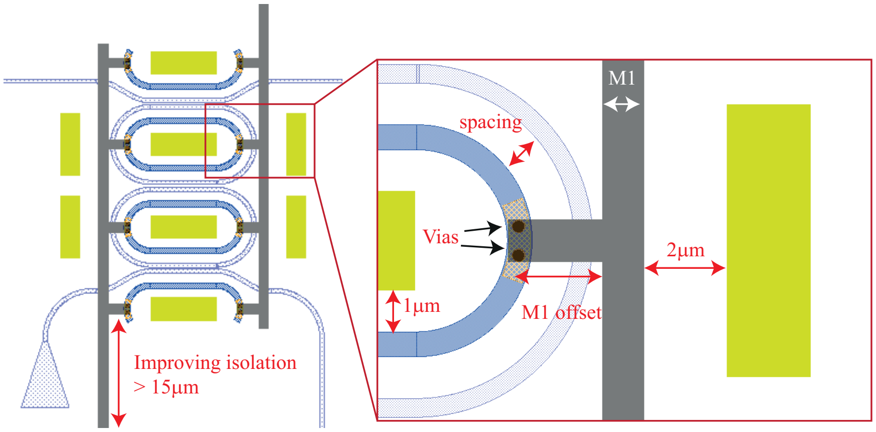

Figure 6.10: Heater optimization

a much smaller improvement. A better trend between the improvement and the coupling length indicates that the M1 density is an important factor which lowers the efficiency of an undercut step. This can be understood by the fact that the metal on top of the structures will take over as the primary heat sink of the structures once the substrate is removed. This situation is avoided in [5], with a much better heater efficiency improvement due to an undercut process step (close to a factor of 10) measured on ring heaters. In [6], following the same UCUT process as in this work, Masood et.al. have shown a much larger improvement of $14.3\times$ on much larger MZI structures where the M1 overlay is minimized and UCUT vias are much larger. Based on these findings, a list of possible heater improvements is presented and illustrated in Fig.6.10.

1. **Longer L$_c$** Design ring resonators if possible with a longer coupling length (L$_c$) and hence smaller bends to decrease the M1 density above the ring.

2. **Smaller heater spacing** The heater spacing now is $1.2\,\mu$m (edge to edge) and was chosen to avoid any coupling between the ring waveguide and the heater waveguide. One can play also with the heater width but this will increase the resistance of the wire. One should avoid that the ring waveguide has the same width as the heater waveguide because then optical coupling is maximized.

3. **M1 offset and width** Adding an offset to the connecting M1 bar and the W vias, will lower the overlap with the broader M1 layer with the heated area above the ring. However, due to the design rule of having a minimum spacing between UCUT and M1, the UCUT vias will move further away, side ways from the ring which might have a negative impact. Also by us-

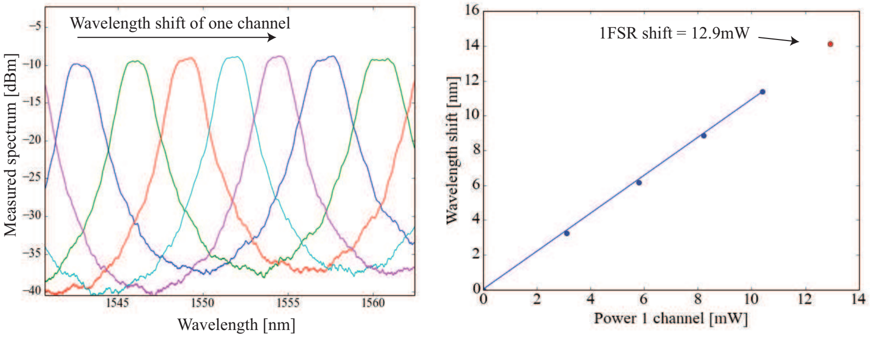

Figure 6.11: The performance of the new best-know heater configuration with an efficiency of $12.9\,\mathrm{mW}$*/channel per FSR.*

ing a more narrow M1 width, the heat sink becomes smaller. The broad connecting M1 layer connecting the adjacent heaters can be placed further away from the ring maximizing the heat isolation.

4. **Larger UCUT vias** UCUT vias should be maximized. This will not only maximize the effect underneath the ring but also the heat isolation next to the ring.

A large design of experiment was set up based on these variations to improve the heater efficiency of a channel filter designed for a 5 channel demultiplexer with a $300\,\mathrm{GHz}$ channel spacing. Some initial results are briefly presented in the following. We compare the best known device of this design of experiment (mask set sipp19) with the earlier best known design which is very similar to the channel filter designed for RR2 F12 M4 400 (mask set sipp08). After substrate removal (UCUT), the performance of this earlier best known device was $36\,\mathrm{mW}$/channel per FSR as listed in 6.3. The new best known design has an efficiency of $12.9\,\mathrm{mW}$/channel per FSR or an improvement of 180%. In Fig.6.11, the wavelength shift of a single channel is shown as well as the relative shift in function of applied power per channel.

In Fig.6.12, the two layouts are compared and a list is given with design specifications. Further research has shown that the largest improvement comes from the smaller M1 width on top of the heaters which was predicted earlier. If a substrate removal has been applied, a close to 100% improvement in efficiency has been found. Without substrate removal, the effect of a smaller M1 width is only limited, indicating that the largest heat sink is the Si substrate. From this experiment it is not clear whether the improvement comes from the fact the middle UCUT region could be made larger and hence improving the substrate removal, or that an extra heat sink has been removed. Another successful improvement is the removal of

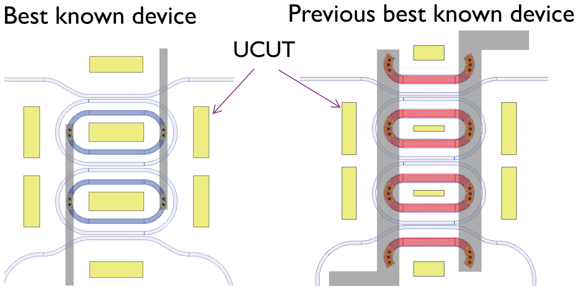

Specs [µm]	New	Old
Doping type	N	P
M1 width	1	3
Heater width	0.6	1.2
Heater spacing	1	1.2
UCUT middle	2.4	0.8
N_o_contacts	2	3
Outer heaters	No	Yes

Figure 6.12: A layout comparison between the best known device and the earlier best known device (RR2 F12 M4 400 as listed in 6.3). An huge improvement of 180% *is achieved with a resulting* $12.9\,\mathrm{mW}$*/channel per FSR.*

P_π [mW]	New	Old	Improvement
Without UCUT	17	25	47%
With UCUT	3.2	9.0	180%

Table 6.6: Efficiency improvement of the new heater configuration with respect to the old heater design, with and without local substrate removal (UCUT). P_π *is the power needed to tune a single ring resonator for a* π *phase shift (FSR/2). The new data is based on measurements from wafers P131822-D13 (UCUT) and D14 (no UCUT), mask set sipp19.*

the outer heaters. This step has demonstrated a 30% improvement indicating that the outer heaters are not necessary. However, a detailed investigation regarding uniformity is still on going. Due to this removal, there is more space at the bus waveguides. Hence, another improvement can be expected if one positions the UCUT regions closer to the ring resonator. By placing the heater waveguide closer to the optical waveguide from $1.2\,\mu\mathrm{m}$ to $1\,\mu\mathrm{m}$, another 30% improvement has been detected. One can bring this waveguide as close as $0.8\,\mu\mathrm{m}$ before a degradation in optical filter performance is detected.

In Tab.6.6, the performance improvement of the new heater configuration is compared to the old configuration expressed in P_π (P_π = power needed to tune a single ring resonator for a π phase shift or FSR/2). Without a local substrate removal, the new heater configuration shows a 47% with respect to the older design. With a local substrate removal P_π of the new heater configuration is $3.2\,\mathrm{mW}$.

6.3.5 Improved ring dimensions

The effective refractive index (n_{eff}) that the light is experiencing in the waveguide can change very locally due to a small fabrication variation in width or height of the waveguide, and can thus be different along the ring. The wavelength shift ($\Delta\lambda_{res}$) that resonances of ring-based demultiplexer experience is due to a change in the mean effective refractive index of the whole ring resonator. The resonance wavelength in a ring is given by eq.6.1, with L the circumference of the ring and m an integer number.

$$\lambda_{res} = \frac{n_{eff}L}{m} \tag{6.1}$$

A change in n$_{eff}$ will thus influence λ_{res} following eq.6.2.

$$\Delta\lambda_{res} = \frac{\Delta n_{eff}L}{m} = \frac{\Delta n_{eff}\lambda_{res}}{n_{eff}} \tag{6.2}$$

The resonance shift ($\Delta\lambda_{res}$) is thus independent from the circumference or FSR of the ring. Around $1530\,\mathrm{nm}$ a change in waveguide width and height of $1\,\mathrm{nm}$ causes a $\Delta\lambda_{res}$ of respectively $1.3\,\mathrm{nm}$ and $2.4\,\mathrm{nm}$. If we want to compensate for this ($\Delta\lambda_{res}$), we will heat up the waveguide in such a way that the n_{eff} is changed again. The power needed to tune ($\Delta\lambda_{res}$) is depending on the circumference (L) of the ring because a larger waveguide area needs to be heated. The larger the ring, the more power you need to tune. In other words, if one uses a ring with a smaller circumference (or a larger FSR), less power is needed to tune a ring which was shifted due to a waveguide variation. In the following we will investigate the performance of a demultiplexer with a large FSR. In order to make a fair comparison we keep the amount of channels equal and we scale the ring resonators to smaller dimension. A four-channel demultiplexer was implemented with two different FSR ($12\,\mathrm{nm}$ and $21\,\mathrm{nm}$) with respectively a 300 and $500\,\mathrm{GHz}$ channel spacing, using both first- and second order ring resonators (RR1 and RR2). The performance of RR1/2 F12 M4 300 is extensively discussed in Section 5.4 and 5.5. The specifications of these four devices (RR1/2 F12 M4 300 and RR1/2 F21 M4 500) are listed in Tab.6.2 on page 6-9. To achieve the larger FSR, the coupling length is reduced from $9\,\mu\mathrm{m}$ to $5\,\mu\mathrm{m}$ and the bend radius from $5\,\mu\mathrm{m}$ to $3\,\mu\mathrm{m}$. This small bending radius could introduce some small bending losses. Because the coupling length is reduced, the gap must become more narrow to achieve the same coupling strength, which makes the design less relaxed against fabrication tolerances. In this case, the gaps are still broad enough to be yielded ($\geq 0.149\,\mu\mathrm{m}$). The performances metric (wafer scale on 14 dies) of all four devices are listed in Tab.6.7.

From this table one can notice that the $1\,\mathrm{dB}$ and $3\,\mathrm{dB}$ BW (BW$_1$ and BW$_3$) becomes much broader for the large-FSR designs (F21), and this for both ring orders (RR1 and RR2). Regarding XT and IL of the channel responses, we see a degradation for large FSR designs which is most probably due to a higher bending loss of the $3\mu\mathrm{m}$-short bends. Another consequence of the short bends is that the n$_{eff}$ is slightly decreased and/or the n$_g$ is slightly increased which causes the channel spacing (CS) to be exactly the designed value of $4\,\mathrm{nm}$, whereas the CS of

Spec	RR1 F12 M4 300	RR2 F12 M4 300	RR1 F21 M4 500	RR2 F21 M4 500
BW_1 [nm]	0.26	0.92	0.44	1.54
BW_3 [nm]	0.49	1.35	0.86	2.36
XT [dB]	-19.4	-20.2	-18.5	-18.6
IL [dB]	-0.53	-0.51	-1.13	-0.87
CS [nm]	2.54	2.54	4	4
FSR [nm]	11.3	11.4	19.5	19.5
XT CT WC [dB]	-15.3	-18.1	-16.5	-16.9
IL CT WC [dB]	-3.7	-1.2	-2.8	-1.4
P per FSR [mW]	123	145	367	461

Table 6.7: Comparison between different devices of generation I demultiplexers with larger FSR, wafer details: P121154-D16.

the small-FSR designs is slightly off (in this case $2.5\,\mathrm{nm}$). This improved accuracy of the channel spacing together with a broader BW can explain the improvement in XT and IL of the worst channel (WC) when collectively tuned (CT) (denoted in the table as XT/IL CT WC) for first-order designs when using a large-FSR design. For second order designs, it turns out that the higher waveguide losses degraded the channel responses enough to degrade the IL and XT when collectively tuned, even with the more accurate CS. Still the first-order, large-FSR design is under performing regarding IL with respect to the second-order, large-FSR design but the difference is smaller in comparison with the small-FSR designs. So far, we can say that the degradation of using smaller rings is only limited using second-order rings and even an improvement using first-order ring resonators. If we investigate the power one needs to tune the whole four-channel array a full FSR, we see that large-FSR designs are significantly less efficient than small-FSR designs. Note that these devices have a substrate undercut step applied to enhance the efficiency. The possible reasons why a large-FSR design with UCUT is less efficient is extensively discussed in the previous paragraph. Although these large-FSR designs would need less power than small-FSR designs to compensate a certain $\Delta\lambda_{res}$ that was caused by e.g. wafer-scale height variations, it turns out that with the current heater implementation the power consumption is not reduced but increased. If one wants to tune the whole demultiplexer $10\,\mathrm{nm}$, $109\,\mathrm{mW}$ is needed using RR1 F12 M4 300 and $189\,\mathrm{mW}$ using RR1 F19 M4 500. That is because the heaters employed for large-FSR rings (smaller rings) are less improved with an undercut due to the high density of the interconnecting M1 layer. Enhancing the heater efficiency of large-FSR designs, will enable the possible power reduction due to a larger-FSR design.

6.4 Increased throughput - scalability

To increase the total throughput of the demultiplexer one can either increase the bit rate per channel and/or increase the total amount of channels. In this section we investigate the performance of nine-channel demultiplexers with a $200 - 300\,\mathrm{GHz}$ channel spacing around $1530\,\mathrm{nm}$ and compare its performance with the 5-channel demultiplexer with a $200 - 300\,\mathrm{GHz}$ channel spacing. These designs were earlier introduced as the DWDM generation II devices and all the design parameters are listed in Tab.6.4. In the following we discuss these design parameters.

6.4.1 Overview designs

Increasing the amount of channels increases the necessary FSR and hence decreases the circumference. E.g. a nine-channel $300\,\mathrm{GHz}$ demultiplexer needs a FSR of $23\,\mathrm{nm}$ (device RR2 F23 M9 300). Decreasing the ring radius to the minimum low-loss bend radius of $3\,\mu\mathrm{m}$, the maximum coupling length to achieve this FSR becomes then $2.2\,\mu\mathrm{m}$. To foresee enough coupling between the bus and the first ring, very narrow gaps $\leq\ 120nm$ are needed which could lead to yielding problems of this device. Therefore we design this demultiplexer with a more relaxed gap resulting in a smaller BW and improved XT ($-30\,\mathrm{dB}$ instead of $-20\,\mathrm{dB}$). To relax this gap/BW trade-off one can use a little denser channel spacing ($200\,\mathrm{GHz}$ instead of $300\,\mathrm{GHz}$), with a smaller FSR ($16\,\mathrm{nm}$) and hence a larger maximum coupling length ($4.4\,\mu\mathrm{m}$) and a larger bend radius of $4\,\mu\mathrm{m}$. However, a denser channel spacing could increase the channel overlap due to resonance variations and thus decrease the overall demultiplexer performance.

In Fig.6.13, a typical transmission OO spectrum of two five-channel demultiplexers is plotted with a channel spacing of $300\,\mathrm{GHz}$ (i.e. RR2 F14 M5 300) and $200\,\mathrm{GHz}$ (i.e. RR2 F9 M5 200). These demultiplexers are then both scaled to a nine-channel device, respectively RR2 F16 M9 200 and RR2 F23 M9 300 and are plotted in the same figure. The two demultiplexer arms of the OO test structure (representing the two polarization states as in Fig.5.28 on page 5-35) are plotted on top of each other and distinguished with a solid and dashed line. All four spectra are shown on the same wavelength scale.

In Tab.6.8, the main specifications of the individual channel responses are listed. Each value is based on the average value of 140 single-polarization demultiplexers on a single wafer. The bandwidth (BW) and free spectral range (FSR) values are the wafer-mean values of the device-mean value over both demultiplexer arms. From this table one can see that our starting device (RR2 F14 M5 300) has the largest BW with respect to the other designs. Decreasing the channel spacing to $200\,\mathrm{GHz}$ lowers consequently the BW if one maintains the XT level during the design. According to the designed specifications, RR2 F23 M9 300 has a little larger BW ($\mathrm{BW}_3 = 1.05\,\mathrm{nm}$) than designed ($\mathrm{BW}_3 = 0.7\,\mathrm{nm}$). In Tab.6.8 we plot

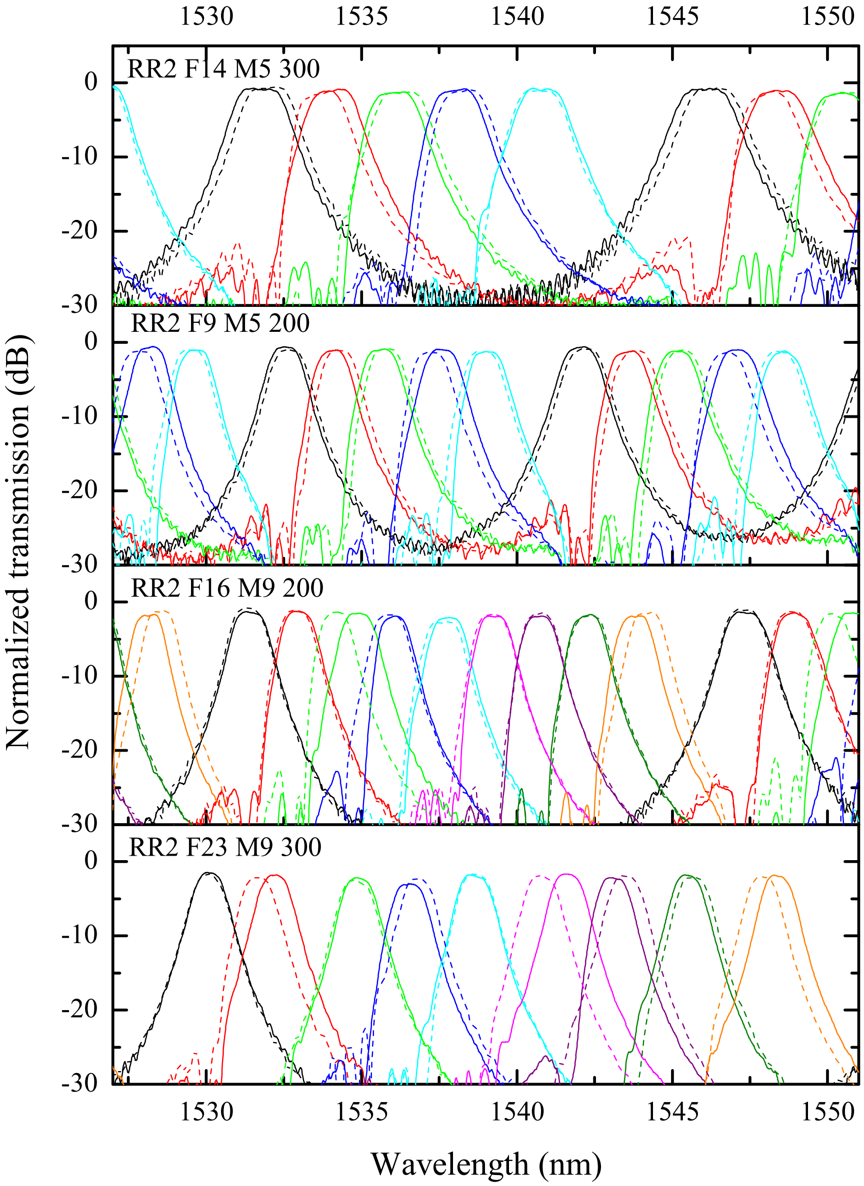

Figure 6.13: Typical transmission the DWDM structures of generation II using the OO test structure for both polarization states (solid/dashed).

Spec	RR2 F14 M5 300	RR2 F9 M5 200	RR2 F16 M9 200	RR2 F23 M9 300
BW_1 [nm]	1.18	0.79	0.78	0.7
BW_3 [nm]	1.6	1.1	1.07	1.05
worst XT [dB]	-17.9	-16	16.4	-23.3
worst IL [dB]	-1.8	-1.6	-2.9	-2.9
FSR [nm]	14.2	9.4	15.9	24
$3\,\sigma\ \lambda_1$ [nm]	9	8.8	8.6	10.2

Table 6.8: Individual channel response performance comparison of DWDM generation II demultiplexers. Eeach value is the average value of 140 single-polarization demultiplexers on a single wafer. Wafer details: P122521-D18.

the wafer-mean value of the worst XT level and worst IL level of all the channels of each device, giving a more realistic perception of the channel responses. For all devices a worst XT level below $-16\,\mathrm{dB}$ is reached with the exception of RR2 F23 M9 300 where the worst XT level is below $-23\,\mathrm{dB}$. This latter value was designed to be $-30\,\mathrm{dB}$, which is lower than other designs due to a restriction on the gap as explained earlier. The channel crosstalk degradation of $7\,\mathrm{dB}$ is large and follows the trend of the larger BW_3 as discussed earlier. Regarding wafer-mean worst IL, a 5-channel demultiplexer has a better value of $-1.8\,\mathrm{dB}$ than the 9-channel designs. This trend can be explained by the fact that the more channels are cascaded, the larger the IL of the last channel, which is indeed typically the worst channel regarding IL. The FSR is nicely following the design values for the different designs with a maximum offset of $0.6\,\mathrm{nm}$. The $3\,\sigma$ value of the variation of the center wavelength of the first channel (λ_1), is for all designs between $8.6\,\mathrm{nm}$ and $10.2\,\mathrm{nm}$.

6.4.2 Channel spacing analysis

A typical channel spacing analysis is performed on the four designs described in previous section and analyzed based on wafer-scale measurements. The channel spacing is defined as the slope of the best fitting between the center wavelengths of the adjacent channel responses in function of their channel number (as visualized in Fig.5.7 on page 5-13). The extracted channel spacings (CS) of both demultiplexer arms are added to each other which makes the total amount of CS to be 140 per design. In Fig.6.14, these extracted CS are plotted and grouped per channel spacing (upper: $300\,\mathrm{GHz}$ or $2.34\,\mathrm{nm}$ and lower: $200\,\mathrm{GHz}$ or $1.55\,\mathrm{nm}$).

From this figure it is clear that devices with a larger FSR for a given CS have a much smaller spreading on their CS. In the case of $300\,\mathrm{GHz}$ CS designs, the $3\,\sigma$ value is almost $3\times$ smaller with a very tight spreading of $0.11\,\mathrm{nm}$ for design RR2 F23 M9 300. However, the wafer-mean value of these CS of this design

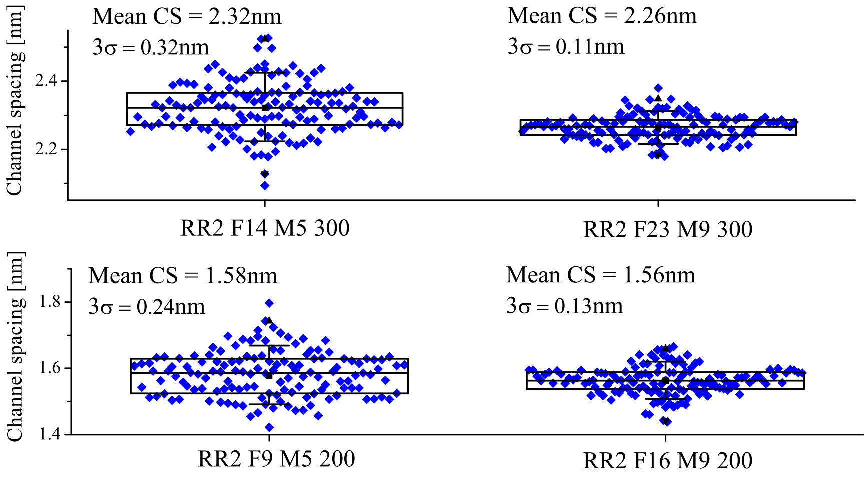

Figure 6.14: Channel spacing variation on the DWDM demultiplexers from generation II. Upper graph: design CS of 300 GHz *or* 2.34 nm*, lower graph: design CS of* 200 GHz *or* 1.55 nm*. Wafer details: P122521-D18.*

(2.26 nm) is a bit off from the designed value of 2.34 nm. This could possibly be explained by the small bending radii which lowers the n_{eff} and thus consequently the CS (re-arrange Eq.(5.1) on page 5-8). We notice a very similar trend for the 200 GHz designs albeit less pronounced. In previous section we haven seen that the CS variation is due to local waveguide variations. The more channels the demultiplexer counts, the more these local variations are flattened out, and thus the smaller the variation on the CS.

In the following we investigate the resonance variation away from the channel spacing. As discussed before, some designs have a wafer-mean CS that is slightly off the designed value. To make the comparison fair between the different designs, the wafer-mean CS is used instead of the as-designed CS. In Fig.6.15, the relative value of each center wavelength deviation away from this design-optimized wafer-mean CS is plotted. For a 5-channel design, this gives 700 resonance deviations (5 channels × 2 arms × 70 devices) and around 1260 for a 9-channel design. On top of these data distribution plot, a box plot representation of this data is given as well with a marker for different percentiles as explained in the figure). From this figure, one can notice that the smallest deviation (3σ value of 0.53 nm) is for design RR2 F9 M5 200 and the largest deviation (3σ value of 0.7 nm) is for RR2 F23 M9 300. We noticed that this deviation becomes consequently larger for designs with a larger FSR. Designs with smaller circumference (larger FSR) have a local ring-n$_{eff}$ which can deviate more than for larger circumference designs since very local waveguide variations are flattened out in larger rings. The ring-

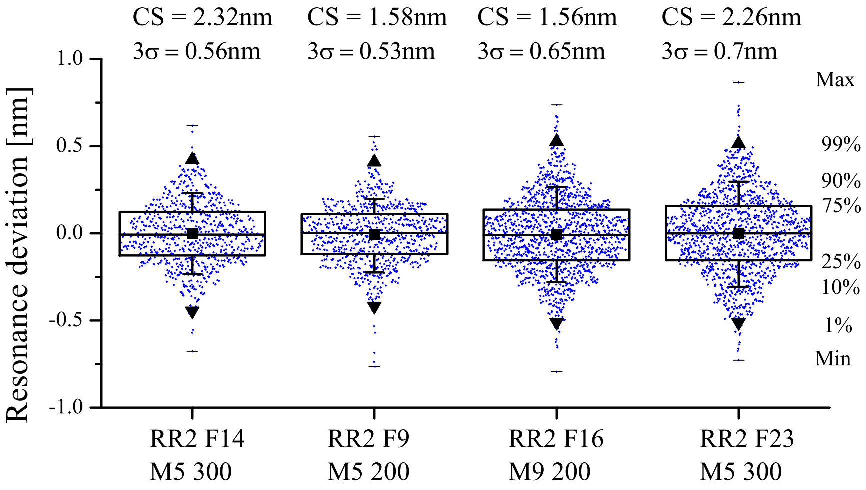

Figure 6.15: Resonance variation away from their ideal spectral position based on the wafer-mean channel spacing. Wafer details: P122521-D18.

	Worst channels XT [dB]			Worst channels IL [dB]		
	mean	P10	P90	mean	P10	P90
RR2 F14 M5 300	-16.6	-19.0	-14.6	-1.8	-2.3	-1.18
RR2 F9 M5 200	-14.4	-16.7	-12.0	-1.57	-2.49	-0.91
RR2 F16 M9 200	-12.2	-15.3	-9.0	-3.6	-5.5	-2.16
RR2 F23 M9 300	-19.2	-21.4	-16.6	-4.26	-6.77	-2.73

Table 6.9: Collectively tuned demultiplexer performance from DWDM generation II. Key performance indicators are the worst-channel performance regarding XT and IL. Wafer details: P122521-D18.

n_{eff} has the meaning of the mean value along the circumference of the ring. These deviations will have a direct impact on the performance of the demultiplexer when using a collective tuning scheme. Especially for designs with a large FSR (largest deviation) and a dense (200 GHz) CS, a significant degradation of XT and IL with respect to the individual channel response are expected. The wafer-mean value and the 10^{th} and 90^{th} percentiles for the worst-channel XT and IL are listed in Tab.6.9. The wafer-mean CS instead of the as-designed CS is used to compare the different designs.

From this table it is easy to compare the performance of the different designs. We discuss each design separately and we use the performance of the worst channel to quantify the performance of the whole demultiplexer. We quantify the degradation due to the scaling of the channel spacing and the amount of channels. We start by discussing our starting design RR2 F14 M5 300, which was extensively investigated in the earlier section 5.7 on page 5-28. Several times we will compare the performance of the demultiplexer with the worst-channel performance of the individual channel response, where we ignored the effect of the resonance deviation. This way we can distinguish between the effects of the resonance deviation (visualized in Fig.6.15) and the scaled individual channel response on the performance of the demultiplexer, listed Tab.6.8. Note that the performance of the demultiplexers worst channel that is used to describe both the individual channel response (Tab.6.8) and the demultiplexers' filter bank under collective tuning (6.9), is not necessarily the same channel.

RR2 F14 M5 300 Our starting device is performing with a wafer-mean worst-channel XT and IL of respectively $-16.6\,\mathrm{dB}$ and $-1.8\,\mathrm{dB}$. By comparing this result with the performance of the individual channel response, listed in tab.6.8, one can notice a further degradation of $1.3\,\mathrm{dB}$ for the worst-channels XT. Due to the very broad BW of the channels ($1\,\mathrm{dB}$ BW of $1.18\,\mathrm{nm}$) the resonance deviations are relatively small ($3\,\sigma = 0.54\,\mathrm{nm}$), which results in nearly no degradation of the worst-channel IL between the individual channel responses and the demultiplexer performance. Note that this an improvement with respect to the first generation 4-channel demultiplexer where we found a $3\,\sigma$ wavelength deviation of $0.7\,\mathrm{nm}$ (see also section 5.4.4). This improvement is most probably related to the improved mask grid discretization (from 5 to $1\,\mathrm{nm}$).

RR2 F9 M5 200 Scaling the 5-channel $300\,\mathrm{GHz}$ CS demultiplexer to a more dense CS using a $200\,\mathrm{GHz}$ CS, one can notice a $2.2\,\mathrm{dB}$ degradation in worst channel XT, ending up with a wafer-mean worst channel XT of $-14.4\,\mathrm{dB}$. We have seen in Fig.6.15 that the absolute deviation for both designs is very similar ($3\,\sigma$ = 0.56 - $0.53\,\mathrm{nm}$). At the other hand, the individual channel response had already a degradation of $1.9\,\mathrm{dB}$ in the performance of the worst-channel XT, with respect to the $300\,\mathrm{GHz}$ CS design variant, which can be seen as the main driver for the degradation of the XT. Although the wafer-mean worst channel IL is a little better with respect to a $300\,\mathrm{GHz}$ CS design, we notice a larger degradation using the 10^{th} percentile.

RR2 F16 M9 200 Scaling the 5-channel $200\,\mathrm{GHz}$ CS demultiplexer to 9-channel one, another degradation of $2.2\,\mathrm{dB}$ is detected regarding worst channel XT, resulting in a wafer-mean worst channel XT of $-12.2\,\mathrm{dB}$. We have seen that the degradation of the XT of the individual channel response was equal between the two $200\,\mathrm{GHz}$ CS designs (both around $-16\,\mathrm{dB}$). On the other hand, we have seen that the 9-channel design had a significant larger resonance deviation ($3\,\sigma$ values of $0.65\,\mathrm{nm}$ and $0.53\,\mathrm{nm}$), which can be seen as the main driver for the extra degradation in XT levels due to the scaling of the amount of channels. This larger resonance deviation has also an immediate effect on the worst channel IL. Comparing with the worst channel IL of the individual channel response (wafer-mean value of $-2.9\,\mathrm{dB}$), we detect another degradation of $0.7\,\mathrm{dB}$ resulting in a wafer-mean worst channel IL of $-3.6\,\mathrm{dB}$. Especially using the 10^{th} percentile, the effect of the resonance deviation on the worst channel IL is significantly enlarged resulting in a degradation of $3\,\mathrm{dB}$.

RR2 F23 M9 300 As discussed earlier it is not possible due to fabrication limits to scale a 5-channel $300\,\mathrm{GHz}$ CS demultiplexer to a 9-channel $300\,\mathrm{GHz}$ CS demultiplexer without lowering the coupling strength between the bus and ring waveguide and thus consequently decreasing the $3\,\mathrm{dB}$ BW of the individual channel responses. A positive consequence of this design adjustment is the improvement of the XT, which is designed to be $-30\,\mathrm{dB}$, $10\,\mathrm{dB}$ lower than the other designs. Due to the very short bending radius of $3\,\mu\mathrm{m}$, we have seen that the coupling is a bit higher than simulated. This is visible in the $3\,\mathrm{dB}$ BW, which was simulated to be $0.7\,\mathrm{nm}$ but measured to be $1.05\,\mathrm{nm}$. Consequently, the XT was much higher than simulated and appeared to be $-23.3\,\mathrm{dB}$ at the designed CS of $2.34\,\mathrm{nm}$ and $-22.8\,\mathrm{dB}$ at the wafer-mean CS of $2.26\,\mathrm{nm}$ (reported XT values are describing the worst channel of the individual channel response). This information is helpful to understand the degradation of the demultiplexers XT. As listed in Tab.6.9, the wafer-mean worst channel XT is $-19.1\,\mathrm{dB}$ which makes RR2 F23 M9 300 the best performing device regarding XT levels. At the same time, this device has the largest XT degradation of $3.7\,\mathrm{dB}$ when employed in a collectively tuned demultiplexer. This relatively large XT degradation can be explained by the resonance deviation which was quantified to be the largest among the different designs ($3\,\sigma$ value of $0.7\,\mathrm{nm}$). The degradation on the worst channel IL is also the largest among the designs and has a wafer-mean value of $-4.3\,\mathrm{dB}$, which is $0.7\,\mathrm{dB}$ worse than RR2 F16 M9 200. The 10^{th} is $-6.8\,\mathrm{dB}$, which is $1.3\,\mathrm{dB}$ lower than RR2 F16 M9 200 and $-4.5\,\mathrm{dB}$ lower than RR2 F14 M5 300.

6.4.3 Conclusion

In this section we have explored the use of more channels and denser channel spacings to increase the bandwidth of the receiver. We increased the amount of channels from 5 to 9 and varied the channel spacing between 300 and $200\,\mathrm{GHz}$. We found that both decreasing the channel spacing and increasing the amount of channels degraded the filter performance in terms of worst channel XT and IL.

We found that by using a denser channel spacing ($200\,\mathrm{GHz}$), the channel spacing deviation is slightly improved with respect to demultiplexers using a wider channel spacing ($300\,\mathrm{GHz}$). However, due to the smaller bandwidth of the filters using a $200\,\mathrm{GHz}$ channel spacing the largest influence on the degradation is still

	Label	L_c μm	R μm	BW_3 nm	K_0	K_1	G_0 μm	G_1 μm
1	RR2 F10 M5 300	6.9	3.8	1.1	0.34	0.05	0.147	0.239
2	RR2 F7 M5 200	11.9	5.3	0.7	0.34	0.05	0.19	0.283
3	RR2 F11 M9 200	4.9	3.5	0.7	0.23	0.018	0.152	0.275

Table 6.10: Overview DWDM devices of generation II for wavelengths around $1310\,\mathrm{nm}$. *Waveguide width of* $0.38\,\mu\mathrm{m}$.

the channel wavelength deviation. Increasing the amount of channels increases the mean channel wavelength deviation slightly ($3\,\sigma$ from $0.56\,\mathrm{nm}$ to $0.7\,\mathrm{nm}$). Using the 9-channel demultiplexers, it is mainly the small ring resonator dimension such as gap and radius that decreases the performance of the demultiplexer.

6.5 DWDM demultiplexers for the O-band (1310 nm)

The wavelength band around $1310\,\mathrm{nm}$ is typically used in telecommunication because of the lowest dispersion in a fiber. Even for relatively short distances of $2\,\mathrm{km}$ this can cause few dB in power penalty depending on the exact implementation. Hence, the smallest power penalty for increasing the bit rate (per channel) can be expected in the O-band. On the other hand, the laser can be made on a GaAs substrate, which is cheaper than InP that is typically used for the C-band. On chip, this shorter wavelength is translated in more challenging fabrication tolerances. Indeed, using a shorter wavelength requires the waveguides to become more narrow to keep the waveguide single mode. In the first experiments using this wavelength, the waveguide width is $0.38\,\mu\mathrm{m}$ (15% smaller). The $220\,\mathrm{nm}$ thickness becomes relatively larger (also 15%) for the optical mode, and the optical mode becomes more confined which lowers the bending losses and improves the coupling efficiency to fiber couplers. The drawback is that the coupling strength is also smaller and typically narrow gaps are need to obtain enough coupling. In the following we present some initial work around 5 and 9-channel DWDM receivers. None of the $1310\,\mathrm{nm}$-devices are investigated on wafer scale and are therefore only shortly described here. The parameters of the DWDM demultiplexers from generation II designed for $1310\,\mathrm{nm}$ are listed in Tab.6.10.

In Fig.6.16, the optical-to-optical spectra around $1310\,\mathrm{nm}$ of three demultiplexers using their OO test structures. A solid and dashed line is used to distinguish the outputs coming from the two separate inputs from this optical-to-optical test structure (see Fig.5.28).

RR2 F10 M5 300 This device is the directly scaled $1310\,\mathrm{nm}$ version of the 5-channel $300\,\mathrm{GHz}$ receiver for $1530\,\mathrm{nm}$ extensively discussed in chapter 5. With

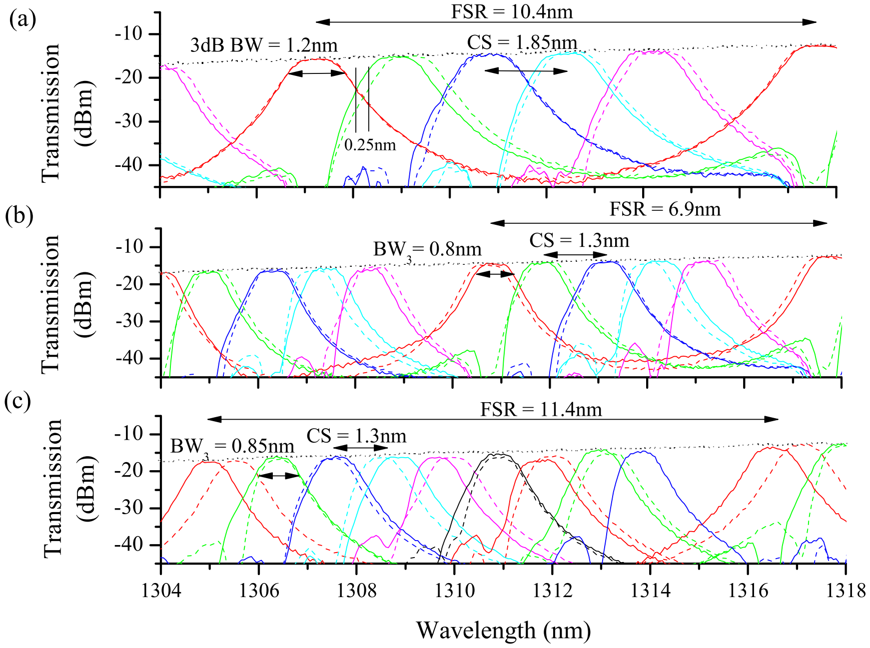

Figure 6.16: The spectra of the DWDM demultiplexers from generation II designed for 1310 nm *(a) RR2 F10 M5 300 (b) RR2 F7 M5 200 and (c) RR2 F11 M9 200. Both polarization states are represented using a solid and dashed line.*

respect to the other $1310\,\mathrm{nm}$ demultiplexers, this device has the most relaxed parameters regarding gap (not too small) and the largest radius. Its spectrum is shown in Fig.6.16(a). Although only a singel device is shown, one can see that this device is performing well against fabrication variations due to its broad BW. The BW_3 is $1.85\,\mathrm{nm}$ and can clearly cope with the $0.25\,\mathrm{nm}$ deviation between the two polarization states of channel 2 (green). The XT is for all channels still below $-17.5\,\mathrm{dB}$.

RR2 F7 M5 200 Moving to a more narrow channel spacing of $200\,\mathrm{GHz}$ or $1.3\,\mathrm{nm}$, the BW_3 is greatly reduced to only $0.85\,\mathrm{nm}$ and one can expect a larger IL and XT degradation due to local resonance deviations. In Fig.6.16(b) one can see that the XT is indeed slightly reduced and ranges between $-14\,\mathrm{dB}$ (between channels 4 and 5) and $-17\,\mathrm{dB}$ (between channel 2 and 3).

RR2 F11 M9 200 Scaling the 5-channel RR2 F7 M5 200 to a 9-channel device, the BW_3 is very similar $0.8 - 0.85\,\mathrm{nm}$. However, we can expect a similar trend as demonstrated using the DWDM demultiplexers designed for $1530\,\mathrm{nm}$. Due to a larger required FSR, the local fabrication variations will have a larger influence on the resonance deviations. This is visible in Fig.6.16(c), where one can notice a large shift between the two polarizations states of channel 1. Overall XT levels between the channels are kept below $-14\,\mathrm{dB}$.

6.6 Conclusion

In this chapter, several improvements were proposed to enhance the performance of WDM receivers based on ring resonators regarding power consumption and bandwidth. Many of these proposals were based on experimental results and can be used to design a new generation of WDM devices with a higher bandwidth and lower power consumption, both for $1530\,\mathrm{nm}$ as for $1310\,\mathrm{nm}$.

By using a more advanced $300\,\mathrm{mm}$ CMOS fabrication facility, the inter-channel deviation has been improved by almost a factor of 2 with a resulting 3σ variation of $0.4\,\mathrm{nm}$. A similar improvement is expected for the intra-channel deviation which will result in a flatter-top behavior of the channel, smaller insertion loss and an improved crosstalk. We also found that by using a $1\,\mathrm{nm}$ instead of a $5\,\mathrm{nm}$ mask discretization step, the inter-channel deviation improved from a 3σ-value of $0.7\,\mathrm{nm}$ to $0.56\,\mathrm{nm}$. These technological improvements will allow us to scale collectively-tuned WDM demultiplexers to a larger amount of channels (> 10) and with a denser channel spacing down to $100\,\mathrm{GHz}$ or $0.8\,\mathrm{nm}$.

Another way of increasing the bandwidth of the receiver is increasing the bit rate per channel. However, this broadens the signal bandwidth considerably and one can expect a signal degradation due to the limited flat-top bandwidth. This will increase the need for broader flat-top channel responses. However, the effect of filter channel response on the signal degradation is not investigated in this work.

References

[1] Shankar Kumar Selvaraja. *Wafer-scale Fabrication Technology for silicon Photonic integrated Circuits*. PhD thesis, Ghent University, 2011.

[2] Shankar Kumar Selvaraja, Peter De Heyn, Gustaf Winroth, Patrick Ong, Guy Lepage, Celine Cailler, Arnaud Rigny, Konstantin K Bourdelle, Wim Bogaerts, Dries Van Thourhout, and Joris Van Campenhout. *Highly uniform and low-loss passive silicon photonics devices using a 300mm CMOS platform*. In The Optical Fiber Communication Conference and Exposition (OFC) and The National Fiber Optic Engineers Conference (NFOEC) 2014, number 1, pages 3–5, 2014.

[3] Ashok V Krishnamoorthy, Xuezhe Zheng, Guoliang Li, Jin Yao, Thierry Pinguet, Attila Mekis, Hiren Thacker, Ivan Shubin, Ying Luo, Kannan Raj, and John E Cunningham. *Exploiting CMOS Manufacturing to Reduce Tuning Requirements for Resonant Optical Devices*. IEEE Photonics Journal, 3(3):567–579, 2011.

[4] William a Zortman, Douglas C Trotter, and Michael R Watts. *Silicon photonics manufacturing.* Optics express, 18(23):23598–607, November 2010.

[5] Po Dong, Wei Qian, Hong Liang, Roshanak Shafiiha, Dazeng Feng, Guoliang Li, John E Cunningham, Ashok V Krishnamoorthy, Mehdi Asghari, and Xin Wang. *Thermally tunable silicon racetrack resonators with ultralow tuning power.* Optics express, 18(19):20298–304, September 2010.

[6] Adil Masood, Marianna Pantouvaki, Guy Lepage, Peter Verheyen, and Joris Van Campenhout. *Comparison of heater architectures for thermal control of silicon photonic circuits*. In Group IV Photonics (GFP), 2013 IEEE 10th International Conference on, page ThC2, 2013.

7

Conclusion and perspectives

7.1 Conclusion

Silicon ring resonators were used to develop two types of very compact and high performance WDM-signal demultiplexing receivers around $1550\,\mathrm{nm}$. The successful integration on a Si platform allows for very cost-effective and mass - manufacturable components.

The first demonstrated receiver is a WDM in-band label extractor with an ultra-dense channel spacings between $12.5-25$ GHz. This label contains the forwarding information that can be used to configure an all-optical packet switch. The second one is a dense WDM data demultiplexer with channel spacings between $100-300$ GHz. This demultiplexer has been optimized to be fabrication tolerant, simple to control for wafer-level fabrication variations and/or laser wavelength drifts and to increase the aggregate bandwidth per fiber (e.g. Ethernet, Infiniband and Fiber Channel).

For both demonstrations several important design improvements were needed in order to meet the required specifications. We believe that we have significantly enhanced the state-of-the-art performance of ring resonators. Two classes of ring resonators were used: a narrow-bandwidth first order ring resonator which is tolerant against sidewall roughness of a waveguide and a broad second-order ring resonator which is tolerant against local fabrication variations.

Ultra-dense WDM label extractor The high confinement of Si waveguides enables very short bend radii which results in very compact and dense structures. However, we found that standard strip waveguides using the quasi-TE polarization suffer from surface-roughness induced backscattering. In narrow-bandwidth ring resonators, the effect of backscattering is enhanced and the required bandwidth of $20\,\mathrm{pm}$ is not reached. Additionally, for certain wavelengths the resonances split, which leads to large fluctuations in both insertion loss and extinction ratio. We also found that due to this backscattering, the reflected power ratio can reach up to $-10\,\mathrm{dB}$ which can possibly cause severe problems at the transmitting laser. Using less confined modes enabled us to design narrow-bandwidth ring resonators that exhibit bandwidths $20\,\mathrm{pm}$ which are free from resonance splitting and an IL of only $3\,\mathrm{dB}$. The reflected power ratio decreased with almost $10\,\mathrm{dB}$. We validated this solution using two types of waveguide, a shallowly-etched waveguide using a quasi-TE mode and a strip waveguide but using the quasi-TM mode. Both approaches are reducing the overlap with the vertical sidewalls, where the roughness is the most severe.

A four-channel ultra-dense WDM label extractor is used to extract error-free an in-band label consisting out of four wavelengths from a highly modulated payload $160\,\mathrm{Gb/s}$ in collaboration with the COBRA group from TU/e. A heterogeneously-integrated InGaAs p-i-n photodiode has been optimized to exhibit a high responsivity for both the TE and TM mode (with an efficiency of respectively 98% and 89%) and is used to convert the optical WDM-label to the electrical domain with a bandwidth of $> 12\,\mathrm{Gb/s}$.

Dense WDM data demultiplexer We have explored the adoption of WDM to increase the aggregate bandwidth of an optical interconnect. By cascading several ring resonators with a small circumference difference between them, one can easily create a scalable demultiplexer. Using second-order ring resonators, the bandwidth can be considerably broadened without relaxing the crosstalk between the channels. We have addressed three typical challenges using WDM demultiplexers based on ring resonators: manufacturability, an simple thermal control and polarization insensitivity. We have demonstrated a robust 4-channel WDM filter using collective tuning. The flat-top response of second-order ring filters is exploited to overcome the wafer- and device-scale irregularities on channel spacing and channel bandwidth arising from fabrication non-uniformity. The improved filter response enables a thermal control mechanism based on collective tuning to track the wavelengths of a WDM laser source on a specified channel grid. After collective tuning with integrated heaters, the 4-channel second-order filter exhibits a worst-channel insertion loss of $-1.39\,\mathrm{dB}$ and a crosstalk of $-18.2\,\mathrm{dB}$ (wafer-level average). By integrating monolytically-grown high-speed Ge photodiodes, a 5-channel $300\,\mathrm{GHz}$-spaced WDM Ge receiver has been demonstrated with a clear open-eye diagram at $20\,\mathrm{Gb/s}$. The polarization-insensitive fiber-referenced response is high ($0.1\,\mathrm{A/W}$) and uniform over all channel responses with a channel crosstalk better than $-15\,\mathrm{dB}$.

An important issue in the current demonstrated WDM receiver is the large power consumption of the heaters, which needs a serious improvement to cope with implementations such as PAM, PSM or CWDM. By lowering the overlap with the interconnecting metal we can minimize an important heat sink and hence maximizing the insulation improvement of a substrate removal step. Initial measurements on a first design optimization have shown a 180% improvement in efficiency with a resulting P_π of $3.2\,\mathrm{mW}$. With this efficiency it cost $12.9\,\mathrm{mW}$ per channel to shift a full FSR. With a polarization diversity circuit this power consumption is doubled to $25.8\,\mathrm{mW}$. Using a bit rate of $25\,\mathrm{Gb/s}$, the power consumption of $1\,\mathrm{pJ/bit}$ (worst case) is reached. A bidirectional single-stage design was also proposed which will half the power consumption but this idea was not implemented in this work.

Further research on Ge photodiodes has shown that the bandwidth can easily be scaled to $50\,\mathrm{Gb/s}$ and possibly faster. We also have shown that by using an advanced fabrication technology on $300\,\mathrm{mm}$ wafers, the amount of channels can easily be increased to 10. This would enable ultra-compact WDM receivers up to $500\,\mathrm{Gb/s}$ in the very near future.

7.2 Perspectives

We believe that the future of Si WDM receivers is very promising. One possible future path is the further integration of CMOS-compatible WDM modulators on the same chip with a flip-chip bonded CMOS integrated modulator drivers and trans-impedance amplifiers. Another future path is the further integration with active III-V components to enable a truly heterogeneously integrated optical switch. The ever-growing attention on Si photonics gives rise to an exponential range of possibilities coming from further technology improvements and packaging, both leveraging other semiconductor technologies. These synergies will enable several breakthroughs in power consumption, e.g. improved CMOS nodes, 3D stacking and microlenses for efficient coupling among many others.